

National and Kapodistrian University of Athens

PhD thesis

**The impact of super massive black holes on star
formation**

Michalis Papachristou

December 21, 2023

Abstract

Observational evidence suggests that the Star formation process in the universe peaked at 3.5 billion years after the Big Bang and declined in the last 10 billion years. While this decline can be partially associated with star formation itself, since stars consume gas and only return a small percentage of gas back to the galactic reserve, cosmological simulations cannot reproduce today's galactic mass distribution in the high-mass branch. This hints at the existence of additional mechanisms negatively impacting star formation in high-mass galaxies.

The presence of supermassive black holes and their impact on their galactic host environment have been proposed as one of the main contributors to this negative feedback effect. As black holes grow in the center of the galaxies, it emits energy from its accretion disk either in the form of radiation pressure or as relativistic plasma jets. This energy can be coupled with the interstellar medium (ISM), affecting the molecular gas essential for forming new stars. Simulating this contribution in cosmological simulations succeeds in reproducing the expected mass distribution in the local universe.

Studies of hydrodynamic simulations of jets propagating through the ISM have shown that they can be a very efficient mechanism for providing this ISM-AGN coupling. Shocks produced from this jet-ISM interaction sweep large areas of a galaxy, heating and causing turbulence in the ISM as the jet percolates and breaks freely into intergalactic space.

This thesis aims to further investigate the jets as feedback mechanisms. In the first part, we focus on constructing and analyzing a radio-selected, multi-epoch, sample of galaxies observed in CO emission lines in the millimeter part of the electromagnetic spectrum to understand their molecular gas content in low and high redshift. This work utilizes a combination of ALMA observations, either as target observations or byproducts of calibration, and measurements from the literature. We detected CO emission in 35% of the sample radio galaxies, with molecular masses ranging from $10^7 < M_{\text{mol}} < 7 \times 10^{10} M_{\odot}$ at low- z and $2 \times 10^{10} \ll M_{\text{mol}} < 7 \times 10^{11} M_{\odot}$ at high- z . In the local universe, the number of sources with detectable molecular gas was slightly lower compared to other types of active galaxies (AGN1 and AGN2), but comparable when adjustments were made for missing radio galaxies. This finding suggests that radio galaxies and these other active galaxies might have similar gas contents in the local universe, aligning with simulation expectations. Also, RGs with a high gas content ($> 10^{10} M_{\odot}$) were not significantly lower with star-forming AGNs, suggesting that they are not entirely "red and dead". At higher redshifts, the observed radio galaxies had a significant amount of molecular gas, with about 1/4 of them having molecular gas amounts comparable to what simulations suggest for typical galaxy halos of that epoch. For the brightest sources, there is a consistency in molecular gas content across all epochs, suggesting that the interplay of inflows, star formation, and radio-mode feedback maintains a certain level of molecular gas.

Another goal of this survey was to lead to the detection of molecular outflows. In the second part of this thesis, we present a detailed kinematic analysis of one of the two sources with obvious kinematic deviations: the early-type galaxy NGC6328, which hosts the closest known Gigahertz Peaked radio Source (GPS) PKS1718-649. The data cubes for the re-calibrated CO(2-1) and CO(3-2) ALMA archival data revealed that the molecular gas had a highly complicated geometry that could not be estimated with any tool available in the literature. Thus, we created a novel accurate warped disk model that incorporates the evolution of the disk due to gravitational potential torques together with the effect of viscous forces. The fitting of the data and the model was done using a Bayesian framework on parameter and model estimation. This choice provided us the opportunity to combine multiple datasets (HI velocities, photometry, dust obscuration patterns) into a single probabilistic model, which resulted in a distribution of possible geometry and mass potential models. These models jointly point out the scenario of a highly warped molecular disk emerging from a merger incident estimated at 400 – 800 Myr ago. From the residuals of the fit, we detect two molecular outflows in the central 200 pc of the galaxy. The outflows, validated through gas excitation analysis and newly observed ionized gas outflows, have a total mass outflow rate of $3 M_{\odot} \text{ yr}^{-1}$ and a kinetic power of $2 - 7 \times 10^{40} \text{ erg s}^{-1}$, which suggests jet-driven outflows as the most plausible scenario for their acceleration. This adds NGC6328 to

the catalog of sources, along with NGC1377, 4C 31.04, ESO 420-G13 and HE 00401105, where jet-induced outflows are detected but outside the current radio emission of the jet.

Motivated by this observation, we delved into various mechanisms and revisited the likelihood of a connection between published molecular outflows and jets. In the third part of this thesis, we conducted a meta-analysis encompassing a sample of 45 local galaxies with detected molecular outflows, augmented by the inclusion of galaxies NGC6328, NGC1377, 4C 31.04, and ESO 420-G13. Our analysis revealed that, for at least half of this extended sample, the jets align both energetically and geometrically with the observed outflows, positioning them as a significant or even dominant mechanism in driving these outflows.

Εκτεταμένη Περιληψη

Όπως αποδεικνύεται από παρατηρησιακά δεδομένα ο ρυθμός παραγωγής αστέρων στο Σύμπαν μειώνεται κατά τη διάρκεια των τελευταίων 10 δισεκατομμυρίων ετών, μια μείωση που αποδίδεται στην ίδια τη δημιουργία των αστέρων και του μικρού ποσοστού αερίου που αυτά επιστρέφουν πίσω στο γαλαξιακό απόθεμα. Προσομοιώσεις εξέλιξης γαλαξιών, χρησιμοποιώντας τις παρατηρήσεις αυτές, αδυνατούν να αναπαράξουν τη σημερινή παρατηρούμενη κατανομή των γαλαξιακών μαζών κυρίως στη περιοχή των γαλαξιών μεγάλης μάζας χωρίς τη χρήση επιπλέον μηχανισμών αρνητικής επίδρασης στο ρυθμό δημιουργίας αστέρων. Οι κύριοι μηχανισμοί που έχουν προταθεί βασίζονται στην υπαρξη γαλαξιακών ανέμων του μοριακού αερίου οι οποίοι εμποδίζουν τη βαρυτική κατάρρευση του κρούου μοριακού αερίου και άρα τη δημιουργία αστέρων είτε λόγω θέρμανσης του είτε λόγω της εκτόξευσης του στο διαγαλαξιακό χώρο. Οι διαφορές μεταξύ των μηχανισμών εγκείται στη πηγή των ανέμων αυτών, η οποία μπορεί να είναι ένας αυξημένος ρυθμός εκρήξεων σουπερνόβα ή το αποτέλεσμα της δραστηριότητας υπερμαζικών μελανών οπών στα κέντρα των γαλαξιών. Σε αυτήν την εργασία εστίασαμε στη δυνατότητα του ενεργού πυρήνα των ενεργών γαλαξιών στο να εναποθέτουν ενέργεια στο μεσοαστρικό περιβάλλον και πιο συγκεκριμένα στη σημαντικότητα των σχετικιστων πιδάκων. Η απόδοση του μηχανισμού αυτού υποστηρίζεται από υδροδυναμικές προσομοιώσεις και πλήθος παρατηρήσεων στο κοντινό Σύμπαν. Για τη πλήρη διερεύνηση του φαινομένου χρειαζόμαστε παρατηρήσεις που να καλύπτουν διαφορετικές φάσεις της ιστορίας του Σύμπαντος.

Για αυτό το λόγο χρησιμοποιήσαμε τη συστοιχία ραδιοτηλεσκοπίων ALMA καθώς αυτή προσφέρει παρατηρήσεις μεγάλης ευασθησίας, μεγάλη διακριτική ικανότητα και ελεύθερο αρχείο παρατηρήσεων πηγών που χρησιμοποιήθηκαν σαν στόχοι ή σαν στόχοι βαθμονόμησης μεμονωμένων παρατηρήσεων. Αναζητήσαμε εκτενώς στη βιβλιογραφία ακριβείς φασματοσκοπικές μετρήσεις της ερυθρομετατόπισης ραδιοφωνικών πηγών που έχουν παρητηρηθεί από την ALMA ώστε μαζί με τη πληροφορία του φασματικού παραθύρου των παρατηρήσεων να μπορούμε να αναζητήσουμε το φασματικό περιεχόμενο που μας ενδιαφέρει να μελετήσουμε (γραμμές εκπομπής). Μέσω της παραπάνω διαδικασίας αναζητήσαμε πηγές οι οποίες περιέχουν τις 4 λαμπρότερες γραμμές εκπομπής μονοξειδίου του άνθρακα, ενός μορίου που εκπέμπει στο ενεργειακό παράθυρο των μικροκυμαων και σε συνθήκες που είναι ευνοϊκές για τη δημιουργία αστέρων (πυκνό, ψυχρό αέριο). Στις πηγές που συλλέξαμε προστέθηκαν και παρατηρήσεις απο την βιβλιογραφίας ώστε να μεγιστοποιήσουμε το δείγμα μας.

Για να μπορέσουμε να βγάλουμε συμπεράσματα για τις ιδιότητες των ενεργών γαλαξιών ανα εποχή, χρειαζόμαστε ένα στατιστικό δείγμα το οποίο να είναι αντιπροσωπευτικό του ουρανού στο ραδιοφωνικό εύρος του φάσματος, οπου έχουμε ισχυρή εκπομπή των γαλαξιών αυτών. Γι αυτό το σκοπό συγκρίναμε τη ροή ακτινοβολίας των πηγών μας σε συγκεκριμένες μπάντες του ραδιοφωνικού φάσματος για τις οποίες έχουμε στη διάθεση μας συνοπτικές και πλήρης καταλόγους όλου του ουρανού. Συγκεκριμένα επιλέξαμε τη συνοπτική επισκόπηση του ραδιο-ουρανού NRAO/VLA Sky Survey (NVSS) στα 1.4 GHz την οποία και συγκρίναμε με τη αντίστοιχη ραδιοφωνική εκπομή των επιλεγμένων πηγών. Η επιλογή του του τελικού δείγματος έγινε μέσω μιας διαδικασίας η οποία συγκρίνει τη κατανομή των ροών ενός υπο-συνόλου του δείγματος μας με τον κατάλογο NVSS, μετρώντας της μέγιστη απόσταση μεταξύ των αθροιστικών συναρτήσεων των κατανομών (D-statistic). Καθώς μειώνουμε το πλήθος του υποσυνόλου, επιλέγουμε το βέλτιστο υπό-δείγμα όπου η απόσταση είναι η ελάχιστη. Συνεχίζουμε να μειώνουμε το πλήθος, μέχρις ότου η βέλτιστη αυτή απόσταση γίνει μικρότερη από μια κρίσιμη τιμή. Η κρίσιμη αυτή τιμή, εξαρτάται από το πλήθος του υπο-δείγματος καθώς το μέγεθος του καταλόγου παραμένει σταθερό. Για την εκτίμηση της, χρησιμοποιήσαμε την ίδια διαδικασία συγκρίνοντας αντί για το δείγμα μας, ένα υποσύνολο του NVSS 1.4 όπου οι μετρήσεις έχουν επιλεχθεί τυχαία εντός των 3 της τυπικής απόκλισης των σφάλματων των μετρήσεων του καταλόγου.

Καταλήξαμε έτσι σε ένα τελικό δείγμα 120 γαλαξιών. Για τις 66 πηγές από τον κατάλογο CO-ARC, εκτελέσαμε ξανά τις διαδικασίες βαθμονόμησης, σύνθεσης και φιλτραρίσματος των τελικών αποτελεσμάτων από τα πρωταρχικά δεδομένα. Αυτό ήταν αναγκαίο γιατί ακόμα και αν κάποιοι από τους γαλαξίες είχαν παρατηρηθεί και σαν στόχοι με επιστημονικό περιεχόμενο, οι παράμετροι για τη σύνθεση των τελικών μετρήσεων που χρησιμοποιήθηκαν από τον πρωταρχικό παρατηρητή (PI), δεν είναι οι βέλτιστοι για το σκοπό μας. Σε

δύο από τις πηγές εντοπίστηκαν νέοι μοριακοί άνεμοι. Συνολικά εντοπίστηκε μοριακό αέριο στο 35% των πηγών από το CO-ARC. Για το συνολικό δείγμα οι πηγές χωρίστηκαν ανάλογα το redshift δημιουργώντας 3 διαφορετικές ισόχρονες εποχές στην κοσμική ιστορία (60 πηγές στο $0.005 < z < 0.3$, 23 πηγές στο $0.3 < z < 1$ και 37 πηγές στο $1 < z < 2.5$).

Συνοπτικά τα αποτελέσματα της μελέτης του δείγματος, δημοσιεύθηκαν από την Audibert et al. 2022, δείχνουν ότι στο τοπικό Σύμπαν, ο αριθμός των ραδιο-πηγών όπου εντοπίσαμε μοριακό αέριο ήταν ελαφρώς λιγότερος από τους αντιστοιχούς άλλου τύπου ενεργούς γαλαξίες, κάτι που συμφωνεί με τις κοσμικές προσομοιώσεις. Σε μεγαλύτερες ερυθρομετατοπίσεις εντοπίστηκαν σημαντικά μεγαλύτερες ποσότητες μοριακού αερίου. Στις ραδιοφωνικά ισχυρότερες πηγές η ποσότητα του αερίου ήταν παρόμοια ανεξαρτήτως της εποχής, κάτι το οποίο πιθανότατα δείχνει ότι ο ρυθμός που το αέριο καταναλώνεται στη δημιουργία αστερών και ο ρυθμός που το αέριο εισρέει στο γαλαξία είναι παρόμοιος, μέσω της αντιστάθμισης που προκαλεί ο πίδακας.

Σε μια από τις πηγές του CO-ARC κατά τη πρωιμη ανάλυση, εντοπίσαμε έντονες κινηματικές διακυμάνσεις μη συμβατές με την κινηματική υπογραφή ενός δίσκου. Η ραδιο - πηγή αυτή, με το όνομα PKS 1718-649 βρίσκεται στο κέντρο του ελλειπτικού γαλαξία NGC6328, και έχει παρατηρηθεί από την ALMA στη περιστροφική γραμμή εκπομπής J=2-1 του μονοξειδίου του άνθρακα και εντός ενός παραθύρου για την αντίστοιχη γραμμή J=3-2. Η ραδιο εκπομπή στο γαλαξία προέρχεται από μια μικρή περιοχή με τη μορφή δύο συμπαγών ραδιο-λοβών σε απόσταση μερικών parsec από το κέντρο. Το ραδιοφωνικό φάσμα της πηγής ακολουθεί μια τυπική καμπύλη ενός Gigahertz Peaked Radio Source (GPS) με μέγιστο στα 3.2 GHz το οποίο συμφωνεί σε πολύ καλό βαθμό με το free-free absorption model (FFA). Το μοντέλο αυτό, όπως και αντίστοιχες προσομοιώσεις, δείχνουν ότι μια τέτοια φασματική υπογραφή παρατηρείται σε νεαρούς πίδακες καθώς προσπαθούν να διασχίσουν την πυκνή γαλαξιακή ύλη. Η αλληλεπίδραση του πίδακα με την ύλη δημιουργεί κρουστικά κύματα τα οποία την ιονίζουν. Η ιονισμένη ύλη με τη σειρά της απορροφά το χαμηλο-ενεργειακό μέρος της ακτινοβολίας synchrotron του πίδακα με αποτέλεσμα να σχηματίζεται το μέγιστο.

Ο γαλαξίας NGC6328 βρίσκεται σε μια σχετικά μικρή απόσταση, στα 62 Mpc ($z=0.014313$), κάνοντας τη πηγή PKS 1718-649 τη κοντινότερη PS πηγή που έχουμε ανακαλύψει και άρα πολύ σημαντική στη προσπάθειά μας να κατανοήσουμε το ρόλο των πιδάκων στη γαλαξιακή εξέλιξη. Η εκπομπή στο οπτικό φάσμα του γαλαξία κυριαρχείται από μία ελλειπτική αστρική άλω (bulge) με προφίλ το οποίο συμφωνεί με πολύ καλή προσέγγιση με τη κατανομή μάζας Hernquist. Λόγω του ελλειψοειδούς σχήματος μοντελοποιούμε μια τροποποιημένη μορφή της παραπάνω κατανομής όπου οι ισούψεις της πυκνότητας σχηματίζουν ένα ελλειψοειδές.

Η συστοιχία ALMA μπορεί να δημιουργήσει παρατηρήσεις εξαιρετικά υψηλής ανάλυσης χρησιμοποιώντας τη τεχνική της ραδιοσυμβολομετρίας, μετατρέποντας τις μετρήσεις πολλών κεραιών στο επίπεδο της Γης σε δεδομένα στο ουράνιο επίπεδο μέσω ενός μετασχηματισμού Fourier. Λόγω του μεγάλου χρόνου παρατήρησης και στις δύο γραμμές CO(2-1), CO(3-2) χρησιμοποιήθηκε και η τεχνική της ιδιο-βαθμονόμησης (self calibration) όπου χρησιμοποιούμε την ισχυρή εκπομπή του γαλαξία για να διορθώσουμε τη διαφορά φάσης ανάμεσα στις κεραίες και άρα να αποκτήσουμε τη καθαρότερη δυνατή εικόνα. Η συνολική μάζα του μοριακού αερίου εκτιμάτε στις $1.1 \times 10^9 M_{\odot}$ ηλιακές μάζες ανάλογα χρησιμοποιώντας το συντελεστή μετατροπής $\alpha_{CO} = 4.6$ για ψυχρό και πυκνό αέριο παρόμοιο με αυτό του Γαλαξία μας.

Μέσω της μελέτης της μέσης ταχύτητας παρατηρούμε ότι το αέριο υπόκειται σε ένα ή περισσότερους δίσκους με πολύπλοκη κινηματική. Εντός μια ακτίνας 600 pc παρατηρούμε ένα δίσκο (με μέγιστο άξονα 72 μοιρών από το βορρά) που αγγίζει μια μέγιστη προβολική ταχύτητα των 300 km s^{-1} , ενώ χαρακτηρίζεται και από μεγάλη διασπορά, της τάξης 100 km s^{-1} . Στη συνέχεια η θέση της μέγιστης μέσης ταχύτητας κινείται από τις 100 μέχρι και τις 180 μοίρες από το βορρά σε μια απόσταση 3.5 kpc, ενώ ταυτόχρονα ο δίσκος φαίνεται να γίνεται όλο και πιο κάθετος σε σχέση με τη γραμμή παρατήρησης. Αυτή η συμπεριφορά φανερώνει ότι μάλλον έχουμε να κάνουμε με ένα στρεβλο δίσκο, δηλαδή ένα δίσκο που αλλάζουν τα γεωμετρικά του χαρακτηριστικά με την απόσταση από το κέντρο. Η συμπεριφορά αυτή είναι εμφανής και σε ακτίνες μεγαλύτερες των 10 kpc μελετώντας τη κινηματική του ουδέτερου υδρογόνου. Η στρέβλωση αυτή μπορεί να συμβεί κατά τη διάρκεια κανιβαλισμού ή εισροής ύλης από γειτονικό γαλαξία όπου δημιουργείται ένας δίσκος υπό γωνία σε σχέση με τον άξονα συμμετρίας της κατανομής μάζας του γαλαξία, όταν αυτή δεν είναι απόλυτα σφαιρική. Ο δίσκος σε αυτή τη περίπτωση μεταπίπτει με ρυθμό που εξαρτάται από τη γωνιακή ταχύτητα, την αρχική γωνία και την ελλειπτικότητα της κατανομής μάζας του γαλαξία. Καθώς όμως η γωνιακή ταχύτητα των εσωτερικών στιβάδων του δίσκου είναι μεγαλύτερη τότε αυτές παρουσιάζουν και μεγαλύτερη μετάπτωση.

Μελετώντας αντίστοιχα και τη διασπορά των ταχυτήτων παρατηρούμε περιοχές με πολύ υψηλή διασπορά (80 km s^{-1}) στο εσωτερικό κομμάτι του δίσκου ($< 700 \text{ pc}$) αλλά και περιοχές αντιδιαμετρικά του κέντρου σε αποστάσεις της τάξης του 1 kpc , συγκριτικά με τις πιο απομακρυσμένες περιοχές του δίσκου όπου η διασπορά είναι της τάξης των $20\text{--}30 \text{ km s}^{-1}$. Μοντελοποιήσαμε το δίσκο του μοριακού αερίου υιοθετώντας ένα μοντέλο κεκλιμένων δαχτυλιδιών το οποίο μπορεί να προσεγγίσει έναν ομοιογενή αλλά και έναν στρεβλό δίσκου κάνοντας τη παραδοχή ότι στο γαλαξία κάθε δαχτυλίδι εκτελεί κυκλική τροχιά με κυκλική ταχύτητα που εξαρτάται από την ακτίνα, σε ένα επίπεδο το οποίο μπορεί να είναι διαφορετικό για κάθε ακτίνα. Στην ακτίνα παρατήρησης η κάθε τροχιά μετασχηματίζεται σε μια έλλειψη λόγω προβολικών φαινομένων η οποία χαρακτηρίζεται από δύο παραμέτρους για κάθε ακτίνα, την παρατηρούμενη εκκεντρότητα (*inclination*) και τη γωνία στην οποία βρίσκεται ο μέγιστος άξονας σε σχέση με το Βορρά (*position angle*). Γνωρίζοντας τις συναρτησιακές σχέσεις για το *inclination*, το *position angle* και τη κυκλική ταχύτητα σε σχέση με την ακτίνα μπορούμε να κατασκευάσουμε ένα μοντέλο για την παρατηρούμενη κατα μήκος της γραμμής παρατήρησης ταχύτητας σε κάθε σημείο του χώρου. Συγκρινόμενη αυτή η ταχύτητα με τις παρατηρούμενες των αντίστοιχων νεφών του μοριακού αερίου από τα δεδομένα μπορούμε να εκτιμήσουμε το καλύτερο δυνατό μοντέλο, ελαχιστοποιώντας τη μέση διαφορά ταχυτήτων μεταξύ μοντέλου και παρατηρήσεων. Για τη βελτιστοποίηση της διαδικασίας αυτής αρχικά κατασκευάσαμε έναν αλγόριθμο ο οποίος εντοπίζει, στο τρισδιάστατο χώρο θέσεων και ταχυτήτων, τα διακριτά νέφη που απαρτίζουν τον γαλαξία.

Για να μπορέσουμε να χτίσουμε ένα μοντέλο που είναι πιο ρεαλιστικό αλλά και ευκολότερα ερμηνεύσιμο επιλέξαμε να παραμετροποιήσουμε τα δαχτυλίδια του δίσκου στο επίπεδο του γαλαξία, μέσω δύο γωνιών $\lambda(r)$ και $\theta(r)$ που περιγράφουν το μοναδιαίο διάνυσμα κάθε δαχτυλιδιού. Εφόσον έχουμε τις γωνίες $\lambda(r)$ και $\theta(r)$ μπορούμε να μεταφερθούμε στις συνήθεις γωνίες στον ουρανό μέσω ενός πίνακα στροφής που παραμετροποιούμε μέσω ενός διανυσματος το οποίο καταδεικνύει το κατεύθυνση του ζ άξονα των γαλαξιακών συντεταγμένων όπως διακρίνεται από τη Γη. Έτσι, εισάγαμε δύο ακόμα παραμέτρους που καλούμαστε να εκτιμήσουμε, για τις οποίες όμως έχουμε μια ικανοποιητική αρχική εκτίμηση από τις εικόνες της αστρικής κατανομής. Για τη ταχύτητα περιστροφής, χρησιμοποιήσαμε το προφίλ του *Herpin*, σύμφωνα με την ανάλυση που δώσαμε προηγουμένως, για την αστρική Άλω, το προφίλ *Navarro-Frenk-White (NFW)* για τη σκοτεινή Άλω και ένα κεπλεριανό προφίλ για τη μελανή οπή στο κέντρο του γαλαξία. Στη συνέχεια χρησιμοποιήσαμε δύο διαφορετικές προσεγγίσεις για τις συναρτησιακές σχέσεις των γωνιών $\lambda(r)$ και $\theta(r)$. Στη πρώτη προσέγγιση θεωρούμε την θέση των δαχτυλιδιών σαν ένα στιγμιότυπο στο χρόνο μια διαδικασίας κανιβαλισμού μεταξύ γειτονικών γαλαξιών. Ο δίσκος του αερίου σε αυτή τη περίπτωση ήταν αρχικά υπό γωνία σε σχέση με τον άξονα συμμετρίας του βαρυτικού δυναμικού από την αστρική άλω με αποτέλεσμα το φαινόμενο της διαφορικής μετάπτωσης. Δηλαδή το δυναμικό λόγω μη σφαιρικής συμμετρίας ασκεί ροπή στο δίσκο ώστε αυτός να μεταπίπτει με διαφορετικό ρυθμό σε κάθε απόσταση από το κέντρο, λόγω διαφορετικής ταχύτητας περιστροφής. Όμως τα γειτονικά δαχτυλίδια ασκούν δυνάμεις μεταξύ τους οι οποίες εξαρτώνται από τη σχετική τους θέση. Έτσι, μετά από κάποιο χρονικό διάστημα εν τέλει τα δαχτυλίδια ευθυγραμμίζονται μεταξύ τους και με έναν από τους άξονες συμμετρίας του δυναμικού. Με βάση ένα σετ των διαφορικών εξισώσεων που προκύπτουν από την παραπάνω διεργασία κατασκευάσαμε δύο διαφορετικά μοντέλα, ένα ενός δυναμικού με αξισυμμετρία (*model A*) και ενός τριαξονικού (*model B*). Τα δύο αυτά μοντέλα έχουν συνολικά 12 και 13 παραμέτρους αντίστοιχα.

Στη συνέχεια χρησιμοποιήσαμε και μια δεύτερη, περισσότερο γενικευμένη, προσέγγιση σχετικά με τη γεωμετρία του δίσκου, παρόμοια με αυτή που χρησιμοποιείται από εργαλεία που ήδη υπάρχουν στην βιβλιογραφία. Σε αυτή η γεωμετρική σύνδεση μεταξύ γειτονικών δαχτυλιδιών επιβάλλεται μέσω μεθόδων *interpolation*. Στη δική μας περίπτωση επιλέξαμε λείες κυβικές καμπύλες (*monotonic cubic splines*) οι οποίες καθορίζονται από 10 σημεία η καθεμία ώστε η γεωμετρία του συστήματος να έχει ελευθερία κινήσεων χωρίς απότομες αλλαγές. Η αρχική τιμή των σημείων αυτών καθορίστηκε επίσης από τις καλύτερες λύσεις των προηγούμενων μοντέλων. Έτσι δώσαμε περισσότερους βαθμούς ελευθερίας στο μοντέλο (*Model C*) ώστε να εντοπίσει λύσεις κοντά σε αυτές που θεωρούμε ότι προσεγγίζουν καλύτερα τη φυσική διαδικασία. Το μοντέλο αποτελείται από 26 παραμέτρους, 20 για τα σημεία θ_i, λ_i σε συγκεκριμένες ακτίνες και τις παραμέτρους που αφορούν τη καμπύλη περιστροφής.

Και στα 3 μοντέλα αναζητούμε τις καλύτερες παραμέτρους συγκρίνοντας το μοντέλο με τα παρατηρησιακά δεδομένα προσπαθώντας να εντοπίσουμε τη πιθανότερη *posterior* τιμή τους μέσω ενός αλγορίθμου *Markov Chain Monte Carlo (MCMC)*. Η *posterior* κατανομή που αναζητούμε για τις παραμέτρους προκύπτει από

τη συσχέτιση της πιθανοφάνειας να παρατηρήσουμε τις ταχύτητες των νεφών των δεδομένων “δεδομένου” του εκάστοτε μοντέλου μαζί με τυχόν πρωθύστερες (prior) πληροφορίες σε σχέση με τις παραμέτρους. Στη ποστεrior προσθέσαμε και την πιθανοφάνεια των παρατηρούμενων ταχυτήτων περιστροφής του ουδέτερου υδρογόνου στα εξωτερικά μέρη του γαλαξία. Για τις πιθανοφάνειες αυτές χρησιμοποιήσαμε **multidimensional Gaussian** κατανομές ενώ οι **prior** κατανομές των παραμέτρων είναι ομοιογενείς (**uniform**) στη περίπτωση που δεν έχουμε κάποια πρωθύστερη πληροφορία ή **Gaussian** για όταν έχουμε κάποια εκτίμηση με τιμή και σφάλμα. Τέτοιες μπορεί να είναι η εκτίμηση για παράδειγμα της μάζας των αστεριών, η διασπορά/ταχύτητα σε κάποια συγκεκριμένη θέση, και γεωμετρικές μετρήσεις σε συγκεκριμένες αποστάσεις, πχ από τη παρατήρηση της σκόνης. Τα αποτελέσματά μας συμφωνούν αρκετά καλά με τις παρατηρήσεις με εξαίρεση 4 περιοχές, δύο στην περιοχή του μικρότερου κεντρικού δίσκου και δύο σε απόσταση της τάξης του 1 kpc.

Ειδικότερα στις κεντρικές περιοχές, που βρίσκονται σε αποστάσεις 100-300 pc από το κέντρο, αποδεικνύουμε ότι οι αποκλίσεις αυτές δεν μπορούν να εξηγηθούν με το μοντέλο των δαχτυλιδιών ακόμα και αν δοκιμάσουμε και διαφορετικές κατανομές του δυναμικού και των γεωμετρικών χαρακτηριστικών τους. Επομένως πρόκειται για αέριο το οποίο δεν βρίσκεται σε κυκλική, ή σχεδόν κυκλική κίνηση. Επίσης εφόσον βρίσκεται σε αποστάσεις μεγαλύτερες των 100 pc από τη κεντρική μελανη σπή, αυτή δεν μπορεί να έχει επιρροή πάνω στη δυναμική τους, ώστε να εξηγείται η μεγάλη ταχύτητα για την ακτίνα αυτή. Πρόκειται λοιπόν για αέριο το οποίο είτε κινείται σε σπειροειδή κίνηση προς το κέντρο του γαλαξία είτε για αέριο το οποίο έχει επιταχυνθεί από κάποιο τοπικό μηχανισμό.

Επίσης, εξετάζοντας τη διέγερση του αερίου μέσω της αναλογίας των δύο γραμμών στο χώρο παρατηρούμε ότι οι περιοχές αυτές είναι διεγερμένες κάτι το οποίο συμφωνεί με παρατηρήσεις του μοριακού αερίου που αλληλεπιδρά βίαια με το πίδακα του γαλαξία, όπως στο κοντινό γαλαξία IC5063. Το σενάριο της αλληλεπίδρασης του αερίου με τον πίδακα στο γαλαξία NGC6328 γίνεται ακόμα πιο πιθανό εξετάζοντας τη γεωμετρική θέση και ταχύτητα των εξεταζόμενων νεφών σε σχέση με τον άξονα του αν τον επεκτείνουμε μέχρι την απόσταση που μας ενδιαφέρει, όπως φαίνεται στο παρακάτω διάγραμμα. Η εκτίμηση του ακριβούς προσανατολισμού του πίδακα έγινε μέσω της σύγκρισης του βόρειου λοβού που κατευθύνεται προς εμάς σε σύγκριση με τον αντίστοιχο λοβό στην αντιδιαμετρική διεύθυνση. Λόγω της σχετικιστικής κίνησης του πίδακα η ροή ακτινοβολίας **synchrotron** στο βόρειο λοβό φαίνεται ισχυρότερη (**boosting**) σε σχέση με την αντίστοιχη στο νότιο. Χρησιμοποιώντας τα βιβλιογραφικά ραδιοφωνικά δεδομένα υπολογίσαμε τη γωνία μεταξύ του πίδακα και της ακτίνας παρατήρησης στις 68 περίπου μοίρες.

Τέλος, εξετάσαμε την ενέργεια και την ορμή που απαιτείται ώστε να έχουμε την απαραίτητη επιτάχυνση των εκροούμενων νεφών. Εκτιμώντας τη μάζα του αερίου στα $2 \times 10^6 M_{\odot}$ και τη μέση ταχύτητα της εκροής βρίσκουμε ότι η ροή μάζας είναι περίπου $3 M_{\odot} \text{ yr}^{-1}$ με κινητική ισχύ $2 - 7 \times 10^{40} \text{ erg/s}$ και ρυθμό παροχής ορμής $3 \times 10^{33} \text{ dyn}$.

Η ενέργεια και η ορμή είναι 1 με 2 τάξης μεγέθους μεγαλύτερη από την ενέργεια που μπορεί να προσδώσουν τα αστέρια μέσω πίεσης ακτινοβολίας ή εμμέσως μέσω εκρήξεων **supernova** χρησιμοποιώντας τις μέγιστες τιμές του ρυθμού παραγωγής αστεριών ($0.8 - 1.8 M_{\odot} \text{ yr}^{-1}$) και το ποσοστό αστρικής μάζας εντός των 300 parsec (1.2% της συνολικής μάζας). Την ίδια στιγμή ο ενεργός πυρήνας δεν έχει την απαραίτητη ισχύ ώστε η πίεση ακτινοβολίας να μπορέσει να προσδώσει την απαραίτητη ορμή, ακόμα και αν χρησιμοποιήσουμε έναν πολλαπλασιαστικό παράγοντα της τάξης του 20, από το μέγιστο αριθμό πολλαπλών σχεδασεων των φωτονίων που εκπέμπονται από το πυρήνα. Με τη συνολική ισχύς του πίδακα να είναι 2 με 3 τάξης μεγέθους μεγαλύτερη από την κινητική ισχύ του πίδακα καταλήγουμε ότι όντως η πιο πιθανή αιτία της εκροής είναι ο πίδακας.

Με βάση την πιθανή συσχέτιση του πίδακα με την μοριακή εκροή καλούμαστε να σχολιάσουμε για πιο λόγο ο πίδακας δεν εντοπίζεται στο ραδιοφωνικό συνεχές των τηλεσκοπίων μας σε αυτές τις αποστάσεις. Ένα από τα πιθανά σενάρια που προτείνουμε είναι ο πίδακας για κάποια προηγούμενη χρονική στιγμή να ήταν ενεργός εναποθετώντας ενέργεια στο περιβάλλον του γαλαξία μέχρις ότου η τροφοδοσία στη κεντρική μελανή σπή διακόπηκε. Σε αυτό το σενάριο η σημερινή κατάσταση του πίδακα είναι αποτέλεσμα της επανενεργοποίησης του ενώ οι διεγερμένες περιοχές έχουν ψυχθεί αρκετά ώστε να μην διακρίνεται η ραδιοφωνική εκπομπή. Ο χρόνος ψύξης για την περιοχή των εκροών είναι στα 150 kyr το οποίο είναι συμβατό με τη χρονική κλίμακα της ζωής των εκροών η οποία εκτιμάται στα 200-700 kyr. Το δεύτερο σενάριο περιλαμβάνει τη παρουσία του πίδακα σε ακτίνες πολύ μεγαλύτερες από την παρατηρούμενη ακτίνα η οποία όμως δεν είναι εμφανής λόγω της σχετικιστικής ταχύτητας του η οποία ενισχύει την ακτινοβολία κατά τη διεύθυνση του πίδακα και

την μειώνει κάθετα σε αυτήν. Σε αυτό το σενάριο ο πίδακας στα πρώτα parsec δεν έχει ευθυγραμμιστεί αρκετά ώστε το φαινόμενο να παίζει ουσιαστικό ρόλο. Όμως στη συνέχεια το φαινόμενο γίνεται 10000 φορές ισχυρότερο ώστε να κρύβει την εκπομπή στο ραδιοφωνικό φάσμα. Κατά την αλληλεπίδραση του πίδακα με το φωτονικό πεδίο μέσω του αντίστροφου μηχανισμού δ μπτον μπορεί να εξηγήσει και τη παρατηρούμενη εκτεταμένη ακτινοβολία X, και το διεγερμένο θερμό μοριακό αέριο αλλά και τις ενδιαφέρουσες περιοχές εξώθεν του κεντρικού δίσκου που σημειώσαμε προηγουμένως. Αξίζει να σημειωθεί ότι ο NGC6328 δεν είναι ο μοναδικός γαλαξίας όπου παρατηρούμε μοριακούς ανέμους λόγω αλληλεπίδρασης του αερίου με τον πίδακα ο οποίος δεν είναι παρατηρήσιμος. Συγκεκριμένα αντίστοιχα φαινόμενα έχουν παρατηρηθεί στους NGC1377, 4C 31.04, ESO 420-G13.

Με μια προσεκτικότερη μελέτη των καταγεγραμμένων μοριακών ανέμων όπως έχουν δημοσιευθεί στη βιβλιογραφία εκτιμήσαμε τη πιθανότητα να υπάρχουν περισσότεροι γαλαξίες όπου οι πίδακες έχουν υποτιμηθεί σαν σημαντικός μηχανισμός. Από τους 45 γαλαξίες των Fluetsch et al. 2019 εκτιμήσαμε ότι περίπου στους μισούς ο πίδακας είναι, ενεργειακά ικανός αλλά και η γεωμετρία των ανέμων τέτοια ώστε να θεωρηθεί σαν από τους πιθανότερους μηχανισμούς παραγωγής αυτών των ανέμων. Τα παραπάνω αποτελέσματα δημοσιεύτηκαν στις Papachristou et al. 2021, 2023.

Ευχαριστίες

Στο σημείο αυτό θέλω να ευχαριστήσω τους ανθρώπους χωρίς τους οποίους η εργασία αυτή δε θα μπορούσε να ολοκληρωθεί. Καταρχάς στην επιβλέπουσα μου, Καλλιόπη Δασύρα για την επιστημονική καθοδήγηση αλλά για την εμπιστοσύνη και την υπομονή που μου έδειξε όλα αυτά τα χρόνια. Θα ήταν λάθος να μην αναφέρω ότι χωρίς την εμπιστοσύνη που μου έδειξε στην αρχή αυτής της διαδρομής, μέσω της συμμετοχής μου στο συγκεκριμένο ερευνητικό έργο, αυτή η εργασία ίσως και να είχε πρώιμα τερματιστεί. Επίσης θα ήθελα να ευχαριστήσω και υπόλοιπα μέλη της τριμελούς επιτροπής, κ. Νεκτάριο Βλαχάκη και κ. Δεσποινα Χατζηδημητρίου για τις πολύτιμες επιστημονικές συμβουλές και καθοδήγηση. Οφείλω πάρα πολλά με όσους και όσες κατα καιρούς συνεργάστηκα μαζί, τον Juan Antonio Fernández Ontiveros, την Anelise Audibert, την Illaria Ruffa, την Αθανασία Γκόγκου, και ειδικά στον Μάρκο Πόλκα αλλά και στα περισσότερα μέλη του τομέα αστροφυσικής του ΕΚΠΑ και του εθνικού αστροσκοπείου Αθηνών, ειδικά στο Χάρη Αποστολάτο, και τον Απόστολο Μαστιχιάδη για την βοήθεια και συμβουλές τους καθώς και τη γραμματέα του τομέα Σοφία Ζαρμπούτη. Ιδιαίτερες ευχαριστίες στους συνδέλφους/ισσες και φίλους/ες, (ειδικά) τον Φώτη Αναγνωστόπουλο, την Στέλλα Μπουλά, τον Αχιλλέα Στραντζαλη και τη Γωγώ Λουκαΐδου, για την πολύτιμη βοήθεια και αμέριστη στήριξη τους. Τελειώνοντας, θα ήταν άδικο να μην ευχαριστήσω τους κοντινούς μου ανθρώπους, τους γονείς μου, τους φίλους και φίλες, και ιδιαίτερα την Ινώ, για την απύθμενη υπομονή που έδειξαν, για τις θυσίες που έκαναν, για την βοήθεια, την ψυχολογική και υλική στήριξη στις αμέτρητες δύσκολες στιγμές όλων αυτών των χρόνων. Χωρίς όλους τους παραπάνω, αυτή η εργασία δεν θα μπορούσε να ολοκληρωθεί.

Contents

Abstract	iii
Εκτεταμένη Περίληψη	v
Ευχαριστίες	xi
Contents	xiii
1 Introduction	1
1.1 Super massive black holes	1
1.2 Active galactic cores	2
1.2.1 Radiative mode AGN	4
1.2.2 Radio-mode AGN and Jets	5
1.3 Feedback Mechanisms	6
1.3.1 Feedback through radiative driven winds	7
1.3.2 Feedback through jets	9
1.3.3 Starbursts outflows	11
1.4 Observation evidences of feedback	12
1.4.1 M-sigma relation	12
1.4.2 Quenching of star formation	13
1.4.3 Luminosity Function	14
1.4.4 Direct observation of fast winds and outflows	15
2 Data Mining and Sample Selection	19
2.1 Molecular gas observations through ALMA	20
2.2 Building CO-ARC	21
2.2.1 Redshift information	21
2.2.2 CO lines in ARC sources	22
2.2.3 Radio - Identification of Parent Galaxy Sample	23
2.2.4 Compiling a consistent subsample of the NVSS/NVSS-Z catalog	24
2.3 Data Reduction: Calibration and Imaging	28
2.3.1 Calibration Procedure	29
2.3.2 Data Integration and Imaging	29
2.4 Results	30
3 A plausible link between dynamically unsettled molecular gas and the radio jet in NGC 6328	39
3.1 General NGC6328 properties	40
3.1.1 Radio emission and AGN	40
3.1.2 Xrays and γ rays	42
3.1.3 Emission lines	42
3.2 ALMA and X-shooter data	43
3.2.1 ALMA data reduction and imaging	44
3.2.2 Molecular gas distribution and kinematics	46
3.3 Building a new gas kinematics and distribution model	51
3.3.1 The need for a new tilted rings model	51
3.3.2 Model description	52
3.3.3 Model setup and projections	58

3.4	Fitting the ALMA Data with Our Models	59
3.4.1	Statistical Inference	59
3.4.2	Modeling an ALMA data cube	62
3.4.3	Clump detection	64
3.4.4	Sampling the final posterior	67
3.5	Results	67
3.5.1	Parameters	67
3.5.2	Residuals as non-rotating gas components	69
3.6	Relevant discussion	74
3.6.1	What drives the inner outflows	74
3.6.2	Why we cannot see the jet?	76
3.6.3	Comparison of the gas distribution with simulations and other observations	77
4	Extended discussion: The jet-outflow connection in nearby galaxies with massive outflows of cold molecular gas	81
5	Conclusions and future work	87
5.1	Conclusions	87
5.2	Future Work: Exploring Warped Disks via Physics Informed Neural Networks	88
A	Appendix	93
A.1	Projection effects	93
A.1.1	Galaxy Frame	93
A.1.2	Sky Frame	93
A.1.3	Connecting the two frames	94
A.1.4	A note regarding similar work in the literature	95
	Bibliography	97

List of Figures

1.1	Black hole discoveries and their spectroscopic spatial resolutions. From Kormendy and Ho 2013.	1
1.2	The bright Quasar 3C273 from Hubble's Wide Field and Planetary Camera 2. Quasar large-scale jet (61 kpc) is also visible in the top left of the image.	2
1.3	Illustration of the AGN dust reverberation mapping method.	2
1.4	The AGN unification scheme from Thorne et al. 2022. Apart from different viewing angles, several different intrinsic properties make up the total AGN zoo. The top-bottom distinction describes the dominance or not of a radio jet, while the left-right is the difference between high and low excitation radio	4
1.5	The two different AGN modes from Heckman and Best 2014	5
1.6	Evolution of a magnetically-arrested disk (MAD) around a spinning BH. The colour represents the logarithm of gas density, taken from Tchekhovskoy et al. 2011	6
1.7	Momentum end energy driven fast winds and outflows. From Zubovas and King 2012	7
1.8	Simulation of jet-ISM interaction. The jet power is 10^{43} erg s ⁻¹ . From Mukherjee et al. 2016.	10
1.9	Messier 82 starburst galaxy imaged from Hubble Space Telescope. http://www.spacetelescope.org/images/heic0604a/	11
1.10	Black hole mass and stellar dispersion relation of local galaxies with direct black hole mass measurements (data from Woo et al. 2013, image from Heckman and Best 2014)	12
1.11	SDSS galaxies distribution on the plane of stellar mass versus specific star-formation rate (star formation over stellar mass). The grayscale indicates the volume-weighted distribution of all galaxies, with each lighter color band indicating a factor of two increase. The distribution shows a bimodality between a main sequence of star-forming galaxies and a red sequence of quenched galaxies. The blue and red contours display the distribution of high and low eddington fraction, representing radiative and jet mode agns respectively.	13
1.12	Star formation quenching observation in comparison with cosmic simulation which incorporate or not, AGN feedback(Dubois et al. 2016)	14
1.13	Left: The observed galaxy stellar mass function and its comparison from recent large-scale cosmological simulations (which include stellar and AGN feedback). The dashed line shows the hypothetical galaxy mass function assuming the cosmic baryon fraction (from Naab and Ostriker 2017). Right: Galaxy stellar mass functions (solid lines) and Dark matter halo mass functions (dotted) and corresponding galaxy stellar mass functions for the Horizon-AGN (black) and Horizon-noAGN (light grey) cosmic simulations. The blue shaded area represents the observations from (González et al. 2011; Bielby et al. 2014; Daddi et al. 2002; Bernardi et al. 2013; Moustakas et al. 2013; Tomczak et al. 2014; Song et al. 2016; Davidzon et al. 2017). From Beckmann et al. 2017.	15
1.14	Grand-scale structure formation (bottom) and gas temperature (top) from the horizon cosmic simulations (Dubois et al. 2014). In the gas temperature we show the difference in gas tmperature and structure if the simulation uses AGN feedback (top right) or not (top left). Image from Dubois et al. 2016	16
1.15	IC5063 jet and ISM interaction. The contours in panel A represent the radio emission, while in panels B and C the ionized gas FeII. The shaded area in panel C indicates the regions where at least 10% of the gas (in molecular or atomic phase) is outflowing. In the panel D is a echmatic rerepresentation of the jet-ISM interaction. From Dasyra et al. 2016.	17
1.16	The interaction of the radio jet from the MS0735.6+7421 cluster central galaxy with the intra-cluster gas (McNamara et al. 2009). The image scale is 700 kpc. In "maintenance mode" feedback jets prevent the intergalactic gas to cool and flow to the galactic core	17

1.17	Left: Observed integrated position velocity plot of the molecular gas in IC5063 from Morganti et al. 2015. The dispersion of the gas indicates the outflows. Right: Simulated position velocity plot of 10^{44} erg s ⁻¹ jet impacted molecular gas for IC5063(Mukherjee et al. 2018).	17
2.1	At the top of the figure are the operational ALMA Bands frequency windows and rest frame frequencies of the CO lines up to CO 4 → 3. Directly below we plot the redshift windows where we can observe them due to redshift. At bottom we plot the number of ARC observations per band	22
2.2	Comparison of CO-ARC cumulative flux distribution with several radio surveys flux limited at the minimum flux of CO-ARC for the specific frequency.	23
2.3	Panel A: NVSS and NVSS with redshift (NVSS-Z) radio flux distributions and a random sample of $N = 80$ simulated dlux distributions based on the procedure we describe in the text. For all distributions we force a flux limit at 0.4 Jy Panel B: Distribution of the d-statistic of the simulated datasets with NVSS-Z.	25
2.4	Behavior of the distribution of D -statistic for different sub-sample sizes N . The central line represents the median value of the D -statistic distribution and the highlighted area the $\pm 1\sigma$. When the size of S^* is relative small we expect that the random noise will have a bigger impact on the distance between the two distributions.	26
2.5	Number of combinations as a function of subsample size	27
2.6	Sample selection algorithm and final sample candidates.	28
2.7	UV plane	29
2.8	Wiegthing	29
2.9	Luminosity functions (LF) for $0.005 < z < 0.3$ in the <i>left</i> panel and for $1 < z < 2.5$ in the <i>right</i> panel. In the local universe, the LF of our CO-selected Radio Galaxies (RGs) is 2-4 orders of magnitude lower than that of main sequence galaxies and star-forming or starburst AGNs, yet it aligns with the LF of AGN types 1 and 2. For the higher redshift range, the LF of RGs is notably lower than model predictions, attributable to the smaller observed population. A correction factor, derived from comparing the radio LF of our sample with the NVSS and UGS galaxy samples, has been applied, resulting in the addition of new, corrected data points to the LF, shown with triangles.	31
2.10	Molecular mass as a function of redshift compared with the semi-empirical predictions for two different dark matter halo masses of $M_{\text{vir}} = 10^{13} M_{\odot}$ and $M_{\text{vir}} = 10^{14} M_{\odot}$ from Popping et al. 2015	32
2.11	Molecular gas density evolution with redshift. The filled circles show the derived densities which are decreasing due to the Malmquist bias. The filled triangles show the corrected values after applying the 1.4 GHz LF correction. The blue lines represent the predictions from the SPRITZ simulation (Bisigello et al. 2021) for the total AGN and AGN dominated (AGN type 1 and 2) populations.	33
3.1	Grand view of NGC6328. Left: Grand-scale (~ 16 kpc) Hubble Space Telescope (WFPC2, F606W band) image (obtained from Wikimedia). Right and top: (~ 30 kpc) UV image (UVM2) from Swift. Right and bottom: IR image at the same scale (from DSS2)	39
3.2	The jet-ISM "dentist drill" interaction of the FFA model by Bicknell et al. 1997. The radiation from the shock photoionizes the ISM clouds which absorb the radio emission at GHz frequencies. . .	40
3.3	Left: The bipolar structure of the young radio source PKS1718-649 as observed from VLBI. The colors represent the spectral index between 8.4 GHz and 22.3 GHz Angioni et al. 2019. Right: Radio spectrum of PKS1718 as observed from ATCA in three epochs of observations (2012 and 2013) and the best fit lines of FFA and SSA models (Tingay et al. 2015).	40
3.4	MHD simulations of a young jet interacting with the ISM successfully reproducing the GHz peak in the radio spectrum of peaked sources. Reproduced from (Bicknell et al. 2018).	41
3.5	The bipolar structure of the you radio source PKS1718-649 as observed from VLBI in different epochs Angioni et al. 2019.	42

3.6	Difference map between the hard (1.5–10 keV) and soft (0.3–1.5 keV) X-rays Positive pixels (blue) depict a hard excess, negative pixels (red) a soft excess (from Beuchert et al. 2018). The black contours represent the warm hydrogen emission (H_2 1–0 S(1) [$2.12 \mu\text{m}$]) from Maccagni et al. 2016a. In the background we added the HST image as an indicator of scale and position. The pink line represents the position angle of the jet	43
3.7	HI emission map. Left: HI intensity map (black contours) on top of I band DSS image. Right: Mean velocity map. Reproduced from (Maccagni et al. 2014). The "S" shape traced by the zero velocities indicate the presence of a warp.	44
3.8	From left to right: zeroth, first, and second moments of the CO(2 – 1) emission. The ellipse in the lower right corner of each panel represents the observational beam. The inset on the right provides a zoomed-in view of the central inner disk-like structure, also highlighted by a black ellipse. . .	45
3.9	From left to right, zeroth, first and second moment of the CO(3 – 2) emission. The black ellipse represents the beam of the observation. Due to spectral coverage limitation only the positive velocities are observed. Thus only the redshifted part of the disk is visible.	46
3.10	HST zoomed view of the central 4 kpc. ALMA CO(2 – 1) (black) and CO(3 – 2) (blue) 4σ contours of the maximum flux per channel. The central North-South oriented dust lane, correlated with the CO emission, along with a less prominent feature to the west marking the start of a faint spiral arm. The elliptical contours represent the stellar distribution from VLT in the J band.	48
3.11	Position velocity slices along three different PA. From the top, PA of the inner disk (72°), PA along the high dispersion areas (170°) and along the PA of the main disk (2°). The contours represent the total emission over the total noise along the width of the slice (100 pc). At the left we present these three slices on top of the average velocity moment map of CO (2-1) emission.	49
3.12	Illustration of projected velocities in a rotating disk depicted through a composition of rings, showcasing three different scenarios of disk warping. At the left the disk has no warp, where in the middle and right the disk has a mild and a strong warp, respectively. The arrows represent the normal vectors of the circular orbits. In the warped configurations, the loci of zero velocities trace an "S" shape curve and the superposition of disk sections creates apparent overlaps when projected onto the plane of the sky.	50
3.13	Left: Settling timescales as a function of radius in the two viscous force approximations. Right: Line of nodes precession as function of radius after 500 Myr used to approximate the settling timescales. The dotted lines represent an approximation of the observable disk precession between the outer disk and the inner disk.	56
3.14	Averaged autocorrelation and fitted exponential kernel function $K(d)$ over distance in pixels . .	64
3.15	Source detection process. The Bayesian Information Criterion (BIC) drops as the model introduces more and more Gaussians. The best model is found for the minimum BIC	65
3.16	The detected clumps and the likelihood algorithm. A single tilted ring is "tested" against the detected clumps (scattered points). If the spatial distance between the ring and the clumps is smaller than a critical (shown as small black lines), then its LOS velocity is compared with the associated clumps velocity. This algorithm is evaluated for all tilted rings. Note that the critical distance here is exaggerated for visualization reasons.	66
3.17	Modeling results: main geometrical parameters as function of radius. The gray band represents the 1σ confidence level of the parameters posterior distribution regarding the axisymmetric model. A: azimuthal angle of the disk in the galaxy coordinates, B: line of nodes in the galaxy coordinates, C: Inclination, D: Position Angle.	68
3.18	3D distribution of the CO(2 – 1) and CO(3 – 2) cloudlets and tilted ring of the model A at two random observable orientations. X and Y axes represent the ra, dec sky coordinates and Z the line of sight. The color represents the integrated flux of each cloud. The units of the axes are in kpc.	68

3.19	Position velocity slices of CO(2-1) and CO(3-2) emission cubes. Panels A and B : Sky projected tilted rings for the axisymmetric potential model (A) and triaxial potential model (B) embedded on top of the CO(2-1) dispersion map. Panels C and D : Slices at angles of 2° and 72° , covering most of the gas emission and the major axes of the inner disk, respectively. Superimposed on these slices are the velocity projections of models A and B. Model C is omitted to avoid clutter, as its projected velocities are similar to those of the other models. The colormap represents the signal-to-noise ratio. Panels E and F : Position velocity slices along the PA of 147° and 170° where we observe the maximum gas dispersion. Embedded in these slits are also the velocity projections of models A and B and C.	69
3.20	Rotational Velocity. The black line represents the best solution of the axisymmetric model, red the triaxial, and blue the generic interpolating model. The gray band represents the 1σ confidence level of the posterior distribution of the parameters with respect to the axisymmetric model. . .	70
3.21	Residuals in the central disk region. A : Maximum projected velocity based of a clump located at a projected radius $R = 200$ pc for different possible orbit radii and inclinations. The blue band represents the observed projected velocity of the CO(2 – 1) emission lines. B : Maximum projected velocity based of a clump located in the central $R \simeq 50$ pc for different possible orbit radii and inclinations. The blue band represents the observed projected velocity of the CO(3 – 2) emission lines. C : Emission line residuals ($\delta V > 100$ km s $^{-1}$) in the central 500 pc disk area in the sky plane. Circles represent the CO(2 – 1) emission and rectangles CO(3 – 2)The green vector is the extrapolated direction of the jet.	71
3.22	Emission line residuals ($dV > 100$ km s $^{-1}$) in the central 500 pc disk from another perspective angle. Circles represent the CO(2 – 1) emission and rectangles CO(3 – 2)The conical shapes represent a hypothetical jet driven bubble responsible for the molecular gas outflow. The green vector shows the direction of the observer. Blue and red vectors show a possible direction of the observed outflows.	72
3.23	[OIII] spectrum centered in 3 different positions along a 240 pc-wide slit (PA 160°). From left to right, -220 pc, -30 pc and 160 pc from the nucleus. For every position, the signal (blue) is averaged over four pixels, corresponding to a physical width of 142 pc along the slit. In each spectrum, we have fitted one narrow and one broad component. At the -30 pc and 160 pc positions, an additional blueshifted (≈ 600 km s $^{-1}$) component was required to obtain a good fit.	72
3.24	Position velocity slice along the PA of 147° . The values represent the average value of $T_{\text{CO}(2-1)} / T_{\text{CO}(3-2)}$ and the contours the CO(2 – 1) intensity.	73
3.25	Corner plot of the parameters for the axisymmetric potential model.	79
4.1	ESO420-613 molecular gas velocity and velocity dispersion. The outflow is located in the north and west at 340 pc from the center. From Fernández-Ontiveros et al. 2020	82
4.2	Left : Collimated molecular gas outflows (colored contours)in NGC1377(Aalto et al. 2020). In grayscale the total CO(3-2) intensity. Right : Kinematic residuals in NGC1068 probing outflows. In black contours the radio emission tracing the jet. From García-Burillo et al. 2019.	83
4.3	Molecular outflows (traced from CO(3-2)) (red and blue contours) in the center of NGC613. The black contours and greyscale image on the right panel represent the radio emission.	83
4.4	Wind vs. driving mechanism energetics for local galaxies with massive molecular wind detections. A : Wind momentum rate vs. radiation pressure of AGN photons. B :Wind kinetic luminosity vs. jet power. The dashed lines indicate different ratios of the plotted parameters. C : Outflow’s momentum rate relation with the total photon momentum output of the galaxy. The dashed lines denote the different values of the ratio of outflow’s momentum rate over bolometric luminosity. The arrows denote upper limit values.	84

5.1	PINN sketch. At the left we have the representations of the functions as NN. We estimate the PDE loss by evaluating and summing the PDE value at a number of collocation points in the (t, r) space. At the same time we estimate the data loss using the NN functions. We minimize the loss by adjusting the NN weights w_i	89
5.2	Draft results of the PINN disk fit. On the left is the NGC6328 data, integrated in space (top) and velocities (bottom). On the right the results of the NN representation of the disk.	90

List of Tables

2.1	CO properties of the 66 CO-ARC sample sources. Note that, even for targets with available multiple-J CO observations, only the properties of lowest-J CO transitions are listed here and used for the luminosity function computations.	34
2.2	CO properties of 54 literature-based sources. The values for the molecular mass listed here are corrected by our adopted CO-to-H ₂ conversion factor. References: Prandoni et al. 2010, Ruffa et al. 2019a, Olivares et al. 2019, Ocaña Flaquer et al. 2010, Leon et al. 2003, Taniguchi et al. 1990, Evans et al. 2005, Saripalli and Mack 2007, Nesvadba et al. 2010, Fotopoulou et al. 2019, Lo et al. 1999, Evans et al. 1996 and Emonts et al. 2014.	35
2.3	Table A.1 - CO-ARC sample ancillary information and information on the reduced ALMA observations.	37
3.1	Resulting parameters for the model A and B and C. M_* is the bulge stellar mass, r_a, r_b, r_c are the three axes scales and $i_{\text{Bulge}}, PA_{\text{Bulge}}$ the orientation of the axis c relative to observer. M_{vir} is the virial mass and c_{vir} the concentration parameter for the dark matter. θ_0 and λ_0 are the starting values of the disk orientation. α is the dissipation settling angle and τ the time after the initial values.	67
3.2	Molecular Outflow Properties	75
4.1	Outflow and AGN properties of galaxies with molecular outflows are from Allison et al. 2014, unless otherwise indicated. For 4C12.50, properties are presented for the nuclear outflow component, as the extended components add little to the energetics (Fotopoulou et al. 2019). Likewise, the infrared luminosity fraction of the southern nucleus comes from resolved star formation rates (Lira et al. 2002). The radio power P_{jet} (for the sources with a certain radio jet detection) is calculated as in Birzan et al. 2008 after the subtraction of the starburst contribution as indicated in the text. Alternative radio power (P_{jet}) computations are as follows: [*] 43.96 for the synchrotron radiation (Fotopoulou et al. 2019), ^{**} 39.3 for the X-ray cavity (Urquhart et al. 2018). ^{***} 43.86 averaged value Punsly and Kharb 2016. ^{****} To find the 1.4GHz flux fraction assigned to the southern nucleus of this galaxy merger, we used the information from spatially-resolved 5 GHz data (Neff et al. 2003). ¹ Condon et al. 1998. ² Allison et al. 2014. ³ Fotopoulou et al. 2019. ⁴ Baan and Klöckner 2006. ⁵ Ryder et al. 1996. ⁶ Dumas et al. 2011. ⁷ Condon et al. 1996. ⁸ Urrutia et al. 2009. ⁹ Greene et al. 2012. ¹⁰ Clemens et al. 2008. ¹¹ Clemens et al. 2010. ¹² Audibert et al. 2019. ¹³ Davies et al. 2017. ¹⁴ Fernández-Ontiveros et al. 2020. ¹⁵ Oosterloo et al. 2019. ¹⁶ Drake et al. 2004. ¹⁷ Husemann et al. 2019b. ¹⁸ Shimizu et al. 2017. ¹⁹ Marvil et al. 2015. ²⁰ Ohyama et al. 2015. ²¹ Sakamoto et al. 2014. ²² Ruffa et al. 2022. ²³ Ruffa et al. 2019b. ²⁴ Husemann et al. 2019a. ²⁵ Lanz et al. 2016. ²⁶ Gruppioni et al. 2016	86

1.1 Super massive black holes

Approximately a century ago, when Karl Schwarzschild first described a solution to Einstein's general theory of relativity for a black hole (BH) (Schwarzschild 1999) a point of infinite density encapsulated within a cosmic event horizon, physicists became captivated by these objects as potential sources of insight into the fundamental properties of the universe. While the inherent properties and mechanism of black holes are captivating, this study will concentrate solely on the influence they exert on their galactic surroundings and overall galactic evolution.

Black holes appear in two distinct categories. The first category comprises stellar black holes, with masses ranging from 5 to several tens of solar masses. These black holes originate from the gravitational collapse of massive stars. The second category includes supermassive black holes (SMBH), which have masses greater than $10^5 M_{\odot}$. The origin of these SMBH remains uncertain. The focus in this work is on SMBH, which typically inhabit central regions of galaxies, as will be discussed later in this section.

We can calculate the sphere of influence, the radius within which a SMBH with mass M_{\bullet} significantly alters the motion of stars in a stellar population, counteracting their regular orbits due to the galaxy's gravitational pull. This is given by the formula:

$$r_{\text{infl}} = G \frac{M_{\bullet}}{\sigma^2} \approx 10.8 \text{pc} \left(\frac{M_{\bullet}}{10^8 M_{\odot}} \right) \left(\frac{\sigma}{200 \text{ km s}^{-1}} \right)^{-2} \quad (1.1)$$

Here, σ represents the velocity dispersion of the stellar population and G is the gravitational constant (Merritt 2003). Consequently, stars within this sphere would exhibit higher orbital velocities leading to an increased velocity dispersion for that specific stellar group. This observable phenomenon has provided direct evidence for the existence of supermassive black holes in the nuclear regions of elliptical galaxies

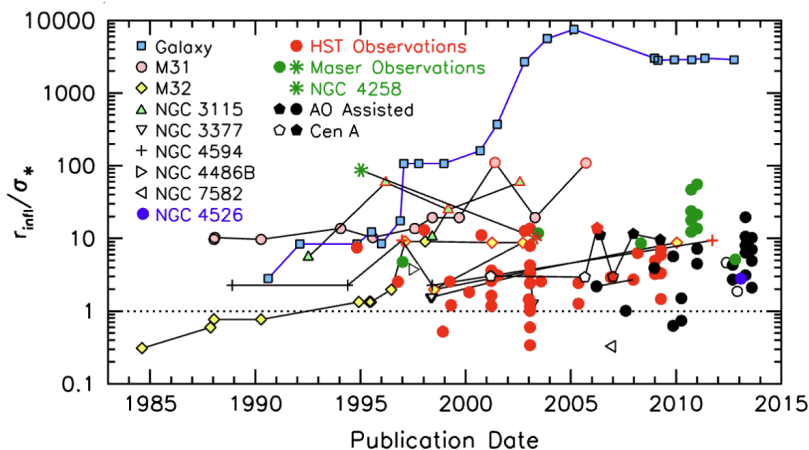


Figure 1.1: Black hole discoveries and their spectroscopic spatial resolutions. From Kormendy and Ho 2013.

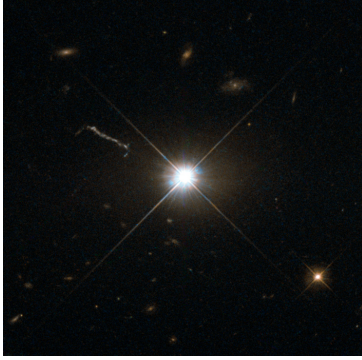


Figure 1.2: The bright Quasar 3C273 from Hubble's Wide Field and Planetary Camera 2. Quasar large-scale jet (61 kpc) is also visible in the top left of the image.

((Wolfe and Burbidge 1970). Over time, as our spectroscopic spatial resolution improved, allowing us to discern distances smaller than r_{infl} , we have been able to detect a growing number of SMBH in our local universe.

1.2 Active galactic cores

The development of high-resolution telescopes and adaptive optics allowed researchers to observe also the direct influence of SMBHs on the orbits of individual stars at the center of the Milky Way galaxy (Figure 1.1). This breakthrough led to the discovery of Sagittarius A*, a SMBH identified by Ghez et al. (2008) and Genzel et al. (2010). Their independent analyses of the region of interest earned them the Nobel Prize in 2020, which they shared with Penrose, who had made significant contributions in theory of black holes (Penrose 1965).

However, even before these direct observations of gravitational attraction, other pieces of evidence had already emerged that hinted at the presence and influence of these cosmic giants.

The optical star-like counterpart of the bright radio source 3C 273 was detected, which exhibited redshifted emission lines of cosmological scale ($z = 0.158$) (Schmidt 1963). According to current cosmology, the estimated luminosity distance is approximately 750 Mpc (Uchiyama et al. 2006). At this distance, its apparent magnitude of 12.9 (V) corresponds to an absolute magnitude of -26.5 , indicating an intrinsic luminosity of around $\sim 3 \times 10^{12} L_{\odot}$ or $1.7 \times 10^{46} \text{ erg s}^{-1}$. This discovery of 3C 273 marked the first identification of similar sources now known as Quasars. Quasars exhibit not only immense power but also rapid variability ($\delta\tau \sim \text{days}$). Assuming that this variability is caused by the same cause (the method shown in Figure 1.3), it implies that the power source is emitted from a small region of space ($r \sim c\delta t \sim 10^2 \text{ AU}$). These extragalactic observations across the sky strongly suggest the existence of a compact source capable of producing extreme power to account for the observed scales and luminosities.

Quasars and radioloud galaxies are subclasses of objects that we now refer to as Active Galactic Nuclei (AGN). AGN's are compact regions at the center of massive galaxies that are powered by the SMBH as

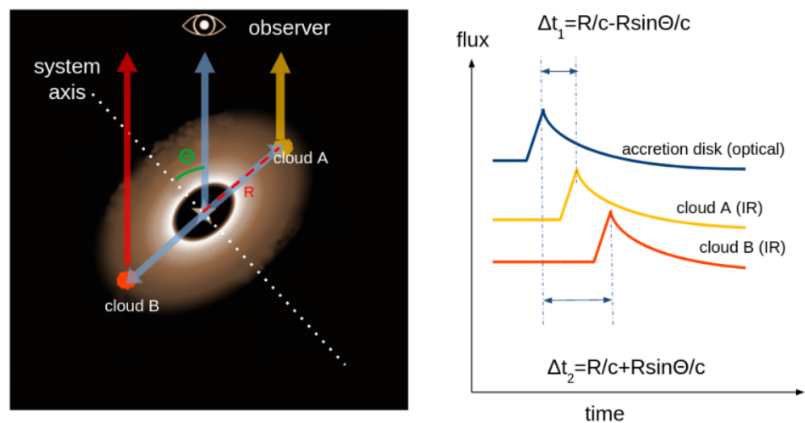


Figure 1.3: Illustration of the AGN dust reverberation mapping method.

they accrete matter. If we assume a constant accretion rate \dot{M} of matter from infinity towards the SMBH the loss of potential energy rate that is converted to radiation is $L = \frac{GM_\bullet \dot{M}}{r_{\min}}$, where r_{\min} is the minimum distance from the SMBH it will reach. In this relation it is obvious the unique property of black holes, that they can provide the maximum possible value of the linear density $\lambda = \frac{M}{r_{\min}}$. Using r_{\min} the Schwarzschild radius $r_s = \frac{2GM_\bullet}{c^2}$ we calculate $\lambda_\bullet \sim \frac{c^2}{G} = 10^{13} \frac{M_\odot}{\text{pc}}$ while a Milky Way-like galaxy has $\lambda_{\text{MW}} \sim 10^6 \frac{M_\odot}{\text{pc}}$ and a solar-like stellar object $\lambda_\odot \sim 10^8 \frac{M_\odot}{\text{pc}}$. This means that a BH is the most efficient engine we know. We can estimate this radiative efficiency η by comparing it with the maximum radiative energy $\dot{M}c^2$, so

$$\eta = \frac{L}{\dot{M}c^2} = 0.06 \text{ to } 0.42 \quad (1.2)$$

depending on the BH spin (Kerr 1963; Shapiro et al. 1983; Marconi et al. 2004; Merloni et al. 2004) and the accretion process*. Based on this we can estimate that with an accretion rate of $1 M_\odot \text{ yr}^{-1}$, a small amount in galaxy scales[†] can provide the luminosity needed to outshine a whole galaxy.

However, the accretion rate of a Supermassive Black Hole (SMBH) cannot indefinitely increase due to the imposition of an upper limit on the luminosity that this process can generate. This constraint is attributed to the Eddington luminosity, the maximum luminosity achievable by a celestial body, such as a star or black hole, when equilibrium is reached between the outward radiation force and the inward gravitational force. The theoretical value for this critical luminosity, considering only Compton scattering for a fully ionized plasma, is expressed as:

$$L_{\text{Edd}} = \frac{4\pi cGM\mu m_p}{\sigma_T} \approx 1.5 \times 10^{46} \left(\frac{M}{10^8 M_\odot} \right) \text{ erg s}^{-1} \quad (1.4)$$

where G is the gravitational constant, M is the mass of the SMBH, μ is the mean molecular weight, σ_T is the Thomson cross section, and m_p is the mass of the proton. Observational evidence, mostly from the local universe, shows that AGN obey this limit; however, we must note that there solutions which allow super-Eddington accretion (Abramowicz et al. 1980). This luminosity corresponds to an accretion rate of

$$\dot{M}_{\text{edd}} = \frac{L_{\text{edd}}}{\eta c^2} \approx 1.8 \left[\frac{\eta}{0.1} \right]^{-1} \left[\frac{M}{10^8 M_\odot} \right] M_\odot \text{ yr}^{-1} \quad (1.5)$$

where η is the radiative efficiency of the flowing material.

As mentioned above, quasars form a specific subclass within the broader category of AGNs. The traditional framework for understanding AGNs

* For example if the gas accretes up to the innermost stable circular orbit (isco) of a non-rotating BH $r_{\text{ISCO}} = 6 \frac{GM}{c^2}$ then $\eta = \frac{1}{6} \approx 0.17$

† The gas mass local to SMBH is $M_G \sim \frac{f_G \sigma^2 r}{G}$ where f_G is the gas fraction and σ the local stellar velocity dispersion. If this is destabilized, it would fall into a dynamical timescale of $\tau_{\text{dyn}} \sim \frac{r}{\sigma}$, giving an accretion rate of

$$\dot{M}_G \approx \frac{M_G}{\tau_{\text{dyn}}} = 304 \left[\frac{f_G}{0.16} \right] \left[\frac{\sigma}{200 \text{ km s}^{-1}} \right]^3 M_\odot \text{ yr}^{-1} \quad (1.3)$$

Of course this is a overestimated value, as the gas will likely accrete with much lower rates through a disk structure in timescales dictated by viscosity.

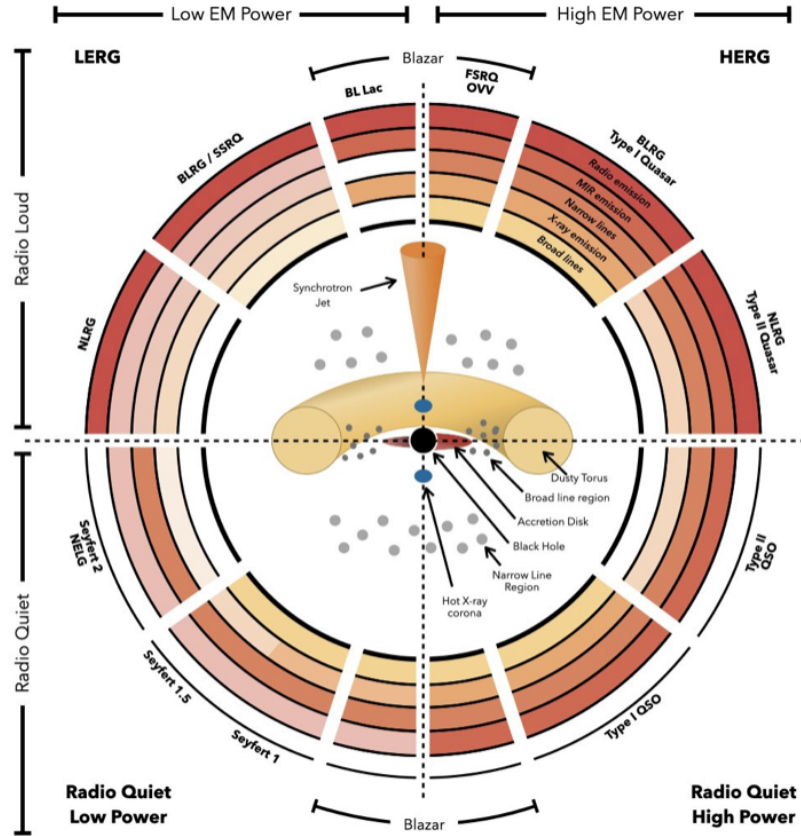


Figure 1.4: The AGN unification scheme from Thorne et al. 2022. Apart from different viewing angles, several different intrinsic properties make up the total AGN zoo. The top-bottom distinction describes the dominance or not of a radio jet, while the left-right is the difference between high and low excitation radio

has been the unification paradigm, which suggests that AGNs can manifest themselves as various observed phenomena, originally interpreted as different classes. According to this model, these classes were differentiated mainly because of the varying viewing angles between the observer and the accretion disk surrounding the central supermassive black hole (SMBH). Simply put, the unification theory posited that Type 1 and Type 2 AGNs were essentially the same astronomical objects viewed from different perspectives. A dusty, toroidal structure, often referred to as the ‘dusty torus’, around the SMBH obscures the inner accretion disk and the broad-line region (BLR) when viewed from certain angles, thereby classifying the object as a Type 2 AGN. On the contrary, when the BLR is visible, the object is classified as a Type 1 AGN. However, more recent studies (Hardcastle et al. 2007; Best and Heckman 2012; Heckman and Best 2014; Hardcastle 2018) have proposed a nuanced understanding, arguing for two fundamentally different types of AGN based on the accretion efficiency of their SMBHs. Radiative-mode AGNs (also known as quasar-mode or cold-mode, characterized by high radiative efficiency) and jet-mode AGNs (also referred to as radio-mode, marked by low radiative efficiency).

1.2.1 Radiative mode AGN

In radiative-mode AGNs, radiation is the primary mode of energy release, facilitated by the radiatively efficient, slow accretion of matter in the SMBH. When the Eddington-scaled accretion rates are moderate ($\dot{m} \approx 0.01 - 1$), the accretion flow forms a geometrically thin, yet optically

thick structure, reaching the innermost stable orbit of the SMBH (Shakura and Sunyaev 1973). This configuration allows the gas to radiate efficiently as a blackbody, with efficiency increasing along with black hole spin ($0.05 \leq \eta \leq 0.3$) (Novikov and Thorne 1973; Frank et al. 2002).

1.2.2 Radio-mode AGN and Jets

At very low Eddington-scaled accretion rates ($\dot{m} = L/L_{\text{Edd}} \leq 10^{-2}$), the material forms a hot, ionized, optically thin and geometrically thick plasma (Esin et al. 1997; Esin et al. 1998). In this regime, the radiatively inefficient disk retains more energy, leading to the development of a two-temperature, advection-dominated accretion flow (ADAF) (Narayan and Yi 1995; Fender et al. 2004; Done et al. 2007). Here, ions provide the pressure at temperatures around $\sim 10^{12}$ K, while electrons primarily emit radiation at $\sim 10^9\text{--}11$ K (Ichimaru 1977; Narayan and Yi 1994; Narayan and Yi 1995; Abramowicz et al. 1995). Characterized by their extended structures, ADAFs resemble a hot corona rather than a traditional disk and are generally less luminous compared to standard accretion disks, with most of the energy channeled into the SMBH.

A similar scenario can occur in super-Eddington accretion flows ($\dot{m} > 1$), where the increased mass flow results in a denser and thicker disk, making it optically thick but radiatively inefficient.

Bipolar magnetic fields, dragged by the thermal and ram pressures of the accreting gas, approach the vicinity of the SMBH's event horizon, becoming threaded onto it. At a certain radius, the magnetic pressure ($F_B \sim B^2/8\pi$) truncates the accretion disk, directing the gas flow along the magnetic field lines. This magnetically arrested disk (MAD) phenomenon was proposed by Bisnovatyi-Kogan and Ruzmaikin 1974 and has been demonstrated in general relativistic magnetohydrodynamic (GRMHD) simulations (Tchekhovskoy et al. 2011; Tchekhovskoy et al. 2012; McKinney et al. 2012).

The interplay between a strong magnetic field and rotation results in the launching of a relativistic jet. Two mechanisms have been proposed

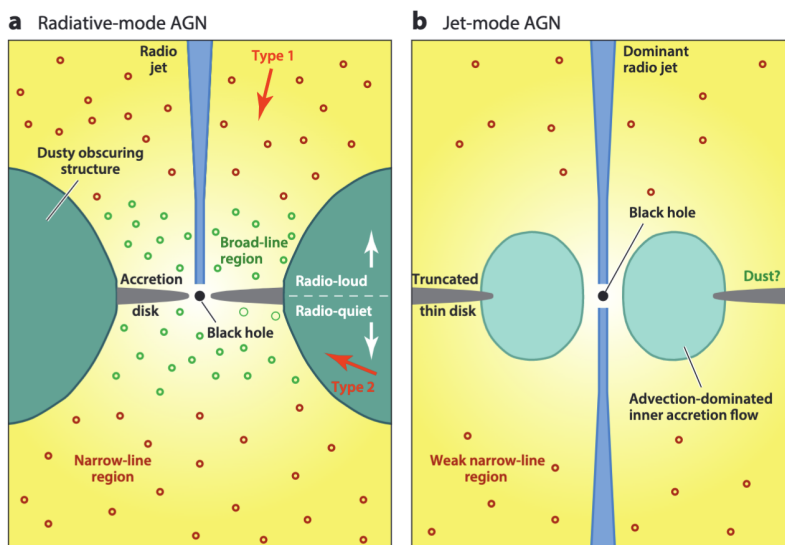
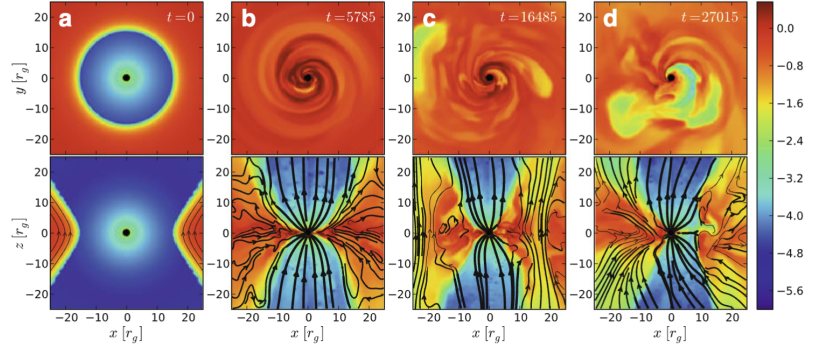


Figure 1.5: The two different AGN modes from Heckman and Best 2014

Figure 1.6: Evolution of a magnetically-arrested disk (MAD) around a spinning BH. The colour represents the logarithm of gas density, taken from Tchekhovskoy et al. 2011



for this phenomenon. Blandford and Payne 1982 suggested that jets are accelerated and collimated by magnetic fields originating from the rotating accretion disk. Alternatively, Blandford and Znajek 1977 proposed that jets are powered by the rotational energy of the spinning black hole, which interacts with the magnetic fields connected to the accretion disk. This second mechanism can utilize a large amount of energy, even during low accretion periods, often resulting in the formation of strong and highly relativistic jets.

The observed radio emission predominantly originates from jets and the lobes they inflate, characterized by synchrotron radiation emitted by relativistic electrons in regions of strong magnetic fields.

1.3 Feedback Mechanisms

Previously, we discussed the efficiency and capability of AGNs to radiate vast amounts of energy. A natural question arises: can this energy impact or influence the rest of the galaxy?

To put this into perspective, consider that the total accretion energy of a $10^9 M_{\odot}$ SMBH is approximately $\sim 2 \times 10^{62}$ erg. Meanwhile, the binding energy of the stellar bulge of an entire galaxy, characterized by mass M_{bulge} and velocity dispersion σ_* , is given by:

$$E_{\text{bulge}} \simeq M_{\text{bulge}} \sigma_*^2 \simeq 2 \times 10^{59} \left[\frac{M_{\text{bulge}}}{10^{11} M_{\odot}} \right] \left[\frac{\sigma_*}{300 \text{ km s}^{-1}} \right] \text{ erg} \quad (1.6)$$

Hence, given a sufficient coupling efficiency $\eta \simeq 0.005 - 0.01$, between the energy output of the AGN and its surrounding environment, the AGN has the ability to significantly impact its environment.

Feedback processes generally manifest in two primary forms: first, through wide-angle winds originating from the vicinity of the AGN, induced by radiation, and second, through jets, which also produce winds but result from the mechanical injection of energy. These winds interact with the local Interstellar Medium (ISM), comprising neutral and molecular gas, and dust. Particularly, the interaction with molecular gas, a crucial ingredient for star formation, can induce turbulence and heat or, if the outflow velocity surpasses the escape velocity, eject the gas out of the galaxy. Such mechanisms can significantly regulate star formation

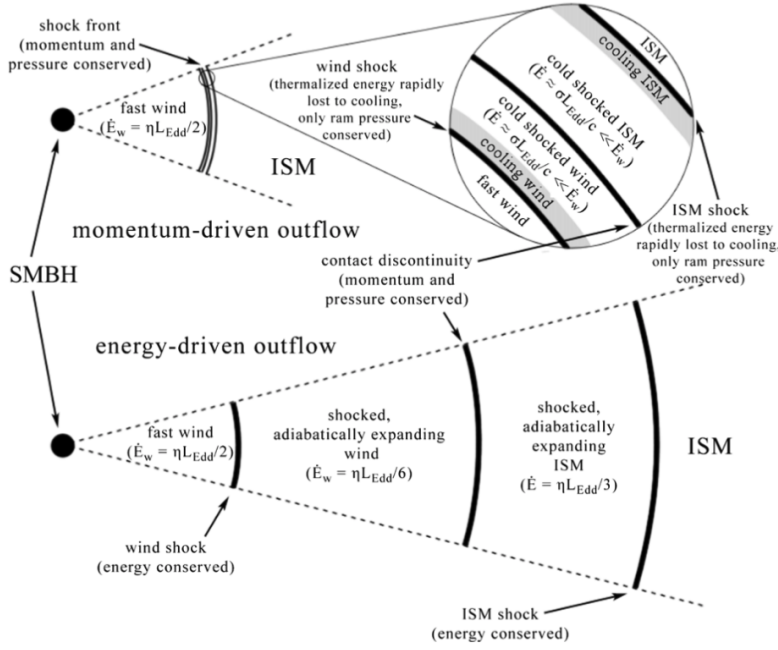


Figure 1.7: Momentum and energy driven fast winds and outflows. From Zubovas and King 2012

within the host galaxy[‡]. Understanding this feedback mechanism is vital, as it reveals the intricate dynamics between the SMBH and its host galaxy and sheds light on the galaxy's overall evolutionary trajectory.

In the following sections, we will explore the various ways through which AGN can interact with their environment and assess whether observational evidence supports these theoretical interactions.

1.3.1 Feedback through radiative driven winds

In the radiative feedback mechanism, the accretion disk around the SMBH emits photons that instigate relativistic winds as we will show later. These winds can provide the needed coupling between the AGN and the Interstellar Medium (ISM). This interaction can be described via momentum conservation as:

$$\dot{M}_w V_w = \tau_w \frac{L_{\text{AGN}}}{c}$$

where \dot{M}_w and V_w are the mass outflow rate and velocity of the wind and τ_w denotes the average number of photon scatters on the wind plasma (optical depth). If we assume that the accretion rate is close to Eddington, $\dot{m} \sim 1$ then

$$\tau_w = \eta^{-1} \left[\frac{V_w}{c} \right] \left[\frac{\dot{M}_w}{\dot{M}_{\text{Edd}}} \right]$$

[‡] Why we consider only the winds-ISM interaction? The dynamic pressure of the wind with a density of ρ_w and velocity V_w is $P_w \sim \rho_w V_w^2$. We can compare the impact of this wind on different objects, such as a solar-like star and a typical gas cloud, by considering the acceleration it can provide. The acceleration of an object under the influence of wind is given by the total force exerted on the object, which can be expressed as $a = (P_w \times A)/M$, where A is its cross section and M is its mass. If we assume that the Sun's cross section is a sphere with a radius equal to that of the heliopause, we get $A_{\odot} \approx (120 \text{ AU})^2 = 3.4 \times 10^{-7} \text{ pc}^2$. Taking into account the radius and mass of the gas cloud as $R_G \sim 50 \text{ pc}$ and $M_G = 5 \times 10^4 M_{\odot}$ respectively, we find that the influence of wind on a star-like system is much weaker than on a gas cloud ($\frac{a_{\odot}}{a_G} \approx 7 \times 10^{-6}$).

For $\tau_w \sim 1$, the outflow velocity is

$$V_w = \eta \frac{\dot{M}_{\text{Edd}}}{\dot{M}_w} c$$

This implies that wind velocities are approximately in the order of $0.1c$. Under these assumptions, the energy rate of the wind is

$$\dot{E}_w = \dot{M}_w \frac{V_w^2}{2} \simeq \frac{L_{\text{Edd}}}{c} \frac{V_w}{2} \simeq \frac{\eta}{2} L_{\text{Edd}} \simeq 0.05 L_{\text{Edd}} \quad (1.7)$$

and the momentum rate

$$\dot{P}_w = \dot{M}_w V_w \sim \frac{L_{\text{Edd}}}{c} \quad (1.8)$$

The fast wind acts as a highly supersonic piston, so it develops a forward shock (ISM shock at radius r_S) and a reverse shock (wind shock at radius r_{SW}) in front and back of the contact discontinuity (r_C) with the ISM. The swept outflowing gas at the contact discontinuity r_C follows the equation of motion

$$\frac{d}{dt} [M_g(r) \dot{r}] + \frac{GM_g(r)[M_\bullet + M(r)]}{r^2} = 4\pi r^2 P \quad (1.9)$$

where $M(r) = \frac{2\sigma^2 r}{G}$ the mass contained up to radius r , $M_g(r) = \frac{2f_g \sigma^2 r}{G}$ the mass of the swept gas, f_g is the gas fraction, σ the dispersion of the local stellar velocity and P the pressure exerted by the wind. The pressure term and the nature of the developed outflow strongly depend on the cooling timescale of the gas. Assuming monatomic gas with $\gamma = 5/3$ and strong shock conditions (Mach number $\gg 1$) the Rankine-Hugoniot jump conditions predict the shock gas temperature of

$$T_{\text{sh}}(V_{\text{sh}}) = \frac{3\mu}{16k} m_p V_{\text{sh}}^2 \approx 1.2 \times 10^{10} \text{ K} \left[\frac{\mu}{0.59} \right] \left[\frac{V_{\text{sh}}}{0.1c} \right]^2$$

The dominant mechanism of cooling at these temperatures is inverse Compton scattering. If the cooling timescale t_{cool} is much shorter than the flow time ($t_{\text{flow}} \sim \frac{r_S}{V_{\text{sh}}}$) (**momentum-driven outflow**) the shocked region radiates away the kinetic energy and compresses to a high density, interacting with the ISM through its ram pressure. In this case, the ram pressure is $4\pi r^2 P \simeq \frac{L_{\text{Edd}}}{c}$. Solving the equation 1.7 for large r tends to a constant expanding velocity of

$$\dot{r}^2 \approx V_e^2 = -2\sigma^2 \left[1 - \frac{M_\bullet}{M_\sigma} \right] - \frac{GM_\bullet}{r} \quad (1.10)$$

where we defined

$$M_\sigma = \frac{f_g \kappa}{\pi G^2} \sigma^4 \approx 3.2 \times 10^8 \left[\frac{f_g}{0.16} \right] \left[\frac{\sigma}{200 \text{ km s}^{-1}} \right]^4 M_\odot \quad (1.11)$$

If the launching speed is larger than the escape velocity of the SMBH the last term can be neglected. This means that the AGN supports a momentum-driven expansion only under the condition of $M_\bullet > M_\sigma$.

On the other hand, if $t_{\text{cool}} \gg t_{\text{flow}}$ the wind adiabatically expands as hot bubble (**energy-driven outflow**). In this case the expanding bubble creates a "snowplow" effect on the ISM, where the pressure is obtained from the energy equation

$$\dot{E} = (\gamma - 1) \frac{d(P\mathcal{V})}{dt} = \frac{\eta}{2} L_{\text{Edd}} - P\dot{V} - \frac{GM_{\text{g}}(r)M(r)}{r^2} \dot{r} \quad (1.12)$$

Solving this equation together with equation of motion results into a new expanding velocity

$$\dot{r} \approx V_e \approx 925 \left[\frac{\sigma}{200 \text{ km s}^{-1}} \right]^{2/3} \text{ km s}^{-1} \quad (1.13)$$

where we have assumed that $V_e \gg \sigma$.

1.3.2 Feedback through jets

Earlier, we delved into the characteristics of radio-dominated AGN. In these systems, the accretion is radiatively inefficient, complicating the direct coupling with the ISM and the initiation of strong winds. Nevertheless, the amalgamation of strong magnetic fields and the rapid rotation of both the SMBH and the accretion disk can launch relativistic collimated winds, known as jets.

The power of a jet can be estimated using the Blandford-Znajek jet launch model. In this model, a large-scale poloidal magnetic field passes through the ergosphere and gets "anchored" in the horizon of the SMBH. The fast rotation creates a toroidal electric field and thus a Poynting flux in the direction of the angular velocity of the disk-SMBH system. The angular frequency of the SMBH horizon is

$$\Omega_{\text{H}} = \frac{ac}{2r_{\text{H}}} \quad (1.14)$$

where $\alpha = \frac{J_{\bullet}}{J_{\text{max}}} = \frac{cJ_{\bullet}}{GM_{\bullet}^2}$ is the dimensionless spin parameter, J_{\bullet} the SMBH angular momentum, $r_{\text{g}} = GM_{\bullet}/c^2$ is the black hole gravitational radius, $J_{\text{max}} = M_{\bullet}r_{\text{g}}c$ and $r_{\text{H}} = r_{\text{g}} \left(1 + \sqrt{1 - \alpha^2} \right)$ the horizon radius. As the magnetic field lines rotate and expand radially, there is a radius (named light cylinder radius, r_{LC}) at which their rotational velocity reaches the speed of light.

$$r_{\text{LC}} = \frac{c}{\Omega_{\text{F}}} \quad (1.15)$$

where $\Omega_{\text{F}} \approx 0.5 \Omega_{\text{H}}$ (Blandford and Znajek 1977; Tchekhovskoy et al. 2010). The Poynting flux from the LC area is

$$P \sim 4\pi r_{\text{LC}}^2 \frac{c}{4\pi} (\mathbf{E} \times \mathbf{B})_r \sim cE_{\theta}B_{\phi}r_{\text{LC}}^2 = \frac{\Phi_{\bullet}^2 \Omega_{\text{H}}^2}{16\pi^2 c} \quad (1.16)$$

where Φ_{\bullet} is the magnetic flux passing through the black hole horizon. In the MAD scenario the magnetic flux can be estimated from the equilibrium between the gravity force and the magnetic pressure,

$$\frac{B^2}{8\pi} \times 4\pi r^2 = \frac{GM_{\bullet} \rho 4\pi r^3}{3r^2} \quad (1.17)$$

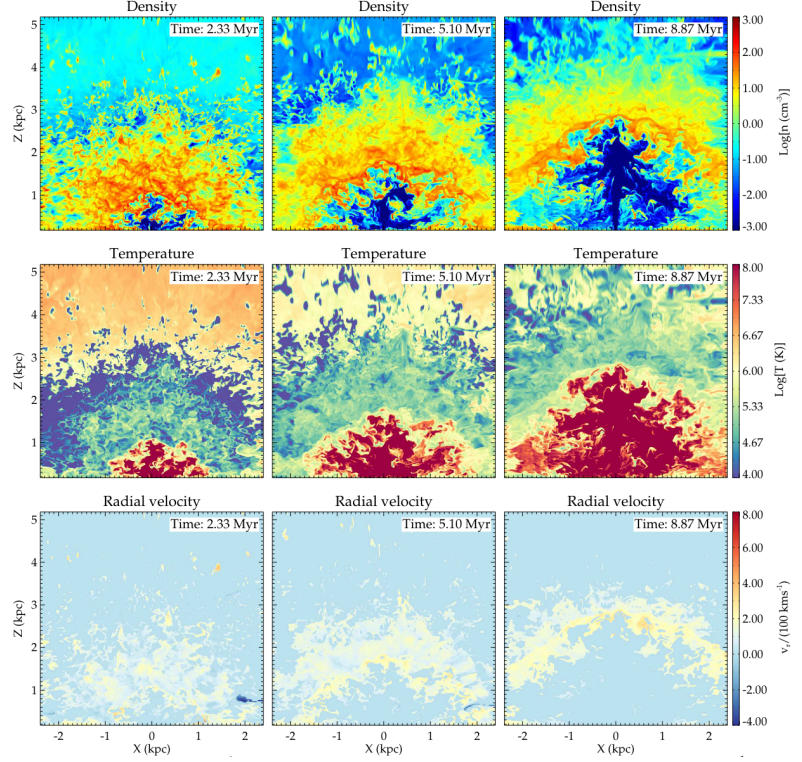


Figure 1.8: Simulation of jet-ISM interaction. The jet power is 10^{43} erg s $^{-1}$. From Mukherjee et al. 2016.

or

$$B \sim 10^5 \text{ G} \left[\frac{M_{\bullet}}{10^8 M_{\odot}} \right]^{-1} \left[\frac{\dot{M}}{2 M_{\odot} \text{ yr}^{-1}} \right]^{-\frac{1}{2}} \left[\frac{v_r}{c} \right]^{-\frac{1}{2}} \quad (1.18)$$

where v_r is the radial velocity of the gas (which tends to the speed of light at the SMBH horizon), \dot{M} is the mass flow and we have used $r = r_g = GM_{\bullet}/c^2$. With this we can estimate the magnetic flux as

$$\Phi_{\bullet} \sim B \times 4\pi r_g^2 \sim 8.6 \times 10^{32} \text{ G cm}^2 \left[\frac{M_{\bullet}}{10^8 M_{\odot}} \right]^{-1} \left[\frac{\dot{M}}{2 M_{\odot} \text{ yr}^{-1}} \right]^{-\frac{1}{2}} \left[\frac{v_r}{c} \right]^{-\frac{1}{2}} \quad (1.19)$$

Using this estimation to expression 1.16 we get

$$\dot{E}_{\text{jet}} \sim 1.6 \times 10^{47} \text{ erg s}^{-1} \left[\frac{a}{1 + \sqrt{1 - a^2}} \right] \left[\frac{M_{\bullet}}{10^8 M_{\odot}} \right]^{-2} \left[\frac{\dot{M}}{2 M_{\odot} \text{ yr}^{-1}} \right]^{-1} \left[\frac{v_r}{c} \right]^{-1} \quad (1.20)$$

where we have used $a = 1$ (maximum black hole spin) for the numerical estimation. Comparing this maximum estimation with the total accretion power ($\dot{M}c^2$) discussed in the previous section, we see that it exceeds it by at least one order of magnitude. This is possible as the jet power comes directly from the SMBH spin and not the mass accretion.

The impact of relativistic jets as a form of AGN feedback is primarily conceptualized through two mechanisms. The first, often termed "maintenance mode" feedback, delves into the capability of jets to excavate kpc-scale lobes in the intergalactic medium (IGM), thereby heating the gas and preventing it from cooling and gravitating toward the galactic core (Fabian 2012; McNamara and Nulsen 2012).

On the other hand, hydrodynamical simulations illustrate a different

scenario at the galactic scale within the interstellar medium (ISM). They demonstrate that jets can efficiently transfer energy to dense matter in their path through the ISM, generating shock waves, exerting ram pressure, and inducing turbulence (Wagner and Bicknell 2011; Wagner et al. 2012; Mukherjee et al. 2016; Mukherjee et al. 2018; Talbot et al. 2022). These simulations have shown that the influence of a jet on its surrounding gas is strongly sensitive to several factors, notably its power, its directional orientation relative to the gas disk, and the clumpiness of the disk. High-power jets, with an energy output of approximately $10^{45} \text{ erg s}^{-1}$, possess the ability to penetrate the ISM and reach intergalactic space much faster compared to lower-power jets ($10^{43} \text{ erg s}^{-1}$). The latter, due to their prolonged interaction within a dense environment, tend to remain embedded, creating high pressure regions that significantly disturb the ISM (Talbot et al. 2022; Mukherjee et al. 2016). Similarly, if the jet is oriented perpendicularly to the disk, it will have a minimal effect on the ISM and will escape faster into the IGM.

1.3.3 Starbursts outflows



Figure 1.9: Messier 82 starburst galaxy imaged from Hubble Space Telescope. <http://www.spacetelescope.org/images/heic0604a/>

In this work we are exclusively focusing on the galactic feedback mechanisms powered by the AGN. However, we must note here that stellar feedback is also an efficient way for a galaxy to regulate its growth. As galaxies grow and consume large proportion of gas producing stars, some of them turn to supernovae injecting huge amounts of energy into the ISM. Assuming the stellar initial mass function (IMF) from Kroupa (2001),

$$\xi_{\text{star}}(m) = k \begin{cases} \left(\frac{m}{0.07}\right)^{-1.3 \pm 0.3} & , 0.07 < m \leq 0.5, \\ \left[\left(\frac{0.5}{0.07}\right)^{-1.3 \pm 0.3}\right] \left(\frac{m}{0.5}\right)^{-2.3 \pm 0.36} & , 0.5 < m \leq 150. \end{cases} \quad (1.21)$$

we can compute the relative population of supernovae prone stars

Initial mass function is an empirical function that describes the initial distribution of stellar during star formation

(> $8 M_{\odot}$ to the total stellar mass by integrating the mass function

$$\frac{M}{M_8} = \frac{\int_{0.07}^{150} \xi(m) dm}{\int_8^{150} \xi(m) dm} = 168.5 \quad (1.22)$$

This means that for every $168.5 M_{\odot}$ of stellar mass produced there is one supernovae. Thus, the power injected by a starburst is

$$\dot{E}_{\text{SN}} \approx 1.8 \times 10^{42} \text{ erg s}^{-1} \left[\frac{E_{\text{SN}}}{10^{51} \text{ erg}} \right] \left[\frac{\dot{M}}{10 M_{\odot} \text{ yr}^{-1}} \right] \quad (1.23)$$

where we used the standard SN energy output of 10^{51} erg and the star formation rate of the archetype starburst galaxy Messier 82 for the numerical approximation. Using the same analogy for a total stellar mass of $10^{11} M_{\odot}$ we get a total energy of 6×10^{59} erg similar to the total bulge binding energy (1.6). This means that to significantly influence the ISM, SN needs an extreme coupling efficiency. However, these estimates are based on very crude approximations with great uncertainties.

1.4 Observation evidences of feedback

In the previous section, we provided a theoretical framework illustrating how an AGN can play a pivotal role in galaxy evolution. In this section, we shift our focus to observational studies that yield either indirect or direct evidence of the effects of AGN feedback. Such evidences are the the observed correlation between the black hole masses with their host mass, the observed decline of star formation and in elliptical galaxies and the discrepancy in the luminosity function between the observations and the prediction of current cosmological models.

1.4.1 M-sigma relation

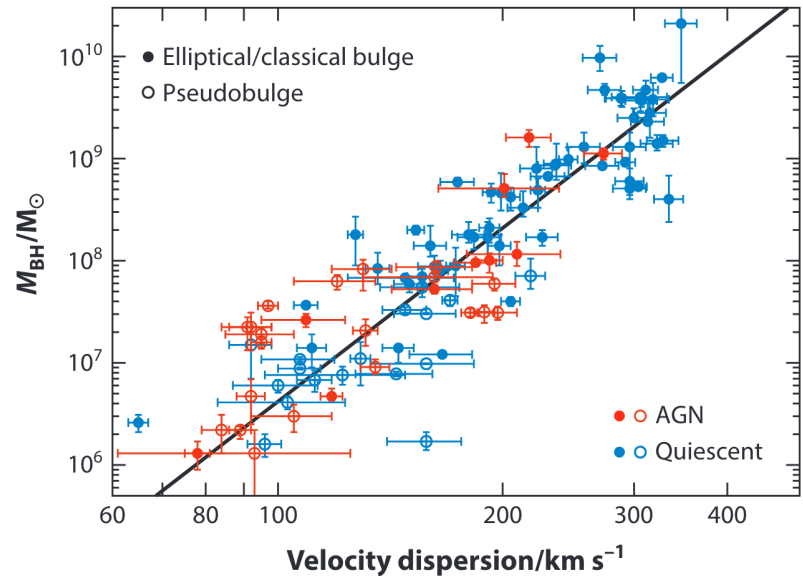


Figure 1.10: Black hole mass and stellar dispersion relation of local galaxies with direct black hole mass measurements (data from Woo et al. 2013, image from Heckman and Best 2014)

The M-sigma relation is a well-established empirical relationship between the mass of the SMBH at the center of a galaxy and the velocity dispersion of the stars in the galaxy's bulge.

$$\frac{M_{\text{BH}}}{M_{\odot}} \simeq 3 \times 10^8 \left[\frac{\sigma}{200 \text{ km s}^{-1}} \right]^{\alpha} \quad (1.24)$$

where $\alpha = 4.4 \pm 0.3$. This relation suggests that there is a close link between the growth of the SMBH and the evolution of its host galaxy, implying a co-evolution. As the black hole grows from the inflow of the gas reservoir of the galaxy it interacts with the host gas regulating its growth, and the stellar population evolved from the same reservoir. This interpretation can be further argued from the momentum driven wind expansion condition in equation 1.10. In order for the AGN to support a momentum-driven expansion the SMBH mass must larger than $M_{\sigma} \simeq 3.2 \times 10^8 \left[\frac{f_{\text{g}}}{0.16} \right] \left[\frac{\sigma}{200 \text{ km s}^{-1}} \right]^4 M_{\odot}$ which is remarkably close to the M- σ relation 1.24. This agreement suggests that as long as SMBH mass remains below this threshold the wind outflow shell cannot expand to galactic scales, as the wind power is not enough to win the bulge potential. However, when the SMBH mass grows above M_{σ} , the growth of the SMBH halts and a rapidly momentum driven wind expands into the galactic medium.

1.4.2 Quenching of star formation

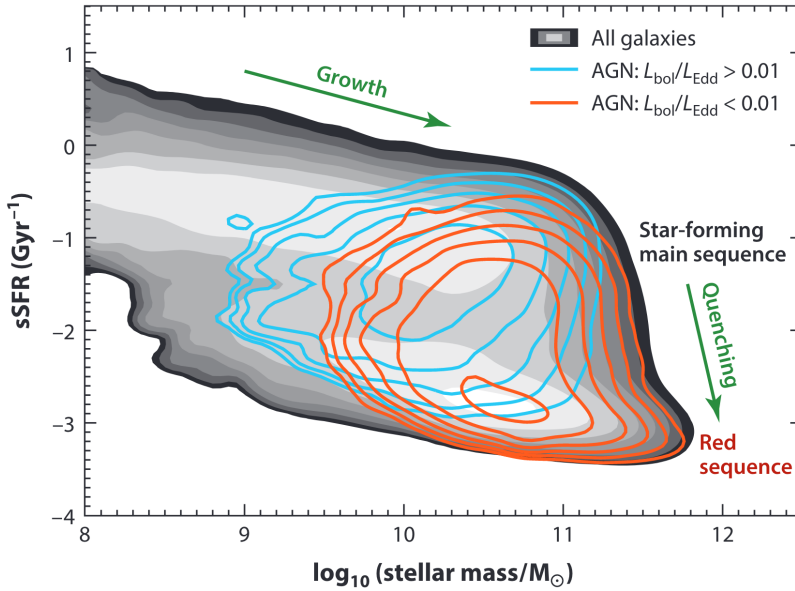


Figure 1.11: SDSS galaxies distribution on the plane of stellar mass versus specific star-formation rate (star formation over stellar mass). The grayscale indicates the volume-weighted distribution of all galaxies, with each lighter color band indicating a factor of two increase. The distribution shows a bimodality between a main sequence of star-forming galaxies and a red sequence of quenched galaxies. The blue and red contours display the distribution of high and low eddington fraction, representing radiative and jet mode agns respectively.

Quenching refers to the phenomenon where in the star formation activity in a galaxy ceases or diminishes significantly. Initial evidence of star formation quenching was gleaned through tracking the star formation rate across cosmic epochs. This endeavor was carried out through surveys spanning radio, infrared (IR), ultraviolet (UV) wavelengths, and specific emission lines ($H\alpha$, OII, $Ly\alpha$). These surveys encapsulate a substantial span of cosmic history, reaching up to redshift 8, revealing a rising phase in star formation rates for $3 < z < 8$, peaking around $z = 2$ when

the universe was 3.5 Gyr old, subsequently followed by a descent to present-day local values (Madau and Dickinson 2014).

Another indication of quenching is the bimodality in the color-magnitude correlation of galaxies (Strateva et al. 2001; Baldry et al. 2004). Mergers between spiral galaxies and classical bulges and ellipticals (Toomre and Toomre 1972; Toomre 1977; Schweizer et al. 1990) can result in the latter being gas-poor and "red and dead", suggesting that something connected with mergers is removing gas and rapidly quenching star formation. AGN feedback has been blamed for this (Springel et al. 2005; Schawinski et al. 2007) as evidenced by the close association of high-luminosity AGNs with post-starburst stellar populations (Kauffmann et al. 2003) and the detection of fast ($\gtrsim 10^3 \text{ km s}^{-1}$) outflows in post-starburst systems (Tremonti et al. 2007).

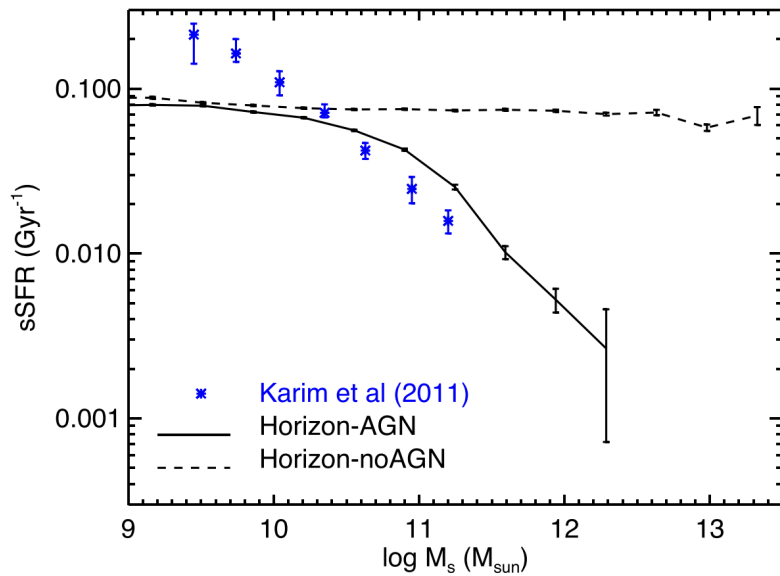


Figure 1.12: Star formation quenching observation in comparison with cosmic simulation which incorporate or not, AGN feedback (Dubois et al. 2016)

1.4.3 Luminosity Function

The luminosity function (LF) provides a statistical measure of the distribution of luminosities amongst galaxies, thereby serving as a critical tool for inferring the underlying physics governing galaxy evolution. The discrepancies observed between the empirical luminosity function and the theoretically predicted mass function of dark matter halos, particularly at the high-mass and low-mass ends, highlight the presence of feedback mechanisms that modulate galaxy formation and evolution. It has been posited that feedback from AGN, notably the radio-mode feedback, significantly contributes to this observed deviation by mitigating the cooling of hot halo gas (Sakelliou et al. 2002; Peterson et al. 2003; Benson et al. 2003; Croton et al. 2006). This mode of feedback is especially effective in quenching star formation in massive galaxies, thus explaining the sharp downturn in the galaxy LF at high masses. On the other end of the mass spectrum, other feedback mechanisms, such as supernova feedback, become more dominant in regulating star formation, as reflected in the steep decline in the LF at low masses (where gravitational potential wells

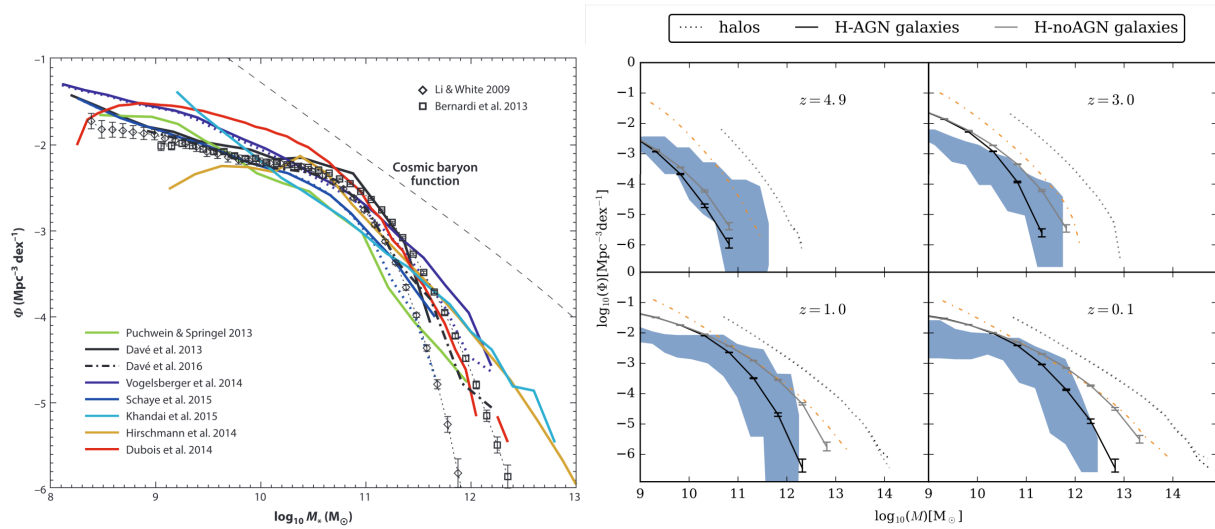


Figure 1.13: **Left:** The observed galaxy stellar mass function and its comparison from recent large-scale cosmological simulations (which include stellar and AGN feedback). The dashed line shows the hypothetical galaxy mass function assuming the cosmic baryon fraction (from Naab and Ostriker 2017). **Right:** Galaxy stellar mass functions (solid lines) and Dark matter halo mass functions (dotted) and corresponding galaxy stellar mass functions for the Horizon-AGN (black) and Horizon-noAGN (light grey) cosmic simulations. The blue shaded area represents the observations from (González et al. 2011; Bielby et al. 2014; Daddi et al. 2002; Bernardi et al. 2013; Moustakas et al. 2013; Tomczak et al. 2014; Song et al. 2016; Davidzon et al. 2017). From Beckmann et al. 2017.

are less deeper, thus feedback from supernovae is more effective) (Fabian 2012).

Recent hydrodynamical cosmological simulations, which incorporate AGN-feedback mechanisms, such as Horizon-AGN (Dubois et al. 2014), have made significant strides in reproducing the observed evolution of galaxy properties across cosmic time. The simulation demonstrates good agreement with observed luminosity functions, stellar mass functions, and other key observables across a wide redshift range ($0 < z < 6$), thereby providing a compelling framework for understanding the intertwined roles of AGN feedback and other processes in shaping the galaxy population over cosmic history (Dubois et al. 2014; Kaviraj et al. 2017).

1.4.4 Direct observation of fast winds and outflows

The most direct observations of AGN feedback are the clearly observed galactic outflows, with numerous AGNs showing outflows ranging from tens to thousands of solar masses per year. However, distinguishing whether these outflows are driven by stellar (SN) feedback or by the AGN can be challenging, especially at outflow velocities less than 500 km s^{-1} .

The most notorious example of wind-driven outflow is the case of the quasar closest to MW at $z = 0.04$, Mrk 231. In the core of the source, ultra-fast outflows (UFOs) are observed through blue-shifted X-ray ionized gas absorption with velocities of $0.07 c$, giving a mass outflow rate of $\sim 1 M_{\odot} \text{ yr}^{-1}$ Feruglio et al. (2015). Outflows are also observed in neutral gas (Morganti et al. 2016) and in cold molecular gas with a total mass outflow of $500 - 1000 M_{\odot} \text{ yr}^{-1}$ (Feruglio et al. 2015). The example of Mrk 231 is consistent with the radiation-wind mechanism, where UFO winds interact with the colder and denser ISM initiating massive outflows. Mrk 231 also has a visible jet, but its estimated radio power is not enough to support the observed outflows.

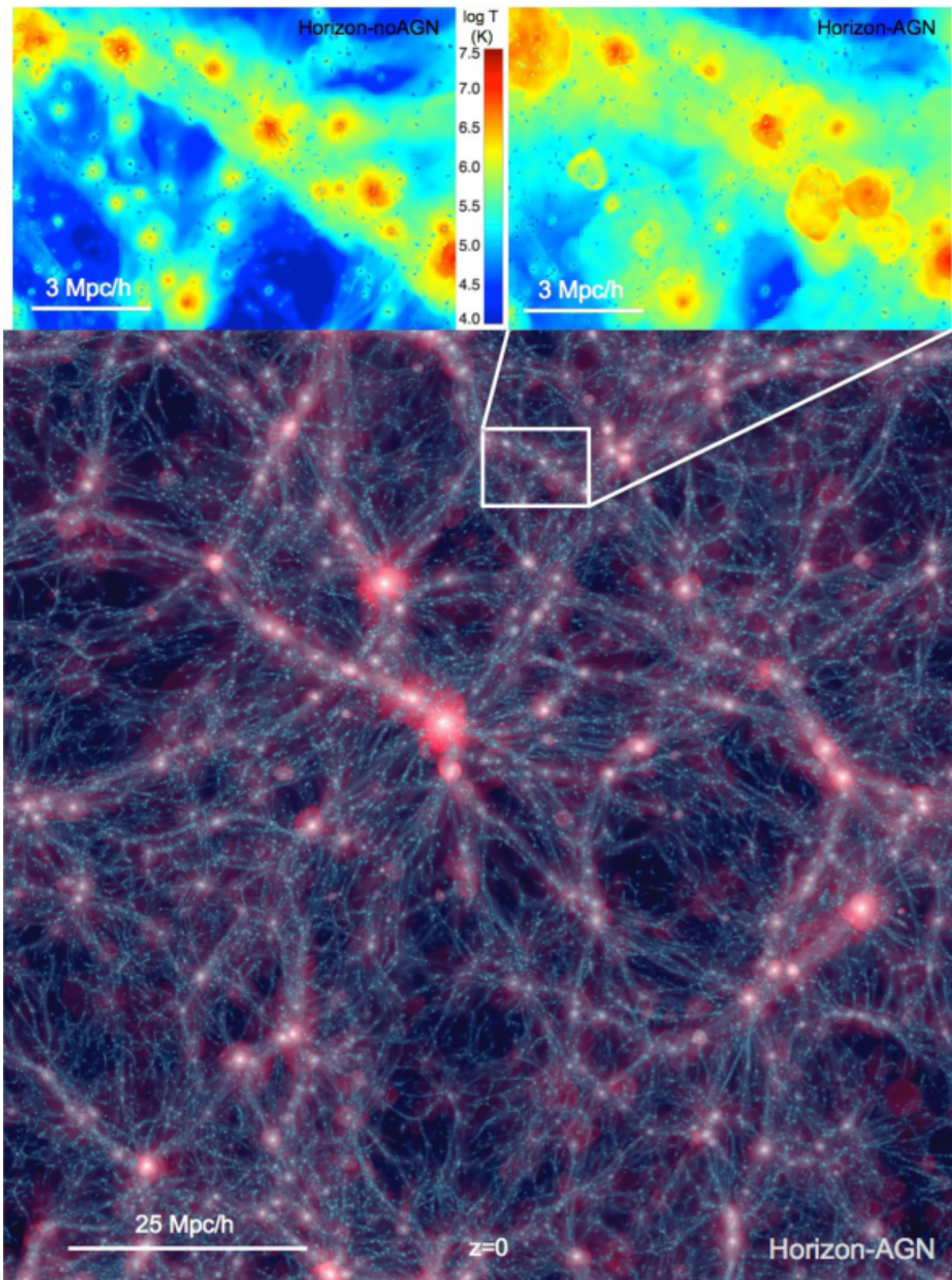


Figure 1.14: Grand-scale structure formation (bottom) and gas temperature (top) from the horizon cosmic simulations (Dubois et al. 2014). In the gas temperature we show the difference in gas temperature and structure if the simulation uses AGN feedback (top right) or not (top left). Image from Dubois et al. 2016

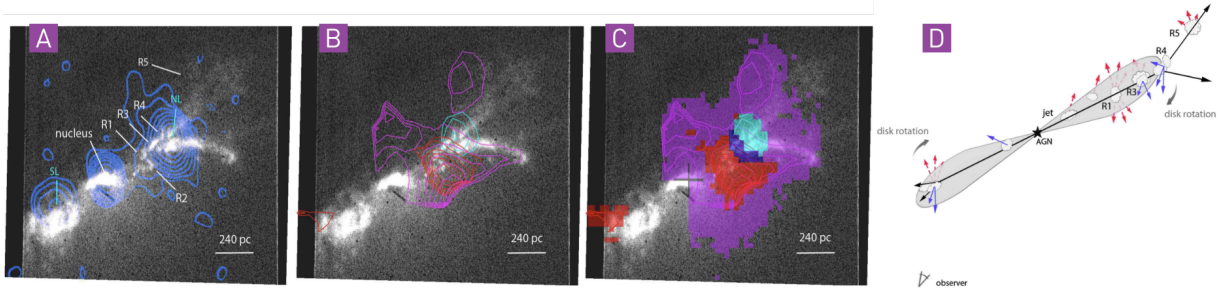


Figure 1.15: IC5063 jet and ISM interaction. The contours in panel A represent the radio emission, while in panels B and C the ionized gas FeII. The shaded area in panel C indicates the regions where at least 10% of the gas (in molecular or atomic phase) is outflowing. In the panel D is a schematic representation of the jet-ISM interaction. From Dasyra et al. 2016.

Radiation driven outflows have been observed in a wide range of redshifts, and especially in high- z young Quasars (King 2003; Harrison 2017; Bieri et al. 2017).

IC5063 on the other hand, a radio-loud Seyfert galaxy has a multiphase outflow (ionized gas, HI and molecular gas components) where the outflow geometry and properties are consistent with a jet driven outflow (Tadhunter et al. 2014; Morganti et al. 2015; Dasyra et al. 2016; Oosterloo et al. 2017). The outflowing cold molecular gas has a mass of $\sim 1.2 \times 10^6 M_{\odot}$ for a total mass outflow rate of $\sim 4 M_{\odot} \text{ yr}^{-1}$.

Radio jets, launched by SMBH, have been observed to impact on large scales, extending to tens of kpc, and can delay the cooling flows from the intracluster medium (ICM)/intergalactic medium (IGM) and the formation of extremely massive galaxies (Fabian 2012; McNamara and Nulsen 2012). This is typically observed in the centers of relatively low-redshift (z) clusters and groups. Furthermore, there is accumulating observational evidence suggesting that the interaction of radio jets with the ISM can drive molecular outflows in various local galaxies (Fotopoulou et al. 2019; Oosterloo et al. 2019; Aalto et al. 2020; Fernández-Ontiveros et al. 2020), including those with low-luminosity AGN (Combes et al. 2013; García-Burillo et al. 2014; Audibert et al. 2019; Ruffa et al. 2022).

As mentioned at the beginning of this section, our primary interest lies in understanding the role of AGN interactions with molecular gas, a key ingredient for star formation. This makes the direct feedback mechanisms involving such interactions particularly crucial. Apart from the prototype-case studies of AGN and jet driven winds, we mentioned above, there are numerous observations of cool molecular gas outflows with debatable driving mechanisms.

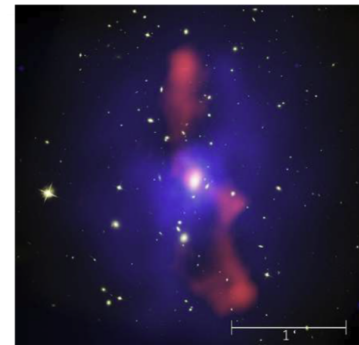


Figure 1.16: The interaction of the radio jet from the MS0735.6+7421 cluster central galaxy with the intra-cluster gas (McNamara et al. 2009). The image scale is 700 kpc. In "maintenance mode" feedback jets prevent the intergalactic gas to cool and flow to the galactic core

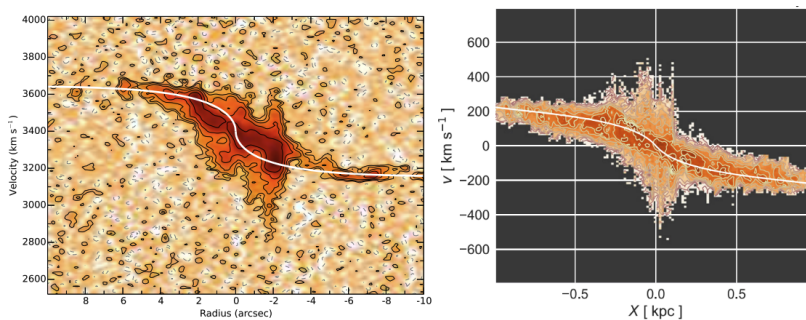


Figure 1.17: Left: Observed integrated position velocity plot of the molecular gas in IC5063 from Morganti et al. 2015. The dispersion of the gas indicates the outflows. Right: Simulated position velocity plot of $10^{44} \text{ erg s}^{-1}$ jet impacted molecular gas for IC5063 (Mukherjee et al. 2018).

In local ($z < 2$) galaxies, Fluetsch et al. (2019) compiled a list of 45 detected molecular outflows using the Atacama Large Millimeter/submillimeter Array (ALMA), Herschel, and other interferometric observations from literature. Most of these outflows lacked information or detection of ionized or neutral gas components. The observed outflow rates suggest a potential for depleting the total molecular gas within a few to tens of million years, a timescale significantly shorter than that of star formation alone. However, when considering the atomic gas component, the depletion timescale extends beyond the typical AGN lifetime (10^8 yrs). This suggests that while AGN-driven outflows can rapidly remove gas from central regions in the local universe, they are unlikely to clear out entire galaxies. Similar results have been presented by Lutz et al. (2020) in a study of 13 local galaxies using ALMA and Northern Extended Millimeter Array (NOEMA) molecular gas (CO 1-0) observations. These studies primarily attributed the outflows to thermal or radiation pressure from the AGN, supernovae, or young stellar populations, with jet-driven mechanisms being plausible in only some specific sources. However, in the latter part of this thesis (section 4), we re-evaluate the role of jets as drivers of gas outflows in these specific sources, finding a plausible jet-outflow connection in about half of the examined AGNs.

At higher redshifts, the detection and interpretation of molecular gas outflows present significant challenges. These difficulties are primarily due to limitations in sensitivity of current observational tools and uncertainties that arise in differentiating outflows from other kinematic features. For instance, irregularities stemming from galaxy mergers can often be mistaken for outflows. Despite these challenges, there have been detections of outflows (Weiß et al. 2012; Feruglio et al. 2017; Carniani et al. 2017; Vayner et al. 2017; Fan et al. 2018; Brusa et al. 2018; Herrera-Camus et al. 2019) at high redshifts, attributed to all possible driving mechanisms. These detected outflows tend to be very extended and fast-moving as a result of detection bias, as our current observational capabilities may only allow us to identify the most extreme cases.

In addition to extragalactic sources, evidence of molecular gas outflows has also been observed in the Milky Way. Bland-Hawthorn and Cohen (2003) described a bipolar structure of cool dust with a total mass of approximately $5 \times 10^5 M_{\odot}$, extending about 140 pc from the Milky Way's plane. This structure aligns with the radio-emitting Galactic Center Lobe (Sofue and Handa 1984), which is itself part of a larger bipolar radio structure measured at 4330 pc (Heywood et al. 2019). This radio structure has a high-energy counterpart observable in X-rays (Ponti et al. 2019). While these radio structures could be attributed to supernovae in the Galaxy's central regions, the total kinetic energy of the molecular outflow, estimated at 10^{56} erg, aligns more closely with the total energy needed to inflate the much larger 12 kpc gamma-ray emitting bubbles, known as the Fermi bubbles (Su et al. 2010; Dobler et al. 2010; Planck Collaboration et al. 2013; Ackermann et al. 2014). These observations hint at a possible AGN-like activity in the Milky Way's recent million-year history (Zubovas et al. 2011; Guo and Mathews 2012; Yang et al. 2012; Bland-Hawthorn and Cohen 2003; Mou et al. 2014; Ruszkowski et al. 2014; Miller and Bregman 2016; Bland-Hawthorn et al. 2019).

Data Mining and Sample Selection

2

Although jets can play a major role in feedback mechanisms, there is still a lack of systematic and statistically meaningful observational measurements for the number of radio galaxies (RGs) with significant gas reservoirs that could be influenced by jet-induced feedback.

Previous research has indicated that most local RGs have lower gas content compared to spiral galaxies or those selected based on infrared criteria (Ruffa et al. 2022). Initiatives to survey RGs at high redshift (z) using CO began in the 1990s and have unveiled either substantial molecular gas reservoirs (characterized by $M_{\text{mol}} \approx 10^{10} - 10^{11} M_{\odot}$) in certain powerful RGs at $z \geq 2$ or gas-depleted in others (Scoville et al. 1997; Papadopoulos et al. 2000; De Breuck et al. 2003; De Breuck et al. 2005; Greve et al. 2004; Nesvadba et al. 2008; Emonts et al. 2011; Emonts et al. 2014; Castignani et al. 2019).

To gain a comprehensive understanding of the role of jets in galactic feedback mechanisms, we required a robust sample of radio-loud galaxies for which molecular gas observations could also be obtained. Our primary observational tool was the Atacama Large Millimeter/submillimeter Array (ALMA), which operates within a spectrum window range ideally suited for CO observations along the cosmic history. This state-of-the-art telescope is also capable of delivering high-resolution observations in the millimeter and submillimeter parts of the spectrum, thus allowing for accurate tracing of molecular gas.

In the subsequent section, we present a novel analysis of CO molecular transitions ranging from rotational numbers $J=1-0$ to $J=4-3$, conducted with ALMA for RGs up to $z < 2.5$. To establish a statistically significant sample, we analyzed CO emissions in a sub-sample of RGs from the ALMA Calibrator Source Catalog. These were selected to be representative of the NRAO/VLA Sky Survey (NVSS) in terms of their redshift and 1.4 GHz flux distribution, down to a limit of 0.4 Jy. By incorporating data from existing literature, we executed a comprehensive archival CO survey of molecular gas in RGs. A primary objective of our study was to analyze the evolution of the gas content in RGs as a function of redshift, a critical factor for accurate benchmarking of cosmological simulations. This analysis also led us to construct, for the first time, the CO luminosity function of RGs at both low and high redshifts. An additional aim was to assess the occurrence of molecular outflows in the RGs within our sample.

Note on Authorship: The majority of the work presented in this chapter conducted from our research group and was published in Audibert et al. 2022. The survey was conceptually designed and funded by the PI, Kalliopi Dasyra who worked on the data reduction algorithms, oversaw the entire procedure and worked on luminosity function creation and interpretation. A. Audibert, I. Ruffa, and J. A. Fernández Ontiveros significantly contributed to the ALMA data reduction. My primary contributions encompassed leading the sample selection, data mining, data qualification, and SED fitting processes. Additionally, I have contributed to the development of initial data calibration pipelines, the optimization of calibration parameters, and the luminosity function fitting.

2.1 Molecular gas observations through ALMA

Observing molecular gas in galaxies poses a series of challenges. Cold molecular gas primarily exists as hydrogen (H_2), a molecule that is symmetric and lacks a permanent electric dipole moment. The most accessible energy transition for H_2 is a quadrupole transition, with an energy difference of $\Delta E = E(J = 2) - E(J = 0) \approx 4.7 \times 10^{-2} \text{ eV}^*$. This corresponds to a temperature of 510 K and results in photon emission at $28.2 \mu\text{m}$. Given the typically low temperatures (15 – 20 K) of stellar nurseries like Giant Molecular Clouds (GMCs), direct observations of H_2 are often limited to absorption lines in the ultraviolet background.

To overcome these limitations, we use alternative molecules that coexist with H_2 but in lower abundances. These include Carbon Monoxide (CO), Ammonia (NH_3), and other molecules such as CS, H_2O , and OH. These molecules serve as proxies for H_2 , allowing us to estimate the presence and quantities of molecular hydrogen gas indirectly. For instance, CO, the second most abundant molecular gas, possesses a permanent dipole moment, facilitating lower energy differences on its energy ladder. The CO(1-0) emission line, for example, has an energy difference $\Delta E = 4.8 \times 10^{-4} \text{ eV}$, corresponding to a temperature of 5.5 K, and resulting in photon emission at 2.6 mm.

The choice of ALMA for our study is primarily due to its capability to operate effectively in the specific spectroscopic bands that are key for observing these molecular emission lines. Additionally, other factors motivating our choice include:

- ▶ **High Sensitivity:** ALMA's unmatched sensitivity enables us to observe distant cosmic sources. This capability is crucial for detecting the presence of molecular gas and understanding the influence of jets across different epochs of the universe.
- ▶ **High Resolution:** The telescope's superior angular resolution allows for detailed mapping of the structure and kinematics of molecular gas. This aids our understanding of possible interactions between jets/AGN and the interstellar medium.
- ▶ **Comprehensive Archives:** ALMA maintains a rich archive of all conducted observations, providing a wealth of raw observational data along with calibration and imaging procedures. These resources are invaluable, granting the flexibility to use existing scientific products or re-analyze the raw data to suit the specific aims of our research.

In addition to this general archive, we also make use of the ALMA Calibrator Source Catalogue (ARC), a specialized resource comprising primarily bright quasars at mm and sub-mm wavelengths, which serve as calibrators (flux, phase, bandpass, etc) for ALMA. The catalogue was created from the compilation of multiple previous catalogues, including the Very Large Array Calibrator Manual, Submillimeter Array and Atacama Compact Array surveys, the Parkes survey, and the Combined Radio All-Sky Targeted Eight-GHz Survey. As such, the ensemble of objects in it is randomly selected and distributed on the sky. The catalogue

* The rotational energy E_{rot} is calculated as $E_{rot} = \frac{h^2}{2I_{H_2}} J(J + 1)$, where J is the rotational quantum number and $I_{H_2} = 5 \times 10^{-48} \text{ kg, m}^2$ is the moment of inertia of H_2

contains information derived for the calibrations, such as the flux of each object at various frequencies, by conducting a regularly grid survey.

The catalogue presents the latest flux measurement for each object in a given band. Typically, two flux measurements are given for the (two sidebands of) band 3, and one flux measurement is given for all other bands. The catalogue can be downloaded from the European Southern Observatory (ESO) archival interface[†] by, e.g., performing an empty query. As of 01/08/2020, the downloaded catalogue contained 8679 entries (i.e., object and band combinations). The number of unique objects (deduced by removing the information on the bands) was 3360.

2.2 Building CO-ARC

We used the python astroquery package (Ginsburg et al. 2019) to mine through ALMA archive for every observation made for each object in ARC (based on it's registered name or sky coordinates), resulting in 25827 observations from 1562 unique sources. About half of the total calibration sources haven't been used for actual observation procedure, but are monitored in a regular basis. Also for some of the sources we found observations in which they were science targets. The combination of calibration and science related data led to a wealth of information that enabled our archival survey to be designed.

2.2.1 Redshift information

In order to find out if a molecular line lies in the frequency window of a calibrator observation we need to know its redshift. We used the astroquery tool to search through the NASA Extragalactic Database (NED) archives for registered redshift information for every object. NED provides a redshift table for every source with a registered redshift and the reference of its origin. During a quick review of these tables we came across with many inconsistencies in the redshift values due to different methods of its estimation (photometric, spectroscopic) or by not taking care about any uncertainties or comments from the authors. If an author uses an inconsistent or inaccurate redshift value from the literature, NED register this value as new one to the source redshift table. This results in contamination of possibly wrong, inaccurate or different redshift values. For our work redshift is a mandatory and sensitive information. A wrong redshift value will result in a type 2 error, meaning that falsely inferring that a source has not CO gas due to wrong frequency window. So we studied every literature entry for every source from NED's redshift tables along with other resources (Simbad and Vizier). Quality assessment was performed by examining the redshift origin for qualification and comments from the authors regarding the sources. We were extra careful selecting automated high quality spectroscopic redshift surveys, as SDSS, because of cases of inconsistencies in the registered redshift values. We used SDSS redshifts when we had a valuable cross-reference on a source.

[†] <https://almascience.eso.org/sc/>

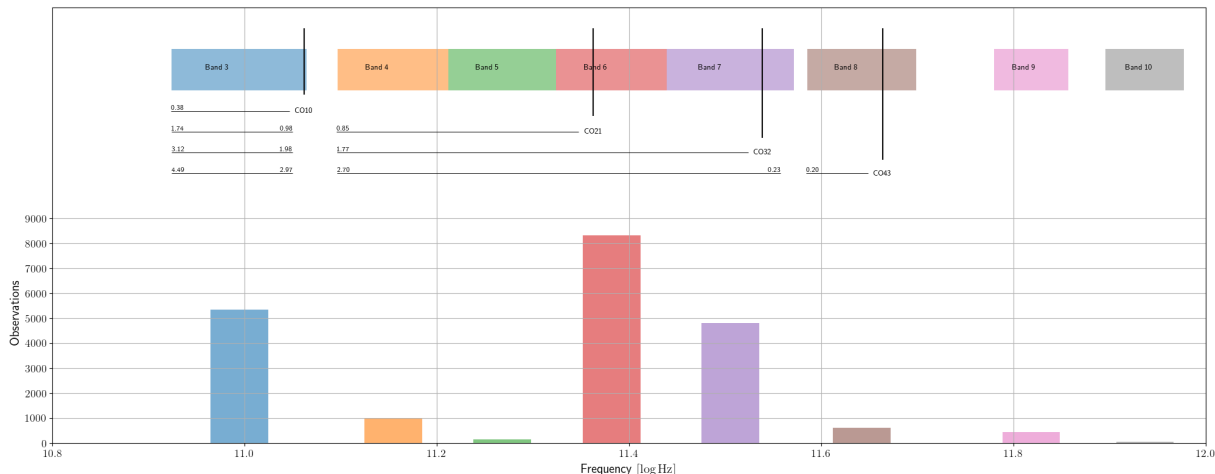


Figure 2.1: At the top of the figure are the operational ALMA Bands frequency windows and rest frame frequencies of the CO lines up to CO 4 \rightarrow 3. Directly below we plot the redshift windows where we can observe them due to redshift. At bottom we plot the number of ARC observations per band

2.2.2 CO lines in ARC sources

Therefore given the redshift information for our sources and their observation history as we mined them from ALMA, we searched for the presence of any molecular line in the CO rotational ladder up to CO 4 \rightarrow 3. We don't count a line if its near the window boundary (given a typical FWHM of 25 km s^{-1}). A total of 675 sources had at least one CO line with any integration time. We kept only sources with a minimum integration time of 5 mins to ensure that the data analysis (e.g., the derivation of error bars) is meaningful.

For some of the objects, the spectral windows of the calibrations cover the frequencies of molecular line transitions as it illustrated in figure 2.1.

As a next step, we had to ensure that only galaxies with radio emission associated with accretion onto black holes were kept. As the goal of our survey is to investigate the role of radio-mode feedback on galaxy evolution, all objects with radio emission associated with star formation activity had to be eradicated. For this reason, we imposed the 1.4 GHz-to- $24 \mu\text{m}$ flux criterion of Bonzini et al. 2013, identifying radio emission in excess of what supernovae can produce in star-forming galaxies via the quantity $q_{24} = \log(S_{24\mu\text{m}}/S_{1.4\text{GHz}})$, which has to be $< 0.5^\ddagger$.

To serve as calibrators, the CO-ARC sources are point sources at millimeter and radio wavelengths (such as quasars or blazars). To also include RGs with spatially-resolved, extended radio jets, we performed an extensive bibliographic search, which provided us with a pool of either single-object or dedicated samples with CO observations (Lim et al. 2000; Evans et al. 2005; Ocaña Flaquer et al. 2010; Ruffa et al. 2019a; Russell et al. 2019; Dabhade et al. 2020). The q_{24} criterion described above was then applied to the selected literature sources, leaving us with a total of 152 galaxies which were then considered suitable to complement our CO-ARC sample. Hereafter, we will refer to the joint CO-ARC and

[‡] The "classical" definition of radio loudness via the R indicator, the ratio between the rest-frame radio-to-optical flux density with typical values of $R \sim 10$ characterizing RGs (Kellermann et al. 1989), is often insufficient to identify radio-quiet (RQ) objects, because both star-forming and RQ galaxies can have low R values.

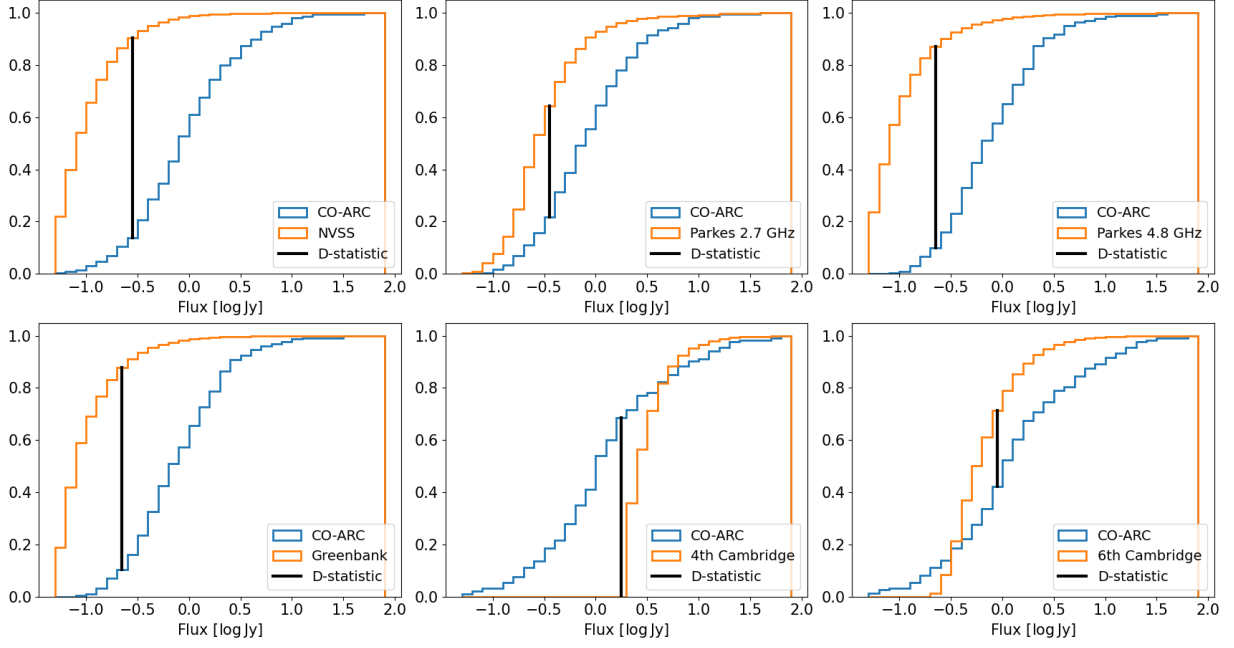


Figure 2.2: Comparison of CO-ARC cumulative flux distribution with several radio surveys flux limited at the minimum flux of CO-ARC for the specific frequency.

bibliographic super-sample of 356 galaxies as the *extended* CO-ARC or eCO-ARC.

2.2.3 Radio - Identification of Parent Galaxy Sample

The radio sky has been studied by several surveys in recent years, including the Sixth Cambridge Survey (6C) at 151 MHz (Hales et al. 1993), the NRAO/VLA Sky Survey (NVSS) at 1.4 GHz (Condon et al. 1998), the Parkes Radio Sources Catalogue (PKS) at 2.7 GHz (Wright and Otrupcek 1990) and at 4.8 GHz (Griffith et al. 1994), the MIT-Green Bank 5 GHz Survey (Bennett et al. 1986), and the Australia Telescope 20 GHz Survey Catalogue (Murphy et al. 2010) (AT20G).

To compile a radio catalogue from a set of mm/sub-mm sources, such as ARC and CO-ARC, we require the radio Spectral Energy Distribution (radio-SED) of each source. We then compare their flux at specific radio bands with existing radio surveys. This comparison enables us to create our radio catalogue by selecting a subsample from CO-ARC that is consistent with a representative sky survey catalogue.

We utilized the astroquery tool to obtain the radio-SEDs through the NASA/IPAC Extragalactic Database (NED), searching by the name of each source. Flux for every source in specific radio bands of the surveys was interpolated using a power law fit to the radio-SED. Figure 2.2 illustrates the varying resemblance between the surveys; deeper surveys like NVSS include fluxes much lower than those from our sources. Consequently, we limited the radio survey fluxes to the lowest flux value of our sources in their specific bands.

The results are displayed in Figure 2.2, where we show the cumulative distributions of CO-ARC and the surveys, limited by the lowest flux of our sources.

Among the various surveys analyzed, Parkes at 2.7 GHz, ATK at 4.8 GHz, NVSS at 1.4 GHz, and Greenbank catalogs all show completeness within the flux range relevant to our sample, meaning that our minimum flux sources were above the flux range where the surveys reached their peak. We chose NVSS as the parent radio survey for multiple reasons. Firstly, NVSS provides a large sky coverage extending to declinations greater than $\delta > -40^\circ$ surpassing the coverage of preceding surveys. Secondly, its sensitivity reaches down to approximately 2 mJy at 1.4 GHz, ensuring completeness for the flux levels of interest—several hundred mJy—as dictated by the 1.4 GHz fluxes of the CO-ARC sources. This sensitivity also assures that the majority of sources found in other surveys are encompassed within NVSS. NVSS has been frequently utilized in multi-wavelength AGN-related surveys, providing a framework to validate our findings. Particularly useful is its synergy with the Sloan Digital Sky Survey (SDSS) for high-precision redshift estimations. Given that our investigation aims to explore gas content as a function of redshift, it is imperative that the parent catalog possess such redshift data. Various efforts to amalgamate radio sources in NVSS with redshift-centric optical and infrared surveys have been undertaken, such as the CENSORS catalog (Best et al. 2003; Brookes et al. 2008) and a unified list comprising NVSS, WENSS, GB6, and SDSS sources (Kimball and Ivezić 2008).

We implemented a data mining approach, querying each NVSS source against all available redshift estimations in the literature. These are stored in the Vizier catalog archive. While these redshift estimations are subject to uncertainties, the sizable number of sources (~ 3000) in our dataset should statistically mitigate these effects. To further refine this process, we introduced a qualification method that examines the number of redshift estimations from different sources, gives weight to highly precise surveys (e.g., Hewett and Wild 2010), and scrutinizes conflicting estimations. This methodology led us to compile the NVSS-Z catalog.

2.2.4 Compiling a consistent subsample of the NVSS/NVSS-Z catalog

The subsequent step involves developing methods to compare the flux distributions of eCO-ARC and the radio survey NVSS-Z and to construct a survey-consistent subsample of eCO-ARC.

Kolmogorov-Smirnov consistency test

A standard statistical approach for this task is the two-sample Kolmogorov-Smirnov (K-S) test (Kolmogorov 1933; Smirnov 1939). In statistical hypothesis testing, the null hypothesis serves as a default assumption that needs to be examined. For the K-S test, this null hypothesis asserts that the two distributions being compared are actually separate random samples drawn from the same underlying distribution.

The test uses as a metric the maximum absolute difference between the two cumulative distributions (CDFs) defined as D -statistic

$$D = \max|S_1(x) - S_2(x)| \quad (2.1)$$

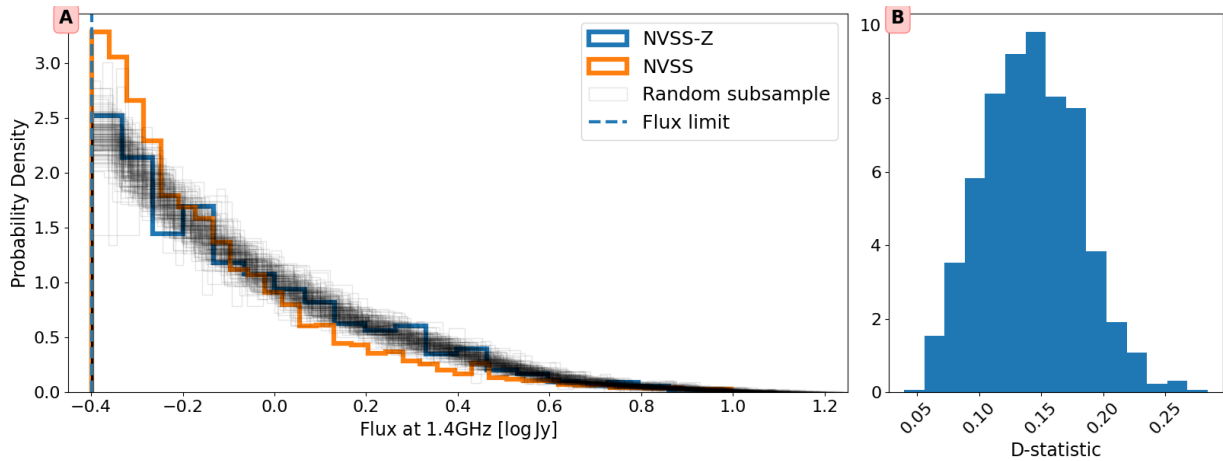


Figure 2.3: Panel A: NVSS and NVSS with redshift (NVSS-Z) radio flux distributions and a random sample of $N = 80$ simulated flux distributions based on the procedure we describe in the text. For all distributions we force a flux limit at 0.4 Jy **Panel B:** Distribution of the d -statistic of the simulated datasets with NVSS-Z.

For calculating the p -value, we refer to the D -statistic value in a reference table or use computational methods designed for the K-S test. The p -value quantifies the probability that a D -statistic as extreme as the observed one could occur randomly if the null hypothesis were true. In other words, the p -value measures how strongly the observed data deviate from what would be expected under the null hypothesis.

The p -value serves as a tool to evaluate the strength of the evidence against the null hypothesis. A low p -value suggests that the observed data are inconsistent with the null hypothesis, thereby providing grounds to reject it at a specified level of statistical significance. Importantly, while a low p -value indicates that the datasets likely come from different distributions, a high p -value does not confirm that the distributions are identical. Rather, it signifies that there is insufficient evidence to suggest they are different. As articulated by Press (2007), due to the intrinsic uncertainties present in any dataset, it's not possible to definitively prove that two sets of data are samples from the same distribution.

Recognizing the limitations of the conventional Kolmogorov-Smirnov (K-S) test in our specific case, we opted for an alternative strategy that tailors the 'critical' value of the D -statistic to our unique requirements. To achieve this, we conducted simulated experiments that mimic real-world observations of the sky, as seen through radio surveys. These simulations account for the known errors associated with the observational data; thus, we were able to simulate a large set of 'nights of observations' that vary slightly from one another but represent the same intrinsic properties of the sources.

By doing so, we estimated the distribution of the D -statistic that would arise when comparing these simulated observations to the 'parent' or original data set. This not only gave us a more accurate D -statistic for our specific case but also provided an invaluable insight into how the D -statistic distribution varies with the size of the simulated sample relative to the parent distribution. Armed with this information, we are better equipped to select the most suitable subsample from the eCO-ARC catalog for our study. So, given a parent flux distribution $S(f)$ we create a second set $S^*(f)$ of size N^* by varying each value of $S(f)$ as

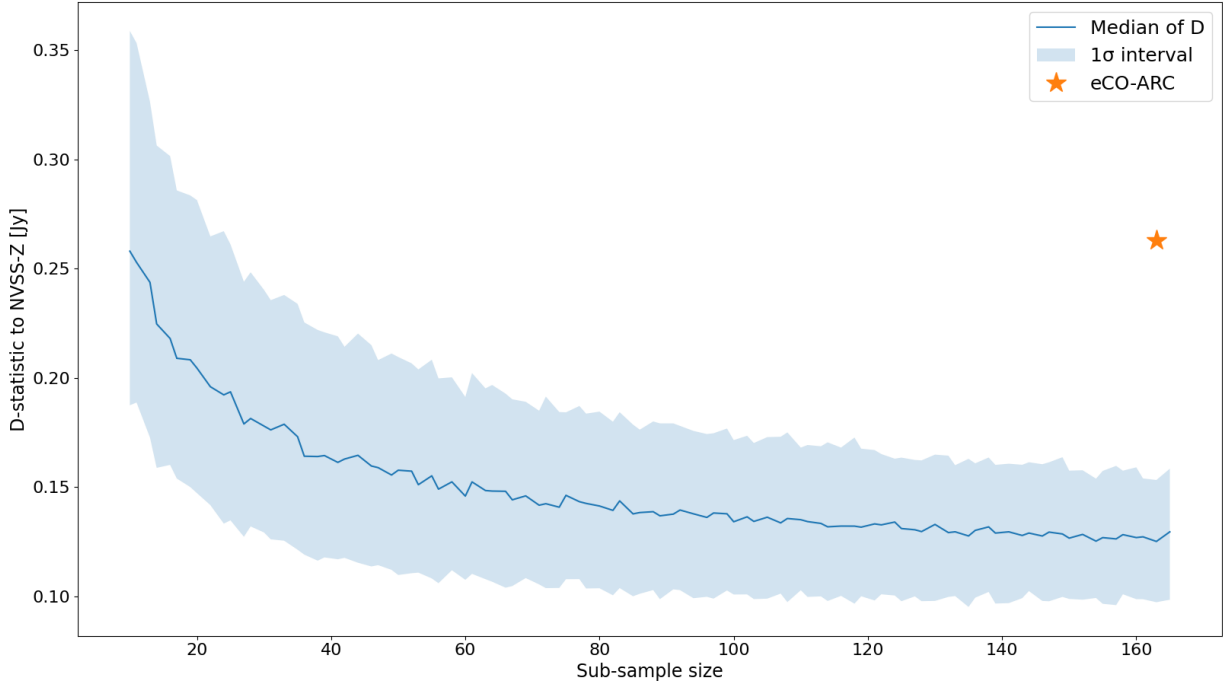


Figure 2.4: Behavior of the distribution of D -statistic for different sub-sample sizes N . The central line represents the median value of the D -statistic distribution and the highlighted area the $\pm 1\sigma$. When the size of S^* is relative small we expect that the random noise will have a bigger impact on the distance between the two distributions.

$S_i^*(f) = \mathcal{N}(S_i(f), \sigma_i(f))$, where we use as a typical error the 10% of the observation, $\sigma_i(f) = 0.1S_i(f)$ and \mathcal{N} is the Normal Distribution. Then we estimate

$$D(N) = \max|S(f) - S^*(f_N)| \quad (2.2)$$

where we now we randomly selected a subset of size N from our simulated distribution.

Executing this method thousands of times per different N we can study the statistical behavior of the D -statistic.

Additionally, it should be noted that another compelling advantage of our tailored D -statistic approach is its invariance to reparameterization of the cumulative distribution variable—in our context, this is the flux. This invariance allows us the flexibility to use either the raw flux $S(f)$ or i.e $S(\log f)$ interchangeably, making our method particularly versatile.

The next step to compile our final catalog is the flux limit we will apply to both the parent survey and our initial sources. Applying the minimum flux of our sources does not provide us with the most possible number of final sources, as radio surveys grow exponentially at lower fluxes, while intial eCO-ARC has most sources in the range of 0.5 Jy. For this reason we established a flux limit of 0.4 Jy which we calculated after some randomized experimental selections.

From the figure 2.3 we can see that 2 consistent flux samples of NVSS-Z, one with size $N = 80$ and the other to be the whole catalog, have a median value of the D -statistic close to 0.15, with the 95% of the values to be less than 0.25. So for two data sets, describing flux distribution we can confidently assume that they are consistent if their D statistic is less than 0.15. In figure 2.4 we see the behavior of the D -statistic for several different sub-sample sizes N .

Algorithm 1: D-statistic sampling algorithm**Input:** MaxIter, σ , SampleSizes, FluxLimit**Data:** NVSS-Z flux distribution: S **Result:** A list D which contains MaxIter randomly sampled values of the D -statistic for different SampleSizes

```

1  $D \leftarrow$  empty list of size SampleSizes
2 for  $N$  in SampleSizes do
3    $D_{\text{tmp}} \leftarrow []$ 
4   while  $i < \text{MaxIter}$  do
5      $S^* \leftarrow \mathcal{N}(S, \sigma)$  for every source
6     keep only  $S^* > \text{FluxLimit}$ 
7      $D_{\text{tmp}} \leftarrow \text{Append}(D_{\text{tmp}}, \max|S - S^*|)$ 
8   end
9    $D[N] \leftarrow D_{\text{tmp}}$ 
10 end

```

From this analysis we can define our selection criterion as the D -statistic between a subsample S_{optimal} of size N_{optimal} . With this definition we can confirm, that the initial eCO-ARC sample with $D \approx 0.26$ at $N = 163$ is not consistent with NVSS-Z. Thus we need to search for a subsample of size N_{optimal} which will meet the above criterion.

This can be done by iterating over a range of subsample sizes $N < N_0$, where N_0 is the starting sample of 163, and randomly sampling the eCO-ARCZ for a sufficient number of iterations per N . For every N we keep the best, lowest D -statistic sample. This simplistic method it is computationally expensive and not optimal, as the number of iterations needed in order to converge to a minima is comparable with the possible configurations. The number of possible configurations for a sample size N can be calculated by using the binomial coefficient

$$\binom{N_0}{N} = \frac{N_0!}{N!(N_0 - N)!}$$

The number of possible configurations grows in a huge number that is impossible to explore, even that we don't need to explore all of them. In order to solve this problem we created a new method with a much higher convergence speed.

Forced Convergence Method

If we have two distributions S_1 and S_2 with N_1, N_2 their sizes accordingly and S_2 is the parent distribution. As we have stated already, we want to find a subsample S of S_1 with size N with the lowest D -statistic between S and S_2 . The D -statistic is independent of any transformation we execute in both of our datasets. So we choose to log transform S_1, S_2 .

Now we bin the transformed datasets S_1 and S_2 with N_B evenly spaced bins. If we hadn't choose a logarithmic transformation almost all of our data would capture only a small fraction of our binned flux space.

For each bin i , we randomly sample from S_{1i} a number of n sources equal with the N_{2i} sources of S_2 at bin i , as it can be understood from the figure ???. We do this for a number of iterations and calculate the

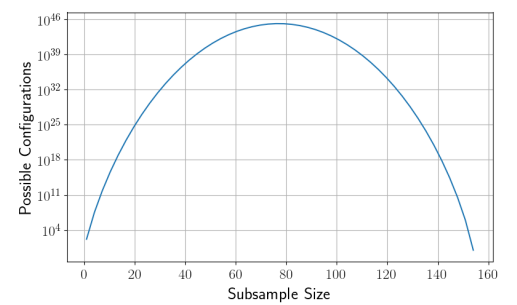


Figure 2.5: Number of combinations as a function of subsample size

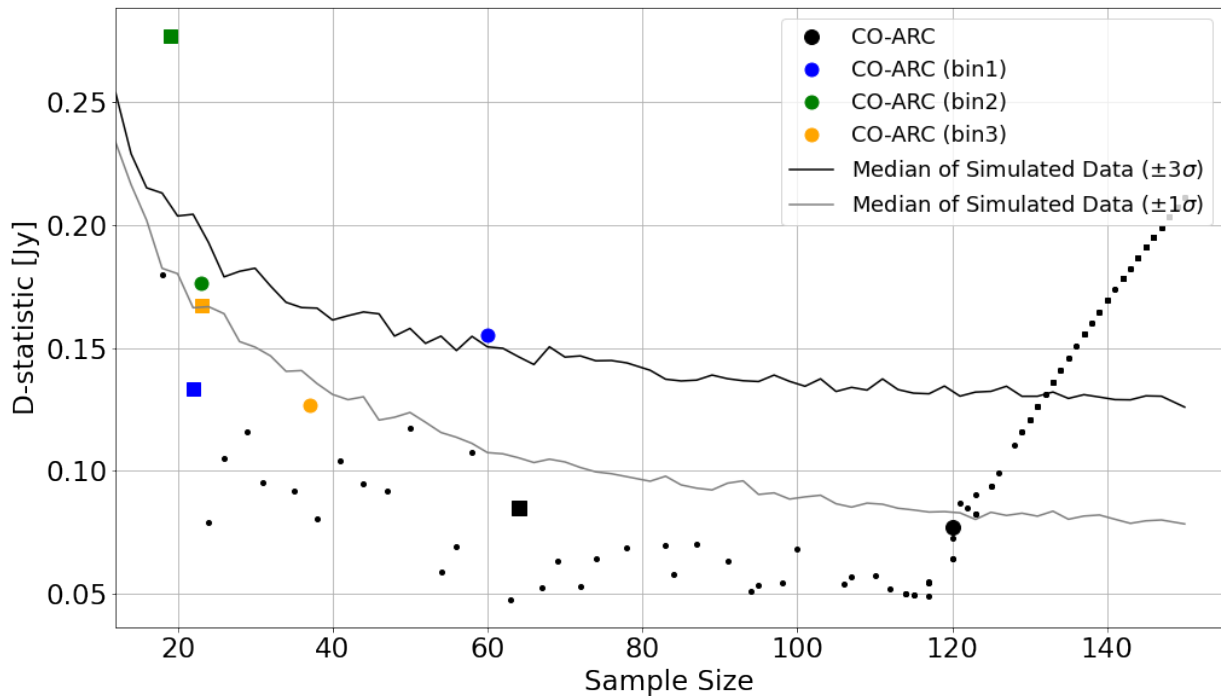


Figure 2.6: Sample selection algorithm and final sample candidates.

D -statistic. As before we keep the best subsample. With this method we have less possible configurations but mostly a physical directing force towards to the optimal D of our minimization problem. This can be understood as the different possible configuration per bin have only a small contribution in the final shape of the distribution.

The resulting convergence can be seen in the figure 2.6. After a sample size of about 120 sources the best D -statistic reaches a plateau before it gets up dew to the statistical behavior of comparing a relative smaller dataset. This plateau is our region of interest for compiling a catalog which is consistent with the parent radio catalog. An extra care was taken for the final sub-sample to be consistent of NVSS-Z also to the separate redshift bins, by fine-tuning the selection process.

2.3 Data Reduction: Calibration and Imaging

Our final sample consists of 120 radio sources, comprising 66 from the CO-ARC catalog and 54 from existing literature. We have identified which observations contain the CO lines of interest as previously described. ALMA provides raw visibility and flux data for each source (observed either as a target or as a flux, phase, bandpass, or polarization calibrator), captured from each pair of antennas participating in the observation. The ALMA observations that contributed to the CO-ARC survey span from Cycle 0 to Cycle 5. The relevant properties of each observing run (e.g. scan intent, on-source integration time, CO transition, etc.) are reported in Table 2.3.

2.3.1 Calibration Procedure

We used the Common Astronomy Software Applications (CASA) (McMullin et al. 2007) for data reduction [§]. The pipeline performs standard calibration and flagging. We used the specific pipeline version which was used to the archival data. In instances where a target source was observed in multiple execution blocks, each block was calibrated individually and subsequently merged using the CASA `concat` task. Flux calibration uncertainty is generally around 10%, as bright quasars often serve as flux calibrators.

Sources observed as bandpass calibrators require a distinct calibration approach. The default pipeline flattens any line emission, as the bandpass calibration aims to correct for frequency-dependent amplitude and phase errors in the observed visibilities. These errors are calculated based on an ideal point-like sky brightness model (typically a bright quasar). As the Fourier Transform of a point-like sky brightness distribution has a constant amplitude in the visibility plane, the bandpass calibration will try to flatten any line emission in the data. To preserve line emission, we manually calibrated the data using custom scripts, where the bandpass calibrator was replaced by the phase or flux calibrator during relevant steps.

2.3.2 Data Integration and Imaging

After the calibration procedure is over we combined the visibilities of sources which were observed through different programs in order to increase integration time. Finally, the calibrated visibilities were imaged, transforming them from the uv-plane (distance between each pair of antennas) to sky coordinates. Due to the varying technical and theoretical limitations of each antenna (side lobes and flux leakage) and incomplete uv-plane coverage (as shown in Figure 2.7), the combined imaging produced artificial noise and glitches due to the Fourier transformation of delta functions. The resulting image was cleaned after sophisticated methods were employed to detect the true signal. CO line emissions were identified and isolated using the CASA task `uvcontsub`, which subtracts a continuum model derived from linear fits to line-free channels. The CASA task `tclean` was used for deconvolution and imaging with various weighting and channel width options. Exploring the parameter space of the imaging process is time-consuming, so we carefully selected the parameter ranges with the biggest impact and experiment with the fine-tuning some of the rest. During the analysis of a cube, multiple iterations of the cleaning are needed, as we already observed with the analysis of the galaxy 4C+12.50 and the nearby galaxy NGC 6328.

In the first case due to uniform weight of the uv plane binning we were losing half of the total flux of the galaxy. This was solved by choosing natural weighing, which uses number of Visibility points per bin (figure: 2.8), reconstructing the final image without losing the extended emission

[§] All procedures were executed using CASA, developed by an international consortium led by NRAO. It offers both a task interface and a Python scripting option as a wrapper of a C++ API backend, providing flexibility and optimized data processing. Importantly, each dataset must be calibrated using the CASA version corresponding to its observation period. <https://casa.nrao.edu>

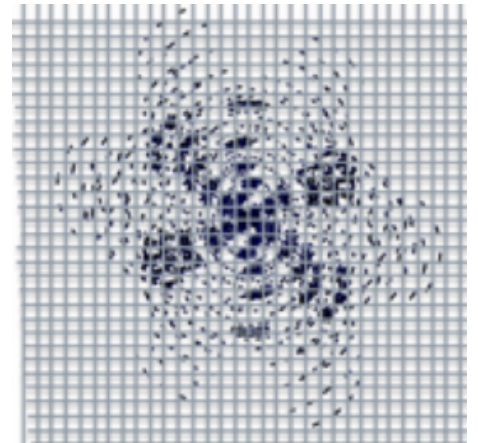


Figure 2.7: UV plane

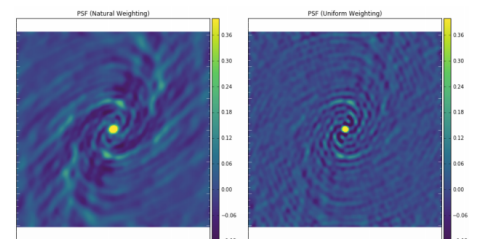


Figure 2.8: Weighting

of the source. In NGC 6328, fine tuning of the imaging parameters was significant for the detection of low emission at the outskirts of the galactic molecular disk used in the rotation curve estimation.

The achieved synthesised beams and root mean square (rms) noise levels of both detections and non-detections are listed in Table 2.1.

2.4 Results

The findings of this study are documented in detail in Audibert et al. (2022) and are briefly summarized in this section. Of the 66 CO-ARC sources examined, CO emission was detected in 17, with a marginal detection noted for J2341+0018. Additionally, 25 out of the 54 literature sources exhibited CO detections. This yields an overall gas detection rate of 35% for the extended CO-ARC (eCO-ARC) survey. The detection rates vary across different redshift ranges: 31 out of 60 sources in the local Universe, 2 out of 23 at intermediate redshifts, and 9 out of 37 at high-redshift.

Spatially-resolved extended molecular gas distributions were identified in six sources —NGC315, IC4374, NGC3100, J0623-6436, NGC6328, and J2009-4349— with a marginal detection also in IC4296. Along them for IC4296, NGC3100 and NGC6328 show interesting kinematic distortions possibly caused from warps or strong non-circular motions. Precise 3D kinematic modeling has demonstrated that disk warps largely account for these distortions in all the sources studied (Ruffa et al. 2019b; Ruffa et al. 2022 for NGC3100 and IC4296; this thesis for NGC6328, which will be elaborated upon in the next chapter). However, in the case of NGC6328, there is compelling evidence of jet-induced outflowing gas. A similar, albeit milder, jet-induced outflow with a mass rate of $\dot{M} = 0.12 M_{\odot} \text{ yr}^{-1}$ has been also partly identified in NGC3100 (Ruffa et al. 2022). Further investigation is required for IC4296, as the marginally detected gas does not permit conclusive interpretations. The molecular masses of the CO-ARC sources were estimated using the CO-to-H₂ conversion equation $M(H_2) = \alpha_{\text{CO}} L'_{\text{CO}(1-0)}$, where $\alpha_{\text{CO}} = 4.36 M_{\odot} (\text{Kkms}^{-1} \text{pc}^2)^{-1}$ is the standard Galactic CO-to-H₂ conversion factor (Tacconi et al. 2013; Bolatto et al. 2013). The molecular mass for the 66 CO-ARC radio galaxies ranges from $1.5 \times 10^7 M_{\odot}$ to $5.2 \times 10^{11} M_{\odot}$ for the 66 CO-ARC radio galaxies. For the literature sources, the estimated mass ranges from $10^6 M_{\odot}$ to $4 \times 10^{11} M_{\odot}$ with the calculations being recalibrated for consistency using $\alpha_{\text{CO}} = 4.36 M_{\odot} (\text{Kkms}^{-1} \text{pc}^2)^{-1}$.

The luminosity function for both local ($0.005 < z < 0.3$, with 60 radio galaxies) and far ($1 < z < 2.5$, with 37 radio galaxies) redshift ranges is calculated using the $1/V_{\text{max}}$ method (Schmidt 1968). This method provides the number density for each luminosity bin as:

$$\frac{\Phi}{\text{Mpc}^{-3} \text{dex}^{-1}} = \frac{1}{\Delta \log L} \sum_i \frac{\omega_i}{V_{\text{max},i}} \quad (2.3)$$

where $\Delta \log L$ is the luminosity bin size, V_{max} the maximum comoving volume that any galaxy i could be observable given its measured 1.4 GHz flux and the survey limit and ω_i the weight shown in Figure ?? corresponding to the completeness correction with respect to the NVSS.

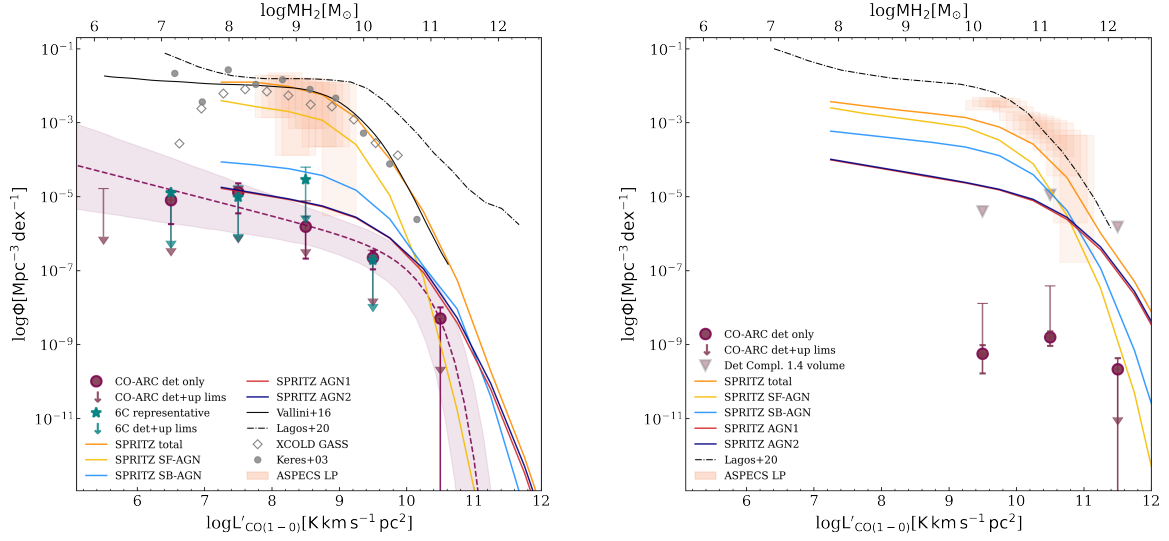


Figure 2.9: Luminosity functions (LF) for $0.005 < z < 0.3$ in the *left* panel and for $1 < z < 2.5$ in the *right* panel. In the local universe, the LF of our CO-selected Radio Galaxies (RGs) is 2-4 orders of magnitude lower than that of main sequence galaxies and star-forming or starburst AGNs, yet it aligns with the LF of AGN types 1 and 2. For the higher redshift range, the LF of RGs is notably lower than model predictions, attributable to the smaller observed population. A correction factor, derived from comparing the radio LF of our sample with the NVSS and UGS galaxy samples, has been applied, resulting in the addition of new, corrected data points to the LF, shown with triangles.

Due to the small number of detections, a luminosity function for intermediate redshifts cannot be estimated. For both the local and far redshift ranges, we present luminosity functions based on both detections alone and an alternative that includes upper limits for non-detections. The H_2 luminosity (and consequently mass) function is shown in the left panel of Figure 2.9 for $z < 0.3$ and in the right panel for $1 < z < 2.5$.

The local luminosity function (LF) is fitted with the analytical expression of the Schechter function (Schechter 1976; Riechers et al. 2019):

$$\log \Phi(L') = \log \Phi^* + \alpha \log \left(\frac{L'}{L^*} \right) - \left(\frac{L'}{\ln(10)L^*} \right) + \log(\ln(10)). \quad (2.4)$$

The resulting parameters are $L^* = 5.83 \times 10^9 \text{ K km s}^{-1} \text{ pc}^2$ which defines the "knee" of the LF. The slope of the faint end of the LF is $\alpha = -0.6$, and the turnover occurs at $\Phi^* = 2.39 \times 10^{-7} \text{ Mpc}^{-3} \text{ dex}^{-1}$.

Local Galaxies Comparing the CO mass function of our local radio galaxies with that from other main sequence galaxy surveys—such as the eXtended CO Legacy Database for GASS (XCOLD GASS) survey (Saintonge et al. 2017; Fletcher et al. 2021), the CO survey of FIR-selected galaxies from the IRAS bright galaxy sample (Keres et al. 2003), the empirical CO luminosity function derived from *Herschel* IR luminosity (Vallini et al. 2016), and the ALMA Spectroscopic Survey in the *Hubble* Ultra Deep Field (ASPECS LP) (Decarli et al. 2019) (refer to figure 2.9)—revealed that the number of radio galaxies (RGs) is 2-4 orders of magnitude lower. This deficit is smaller for higher gas mass. Further comparisons of the molecular gas content in our sample with the semi-empirical predictions for star-forming galaxies from Popping et al. (2015) (as illustrated in figure 2.10) indicate a deficit of 1-2 orders of magnitude for the local universe. However, this deficit decreases with increasing redshift, becoming

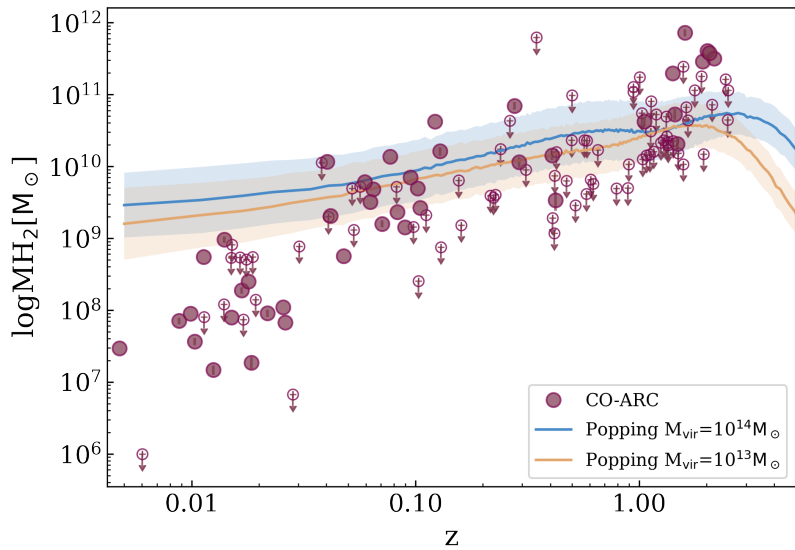


Figure 2.10: Molecular mass as a function of redshift compared with the semi-empirical predictions for two different dark matter halo masses of $M_{\text{vir}} = 10^{13} M_{\odot}$ and $M_{\text{vir}} = 10^{14} M_{\odot}$ from Popping et al. 2015

negligible at $z \gtrsim 0.1$ where the molecular mass content of our sample is consistent with the predictions.

In the context of AGN populations, we utilized the spectro-photometric realisations of infrared-selected targets at all- z (SPRITZ) simulations. These simulations encompass AGN-dominated galaxies with varying degrees of star formation and suggest that approximately one in every four RGs possesses gas reservoirs akin to those found in pure type 1 or type 2 AGNs.

Higher Redshift Moving to higher redshifts ($1 < z$), the molecular gas mass content of radio galaxies (RGs), when detected, is significantly larger, often exceeding the expected amounts for typical galaxy halos (figure 2.10).

However, the population of RGs in this redshift range is considerably smaller. Consequently, the mass function of their gas is notably lower compared to what simulations predict. This disparity arises partly due to the flux limit imposed by our survey and the nature of the RGs' continuum spectrum at GHz frequencies. The spectrum tends to decrease with frequency, undergoing a strong K-correction. In contrast, the fluxes of CO lines and continuum at mm wavelengths increase with frequency, resulting in a negative K-correction and enhancing their detectability at high- z . Given that high- z radio galaxies have substantial gas content, these galaxies are likely to be susceptible to jet-induced AGN feedback.

By comparing the radio LF of 1.4GHz emissions in our sample with the NVSS and UGS galaxy sample from Condon et al. (1998) and Condon et al. (2002) for the local universe, we found that only about 1 in 7,000 was observed. Thus under the assumption that the radio LF for the high- z is similar to the local universe we utilize this ratio to correct this detection bias. Then we estimated the evolution of gas content by integrating $L'\Phi(L')$ across all LF bins and converting it to mass. The molecular gas density $\rho(M_{\text{H}_2})$ was then determined from this mass per comoving Mpc^3 of the Universe, at various epochs (Fig 2.11). Given that

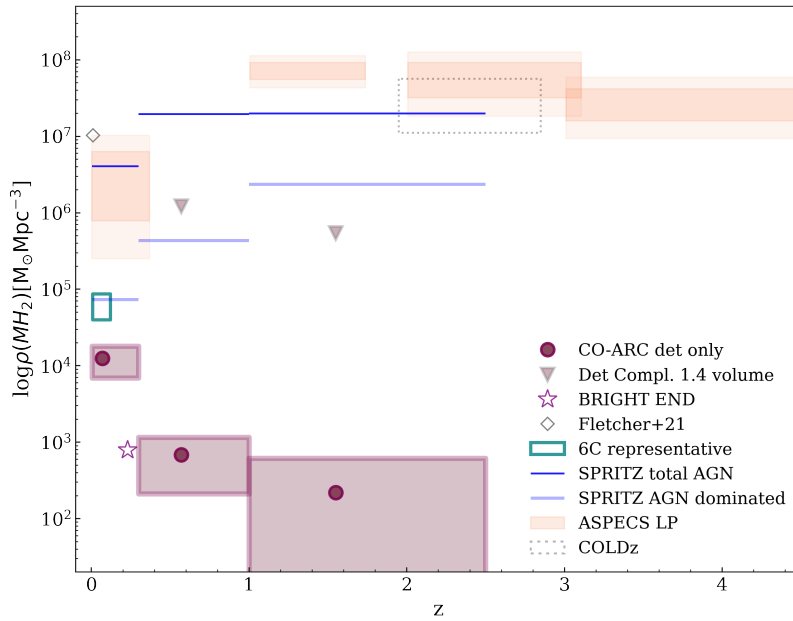


Figure 2.11: Molecular gas density evolution with redshift. The filled circles show the derived densities which are decreasing due to the Malmquist bias. The filled triangles show the corrected values after applying the 1.4 GHz LF correction. The blue lines represent the predictions from the SPRITZ simulation (Bisigello et al. 2021) for the total AGN and AGN dominated (AGN type 1 and 2) populations.

high- z radio galaxies have substantial gas content, these galaxies are likely to be susceptible to jet-induced AGN feedback.

The corrected evolution of gas content aligns with that of AGN1 plus AGN2, as observed in the local Universe. Therefore, under the assumption that both detectable and undetectable RGs share a similar gas mass distribution, the quantity of gas contained within RGs and AGN at $z > 1$ appears to be comparable.

Table 2.1: CO properties of the 66 CO-ARC sample sources. Note that, even for targets with available multiple-J CO observations, only the properties of lowest-J CO transitions are listed here and used for the luminosity function computations.

Galaxy	Line	Beam size ("×")	σ_{rms} (mJy/beam)	$S_{\text{CO}}\Delta v$ (Jy km s ⁻¹)	FWHM (km s ⁻¹)	v_{res} (km s ⁻¹)	log(MHz) (M _⊙)	log(L' _{CO(1-0)}) (K km s ⁻¹ pc ²)
J1000-3139	CO(2-1)	0.97×0.71	0.40	18.38± 0.59	368.53	20.00	7.85±6.87	7.21±6.22
J1109-3732	CO(2-1)	0.6×0.5	0.46	6.93± 0.35	452.27	20.00	7.56±6.61	6.92±5.97
J1336-3357	CO(2-1)	0.63×0.57	0.34	1.89± 0.29	781.79	20.00	7.17±6.33	6.52±5.68
J1723-6500	CO(2-1)	0.27×0.19	0.24	93.80± 2.15	533.90	20.00	8.98±7.98	8.34±7.34
J1945-5520	CO(1-0)	1.8×1.6	2.20	<17.99	300.00	100.00	<8.91	<8.28
J0057+3021	CO(2-1)	0.5×0.32	0.18	13.52± 0.20	582.32	20.00	8.27±7.29	7.63±6.64
J1301-3226	CO(2-1)	0.68×0.65	0.31	<5.15	300.00	100.00	<7.87	<7.22
J2131-3837	CO(2-1)	0.67×0.61	0.51	1.08± 0.18	540.65	20.00	7.27±6.56	6.62±5.92
J1407-2701	CO(2-1)	0.69×0.59	0.32	3.75± 0.50	147.77	20.00	7.96±7.00	7.31±6.35
J2009-4849	CO(2-1)	0.64×0.58	0.40	6.17± 1.03	448.41	22.00	9.20±8.26	8.56±7.61
J1008+0029	CO(1-0)	2.21×1.95	0.64	<0.74	300.00	100.00	<9.16	<8.52
J1221+2813	CO(1-0)	2.14×1.39	0.07	<0.11	300.00	180.00	<8.40	<7.76
J0623-6436	CO(1-0)	0.79×0.6	0.28	4.68± 0.91	671.67	100.00	10.21±9.33	9.57±8.69
J1217+3007	CO(1-0)	2.56×1.51	0.23	<0.21	300.00	100.00	<8.88	<8.24
J1427+2348	CO(1-0)	1.78×1.32	0.27	<0.28	300.00	100.00	<9.18	<8.55
J1332+0200	CO(1-0)	2.74×2.24	0.75	<0.39	300.00	100.00	<9.59	<8.95
J1356-3421	CO(1-0)	1.1×0.88	0.28	<0.34	300.00	100.00	<9.56	<8.93
J0943-0819	CO(1-0)	4.78×2.19	0.69	<0.36	300.00	100.00	<9.60	<8.96
J1220+0203	CO(1-0)	0.34×0.26	0.36	<1.39	300.00	102.00	<10.24	<9.60
J1547+2052	CO(1-0)	0.23×0.21	0.58	<2.83	300.00	100.00	<10.63	<9.99
J2341+0018	CO(1-0)	0.7×0.57	0.55	4.16± 0.56	350.00	20.00	10.84±9.93	10.20±9.29
J1305-1033	CO(1-0)	0.47×0.42	0.14	0.67± 0.17	173.67	100.00	10.06±9.25	9.42±8.61
J0242-2132	CO(1-0)	0.74×0.63	0.30	<0.41	300.00	100.00	<9.95	<9.31
J0006-0623	CO(1-0)	2.27×1.3	44.60	<23.17	300.00	100.00	<11.79	<11.15
J1505+0326	CO(3-2)	0.81×0.44	0.81	3.28± 0.26	376.56	20.00	10.15±9.31	9.50±8.66
J0748+2400	CO(3-2)	1.22×0.99	0.61	<0.44	300.00	100.00	<9.28	<8.63
J0510+1800	CO(3-2)	0.65×0.46	0.41	<0.26	300.00	20.00	<9.07	<8.42
J2349+0534	CO(3-2)	7.77×5.09	3.13	<1.63	300.00	100.00	<9.87	<9.22
J2141-3729	CO(3-2)	1.4×1.04	0.96	0.73± 0.24	255.50	20.00	9.53±8.99	8.88±8.34
J0914+0245	CO(3-2)	0.05×0.04	0.16	<3.34	300.00	100.00	<10.20	<9.55
J1038+0512	CO(2-1)	2.26×1.94	0.95	<0.49	300.00	100.00	<9.80	<9.16
J0940+2603	CO(3-2)	0.11×0.09	0.68	<3.58	300.00	60.00	<10.37	<9.71
J1610-3958	CO(3-2)	1.02×0.81	0.53	<0.41	300.00	100.00	<9.46	<8.80
J2239-5701	CO(3-2)	6.96×5.44	5.18	<2.69	300.00	100.00	<10.36	<9.71
J1058-8003	CO(3-2)	1.66×1.09	0.89	<0.46	300.00	100.00	<9.61	<8.96
J0106-4034	CO(4-3)	7.07×3.59	7.73	<4.02	300.00	100.00	<10.36	<9.66
J0217-0820	CO(2-1)	1.91×1.46	0.58	<0.30	300.00	100.00	<9.81	<9.17
J2320+0513	CO(2-1)	1.2×1.19	0.48	<0.25	300.00	100.00	<9.76	<9.12
J2000-1748	CO(2-1)	0.4×0.27	0.36	<0.68	300.00	100.00	<10.23	<9.59
J1010-0200	CO(4-3)	1.17×0.74	0.63	<0.37	300.00	100.00	<9.70	<9.00
J0329-2357	CO(4-3)	0.43×0.33	0.54	<0.80	300.00	100.00	<10.03	<9.33
J0946+1017	CO(2-1)	0.39×0.34	1.98	<2.92	300.00	100.00	<11.24	<10.59
J0909+0121	CO(2-1)	0.71×0.66	1.12	<0.89	300.00	100.00	<10.74	<10.09
J1351-2912	CO(2-1)	2.32×1.87	0.38	<0.20	300.00	100.00	<10.10	<9.45
J1743-0350	CO(4-3)	0.72×0.55	0.06	2.26± 0.04	145.99	80.00	10.62±9.65	9.92±8.95
J0125-0005	CO(2-1)	3.26×2.52	0.42	<0.21	300.00	90.00	<10.15	<9.51
J0239-0234	CO(4-3)	0.4×0.32	0.47	<0.70	300.00	100.00	<10.16	<9.46
J0837+2454	CO(2-1)	0.9×0.79	0.66	<0.42	300.00	100.00	<10.49	<9.84
J0118-2141	CO(4-3)	0.6×0.53	0.77	<0.72	300.00	100.00	<10.21	<9.51
J0112-6634	CO(2-1)	0.54×0.47	0.61	<0.64	300.00	100.00	<10.72	<10.08
J1304-0346	CO(2-1)	0.71×0.65	0.31	<0.23	300.00	100.00	<10.33	<9.68
J2134-0153	CO(2-1)	1.52×1.25	0.47	<0.24	300.00	100.00	<10.37	<9.72
J1359+0159	CO(2-1)	0.7×0.55	0.31	<0.26	300.00	100.00	<10.41	<9.77
J0529-7245	CO(2-1)	2.38×2.16	0.89	<0.21	300.00	20.00	<10.33	<9.69
J1147-0724	CO(4-3)	0.55×0.37	0.58	<0.66	300.00	100.00	<10.29	<9.59
J0343-2530	CO(2-1)	1.47×1.19	0.38	<0.19	300.00	100.00	<10.35	<9.71
J1419+0628	CO(3-2)	0.39×0.3	0.17	0.98± 0.18	410.76	100.00	10.72±9.95	10.07±9.30
J0954+1743	CO(4-3)	0.87×0.78	0.46	0.58± 0.09	193.30	20.00	10.31±9.61	9.61±8.91
J2056-4714	CO(2-1)	2.23×1.77	0.23	<0.12	300.00	100.00	<10.18	<9.54
J1520+2016	CO(3-2)	0.47×0.32	0.13	<0.17	300.00	100.00	<10.03	<9.38
J1107-4449	CO(2-1)	0.97×0.8	0.91	4.98± 0.15	43.74	20.00	11.86±10.90	11.21±10.26
J0219+0120	CO(2-1)	0.86×0.65	0.66	<0.45	300.00	100.00	<10.82	<10.18
J1136-0330	CO(2-1)	2.49×2.19	0.55	<0.29	300.00	100.00	<10.64	<10.00
J1146-2447	CO(4-3)	2.3×1.47	0.49	<0.25	300.00	100.00	<10.17	<9.47
J0403+2600	CO(4-3)	0.06×0.04	0.11	<1.07	300.00	100.00	<10.86	<10.16
J0106-2718	CO(3-2)	1.43×1.09	0.59	<0.31	300.00	100.00	<10.64	<9.99

Table 2.2: CO properties of 54 literature-based sources. The values for the molecular mass listed here are corrected by our adopted CO-to-H₂ conversion factor. References: Prandoni et al. 2010, Ruffa et al. 2019a, Olivares et al. 2019, Ocaña Flaquer et al. 2010, Leon et al. 2003, Taniguchi et al. 1990, Evans et al. 2005, Saripalli and Mack 2007, Nesvadba et al. 2010, Fotopoulou et al. 2019, Lo et al. 1999, Evans et al. 1996 and Emonts et al. 2014.

Galaxy	z	$\log(M_{\text{H}_2})$ (M_{\odot})	$\log(L'_{\text{CO}}(1-0))$ ($\text{K km s}^{-1} \text{pc}^2$)	$f_{1.4\text{GHz}}$ (Jy)	reference
NGC1399	0.005	7.47	6.83	0.639	Prandoni et al. 2010
IC1459	0.006	<6.00	<5.36	0.840	Ruffa et al. 2019
NGC4696	0.010	7.95	7.31	3.922	Olivares et al. 2019
NGC3801	0.011	8.74	8.10	1.141	Ocaña-Flaquer et al. 2010
NGC7626	0.011	<7.90	<7.26	0.627	Leon et al. 2002
NGC 193	0.014	<8.08	<7.44	1.375	Leon et al. 2002
J0048+3157	0.015	<8.73	<8.09	0.401	Taniguchi et al 1990
NGC5127	0.015	7.90	7.26	0.500	Ocaña-Flaquer et al. 2010
NGC5490	0.016	<8.73	<8.09	0.971	Ocaña-Flaquer et al. 2010
NGC5141	0.018	<8.70	<8.06	0.638	Ocaña-Flaquer et al. 2010
NGC541	0.018	8.40	7.76	0.826	Ocaña-Flaquer et al. 2010
NGC741	0.019	<8.74	<8.10	0.635	Evans et al. 2005
NGC2329	0.019	<8.15	<7.51	0.512	Leon et al. 2002
IC1531	0.026	8.04	7.40	0.505	Ruffa et al. 2019
3C442	0.026	7.83	7.19	2.216	Ocaña-Flaquer et al. 2010
PKS0718-34	0.028	<6.83	<6.19	1.909	Ruffa et al. 2019
3C465	0.030	<8.89	<8.25	6.134	Ocaña-Flaquer et al. 2010
ESO422-G028	0.038	<10.05	<9.41	1.500	Saripalli et al. 2007
Arp187	0.040	10.07	9.43	1.461	Evans et al. 2005
J0758+3747	0.041	<9.30	<8.66	1.734	Ocaña-Flaquer et al. 2010
3C305	0.042	9.31	8.67	2.950	Ocaña-Flaquer et al. 2010
NGC326	0.048	8.75	8.11	1.231	Ocaña-Flaquer et al. 2010
J1521+0420	0.052	<9.69	<9.05	0.551	Evans et al. 2005
B21101+38	0.053	<9.12	<8.48	0.648	Ocaña-Flaquer et al. 2010
3C390.3	0.057	<9.72	<9.08	10.225	Evans et al. 2005
J0119+3210	0.059	9.78	9.14	2.483	Ocaña-Flaquer et al. 2010
4C26.42	0.063	9.51	8.87	0.925	Olivares et al. 2019
4C29.30	0.065	9.68	9.04	0.514	Ocaña-Flaquer et al. 2010
OQ208	0.077	10.14	9.50	0.703	Ocaña-Flaquer et al. 2010
B2 1707+34	0.082	<9.72	<9.08	0.474	Evans et al. 2005
Abell2597	0.083	9.36	8.72	1.627	Olivares et al. 2019
3C326	0.090	9.15	8.51	2.292	Nesvadba et al. 2010
3C321	0.095	9.85	9.21	3.352	Ocaña-Flaquer et al. 2010
PKS0745-191	0.102	9.69	9.05	2.003	Olivares et al. 2019
PKS1559+02	0.105	9.42	8.78	7.905	Ocaña-Flaquer et al. 2010
4C26.35	0.112	<9.32	<8.68	0.400	Saripalli et al. 2007
4C12.50	0.122	10.62	9.98	5.155	Fotopoulou et al. 2019
4C12.03	0.156	<9.80	<9.16	1.500	Saripalli et al. 2007
PKS2128-123	0.501	<10.99	<10.35	1.895	Lo et al. 1999
3C285	0.790	<9.69	<9.05	1.601	Evans et al. 2005
B0235+164	0.940	<11.11	<10.47	1.473	Lo et al. 1999
J0830+2410	0.941	<11.03	<10.39	0.841	Lo et al. 1999
3C368	1.131	<10.90	<10.26	1.087	Evans et al. 1996
J1022+3041	1.320	<10.69	<10.05	0.590	Lo et al. 1999
MRC0114-211	1.410	11.29	10.65	3.723	Emonts et al. 2014
3C68.2	1.575	<11.39	<10.75	0.909	Evans et al. 1996
MRC1017-220	1.768	<11.06	<10.42	0.539	Emonts et al. 2014
MRC0324-228	1.898	<11.25	<10.62	0.459	Emonts et al. 2014
MRC0152-209	1.921	11.46	10.82	0.425	Emonts et al. 2014
MRC0156-252	2.016	11.61	10.97	0.423	Emonts et al. 2014
MRC2048-272	2.060	11.58	10.94	0.485	Emonts et al. 2014
Spiderweb	2.156	11.50	10.86	0.815	Emonts et al. 2014
MRC0406-244	2.433	<11.21	<10.57	0.629	Emonts et al. 2014
MRC2104-242	2.491	<11.06	<10.42	0.447	Emonts et al. 2014

Galaxy	Coordinates (J2000)	z	$f_{1.4}$ (Jy)	PID CO(1-0)	intent CO(1-0)	PID CO(2-1)	intent CO(2-1)	PID CO(3-2)	intent CO(3-2)	PID CO(4-3)	intent CO(4-3)	redshift reference
J1000-3139,NGC3100	06:10:12.55 -31:39:52.35	0.009	0.558	-	-	2015.1.01572.S	28.7 ^T	-	-	-	-	Jones et al. (2009)
J1109-3732,NGC3557	23:29:24.80 -37:32:21.02	0.010	0.401	-	-	2015.1.01572.S	22.68 ^T	-	-	-	-	Jones et al. (2009)
J1336-3357,IC4296	12:09:45.80 -33:57:57.30	0.012	3.131	-	-	2015.1.01572.S	51.4 ^T	-	-	-	-	Smith et al. (2000)
J1723-6500,NGC6328	20:55:16.30 -65:00:36.48	0.014	3.636	-	-	2015.1.01359.S	113 ^T	-	-	-	-	Fosbury et al. (1977)
J1945-5520,NGC6812	08:21:03.43 -55:20:48.84	0.015	0.690	2011.0.00046.S	5.04 ^P	-	-	-	-	-	-	Jones et al. (2009)
J10057-3021,NGC0315	14:27:13.25 +30:21:08.81	0.017	1.550	-	-	2017.1.00301.S	84.7 ^T	-	-	-	-	Peterson (1979)
J1301-3226,ESO443-G024	03:15:11.93 -32:26:28.97	0.017	1.298	-	-	2015.1.01572.S	24.2 ^T	-	-	-	-	Smith et al. (2000)
J12131-3837,NGC7075	10:53:14.94 -38:37:04.65	0.018	0.668	-	-	2015.1.01572.S	24.7 ^T	-	-	-	-	Jones et al. (2009)
J1407-2701,IC4374	19:52:26.69 -27:01:04.39	0.022	0.706	2017.1.00629.S	28.7 ^T	2015.1.00644.S	87.7 ^T	-	-	-	-	Smith et al. (2000)
J15164-0701,UGC09799	13:11:07.34 +07:01:17.83	0.035	3.934	-	-	2015.1.00627.S	81.6 ^T	-	-	-	-	SDSS dr12 Pacris et al. (2017)
J2009-4849,HB89 2005-489	14:21:20.86 -48:49:53.72	0.071	1.117	-	-	2013.1.00523.S	12.1 ^P	-	-	-	-	Richter et al. (2016)
J10088-0029,PKS10054+007	08:02:52.65 +00:29:59.60	0.098	0.600	2019.1.00102.S	14.1 ^P	-	-	-	-	-	-	Owen et al. (1995)
J1221+2813,W Com	17:22:55.35 +28:13:58.50	0.103	0.738	2015.1.00727.S	90.7 ^T	-	-	-	-	-	-	Shaw et al. (2013)
J0623-6436,WISEJ1062307-643620	23:46:55.95 -64:36:20.6	0.129	0.400	2015.1.01522.S	5.24 ^T	-	-	-	-	-	-	Pietsch et al. (1998)
J1217+3007,FBQS1217+3007	16:28:01.23 +30:07:00.64	0.130	0.539	2015.1.00727.S	9.6 ^P	2015.1.00820.S	3.0 ^P	-	-	-	-	-
J1427+2348,FBQS142700+234800	00:45:05.88 +23:48:00.04	0.160	0.452	2017.1.00616.S	18.14 ^P	-	-	-	-	-	-	Richter et al. (2016)
J1332+0200,3C287.1	11:13:19.06 +02:00:45.70	0.216	3.000	2017.1.01359.S	12.7 ^P	-	-	-	-	-	-	-
J1356-3421,PKS1353-341	17:01:20.88 -34:21:10.84	0.223	0.811	2017.1.00629.S	20.7 ^T	2015.1.00804.S	3.53 ^P	-	-	-	-	Veron-Cetty et al. (2000b)
J0943-0819,PKS0941-08	01:54:14.17 -08:19:30.81	0.228	1.828	2012.1.00915.S	10.6 ^P	-	-	-	-	-	-	Son et al. (2012)
J1220-0203,UM 492	185:03:00 -2:03:43.2	0.240	0.548	2016.1.00140.S	2.1 ^P	-	-	2016.1.00994.S	1.5 ^P	-	-	Hewet & Wild (2010)
J1547+2052,PG 1545+210	20:55:53.07 +20:52:16.61	0.264	1.456	2017.1.01249.S	4.5 ^C	2016.1.01481.S	0.6 ^C	-	-	-	-	SDSS dr6
J2341+0018,PKS2338+000	19:16:43.65 +00:18:33.34	0.277	0.441	2017.1.00629.S	21.67 ^T	-	-	-	-	-	-	Katger et al. (1998)
J1305-1033,PG 1302-102	04:23:15.39 -10:33:19.38	0.278	0.739	2015.1.00329.S	38.3 ^T	-	-	-	-	-	-	Wisotzki et al. (2000)
J0242-2132,PKS0240-217	16:38:58.65 -21:32:25.94	0.314	1.003	2017.1.00629.S	21.7 ^T	-	-	-	-	-	-	Wright et al. (1983)
J0006-0623,PKS0003-066	01:33:28.38 -06:23:35.34	0.347	1.704	2012.1.00080.S	6 ^B	-	-	-	-	-	-	Jones et al. (2009)
J1505-0326,HB89 1502+036	10:16:37.16 +03:26:30.81	0.408	0.416	2017.1.00629.S	5 ^P	-	-	2015.1.00971.S	7.06 ^P	-	-	Hewet & Wild (2010)
J0748+2400,PKS0745+241	21:09:01.64 +24:00:24.11	0.410	1.035	-	-	-	-	2015.1.01178.S	8.06 ^P	-	-	Hewet & Wild (2010)
J0510+1800,PKS0507+17	05:30:35.54 +18:00:41.58	0.416	0.711	-	-	-	-	2012.1.00275.S	19.7 ^P	-	-	Perlmán et al. (1998)
J2349+0534,WISEJ234921+053439	21:20:15.77 +05:34:39.87	0.419	0.445	-	-	-	-	2012.1.00193.S	7.6 ^P	-	-	-
J2141-3729,PKS2138-377	13:28:06.74 -37:29:12.99	0.423	0.480	-	-	-	-	2019.1.01229.S	12.1 ^P	-	-	Jones et al. (2009)
J0914+0245,PKS0912+029	18:39:28.70 +02:45:59.25	0.427	0.540	-	-	-	-	2017.1.00255.S	3.02 ^P	-	-	Hewet & Wild (2010)
J1038+0512,PKS1036+054	15:41:41.70 +05:12:29.09	0.473	0.601	-	-	2017.1.01558.S	3.02 ^P	2011.0.00016.S	36.89 ^P	-	-	Healey et al. (2008)
J0940+2603,B2 0937+26	01:03:40.84 +26:03:29.95	0.498	0.460	-	-	-	-	2017.1.00277.S	6.05 ^P	-	-	Glikma et al. (2007)
J1610-3958,WISEJ161021-395858	02:35:28.19 -39:58:58.33	0.518	0.598	-	-	-	-	2015.1.00791.S	9.07 ^P	-	-	Landt et al. (2001)
J2239-5701,PKS2236-572	03:47:58.5 -57:01:01	0.569	0.432	-	-	-	-	2017.1.00704.S	6.05 ^P	-	-	Titov et al. (2011)
J1058-8003,PKS1057-79	20:40:49.65 -80:03:54.16	0.581	0.997	-	-	2016.2.00115.S	18.13 ^P	2016.2.00115.S	18.13 ^P	-	-	Sbarufatti et al. (2009)
J1016-4034,HB89 0104-408	16:41:16.61 -40:34:19.96	0.584	0.768	-	-	2017.1.00886.L	60 ^P	2017.1.00886.L	60 ^P	-	-	White et al. (1988)
J0217-0813,PKS0214-085	10:15:39.93 -08:20:52.35	0.607	0.459	-	-	-	-	2017.1.00562.S	7.06 ^P	-	-	Hewet & Wild (2010)
J2320+0513,HB89 2318+049	14:11:12.85 +05:13:49.95	0.622	0.735	2018.1.00478.S	4.02 ^P	-	-	-	-	-	-	Schmidt (1977)
J2000-1748,HB89 1958-179	12:14:16.36 -17:48:57.67	0.652	0.751	2018.1.01533.S	7.56 ^P	-	-	-	-	-	-	Drinkwater et al. (1997)
J1010-0200,4C -01.21.02	08:42:54.99 -02:00:19.57	0.890	0.680	2018.1.00576.S	5.04 ^B	-	-	-	-	-	-	Croom et al. (2004)
J1010-0200,4C -01.21.02	08:42:54.99 -02:00:19.57	0.890	0.680	-	-	-	-	2018.1.00583.S	3.53 ^P	-	-	-

Galaxy	Coordinates		z		PID		intent		PID		intent		PID		intent		redshift reference
	(J2000)	(Jy)	z	$f_{1.4}$	CO(1-0)	CO(1-0)	CO(2-1)	CO(2-1)	CO(3-2)	CO(3-2)	CO(4-3)	CO(4-3)	CO(1-0)	CO(1-0)	CO(2-1)	CO(2-1)	
J0329-2357,PKS0327-241	04:28:31.13-23:57:08.77	0.895	0.683	-	-	-	-	-	-	-	-	-	-	-	-	-	Baker et al. (1999)
J0946+1017,WISEJ094635+101706	02:38:46.05+10:17:06.13	1.004	0.406	-	-	-	-	-	-	-	-	-	-	-	-	-	Hewett & Wild (2010)
J0909+0121,HB89 0906+015	17:17:31.37+01:21:35.62	1.025	0.954	-	-	-	-	-	-	-	-	-	-	-	-	-	Hewett & Wild (2010)
J1351-2912,PKS1348-289	15:56:42.58-29:12:17.65	1.034	0.523	-	-	-	-	-	-	-	-	-	-	-	-	-	Hook et al. (2003)
J1743-0350,HB89 1741-038	01:59:41.98-03:50:04.56	1.054	1.652	-	-	-	-	-	-	-	-	-	-	-	-	-	Zafar et al. (2013)
J1025-0005,UM321	21:22:12.66-00:05:55.93	1.076	1.275	-	-	-	-	-	-	-	-	-	-	-	-	-	Hewett & Wild (2010)
J0239-0234,HB89 0237-027	15:56:22.08-02:34:40.91	1.116	0.400	-	-	-	-	-	-	-	-	-	-	-	-	-	Fricke et al. (1983)
J0837+2454,FBQSJ083740+245423	09:25:03.69+24:54:23.12	1.126	0.514	-	-	-	-	-	-	-	-	-	-	-	-	-	Hewett & Wild (2010)
J0118-2141,HB89 0116-219	19:44:18.93-21:41:30.14	1.161	0.498	-	-	-	-	-	-	-	-	-	-	-	-	-	Hewitt & Burbidge (1987)
J0112-6634,PKS0110-668	18:04:43.69-66:34:45.19	1.189	0.439	-	-	-	-	-	-	-	-	-	-	-	-	-	Titov et al. (2011)
J1304-0346,HB89 1302-034	04:10:54.63-03:46:02.55	1.250	0.958	-	-	-	-	-	-	-	-	-	-	-	-	-	Wills & Lynds (1978)
J2134-0153,HB89 2131-021	11:32:34.65-01:53:17.24	1.285	2.040	-	-	-	-	-	-	-	-	-	-	-	-	-	Drinkwater et al. (1997)
J1359-0159,HB89 1356+022	17:51:47.24+01:59:54.56	1.326	0.777	-	-	-	-	-	-	-	-	-	-	-	-	-	Hewett & Wild (2010)
J0529-7245,PKS0530-727	10:22:30.63-72:45:28.51	1.340	0.400	-	-	-	-	-	-	-	-	-	-	-	-	-	-
J1147-0724,HB89 1145-071 01	08:57:53.31-07:24:41.14	1.342	0.878	-	-	-	-	-	-	-	-	-	-	-	-	-	Wilkes (1986)
J0343-2530,PKS0341-256	07:49:52.86-25:30:17.41	1.419	0.602	-	-	-	-	-	-	-	-	-	-	-	-	-	Hook et al. (2003)
J1419+0628,3C298	22:47:02.68+06:28:34.76	1.438	6.060	-	-	-	-	-	-	-	-	-	-	-	-	-	Hewett & Wild (2010)
J0954+1743,HB89 0952+179	04:44:12.35+17:43:31.22	1.477	1.184	-	-	-	-	-	-	-	-	-	-	-	-	-	Hewett & Wild (2010)
J2056-4714,HB89 2052-474	02:04:05.40-47:14:47.63	1.489	2.949	-	-	-	-	-	-	-	-	-	-	-	-	-	Jauncey et al. (1984)
J1520+2016,3C318	14:01:21.73+20:16:05.80	1.572	2.427	-	-	-	-	-	-	-	-	-	-	-	-	-	SDSS dr12 Pacris et al (2017)
J1107-4449,HB89 1104-445	22:47:10.41-44:49:07.62	1.598	2.116	-	-	-	-	-	-	-	-	-	-	-	-	-	Peterson et al. 1979b
J0219+0120,PKS0216+011	10:46:45.37+01:20:59.87	1.623	0.518	-	-	-	-	-	-	-	-	-	-	-	-	-	Allington-Smith (1991)
J1136-0330,4C-03_44	06:06:08.65-03:30:29.50	1.648	0.400	-	-	-	-	-	-	-	-	-	-	-	-	-	Hook et al. (2003)
J1146-2447,HB89 1143-245	17:32:02.4-24:47:31.2	1.94	0.885	-	-	-	-	-	-	-	-	-	-	-	-	-	Drinkwater et al. (1997)
J0403+2600,HB89 0400+258	04:03:05.59+26:00:01.50	2.109	1.367	-	-	-	-	-	-	-	-	-	-	-	-	-	Healey et al. (2008)
J0106-2718,HB89 0104-275	16:36:32.4-27:18:10.8	2.486	0.400	-	-	-	-	-	-	-	-	-	-	-	-	-	Croom et al. (2004)

Table 2.3: Table A.1 - CO-ARC sample ancillary information and information on the reduced ALMA observations.

A plausible link between dynamically unsettled molecular gas and the radio jet in NGC 6328

3

Note on Authorship: The majority of the work presented in this chapter was conducted by me and published in Papachristou et al. (2021) and Papachristou et al. (2023). I. Ruffa guided me through self-calibration and imaging process of ALMA raw data. M. Polkas significantly contributed on analyzing and deriving specific jet properties and interpretation of the jet boosting scenario.

As we mentioned earlier in this thesis, one of the most interesting sources we studied during the analysis of CO-ARC catalog was NGC6328. The reason of our focus in this source is that we have clear evidence of out-of-dynamic-equilibrium kinematics in both its cold and warm gas phases (Maccagni et al. 2014; Maccagni et al. 2016b; Maccagni et al. 2018) and their likely spatial correlation with the radio-jet.

In the next section we will provide an extent review of NGC6328 properties from the literature. Next, we present our novel approach to the kinematic modeling of the cold gas disk of the galaxy and the optimal 3D model that describes its structure. There, emphasis is given to the nature of the clouds that strongly deviate from the optimal model in the form of outflowing gas. Finally, we investigate the possible connections of the outflows with the AGN and the jet.

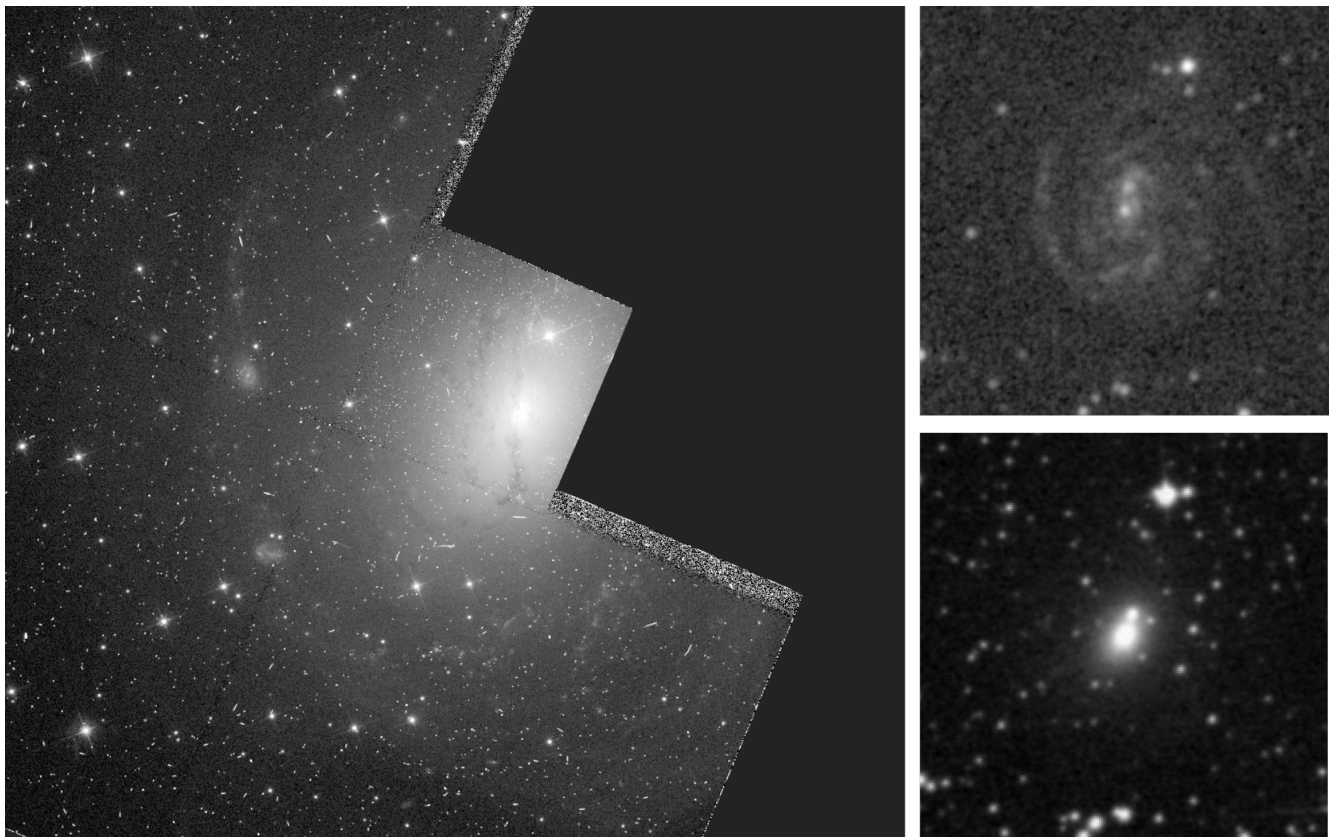


Figure 3.1: Grand view of NGC6328. Left: Grand-scale (~ 16 kpc) Hubble Space Telescope (WFPC2, F606W band) image (obtained from [Wikimedia](#)). Right and top: (~ 30 kpc) UV image (UVM2) from Swift. Right and bottom: IR image at the same scale (from DSS2)

3.1 General NGC6328 properties

NGC 6328 is an early type, nearby galaxy ($D = 62.88$ Mpc at $z = 0.014$) at low Galactic latitude (RA = 17:23:41.03 and DEC = -65:00:36.615). The optical surface brightness of the stellar population is dominated by a Sérsic * 1/4 profile elliptical bulge which is major axes is oriented at PA = 150° and the axis ratio is $b/\alpha = 0.72$. Except the bulge faint extended spiral features visible almost face-on (Veron-Cetty et al. 1995). These features are also visible from *Neil Gehrels Swift Observatory* maps obtained using Ultraviolet/Optical Telescope (UVOT) Filters (UVM2 at 2246 Å and UVW2 at 1928 Å) and the Hubble Space Telescope (HST) through Wide Field and Planetary Camera 2 (WFPC2) in the F606W band where they are observed also through dust absorption (seen in figure 3.1). HST revealed also, closer to the center, a near edge-on North-South oriented dust lane in the central $23'' \approx 7$ kpc.

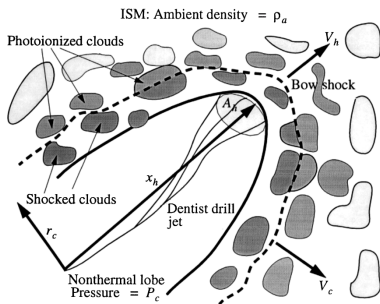


Figure 3.2: The jet-ISM "dentist drill" interaction of the FFA model by Bicknell et al. 1997. The radiation from the shock photoionizes the ISM clouds which absorb the radio emission at GHz frequencies.

3.1.1 Radio emission and AGN

At its core, NGC6328 harbors an AGN associated radio-source named PKS1718-649. Overall, the AGN is characterized as a low luminosity AGN (LLAGN) with a low-ionization nuclear emission-line region (LINER)(Filippenko 1985). The radio spectrum of PKS1718-649 has steep spectral index at high frequencies and a turnover peak at around 3.2 GHz. This characteristic feature categorizes PKS1718-649 in under the general term of Peaked-Spectrum Radio Sources (PS) (O'Dea and Saikia 2021) (more precisely as a GigaHertz Peaked Spectrum radio source (GPS). The turnover in the radio spectrum of PS sources is commonly thought to necessitate some form of absorption mechanism, as proposed in various studies (e.g., de Kool and Begelman, 1989; O'Dea, 1998; Tingay and de Kool, 2003). These sources are also compact and thus associated with young radio jets that interact with the host galaxy's interstellar medium

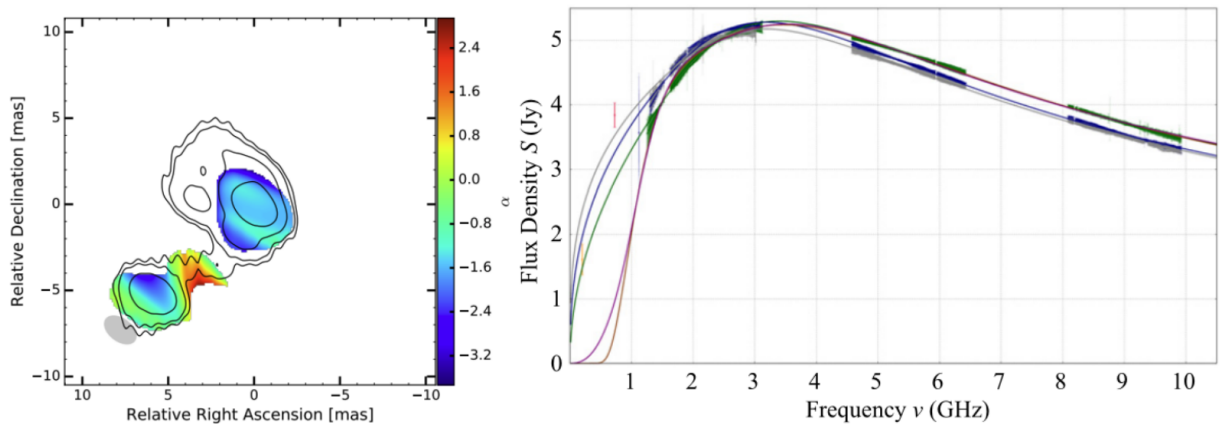


Figure 3.3: **Left:** The bipolar structure of the young radio source PKS1718-649 as observed from VLBI. The colors represent the spectral index between 8.4 GHz and 22.3 GHz Angioni et al. 2019. **Right:** Radio spectrum of PKS1718 as observed from ATCA in three epochs of observations (2012 and 2013) and the best fit lines of FFA and SSA models (Tingay et al. 2015).

* Sérsic profile (Sérsic 1963) is a model which use to describe the intensity I of galaxy with distance from its center r . Its form is $\ln I(r; I_0, k, n) = \ln I_0 - kr^{1/n}$ where I_0 is the intensity at the center and n is the Sérsic index controlling the shape of the curve. Most elliptical galaxies have a value $n = 4$ which is known as de Vaucouleurs's law (de Vaucouleurs 1948)

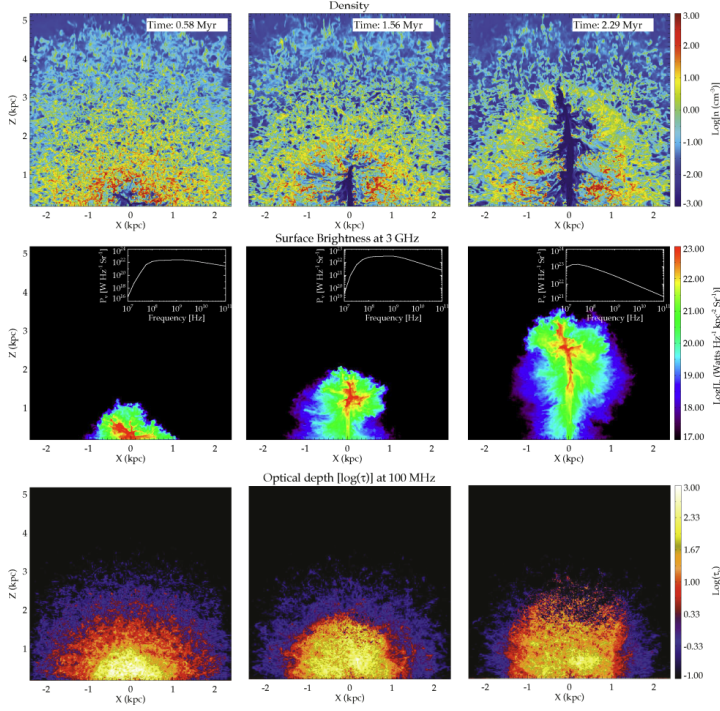


Figure 3.4: MHD simulations of a young jet interacting with the ISM successfully reproducing the GHz peak in the radio spectrum of peaked sources. Reproduced from (Bicknell et al. 2018).

(ISM) on scales ranging from parsecs to approximately 10 kpc. Two primary mechanisms have been proposed to account for this observed peak: free-free absorption (FFA) of the synchrotron radiation by the ionized, shocked, and dense ISM (Bicknell et al. 1997) and synchrotron self-absorption (SSA) (Kellermann and Pauliny-Toth 1969). For PKS 1718-649, the FFA model appears to provide the best fit (Tingay et al. 1997) while close monitoring of the source reveals significant variability, likely due to a mixture of intrinsic processes associated with the dense local environment and to adiabatic losses of the synchrotron-emitting lobes (Tingay et al. 2015).

The FFA model postulates that the radio jet, upon interacting with the local dense ISM, induces shocks and subsequently generates a power-law distribution of electron density in the ionized ambient medium which absorbs part of the radio emission creating the observed peak. Although the FFA model seems to better explain the spectral features of PKS 1718-649, it's worth noting that SSA often provides a more accurate description for peaked spectrum sources in general (O'Dea and Saikia 2021). The likely young jet-ISM interaction associated with PS sources makes them suitable candidates, and especially NGC6328 as it is the nearest detected PS source to date, for better understanding their role as an AGN feedback mechanism.

High-resolution (~ 0.3 pc) Very Long Baseline Interferometry (VLBI) observations resolve PKS1718-649 into a bipolar structure, with the two lobes being separated by a projected distance of ~ 2 pc (Tingay et al. 1997; Tingay and de Kool 2003) agreeing with the GPS linear size (LS) and 5 GHz flux correlation (Liao and Gu 2020a).

The spectral index (see Figure 3.3) between 8.4 GHz and 22.3 GHz suggests that the core of the young radio source is strongly absorbed in these frequencies, and is located between the two lobes. The structure is unresolved at lower resolution observations at 2.3 GHz (beam of 3.8

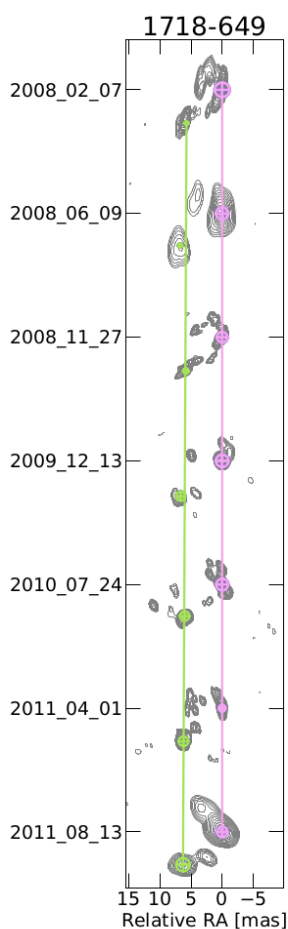


Figure 3.5: The bipolar structure of the radio source PKS1718-649 as observed from VLBI in different epochs Angioni et al. 2019.

arcsec) (Tingay et al. 1997) from Australia Telescope Compact Array (ATCA) giving a total flux of 4.6 Jy, coincident with the optical nucleus of its host galaxy, with no extended structure at a dynamic range of 1000:1 (Tingay et al. 1997). Newer ATCA observations (Maccagni et al. 2014) with higher sensitivity (dynamic range of 5600:1) do not also resolve the source at a resolution of 8.7 kpc.

The source has been monitored for more than three years through the TANAMI project to study the kinematics and variability of the radio-lobes/hot-spots. In contrast with other radio-sources where the hot-spots can be followed and analyzed the source showed a more complex behavior where the components were not always clearly resolved. Angioni et al. 2019 fitted a simple linear model for the brightest components for every epoch estimating an angular separation speed $\mu = 0.13 \pm 0.06 \text{ mas yr}^{-1}$ and a corresponding apparent speed $\beta_{\text{app}} = 0.13 \pm 0.06$.

3.1.2 Xrays and γ rays

NGC6328 observations in the X-rays conducted by *Chandra* (Siemiginowska et al. 2016) and *XMM-Newton* (Beuchert et al. 2018) revealed a two-component emission: A comptonized hard X-rays at the center and an extended soft X-ray emission at kpc scale from a collisionally ionized and hot gas. PKS 1718-649 is also one of the few non-blazar γ -ray sources detected by Fermi-LAT (Migliori et al. 2016).

3.1.3 Emission lines

Observations of atomic hydrogen in NGC 6328 have been conducted by Veron-Cetty et al. 1995 and Maccagni et al. 2014 using the ATCA. The observations revealed a massive HI disk with a total mass of $M_{\text{HI}} = 1.1 \times 10^{10} M_{\odot}$ (Maccagni et al. 2014). The disk kinematics had been best modeled as a warped disk, using an almost constant circular velocity of 220 km s^{-1} . In this warped disk model the central $30''$ (or 8.5 kpc), the disk is highly inclined, with an inclination angle i of $\sim 90^{\circ}$, and oriented along the position angle (PA) of the observed dust lane (180°). In outer regions, up to $80''$ (or 23 kpc), the disk slowly warps to a face-on geometry ($i = 30^{\circ}$ and $\text{PA} = 110^{\circ}$), consistently with the galaxy's spiral features (Maccagni et al. 2014). Further out (past the $80''$ radius), asymmetric features are present north-west and south of the disk. These deviate from regular rotation, and they are attributed to an ongoing merger or interaction (Veron-Cetty et al. 1995; Maccagni et al. 2014).

In the UV, NGC6328 has been detected in H_{α} and $Ly\alpha$ emission (total flux of $2.7 \times 10^{-13} \text{ erg cm}^{-2} \text{ s}^{-1}$ and $1 - 3.5 \times 10^{-13} \text{ erg cm}^{-2} \text{ s}^{-1}$ respectively) through observations conducted from CTIO 1.5m telescope (Keel and Windhorst 1991 using complementary data from Filippenko 1985). The H_{α} ionized gas emission has been resolved a North-South extended emission likely tracing the dense highly inclined disk structure seen in HI and dust obscuration in HST. Regarding the UV continuum Keel and Windhorst 1991 argue that it is dominated from starlight, however Filippenko 1985 detects a 6% excess at 5460 \AA associated with the AGN.

In the infrared NGC6328 has been studied spectroscopically through *SPITZER* at ≈ 5 to $35 \mu\text{m}$ (Willett et al. 2010). In the spectra has been

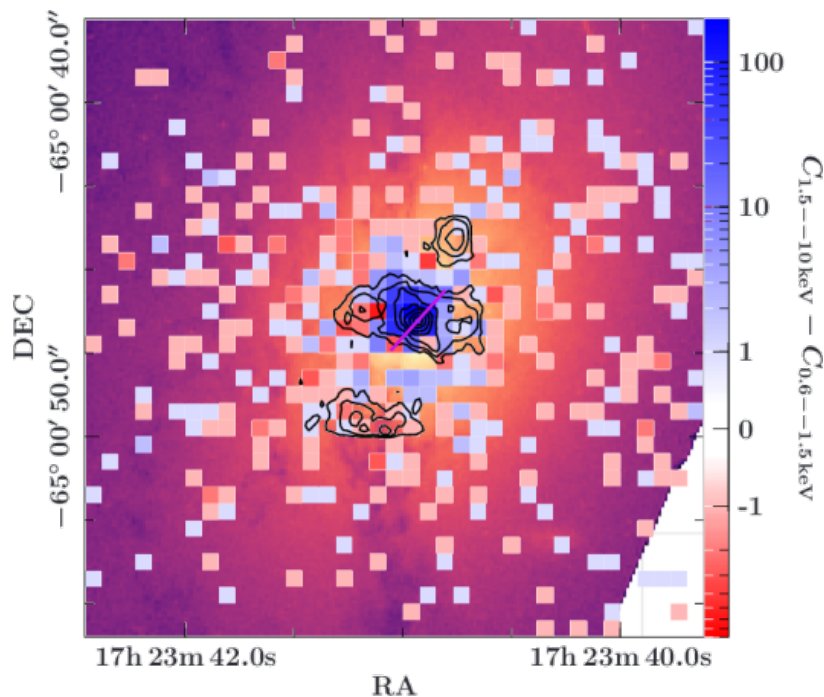


Figure 3.6: Difference map between the hard (1.5–10 keV) and soft (0.3–1.5 keV) X-rays. Positive pixels (blue) depict a hard excess, negative pixels (red) a soft excess (from Beuchert et al. 2018). The black contours represent the warm hydrogen emission (H_2 1–0 S(1) [$2.12 \mu\text{m}$]) from Maccagni et al. 2016a. In the background we added the HST image as an indicator of scale and position. The pink line represents the position angle of the jet

detected moderate ($\sim 2.5 \times 10^7 L_\odot$) polycyclic aromatic hydrocarbon (PAH) emission, silicates SiIII at $2.4 \times 10^6 L_\odot$ and [OIV], [FeII] with luminosities of $5.6 \times 10^5 L_\odot$ and $7.4 \times 10^5 L_\odot$ accordingly. The fine structure emission lines [NeII] and [NeIII] are also detected with luminosities of $6.3 \times 10^6 L_\odot$ and $3.8 \times 10^6 L_\odot$ accordingly. From these lines authors have estimated the star formation rate of NGC6328 to $1.8 \pm 0.1 M_\odot \text{yr}^{-1}$ from the [NeII] [NeIII] lines and $0.8 M_\odot \text{yr}^{-1}$ using the 6.2 and $11.3 \mu\text{m}$ PAH features. This estimation together of an estimated stellar mass of $1 - 4 \times 10^{11} M_\odot$ (Maccagni et al. 2014) puts NGC6328 towards the red and dead part of the galaxies.

Finally, NGC6328 has been observed through Very Large Telescope (VLT) Spectrograph for INtegral Field Observations in the Near Infrared (SINFONI) mapping the distribution and kinematics of warm molecular hydrogen at $2.12 \mu\text{m}$ (1-0) S(1) and $1.95 \mu\text{m}$ (1-0) S(3) by Maccagni et al. 2016a. In the total cover of around $1.5 \text{ kpc} \times 1.5 \text{ kpc}$ the excited H_2 has a total mass of $1 \times 10^4 M_\odot$ and excitation temperature of 1100 – 1600 K. In the central 700 pc of the galaxy warm H_2 traces a nearly edge-on inner disk at PA of 85° , almost perpendicular to the dust lane. In the outer disk, two warm H_2 blobs have been detected in opposite directions, at a projected distance of 1 – 1.5 kpc, close to the radio jet axis, and close to the dense dust structure seen in HST. This axis also happens to be nearly parallel to the major axis of the stellar isophote curves (PA $\sim 150^\circ$).

3.2 ALMA and X-shooter data

In this work, we present a new kinematic analysis of the molecular gas in NGC 6328, utilizing previous CO(2-1) observations (Maccagni et al. 2018) and more recent CO(3-2) data obtained with ALMA. We also used archival ancillary data from the X-shooter instrument on the VLT, which provides simultaneous coverage of the optical and near-infrared spectral

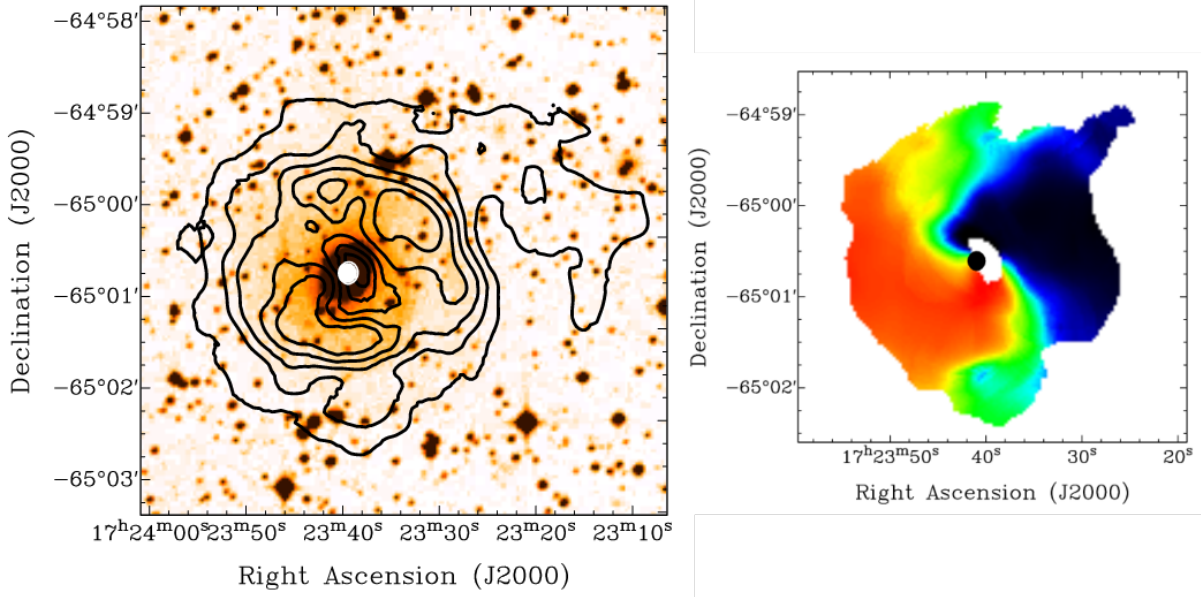


Figure 3.7: HI emission map. **Left:** HI intensity map (black contours) on top of I band DSS image. **Right:** Mean velocity map. Reproduced from (Maccagni et al. 2014). The "S" shape traced by the zero velocities indicate the presence of a warp.

ranges. These data (PI: Maccagni and program name: 105.20QD.001) are not yet published. They have only been publicly released and calibrated through the standard pipeline. We used the X-shooter data to present basic ionized gas properties of NGC 6328, particularly in the central regions of the galaxy. While a detailed analysis of these data is beyond the scope of this paper, we note that they provide valuable complementary information to the ALMA data analysed here, and will be discussed in more detail in future works.

3.2.1 ALMA data reduction and imaging

NGC6328 was observed using ALMA Band 6 at rest frame frequency ν_{rest} of 230.5 GHz (project ID: #2015.1.01359.S, PI: F. Maccagni) in September 2016, and using Band 7 at $\nu_{\text{rest}} = 345.8$ GHz (project ID: #2017.1.01638.S, PI: S. Kameno), in January 2018. The phase center of the observations was the position of the nucleus ($\delta_{\text{RA}} = 17:23:41.03$ and $\delta_{\text{DEC}} = -65:00:36.615$) with a single pointing covering a Field of View (FoV) of $25''$ in Band 6 and $18''$ in Band 7.

The ALMA Band 6 observations were carried out with 39 12-m antennas and an extended array configuration with baseline lengths ranging from 15 to 2483 m. The on-source integration time was 1.85 hours. The correlator setup was selected to center the CO(2-1) line with a velocity range of ± 1200 km/s in the 1.86 GHz bandwidth and a channel width of 7.8 MHz (20 km s^{-1}).

The data were calibrated using the Common Astronomy Software Applications (CASA) (McMullin et al. 2007), version 4.7, and the calibration scripts provided by the ALMA archive. J1617-5848, J2056-4714, and J1703-6212 were respectively used as flux, bandpass, and phase calibrators resulting in 15% accuracy. The data were imaged using the CASA *tclean* task with Briggs weighting and a robust parameter of 2, in order to

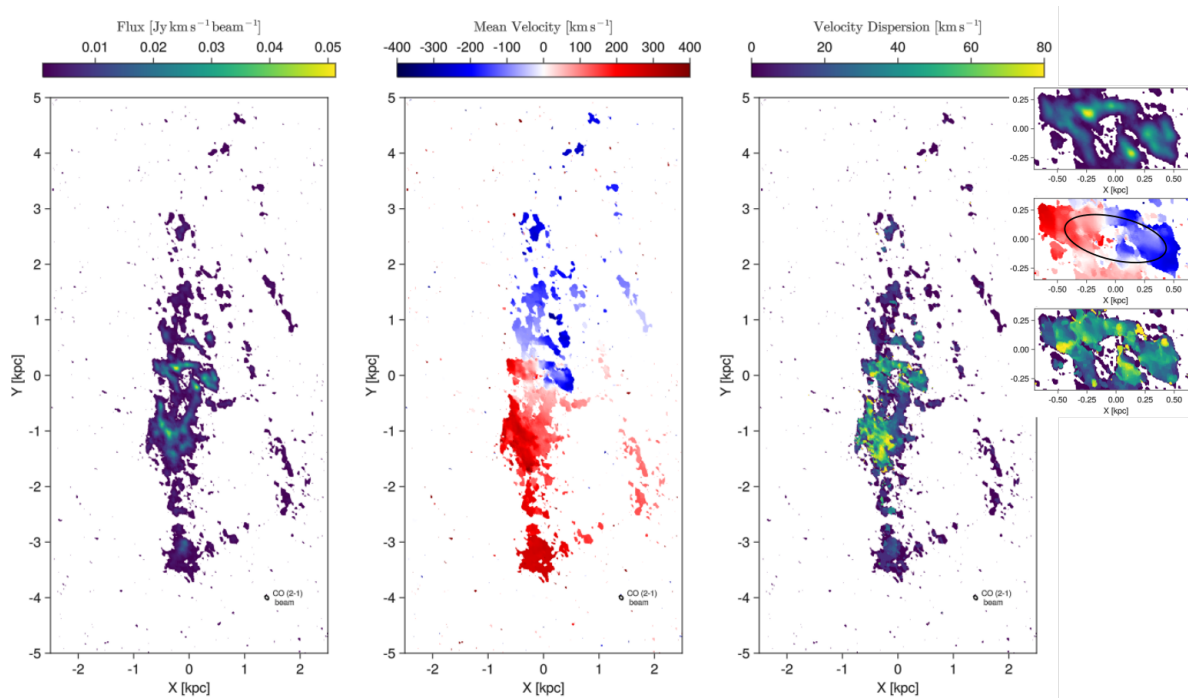


Figure 3.8: From left to right: zeroth, first, and second moments of the CO(2 – 1) emission. The ellipse in the lower right corner of each panel represents the observational beam. The inset on the right provides a zoomed-in view of the central inner disk-like structure, also highlighted by a black ellipse.

maximize the sensitivity, resulting in a synthesized beam of $0''.27 \times 0''.19$ at $PA=33.75^\circ$. The images were binned to a 20 km s^{-1} (15.2 MHz) spectral resolution and corrected for primary beam attenuation.

The continuum map was made using natural weighting, resulting in a signal-to-noise ratio (SNR) of 400. After five iterations of phase-only self-calibration and one iteration amplitude and phase self-calibration, the SNR was raised to 7912 with an rms of 0.04 mJy/beam. The restoring beam is $0''.194 \times 0''.107$ at $PA = 21.5^\circ$. In the continuum map the radio source is unresolved. The CO(2 – 1) line emission cube was obtained after subtraction of the continuum in the line-free channels with the CASA task `uvcontsub`. The rms noise was estimated to 0.04 mJy/beam with a restoring beam is $0''.272 \times 0''.186$ at $PA = 34.8^\circ$.

The ALMA Band 7 observations were carried out with 44 antennas and baselines ranging from 15 to 1400m. The shortest baseline provides a larger recoverable angular scale of about $11''$. The total integration time was 44.7 minutes. The galaxy was observed in dual-polarization mode with 2 GHz total bandwidth and 128 channels per spectral window (SPW), corresponding to $\sim 13.7 \text{ km s}^{-1}$ velocity resolution. The choice of the tuning setup was to provide simultaneous observations of CO(3 – 2) HCO⁺(4-3) and CS(7-6) emission lines and therefore the SPW of the CO(3 – 2) line emission did not center the observed frequency of the CO(3 – 2) line, missing out the negative velocities. The data reduction was performed using CASA version 5.4.0-70. For the phase and bandpass calibrations, J1703-6212 and J1647-6438 were used, respectively. The flux was calibrated using J1427-4206, assuming that at 350GHz the flux density is 2.19 Jy (for a spectral index of -0.52), and resulting in an accuracy of 8%. The continuum map was made using the CASA `tclean` task with

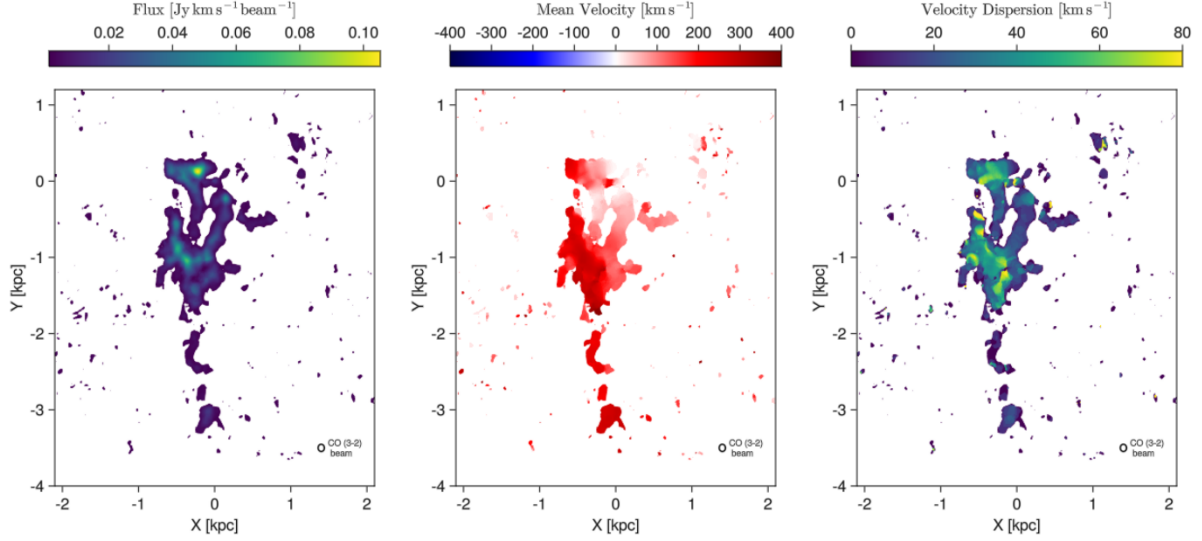


Figure 3.9: From left to right, zeroth, first and second moment of the CO(3 – 2) emission. The black ellipse represents the beam of the observation. Due to spectral coverage limitation only the positive velocities are observed. Thus only the redshifted part of the disk is visible.

natural weighting, resulting in a signal-to-noise ratio of 186. After five iterations of phase-only self-calibration, and one iteration of amplitude and phase self-calibration, a SNR of 5063 was reached, with an rms of 0.044 mJy/beam, a restoring beam of $0''339 \times 0''269$ and PA = 6.9° . After subtracting the continuum and cleaning using the same criteria as in Band 6, we obtained a CO(3 – 2) data cube with a restored beam of $0''320 \times 0''275$ at PA = 2.2° , and an rms noise of 0.297 mJy/beam per channels of 20 km s^{-1} .

3.2.2 Molecular gas distribution and kinematics

ALMA data final products are 3 dimensional, with two dimensions of space (RA, DEC), often called spatial-pixels or spaxels, and one dimension of frequencies ν which are transformed into line of sight (LOS) velocities v using the Doppler shift law defined as

$$V = \frac{\nu_0 - \nu}{\nu_0} c \quad (3.1)$$

where ν_0 is the lab rest frame frequency of the line which in our case is CO(2 – 1) at 230.538 GHz and CO(3 – 2) at 354.796 GHz. However due to cosmological Hubble flow the intrinsic rest frequencies are redshifted also by a factor $(1+z)^{-1}$. This means that ν_0 is now redshifted to 227.355 GHz and 349.897 GHz for CO(2 – 1) and CO(3 – 2) respectively.

CO emission lines are easily excited and thus tracing dense cold molecular gas, as we explained also in chapter 2, producing a Gaussian line profile centered at the LOS velocity and with a dispersion broadening dominated by the random motions of the gas clouds or turbulence. We can estimate the expected turbulence of cloud with size L using the Larson laws (Larson 1981) which used observation from Milky Way galaxy to understand the relation between velocity dispersion and linear size of molecular clouds

which is giving values as

$$\sigma = 6 \left[\frac{L}{100 \text{ pc}} \right]^{0.38} \text{ km s}^{-1} \quad (3.2)$$

However this value is about one single molecular cloud. Looking at extragalactic sources we integrate light from an ensemble of clouds which have relative velocities with each other growing the observed velocity dispersion. Finally, the width of the emission line is convoluted with the spectral resolution of the telescope and several extrinsic factors (such as atmospheric conditions), rising the value even more.

In our case, we convolved the emission in a minimum of 20 km s^{-1} resolution in order to balance the signal to noise ratio and the velocity resolution. So, we estimate a typical velocity dispersion of a regular emitting gas to around $20 - 30 \text{ km s}^{-1}$.

Apart from the mean LOS velocity of the molecular clouds and their dispersion we can also estimate the total mass of the molecular gas assuming that is proportional to the intensity of emission line. We note here that in resolved clouds (i.e. in the Milky Way) this assumption is wrong as soon as the molecular clouds are optically thick. However, collecting the diffusive radiation from an ensemble of many clouds acts as like observing an optically thin gas making the assumption valid (Stahler and Palla 2008). As we have the CO line luminosity we finally can estimate the total mass using the relative abundance with the H_2 gas. For the line luminosity we use the Solomon and Vanden Bout (2005) formula (for the CO(2 – 1) emission):

$$L'_{\text{CO}(2-1)} = 3.25 \times 10^7 \int Idv \frac{D_L^2}{v_{\text{CO}(2-1)}^2 (1+z)^3} \quad [\text{K kms}^{-1} \text{ pc}^2] \quad (3.3)$$

where $\int Idv$ is the integrated emission, $D_L = 62.88 \text{ Mpc}$ is the luminosity distance and $v_{\text{CO}(2-1)}$ is the rest-frame CO(2 – 1) frequency in GHz. Integrating the whole field of view of NGC6328 and keeping only areas with signal higher than three times the local rms noise level we get a value of $L'_{\text{CO}(2-1)} = 3.28 \times 10^8 \text{ K kms}^{-1} \text{ pc}^2$. From the integrated luminosity, we estimate the total molecular gas mass to be $1.8 \times 10^9 M_\odot$, using the relation $M_{\text{H}_2} = a_{\text{CO}} L'_{\text{CO}}$ (Solomon et al. 1997). We adopt a Galactic value of $4.6 M_\odot (\text{K kms}^{-1} \text{ pc}^2)^{-1}$ (Bolatto et al. 2013) for the conversion factor a_{CO} , and a CO(2 – 1) to CO(1 – 0) flux ratio of 4.

Moment maps

Now in order to have a better understanding of the distribution and kinematics of the molecular gas we need to encode the 3D data to a more interpretable structure. The most useful and standard procedure is to create 2D spatial maps containing the most quantity of information. This method is called method of moments in which we create a map for the total integrated along the LOS mass (0th moment)

$$M_0 = \int_v dv \quad (3.4)$$

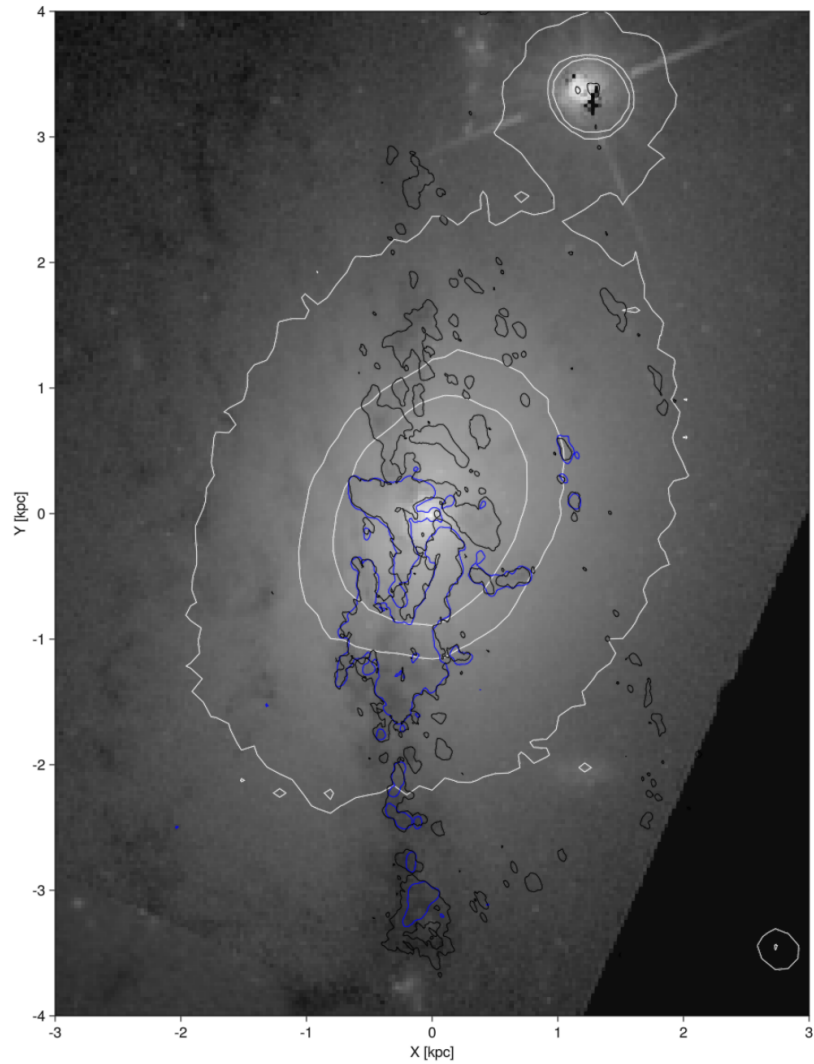


Figure 3.10: HST zoomed view of the central 4 kpc. ALMA CO(2 – 1) (black) and CO(3 – 2) (blue) 4σ contours of the maximum flux per channel. The central North-South oriented dust lane, correlated with the CO emission, along with a less prominent feature to the west marking the start of a faint spiral arm. The elliptical contours represent the stellar distribution from VLT in the J band.

the mean velocity of the gas (1st moment)

$$M_1 = \frac{\int v I_v dv}{M_0} \quad (3.5)$$

and the mean velocity dispersion (2nd moment)

$$M_2 = \frac{\int I_v (v - M_1)^2 dv}{M_0} \quad (3.6)$$

The resulting maps are shown in figure 3.8 and 3.9 for the emission cubes of CO(2 – 1) and CO(3 – 2) respectively. From these maps we note several observations.

The CO emission consists mainly of a highly inclined, disk-like structure extending out to $15''$ (4.3 kpc). This distribution is spatially correlated with the dust absorption visible in Figure 3.1. The main disk structure is clumpy and asymmetric with respect to the center of the galaxy, with 66% of the total intensity belonging to the southern part of the disk and concentrated in an area 1.3 kpc^2 wide, around 1 kpc South-West from the center (30% of the total intensity). Apart from this massive area the

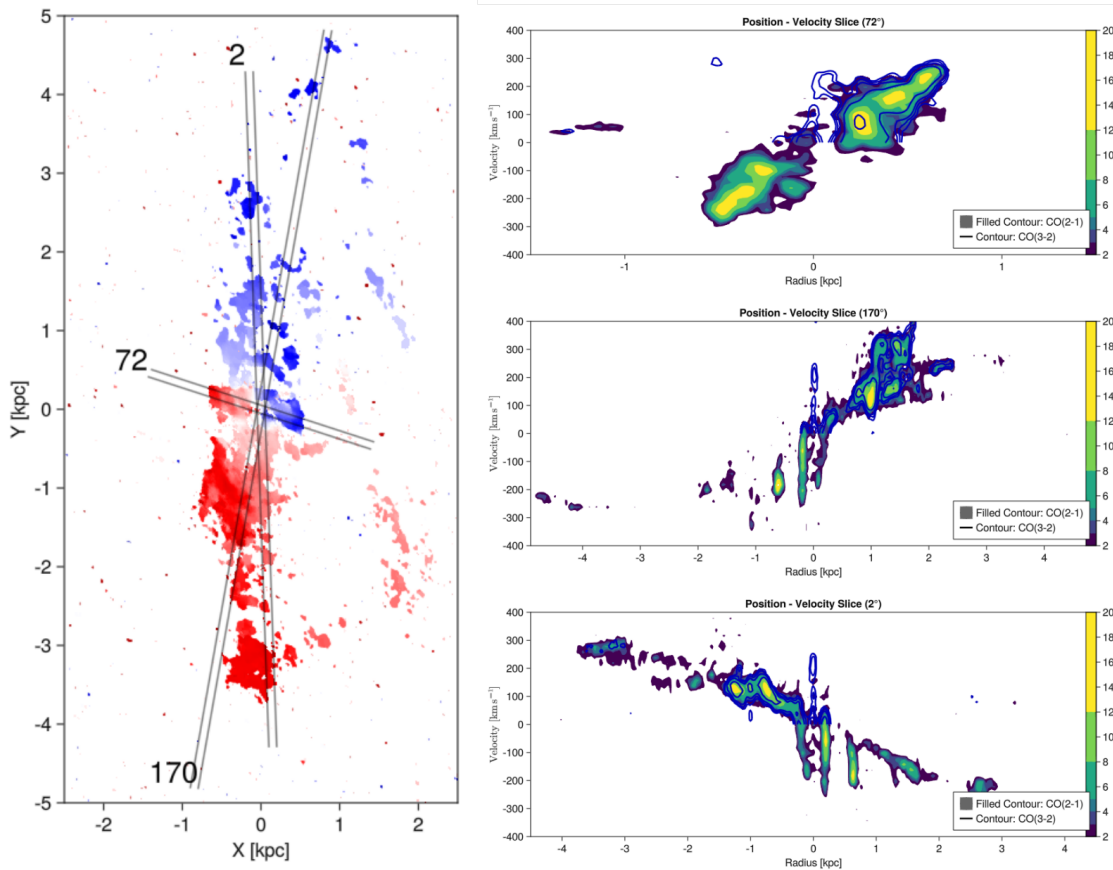


Figure 3.11: Position velocity slices along three different PA. From the top, PA of the inner disk (72°), PA along the high dispersion areas (170°) and along the PA of the main disk (2°). The contours represent the total emission over the total noise along the width of the slice (100 pc). At the left we present these three slices on top of the average velocity moment map of CO (2-1) emission.

molecular clouds density is dropping with the observed distance from the center. East from this main disk there are filamentary features that could be associated with spiral arms, tidal tails, or polar rings.

From both the integrated intensity and the mean velocity maps of the CO(2 – 1) and CO(3 – 2) lines (Figures 3.8 and 3.9), we identify multiple gas structures. In the inner regions, it is evident the presence of a bright molecular structure extending up to 650 pc, with $i \approx 65^\circ$ and PA = 72° closely aligned with the warm H₂ emission (Maccagni et al. 2016b). This structure appears disk-like but could also resemble a ring.

The kinematics observed in the mean velocity and velocity dispersion map (Figure 3.8, middle panel) suggests the presence of a warp, as the position angle clearly changes from 140° at 1.4 kpc to 180° at the maximum extent of 4 kpc. In the South-West (SW) portion of the disk, there is a massive substructure spanning an area of approximately 1.3 kpc^2 , centered at $\approx 1 \text{ kpc}$ from the center. This substructure has a mass of around $\sim 10^8 M_\odot$ (assuming $a_{\text{CO}} = 4.6 M_\odot (\text{K km s}^{-1} \text{ pc}^2)^{-1}$), exhibits the maximum observed velocities (exceeding 350 km s^{-1}) and velocity dispersion (with values exceeding 80 km s^{-1}). A similar behavior can be observed in the opposite direction (PA $\approx -30^\circ$), though in much smaller and less massive clumps of molecular gas. Both of these regions coincide with notable H₂ regions outside of the inner disk (Maccagni

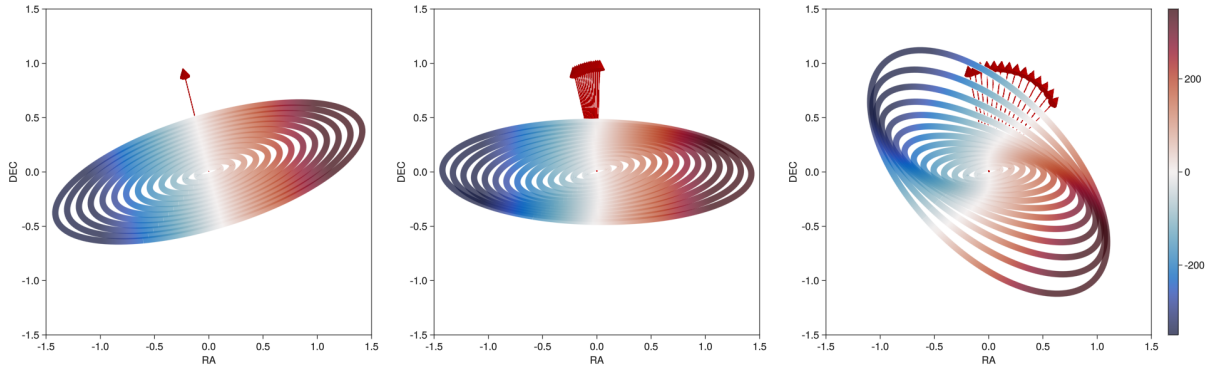


Figure 3.12: Illustration of projected velocities in a rotating disk depicted through a composition of rings, showcasing three different scenarios of disk warping. At the left the disk has no warp, where in the middle and right the disk has a mild and a strong warp, respectively. The arrows represent the normal vectors of the circular orbits. In the warped configurations, the loci of zero velocities trace an "S" shape curve and the superposition of disk sections creates apparent overlaps when projected onto the plane of the sky.

et al. 2016b).

Position velocity slices

Except from the 2D spatial dimensions of the moment maps we can infer the gas kinematical properties through 2D position-velocity slices. These are images created by taking a slice with spatial thickness w which passes through the center of the galaxy and integrating along the thickness. This way we create a map where the one dimension (x) is the distance from the center and the other (y) is the LOS velocity. In a regular rotating disk we expect that if the slice is along the major axis of the disk as it is projected to the sky we will see dense components tracing the rotation curve of the disk. This rotation curve however must be corrected for the disk inclination[†].

In figure 3.11 we plot the position velocity slices at 3 selected angles. At 72° where we observe the major axes of what seems to be an inner disk and at 2° and 170° where we observe the maximum extent of the molecular gas, and we expect the major axes of the main disk. Here we can have a better look on the high dispersion areas and focus on also some more interesting features such as high dispersion areas also in the more central part of the gas.

All the background we provided is coming to this. What is the cause of this high dispersion areas? Overall we could directly accept that we are observing high turbulence areas, or gas out of regular rotation kinematics and try to understand the nature and the cause of it (i.e. supernovae, AGN, jets etc).

However, we could observe high dispersion due to extrinsic reasons such as projections effects. If the disk has not a single fixed orientation over radius then we can observe different intrinsic areas of the disk in the same sky positions, which means different LOS velocities in the same spatial area of the cube. This can be seen in the illustration on figure 3.12 where as the warps of the disk strengthens we observe multiple regions

[†] Using the equation A.8 when $\phi = PA$ we get $v_{los} = v \sin i$, so in order to get the intrinsic rotational velocity from the observed v_{los} we need to divide by $\sin i$

where different parts of the disk overlap, leading to a superposition of line-of-sight velocities.

3.3 Building a new gas kinematics and distribution model

To fully investigate the kinematics of the molecular gas in NGC6328 we used the tilted rings method. In this method we create a series of rings where each ring has its own rotational velocity and orientation, or other properties (velocity dispersion, gas density etc). Then by using the projected LOS velocity we can create a model of the disk and compare it with observations. In the next paragraphs we will first explain the need for our new methodology, then describe our model and finally the way the comparison with the data is implemented.

3.3.1 The need for a new tilted rings model

This is a standard method which is used extensively in the literature on inferring the kinematical properties of extended gas emission observations (such as HI and molecular gas). Most tilted rings code, such as *diskfit* (Spekkens and Sellwood 2007; Sellwood and Sánchez 2010; Sellwood and Spekkens 2015), work using the 2D moment maps we explained previously and return as a result a tabulated set of the properties (circular velocity, position angle and inclination, surface density, dispersion, etc) of each ring. They also include non-axisymmetric components such as bars or spirals which introduce radial motions (inflows or outflows) and thus much more tabulated parameters[‡]. This approach can give good results when the disk is close to flat with small warps only on the outskirts of the galaxy, so the combination of circular and streaming radial motions can be easily identified into the mean velocity map.

However, in occasions like NGC6328 where we suspect the presence of a strong warp or -worse- a combination with non-axisymmetric components (such as a bar) the above approach cannot give us accurate results. First of all, given the spatial overlapping of gas emission, we cannot trust that the first-moment map is giving us a trustworthy result. The first-moment map estimates the average velocity weighted by the cloud masses. So, in the case where we have clouds emitting at 50 km s^{-1} and 200 km s^{-1} , in the same spatial position, with a flux of 0.02 and 0.01, respectively, the estimated mean velocity will be at 100 km s^{-1} . Except for this data-oriented problem, we have the problem with the highly degenerate models. Because the models are extremely generic, meaning they use large number of parameters¹ and that they provide minimum interpretability on the results and the inferred parameters. This happens because the parameters either they are not treated as coherent or correlated structures or if they are, they are simplistic (interpolation, etc.) without any physical meaning or bounds. Also, due to these problems, the optimization problem (minimization of $\text{model}(\text{parameters}) - \text{data}$) is non-convex with a huge number of local minima making it extremely difficult to provide the optimal solution.

1: A generic method must have at least 3 parameters (v, i, PA) per ring. If one ring is similar in size of the beam, the number of rings in our ALMA data (beam=80 pc) will be around 68. This means 204 parameters without using any non-axisymmetric models

[‡] check appendix

Recently, there have been attempts to use fully 3D data from the cube with ^{3D}Barolo (Teodoro and Fraternali 2015), KinMS (Davis et al. 2020), GalPak3D (Bouché et al. 2015a; Bouché et al. 2015b) and TiRiFiC (Józsa et al. 2007). In all these codes, even the problem of the information loss, due to dimension reduction, is resolved, the problem of model/parameter degeneracy remains. There are also more problems regarding the model selection and optimization, which we will further discuss in the section where we describe our own methodology.

3.3.2 Model description

In order to resolve all the issues we mentioned before, we implemented a new model which incorporates physical principles to depict the galaxy's 3D structure and kinematics. Additionally, our code includes an alternative model that employs interpolation schemes for the rings' geometrical properties in the galaxy plane, akin to traditional methods. This alternative model is initialized using the resulting geometry derived from the physically-motivated model, but it allows for more flexibility in case the physical model might be overly constraining or not fully applicable. However in both approaches we implemented a similar rotation curve model.

Rotation curve model

One of the major parameters of the tilted rings models is the intrinsic rotational velocity of each ring. As we said earlier generic codes estimate a set of 'best' and **independent** rotational velocities $v(r_i)$ for each ring at radius r_i . Instead we modelled our rotation curve using known information from the properties of the galaxy.

We used a gravitational potential comprised of three components: a SMBH, a bulge, and a dark matter halo. We did not use any further stellar or gas components (such as disks) because their mass is too small to significantly influence the kinematics.

For the bulge (the most massive stellar component) we used the Hernquist potential (Hernquist 1990) of a spherical stellar density distribution. This distribution is a very good approximation of the Sérsic profile with $n = 4$ which closely assembles the bulge light profile of the galaxy. Hernquist model depends on the total stellar mass of the bulge (M_*) and a scale length (r_a) and has a stellar density of

$$\rho(r) = \frac{M_* r_a}{2\pi r} \frac{1}{(r + r_a)^3} \quad (3.7)$$

which provide a potential

$$\Phi(r) = -\frac{GM_*}{r + r_a} \quad (3.8)$$

The rotational velocity is found from solving the centripetal acceleration

$\frac{v^2(r)}{r} = |\vec{F}|$ as

$$v_{\text{Bulge}}(r; M_*, r_a) = \sqrt{r \frac{d}{dr} \Phi(r)} = \frac{\sqrt{GM_* r}}{r + r_a} \quad (3.9)$$

Additionally, as the ALMA data can be resolved close to the SMBH sphere of influence² we added a Keplerian component

$$v_{\text{SMBH}}(r) = \sqrt{\frac{G M_{\text{SMBH}}}{r}} \quad (3.10)$$

For the dark matter halo component, we used the Navarro–Frenk–White profile (NFW) (Navarro et al. 1996). The NFW density profile is a two parameterized formula of the density of galaxies dark matter halos

$$\rho_{\text{DM}}(r) = \frac{\rho_s}{(r/r_s)(1 + (r/r_s))^2} \quad (3.11)$$

where r_s and ρ_s are a characteristic radius and density. A halo of virial mass M_{vir} is defined as the radius within which the mean density is Δ_{vir} (≈ 337 for ΛCDM , $\Omega_m = 0.3$ and $z = 0$) times the mean universal density ρ_u at that redshift.

$$M_{\text{vir}} = \frac{4\pi}{3} \Delta_{\text{vir}} \rho_u R_{\text{vir}}^3 \quad (3.12)$$

Using the parameterization of Bullock et al. (2001)

$$\frac{M_{\text{vir}}}{10^{11} h^{-1} M_{\odot}} \simeq \left[\Omega_0 \frac{\Delta_{\text{vir}}(z)}{200} \right] \left[\frac{R_{\text{vir}}(1+z)}{75 h^{-1} \text{kpc}} \right]^3 \quad (3.13)$$

$$\frac{V_{\text{vir}}}{75 \text{ km s}^{-1}} \simeq \left[\frac{R_{\text{vir}}}{75 h^{-1} \text{kpc}} \right] \left[\Omega_0 \frac{\Delta_{\text{vir}}(z)}{200} \right]^{1/3} (1+z)^{3/2} \quad (3.14)$$

we can solve for V_{vir} and R_{vir} as a function of the M_{vir}

$$\frac{V_{\text{vir}}}{75 \text{ km s}^{-1}} \simeq (1+z)^{1/2} \left[\frac{M_{\text{vir}}}{10^{11} h^{-1} M_{\odot}} \right] \left[\Omega_0 \frac{\Delta_{\text{vir}}(z)}{200} \right]^{2/3} \quad (3.15)$$

$$\frac{R_{\text{vir}}}{\text{kpc}} = \frac{75 h^{-1}}{1+z} \left[\Omega_0 \frac{M_{\text{vir}}}{10^{11} h^{-1} M_{\odot}} \frac{\Delta_{\text{vir}}(z)}{200} \right]^{1/3} \quad (3.16)$$

The circular velocity component due to dark matter halo is

$$v_{\text{DM}}^2(r; M_{\text{vir}}, c_{\text{vir}}) = V_{\text{vir}}^2 \frac{c_{\text{vir}}}{A(c_{\text{vir}})} \frac{A(r/R_{\text{vir}})}{r/R_{\text{vir}}} \quad (3.17)$$

where $A(x) = \log(1+x) - \frac{x}{1+x}$. The only parameters are M_{vir} , and the concentration parameter $c_{\text{vir}} = R_{\text{vir}}/r_s$.

Detailed observations of WMAP3 show a correlation between the concentration parameter and virial mass

$$\log c_{\text{vir}} = 0.971 - 0.094 \log (M_{\text{vir}} / [10^{12} h^{-1} M_{\odot}])$$

which can give as the opportunity to remove it as a free parameter as the DM component it is not strongly affect the rotation curve in the molecular gas region.

2: For the SMBH, we used a mass of $4.1 \times 10^8 M_{\odot}$ (Willett et al. 2010)

The resulting rotational curve model is dependent on 4 parameters (we use the literature value of the SMBH mass).

$$v(r; M_*, r_a, M_{\text{vir}}, c_{\text{vir}}) = \sqrt{v_{\text{SMBH}}^2(r) + v_{\text{Bulge}}^2(r; M_*, r_a) + v_{\text{DM}}^2(r; M_{\text{vir}}, c_{\text{vir}})} \quad (3.18)$$

For the rest of our work we assume that non-circular velocities are negligible.

Physically-connected rings model

This approach captures the warped structure of the disk resulting from gas infall towards an ellipsoidal or triaxial gravitational potential. In a non-spherical potential, it is widely accepted that the gas will precess due to the torques induced by the gravitational potential of the stars until it eventually relaxes back into alignment with one of the preferred axes, commencing either clockwise or counter-clockwise rotation. Rings at smaller radii precess more rapidly due to their higher angular velocity, which leads to a warped disk structure. The differences in angular velocity and precession rates between neighboring rings generate internal torques. These internal torques serve as dissipative forces, promoting the alignment of each ring with its neighbors and eliminating the component of the gas's angular momentum that's perpendicular to the stellar angular momentum direction, thus facilitating the settling of the gas to the potential's preferred axes. Over time, these processes result in the alignment or counter-alignment of the gas with the stellar angular momentum. This alignment transpires over timescales ranging from hundreds of millions to billions of years (Tohline et al. 1982; Lake and Norman 1983; Steiman-Cameron and Durisen 1988; Sparke 1996; Davis and Bureau 2016).

Assuming that precession is slow compared to the time taken for one complete orbit, the change in the orbital orientation

$$\hat{n}(t, r) = \begin{pmatrix} -\sin \theta(t, r) \sin \lambda(t, r) \\ \sin \theta(t, r) \cos \lambda(t, r) \\ \cos \theta(t, r) \end{pmatrix} \quad (3.19)$$

due to the asphericity of the galaxy and viscous forces can be calculated by averaging the torque induced over an orbital motion as follows:

$$\frac{d\theta}{dt} = -\frac{T_\theta}{h \sin \theta} - f_\theta(t, r, \theta, \lambda) \quad (3.20)$$

$$\frac{d\lambda}{dt} = \frac{T_\lambda}{h \sin \theta} \quad (3.21)$$

where $T_{\theta, \lambda} = -\frac{\partial \langle \Phi \rangle(r, \theta, \lambda)}{\partial (\lambda, \theta)}$ represents the torques exerted on the ring in the θ and λ directions due to the asphericity of the potential Φ , $h(r) = rV_c(r)$ is the orbital angular momentum per unit mass and $V_c(r)$ is the rotation curve we defined in the previous section. The quantity $\langle \Phi \rangle(r, \theta, \lambda)$ denotes the gravitational potential averaged along the circular orbit/ring as

$$\langle \Phi \rangle(r, \theta, \lambda) = \frac{1}{2\pi} \oint_{r, \theta, \lambda} \Phi(\psi, r, \theta, \lambda) d\psi \quad \text{where } 0 \leq \psi \leq 2\pi \quad (3.22)$$

From the conservation of angular momentum we have

$$\frac{d\vec{L}}{dt} = \vec{T} \quad \text{or} \quad h \frac{d\hat{n}}{dt} = \vec{r} \times \nabla \langle \Phi \rangle$$

$$h \dot{\theta} \hat{\theta} + h \sin \theta \dot{\lambda} \hat{\lambda} = \frac{1}{\sin \theta} \frac{\partial \langle \Phi \rangle}{\partial \lambda} \hat{\theta} + \frac{\partial \langle \Phi \rangle}{\partial \theta} \hat{\lambda}$$

The potential that provides the necessary asymmetries for the above precession is assumed to be that of the bulge. Thus, we use a modified Hernquist bulge for the stellar density with total stellar mass M and scale lengths $r_a, r_b,$ and r_c (in case of an axisymmetric bulge $r_a = r_b$), which is defined as

$$\rho_h(\mu) = \frac{M}{2\pi abc} \frac{1}{\mu(1+\mu)^3} \quad \text{where} \quad \mu^2 = \frac{x^2}{r_a^2} + \frac{y^2}{r_b^2} + \frac{z^2}{r_c^2} \quad (3.23)$$

From this we get the potential for every position x, y, z using the method of ellipsoidal shells (Chandrasekhar 1969; Binney and Tremaine 2008),

$$\Phi_{\text{bulge}}(\xi) = -\frac{GM}{2} \int_0^\infty \frac{du}{\sqrt{r_a^2 + u} \sqrt{r_b^2 + u} \sqrt{r_c^2 + u} [1 + \xi(u)]^2} \quad (3.24)$$

where

$$\xi^2(u) = \frac{x^2}{r_a^2 + u} + \frac{y^2}{r_b^2 + u} + \frac{z^2}{r_c^2 + u} \quad (3.25)$$

Diffusive forces

The function $f_\theta(t, r, \theta, \lambda)$ represents the effect of viscous forces arising from the interaction between adjacent rings. For the evolution of the polar angle (tilting), as described in equation 3.20, we employ the dissipative force definition from Steiman-Cameron and Durisen (1988) to define the quantity

$$f_\theta(t, r, \theta, \lambda) = \frac{3 \sin 2\theta}{2} \frac{t^2}{t_e^3} \quad (3.26)$$

where t_e is the timescale required for the gas to settle. In this approach, we use the stress-free approximation, where the effect of dissipative forces on twisting 3.21 is considered negligible compared to their effect on tilting (Steiman-Cameron and Durisen 1988).

First approximation This timescale is dependent on the geometric and physical characteristics of each ring and its neighbors. In Steiman-Cameron and Durisen 1988, the authors approximated the inner-torques between adjacent rings as resulting from viscous transport of angular momentum, through cloud-cloud collisions, computing t_e via the gas viscosity and higher-order derivatives.

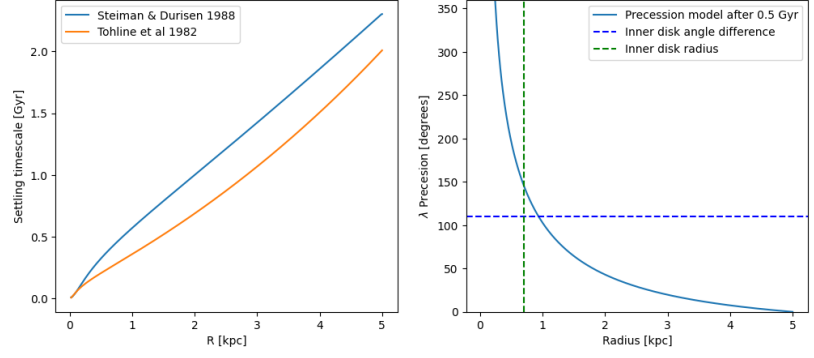
$$t_e(r) = \left[\frac{\nu(r)}{6} \left(\frac{d\dot{\lambda}}{dr} \right)^2 \right]^{-1/3} \quad (3.27)$$

where ν is the kinematic viscosity and dot symbolizes the time derivative. We can approximate the kinematic viscosity using

$$\mu = \rho l \sigma_{\text{clouds}} \quad \text{or} \quad \nu = l \sigma_{\text{clouds}} \quad (3.28)$$

where μ is the dynamic viscosity, l is the mean free path and σ_{clouds} the velocity dispersion of the clouds. Note that we are describing cloud-to-cloud collision and not just molecular gas. In order to estimate l we

Figure 3.13: **Left:** Settling timescales as a function of radius in the two viscous force approximations. **Right:** Line of nodes precession as function of radius after 500 Myr used to approximate the settling timescales. The dotted lines represent an approximation of the observable disk precession between the outer disk and the inner disk.



make the assumption that a cloud collision occurs once in a one epicyclic frequency k^{\S} , so $l \approx c \frac{\sigma_{\text{clouds}}}{\kappa}$ where c is a parameter that controls the likelihood of collision in one epicyclic period. We expect $c < 1$. Now the approximation of the kinematic viscosity is as follows.

$$v(r) \approx \frac{c \sigma_{\text{clouds}}^2(r)}{\kappa(r)} \quad (3.30)$$

where we have functional notation as these parameters are function of radius.

The next term we need to estimate is the mixed derivative of $\frac{d\dot{\lambda}}{dr}$. Without solving the complicated system of mixed partial differential equations (3.20 and 3.21 together with 3.26) we can approximate $\dot{\lambda}$ in simple precession scenario, without viscous forces and simple axisymmetric potential representation as

$$\dot{\lambda}(r) = \epsilon \cos \theta \Omega(r) \quad (3.31)$$

where ϵ describes the ellipticity of the stellar isophotes, θ is the inclination of the disk to potential equator (remains constant in an axisymmetric potential) and $\Omega(r)$ the regular angular velocity. Now by differentiating $\dot{\lambda}$ over the radius and using our approximation of the kinematic viscosity we get a settle timescale $t_e(r)$ as seen in 3.13

Second approximation In order to avoid solving the partial derivative system (due to the mixed derivatives in equations 3.20,3.21 together 3.26), we also chose to test a simpler approach introduced by Tohline et al. (1982). In this work authors defined the settling timescale as

$$t_e = \frac{\alpha}{|\dot{\lambda}(r) - \dot{\lambda}_0|} \quad (3.32)$$

[§] The epicyclic period in a galaxy refers to the time it takes for a star (or a cloud) to complete one oscillation perpendicular to its circular orbit around the galactic center. In other words, while a star orbits the center of a galaxy in a roughly circular path, it also oscillates radially in and out, as well as vertically up and down, relative to the galactic plane. These oscillations are described as epicyclic motions. The epicyclic frequency (κ) is often used to describe these oscillations and is defined as:

$$\kappa^2 = 2\Omega \left(\frac{d\Omega}{dR} + \Omega \right) \quad (3.29)$$

where Ω is the angular velocity of the circular orbit and R is the radius of the orbit.

This much simpler expression, was based on the observation that the gas will have settled once it has precessed through an angle $\alpha = \pi/2$ around the main axis.

In figure 3.13 we compare the two methods. In fact, the timescale can have significantly different values. However, for several reasons, we chose the approximation of Tohline et al. 1982. More specifically:

- ▶ PDE solvers are much more computational complex and prone to numerical errors and instabilities.
- ▶ The behavior of the timescales tends to produce similar estimations, especially by fine-tuning the parameters.
- ▶ The approach of Steiman-Cameron and Durisen (1988) introduces more unknown parameters.
- ▶ In our problem, we have already introduced a number of assumptions that surpass the need for more complex models.

Also, in order to add more flexibility to the timescale estimation, we chose to treat the angle α as a fitting parameter.

Running the model

Overall the model executes two numerical integrations, one for the seminfinite integral of the ellipsoidal shells (equation 3.24) and its average along one orbit/ring (equation 3.22). After extensive experimentation, we established an upper limit for the "infinite" boundary to 10^6 kpc for the potential integration and an absolute tolerance of 10^{-5} in order to achieve an accurate approximation and preserve computation time. Both numerical integrations are conducted with the adaptive Gauss-Kronrod quadrature method (QuadGK) using the quadgk.jl package (Johnson 2013) in the numerical Julia language ecosystem (Bezanson et al. 2015).

The partial derivatives of the "numerically estimated" average potential in the ϕ and θ directions are calculated using the forward mode automatic differentiation method (AD) using the ForwardDiff.jl Julia package (Revels et al. 2016). Automatic differentiation significantly outperforms classical differentiation methods, providing, as with the better speed and accuracy.

As we have calculated the partial derivatives (torques), we solved the set of differential equations (3.20 and 3.21) using the state-of-the-art DifferentialEquations.jl package (Rackauckas and Nie 2017) of Julia. The choice of the specific package was crucial due to its auto-stiffness detection algorithm, which evaluates different integration solvers at different steps. In our case, the algorithm of choice was a combination of TSIT5 (Tsitouras 2011) and Rosenbrock23 (Rosenbrock 1963) methods.

The result of the above chain of integration and differentiation processes is a set of $\theta(t)$ and $\phi(t)$ functions for a specific radius of the ring. This means that we cannot get the needed $\theta(t, r)$, $\phi(t, r)$ directly, which was the reason we avoided the viscous force of the mixed derivative $\frac{\partial^2}{\partial t \partial r}$ (equation 3.27). To get a set of solutions in the full time and radii, we solve in-parallel (using multi-threading) the time evolution for a set of predefined rings and then interpolate between them. Using a 32 thread environment we chose a set of 32 or 64 radii unevenly distributed (from 0.03 kpc to 6 kpc and denser in the central kpc) and integrated up to

2 Gyrs. The whole process, after several code and memory optimizations, is executed in sub-second timescales.

Generic tilted rings model

Except for the physically-connected ring model, we employed a more generic model which uses the rotation velocity defined in section 3.3.2 but for the geometrical properties $\theta(r), \lambda(r)$ (note that there is no time evolution) it uses an interpolation scheme, similar to the methods used in the literature, based on a specific set of N pairs $(r_k, \theta_k, \lambda_k)$ which are fitable parameters. For interpolation we used the Piecewise Cubic Hermite Interpolating Polynomial (PCHIP) (Fritsch and Butland 1984) in order to avoid large gradients and get smooth solutions. The generic model was used with an initial solution from the physically-connected ring model. In this way we allowed more flexibility and small deviations from the physical models to avoid overfitting with unreasonable solutions.

3.3.3 Model setup and projections

In the above sections, we provided the framework of how our model works. Given a set of parameters, which is different to model setup (physically-connected rings or generic rings) it results on a set of tilted rings, or more specifically for a given radii r_k , a set of v_k, θ_k, λ_k . In the case of the generic model, this set is unique, and in the case of the physically-connected rings is a single set for every time step in the evolution of a warped disk. As we will explain later in the data fitting procedure, this difference is irrelevant as the fitter compares the data with a single tilted rings set every time.

Before fitting the data (as we explain later), the resulting tilted rings must be projected to the sky plane to get the final $v_k^{\text{los}}, i_k, \text{PA}_k$. This is done by using a reference ring oriented as $(i_{\text{Bulge}}, \text{PA}_{\text{Bulge}})$ in the sky and creating a rotation matrix as explained in the Appendix A.1.3

Using these setups, we created three different models. Models **A** and **B**, are using the physical model that describes the time-dependent evolution of a set of tilted rings within a triaxial or axisymmetric bulge potential accordingly. The physical approach in models A and B captures the warped disk motion and structure, which results from gas infalling towards the gravitational potential, feeling torques from a non-spherical potential, and dissipative forces. The third model, named **C**, uses the generic interpolated model that we described earlier.

For models A and B, there are 12 and 13 fitable parameters, respectively. These include the bulge stellar mass, the scale size on the three axes r_a, r_b, r_c (for the axisymmetric model, $r_a = r_b$), the virial mass and concentration parameter of the dark matter component, the initial values of $\theta(0, r) = \theta_0$ and $\lambda(0, r) = \lambda_0$, the settling angle α and the orientation of the reference ring $(i_{\text{Bulge}}, \text{PA}_{\text{Bulge}})$. As the physically-connected creates multiple rings for every time step in the disk evolution, there is an extra parameter that can be exported, the time elapsed from the initial configuration τ .

For model C, $\theta(r)$ and $\lambda(r)$ are generated using an interpolated set of $N = 10$ pairs $(r_k, \theta_k, \lambda_k)$, which are fitable parameters. The rotation curve

uses the same parameters as the other models, which are the stellar mass of the bulge, the scale size of the bulge r_a , and the virial mass of the dark matter component, for a total of 26 parameters together with the orientation of the reference ring ($i_{\text{Bulge}}, \text{PA}_{\text{Bulge}}$).

3.4 Fitting the ALMA Data with Our Models

3.4.1 Statistical Inference

Likelihood Analysis

Likelihood analysis is a standard statistical framework essential for fitting models to empirical data. This analysis aims to estimate the parameters of various models under consideration, thereby quantifying how well these models describe the observed phenomena.

Given a set of measurements and their errors (x_i, y_i, σ_i) from a dataset D of size N , and a model $M(x; \bar{\theta})$ where $\bar{\theta}$ is a vector of the free parameters, the likelihood is the probability function for obtaining the exact measurements given the model, denoted as $\mathcal{P}(D|M(x; \bar{\theta}))$. Assuming that the probability distribution of the data \mathcal{N} is Gaussian and that the data points are independent, the likelihood function can be expressed as

$$\mathcal{L}(D, \bar{\theta}) = \mathcal{P}(D|M(x; \bar{\theta})) = \prod_{i=1}^N \mathcal{N}(M(x_i; \bar{\theta}) - y_i, \sigma_i) \quad (3.33)$$

It is more convenient to use the natural logarithm of the likelihood.

$$\log \mathcal{L}(D, \bar{\theta}) = -\frac{N}{2} \log(2\pi \sum_{i=1}^N \sigma_i^2) - \sum_{i=1}^N \frac{(M(x_i; \bar{\theta}) - y_i)^2}{2\sigma_i^2} \quad (3.34)$$

where we have expanded the Gaussian distribution function. As the first term is constant, denoted $K = -N \log(2\pi \sum_{i=1}^N \sigma_i^2)$, equation 3.34 can also be written as

$$\log \mathcal{L}(D, \bar{\theta}) = \frac{1}{2} \left(K - \sum_{i=1}^N \frac{(M(x_i; \bar{\theta}) - y_i)^2}{2\sigma_i^2} \right) \equiv \frac{1}{2} (K - \chi^2(D, \bar{\theta})) \quad (3.35)$$

where $\chi^2 = \sum_{i=1}^N \frac{(M(x_i; \bar{\theta}) - y_i)^2}{\sigma_i^2}$ is the widely used chi-square expression in the literature.

The likelihood analysis consists of finding the set of parameters that better describe the data, under the assumption that the model is correct. This can be achieved by finding $\bar{\theta}^*$ that maximizes the likelihood function, a method referred to as Maximum Likelihood Estimation (MLE):

$$\bar{\theta}^* = \arg \max \mathcal{L}(D, \bar{\theta}) = \arg \min \chi^2(D, \bar{\theta}) \quad (3.36)$$

Along with the MLE estimation of the parameters $\bar{\theta}^*$, another question that we need to answer is related to the confidence intervals of the parameters, the variances (errors) of each specific parameter, and the covariance (correlations) between them. Before continuing, we need to generalize the previous definitions in the case that the data points are not independent, implying that there is a non-zero covariance matrix \mathbf{C} of size $N \times N$. The previous case of independent data translates into $\mathbf{C} = \text{diag}\left(\frac{1}{\sigma_i^2}\right)$, so that values outside the diagonal are zeros.

Now, the likelihood is defined as

$$\mathcal{L}(\bar{\theta}) = \frac{1}{\sqrt{(2\pi)^N \det(\mathbf{C})}} \exp\left(-\frac{1}{2} \mathbf{R}^\top \mathbf{C}^{-1} \mathbf{R}\right) \quad (3.37)$$

where $\mathbf{R} = \mathbf{D} - \mathbf{M}(\bar{\theta})$ denotes the residuals (data model) and $\mathbf{M}(\bar{\theta})$ represents the model points created from the parameters. The chi-square term is

$$\chi^2(\bar{\theta}) = \mathbf{R}^\top \mathbf{C}^{-1} \mathbf{R} \quad (3.38)$$

To approximate the covariance of the estimated MLE parameters, we use the Fisher Information Matrix, defined as

$$F_{ij} = -\mathbb{E}\left[\frac{\partial^2 \ln \mathcal{L}}{\partial \theta_i \partial \theta_j}\right] \quad (3.39)$$

where $\mathbb{E}[X] = \int_{-\infty}^{\infty} x f(x) dx$ represents the expected or average value of the distribution. For Gaussian-distributed data, we obtain the following.

$$F_{ij} = \frac{1}{2} \text{Tr}\left(\mathbf{C}^{-1} \frac{\partial \mathbf{M}}{\partial \theta_i} \mathbf{C}^{-1} \frac{\partial \mathbf{M}}{\partial \theta_j}\right) \quad (3.40)$$

where $\frac{\partial \mathbf{M}}{\partial \theta_i}$ is the derivative of the model with respect to θ_i (the Jacobian). Finally, the covariance matrix of the parameters is $\Sigma \approx \mathbf{F}^{-1}$, so the MLE estimated parameters with the one-sigma (68.3%) confidence intervals are

$$\theta_i = \theta_i^* \pm \sqrt{\Sigma_{ii}} \quad (3.41)$$

where Σ_{ii} is the i -th diagonal element of Σ .

Bayesian Approach

The methods described in the previous section adhere to the frequentist statistical approach, characterized primarily by the Maximum Likelihood Estimate. In this viewpoint, the parameters are considered to be fixed but unknown quantities. The confidence intervals represent the range of values within which we would expect these fixed parameters to fall if the experiment were infinitely repeated. Although MLE provides point estimates and associated confidence intervals, these intervals do not

convey a probability distribution of the parameters conditioned on the observed data.

In contrast, Bayesian statistics offers a probabilistic framework that facilitates direct probabilistic interpretation of model parameters based on both the data and prior information. Bayesian statistics utilize Bayes' theorem to adjust our beliefs about model parameters in light of new data, expressed mathematically as:

$$\mathcal{P}(\bar{\theta}|D) = \frac{\mathcal{P}(D|\bar{\theta})\mathcal{P}(\bar{\theta})}{\mathcal{P}(D)} \quad (3.42)$$

In this equation, $\mathcal{P}(\bar{\theta}|D)$ represents the posterior distribution of the parameters, given the observed data. $\mathcal{P}(D|\bar{\theta})$ is the likelihood of the data given the parameters, which was discussed earlier. $\mathcal{P}(D)$ denotes the evidence, reflecting the degree of belief in observing the data, and $\mathcal{P}(\bar{\theta})$ is the prior distribution, representing our initial knowledge or beliefs about the model parameters. It is noteworthy that if our priors are flat (uniform over the parameter space), the Bayesian approach yields results analogous to those obtained using the MLE approach.

Numerical Optimization

In both the frequentist and Bayesian approaches, we can employ numerical optimization techniques to determine the optimal θ^* and their uncertainties. In the frequentist approach, these point estimates arise from the MLE method previously described. In contrast, the Bayesian approach yields not point estimates but probability distributions for the parameters. Nevertheless, we can use point estimates from these distributions using either their mean or mode, the latter of which is termed the Maximum A Posteriori Probability (MAP).

To comprehensively explore the full posterior distribution, we implement the Markov Chain Monte Carlo (MCMC) method. MCMC algorithms are powerful tools for estimating the distribution of parameters, especially in cases where analytical solutions are unfeasible. These algorithms generate samples from the posterior distribution, which are then used to approximate the entire distribution and infer the properties of the parameters.

In scenarios where the gradient of the posterior function is unknown, which is the case in models with such complexity, regular samplers are inapplicable. Thus, we utilize the Affine Invariant Markov Chain Monte Carlo (MCMC) Ensemble sampler (Goodman and Weare 2010; Foreman-Mackey et al. 2013) and its julia implementation of Vesselinov and O'Malley (2013).

This sampler employs multiple walkers to approximate the gradient of the posterior, thus allowing for a more accurate exploration of the parameter space. By leveraging the information from numerous walkers, this approach mitigates the challenges posed by unknown gradients and facilitates a more reliable inference of the posterior distribution. This makes it especially valuable for our analysis given the complexities and uncertainties associated with the models and data at hand.

3.4.2 Modeling an ALMA data cube

In Section 3.3.2 we presented a model which uses a set of parameters to provide a set of tilted rings oriented in the sky plane $v_k^{\text{los}}, i_k, \text{PA}_k$. The next issue we need to resolve is how we compare these rings with an ALMA data cube. The first thing we tried was to simulate an ALMA cube from these rings and simply abstract the "real" one to find the residuals. Then we will try to minimize the residuals in conjunction with the methods mentioned in the previous section.

The first thing we need to do to construct our model cube M is to establish the spatial distribution of the rings. As we show in the appendix A.1.2 the projected rings create an elliptical sky distribution. However, when we try to create a disk structure under a set of rings, there are two strong issues. First, as we can see in Figure 3.12 when there is a warp, there are artificial gaps that are observed in the sky plane. The gaps increase as the warp becomes stronger. Second, the rings are defined as ellipses with no width. If we need to define a width (similar to the beam or bigger to have better cover), then the two ellipses that are describing the inner and outer boundary cannot have the same inclination, as two ellipses with the same inclination do not have the same distance everywhere. They tend to be fatter near the major axes and thinner near the minor axes. The first issue has been resolved by over-sampling, creating dense and overlapping rings. The next issue has been resolved by calculating two different inclinations, from the ring inclination, on the inner and outer ellipse so the width remain constant along the ring. The next thing is how we will treat the "4th" dimension of the cube, the observed flux. As we said before, in every spatial pixel (spaxel) of the cube there is a velocity dimension where the flux shows emission lines. An emission line has a Gaussian distribution profile which is defined by its central velocity v_c , its dispersion σ_v , and its maximum intensity F_{max} . Expecting strong warps means that in single spaxel we have more than one emission lines, with different properties, which could also overlap. We tackled this problem by using the data itself during the model creation. When a spaxel is inside a ring width, calculate the central velocity based on the spaxel location along the ring and assign a flux intensity by using the maximum flux from the data at small window of voxels (a x, y, v pixel with a single flux value) near the model-proposed velocity. The velocity dispersion is always the same.

If the ring at radius r has inclination i and width dr then the inclination of the "inner boundary" and "outer boundary" ellipses would be

$$i_{\text{in}} = \arctan(\sqrt{k_1^2 - 1}) \quad (3.43)$$

$$i_{\text{out}} = \arctan(\sqrt{k_2^2 - 1}) \quad (3.44)$$

where

$$k_0 = \sqrt{1 + \tan^2 i} \quad (3.45)$$

$$k_1 = \frac{r - dr}{r/k_0 - dr} \quad (3.46)$$

$$k_2 = \frac{r + dr}{r/k_0 + dr} \quad (3.47)$$

$$(3.48)$$

A different, and more "correct" approach would be to use different models for the intensity and velocity dispersion as a function of radius and create a model cube without using the data. However, we need to properly create such models. For example in the literature there are used exponential decreasing intensity and dispersion models which introduce at least 6 more parameters. Also, given the clumpy molecular gas emission, radial-based models probably are inducing strong behavior on the general model and bias the fitting procedure.

Some of the more significant problems, however, are with the likelihood of the observation given such model. The chi-square which needs to be minimized (the parameters that minimize the chi-square are the same

which maximize the likelihood) should look something like this.

$$\chi^2(\bar{\theta}) = \sum_i^{N_x N_y N_v} \frac{(F_i - F_{\text{model}}(\bar{\theta}))^2}{\sigma_i^2} \quad (3.49)$$

where F_i , σ_i is the flux and noise at voxel i , F_{model} is the model we described earlier and $N_x = N_y = 1680$ the spatial number of pixels (RA and DEC) and $N_v = 123$ the velocity pixels. From this expression we see two significant issues. First, the chi-square will be dominated from larger flux, thus more massive areas. This means that the model cube will be biased towards these areas and mostly fall in local minima. As we want to infer the geometry of the disk, any emission above 3σ must be equally significant. This issue could be solved by introducing strong priors (which can also be used as boundaries) on the parameters and maximizing the posterior or a new chi-square expression instead

$$\chi_{\text{post}}^2(\bar{\theta}) = \sum_i^{N_x N_y N_v} \frac{(F_i - F_{\text{model}}(\bar{\theta}))^2}{\sigma_i^2} + \sum_i^{N_\theta} \frac{(\theta_i - \theta_{\text{prior}})^2}{\sigma_{\theta,i}^2} \quad (3.50)$$

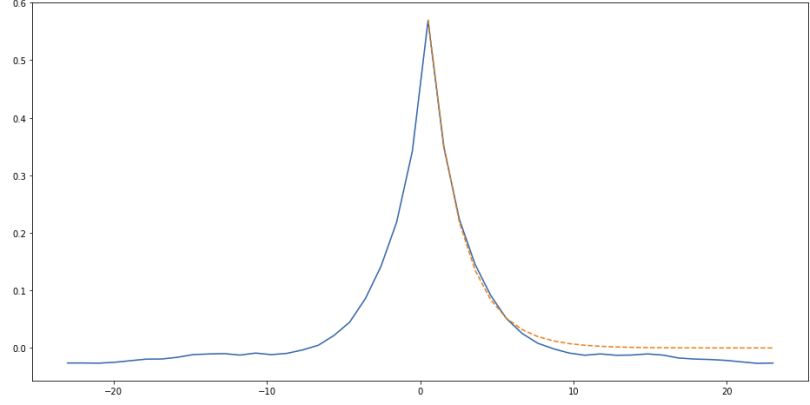
where we have used, as an example, Gaussian priors for every parameter θ_i . This opens the second issue: the correlations between the data. If in the above example use 12 parameters (for the axisymmetric model A), then the relative weight between the two terms in 3.50 will be $N_x N_y N_v / N_\theta \approx 2.9 \times 10^7$, which means that the prior term needs a 10^7 extra weight or such strong priors which will produce this effective weight. The deeper reason, however, for this annoying effect is that the data are correlated through systematic effects (spatial beam, velocity resolution) but also due to the way the model works (Wolff et al. 2017; Davis et al. 2017; Smith et al. 2019; Wolff et al. 2021).

One of the most efficient ways we can infer the autocorrelation information is by using

$$\mathbf{A} = \text{ifft}(\text{fft}(\mathbf{R})\text{fft}^*(\mathbf{R})) \quad (3.51)$$

where \mathbf{R} is the residual cube for a set of random parameters and fft and ifft are the, 3 dimensional, forward and inverse Fast Fourier Transform (FFT) respectively. The star symbol refers to the complex conjugate. Executing this for different sets of parameters and averaging we get an approximation of the autocorrelation cube. If there are no data correlations \mathbf{A} would have values only at zero frequencies (exactly the central voxel). The next step is to slice the cube \mathbf{A} in each velocity channel and understand the spatial behavior. This can be done by fitting a kernel function $K(d)$ into the average radial signal as a function of the distance from the central pixel. One of the most useful and generic such kernel functions is the Mattern Kernel; however, for simplicity we used an exponential function. Now we can construct a covariance matrix **for every channel i** , starting from the diagonal and filling the parallel diagonals based on the fitted kernel function, as seen in 3.52.

Figure 3.14: Averaged autocorrelation and fitted exponential kernel function $K(d)$ over distance in pixels



$$C_i = \begin{bmatrix} \sigma^2 + K(0) & K(1) & K(2) & \cdots & \cdots \\ K(1) & \sigma^2 + K(0) & K(1) & \cdots & \vdots \\ K(2) & K(1) & \sigma^2 + K(0) & \ddots & \vdots \\ \vdots & \ddots & \ddots & \ddots & \vdots \\ \cdots & \cdots & \cdots & \cdots & \cdots \end{bmatrix} \quad (3.52)$$

The covariance matrix (for every velocity channel) has a size of $N_x N_y \times N_x N_y$. The corrected chi square is now computed as

$$\chi^2 \sim \sum_i^{N_v} \mathbf{R}_i^T \mathbf{C}_i^{-1} \mathbf{R}_i \quad (3.53)$$

where we add for all the velocity channels. This methodology has a lot of assumptions and it is computationally and memory heavy.

For all these reasons, we took another approach. Instead of trying to create a model cube to compare with the data, we encoded the cube data in a more useful way.

3.4.3 Clump detection

We implemented a source detection process that encodes the data-cube into a set of M individual clumps with sky projected coordinates $\{(x_m, y_m, V_m)\}_{m=1}^M$ through a source detection process. The first step of the process is iterating over all the spaxels of the cube and fitting N Gaussian-shaped emission lines per spaxel (x, y) using the equation

$$S^{x,y}(V, \{V_c\}_{i=1}^N, \{F\}_{i=1}^N, \{\sigma\}_{i=1}^N) = \sum_{i=1}^N F_i \exp\left(-\frac{(V - V_{c_i})^2}{2\sigma_i^2}\right)$$

The number of Gaussian components N is determined using the Bayesian Information Criterion (BIC), as a model comparison criterion that balances the goodness of fit and the number of model parameters. Assuming that the likelihood of observing the signal on each spaxel is a Gaussian with root mean square noise σ_F the BIC is defined as

$$\text{BIC} = \chi^2 + k \log(n) + n \log(2\pi \sigma_F^2)$$

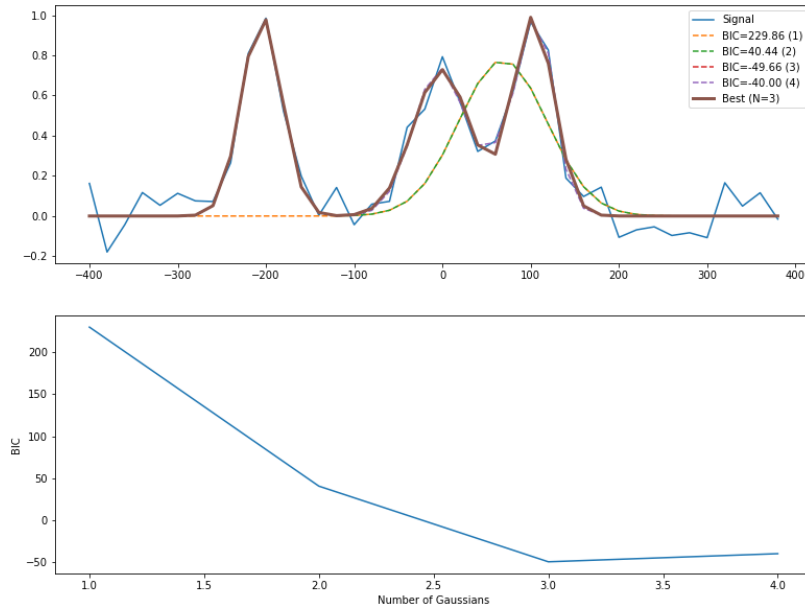


Figure 3.15: Source detection process. The Bayesian Information Criterion (BIC) drops as the model introduces more and more Gaussians. The best model is found for the minimum BIC

where k is the number of fitted parameters, which in our case is $k = 3 \times N$ and n the size of the signal in one spaxel. Adding more Gaussian components to the emission line model can lead to overfitting of the data, where the model becomes too complex and captures the noise. To avoid overfitting, we stop adding more components to the model when the BIC is minimized. The process can be seen in the simulated data in Figure 3.15

After the process of fitting multiple lines sources per spaxel is finished, we merge them together into single clumps by starting from the brightest source and following the dropping flux to their neighbors. This methodology is similar to the astronomical dendrogram algorithm which we have also tested through the `astrodendro` package in Python (McDonald et al. 2013).

The reason we have introduced our new methodology rather than directly using the, similar, estimated clumps from `astrodendro` was that we wanted to use physically motivated constraints to the fitting procedure. For example, the dendrogram algorithm can combine fluxes to the same clump ("leaf") with a final velocity dispersion of $\sim 80 \text{ km s}^{-1}$ or with sizes of a few kpc as long as the data are smooth enough to support it. As our intention is to fit a warped disk assuming typical molecular clump properties, we added constraints supporting our scenario. However, the comparison of the two methods gave similar results.

Likelihood

Using the above method we found $N = 280$ observable molecular clouds with sky projected coordinates $\{(x_n, y_n, V_n)\}_{n=1}^N$. With this way we assume that we can avoid the non-diagonal terms in the covariance of the data. Now the likelihood can be constructed by raising the question, if the tilted model is correct, what is the probability of observing the data (the inferred clouds). Before answering this question we need to understand what the tilted rings model is providing to us. Given the set of parameters, the model returns a set of ellipses (spatial information)

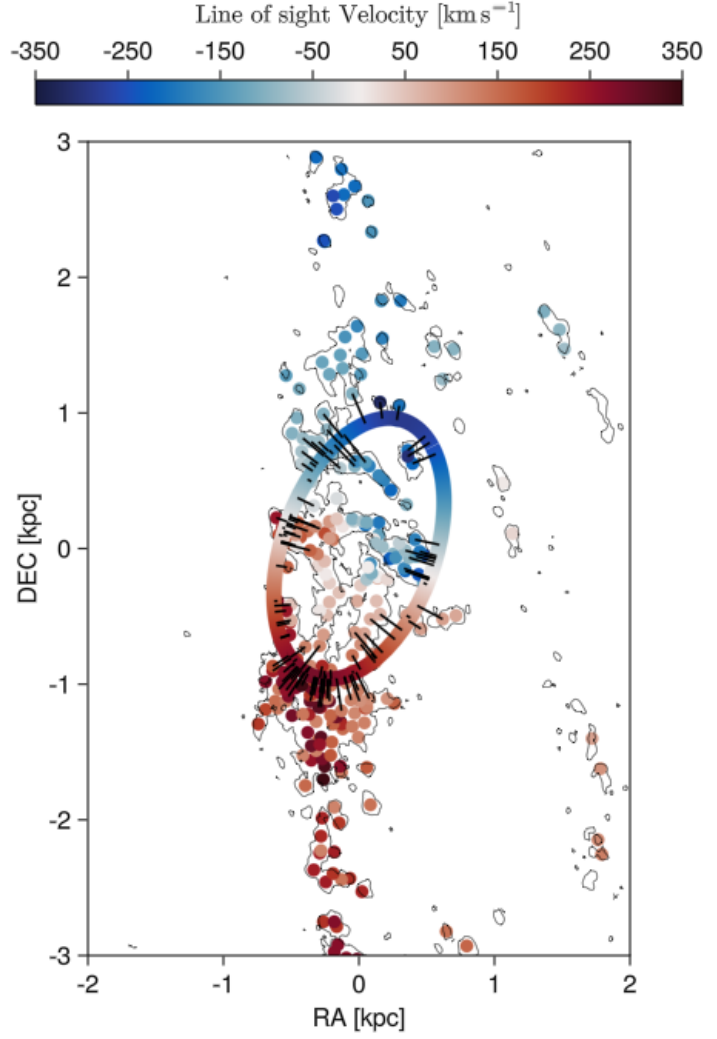


Figure 3.16: The detected clumps and the likelihood algorithm. A single tilted ring is "tested" against the detected clumps (scattered points). If the spatial distance between the ring and the clumps is smaller than a critical (shown as small black lines), then its LOS velocity is compared with the associated clumps velocity. This algorithm is evaluated for all tilted rings. Note that the critical distance here is exaggerated for visualization reasons.

and the corresponding LOS velocity at each position (angle) along these ellipses. The natural way to proceed is to estimate for every ring who are the clouds that are cospatial and then compare the difference in LOS velocities. To do this we have constructed an algorithm which calculates for every cloud the minimum spatial distance (in sky coordinates) from every ring of our geometrical model. If this distance is below a critical limit (i.e. comparable with the beam size), the code calculates the projected velocity difference $\delta V_{nk} = |V_n - V_{\text{los}}(\phi_{\text{closest}}; V_{ck}, i_k, \phi_{0k})|$, with ϕ_{closest} corresponding to the closest spatial position on the projected ellipse of the k ring. The whole process can be depicted in Figure 3.16. When δV is calculated for all the possible neighbouring rings, the code assigns the smallest one to the cloud m so $\delta V_n = \min(\delta V_{nk})$. Assuming a Gaussian likelihood of observing these velocity differences, the likelihood is then:

$$\log \mathcal{P}(\text{clouds}|\bar{\theta}) = -\frac{1}{2} \left(\sum_{n=1}^N \frac{\delta V_n^2}{\sigma_V^2} + N \log(2\pi\sigma_V^2) \right) \quad (3.54)$$

where σ_V is a measure of the dispersion of the clouds' velocity from a perfectly rotating disk.

3.4.4 Sampling the final posterior

The final posterior probability is

$$\mathcal{P}(\bar{\theta}|\text{clouds}) \sim \mathcal{P}(\text{clouds}|\bar{\theta}) \times \mathcal{P}(\bar{\theta}) \times \mathcal{P}(\text{rings}|\bar{\theta}) \times \mathcal{P}(\text{HI disk}|\bar{\theta}) \quad (3.55)$$

where the latter two terms are defined for the first time. In general,

- ▶ $\log \mathcal{P}(\text{clouds}|\bar{\theta})$ is the likelihood of the ALMA inferred clouds (3.54)
- ▶ $\mathcal{P}(\text{clouds}|\bar{\theta})$ is the prior joint distribution of the parameters (i.e. the stellar distribution and mass from Maccagni et al. 2016b, $a \sim \pi/2$ for the viscous force in models A and B etc).
- ▶ $\mathcal{P}(\text{rings}|\bar{\theta})$ is a likelihood distribution which compares the geometry of specific rings with the geometry obtained from different methods (i.e. from the dust distribution, or the HI disk).
- ▶ $\mathcal{P}(\text{HI disk}|\bar{\theta})$ is similarly a likelihood distribution that compares the rotation velocity with the HI rotational velocity data points from Veron-Cetty et al. 1995 and Maccagni et al. 2014. We selected the HI data points only for the outer part of the galaxy to avoid any influence of the warp. This provides us with better accuracy on the dark-matter component of the model and thus more accurate description of the overall velocity curve.

In the next sections, we provide the best results after sampling the expression 3.55 with the MCMC sampler we discussed in Section 3.4.1.

3.5 Results

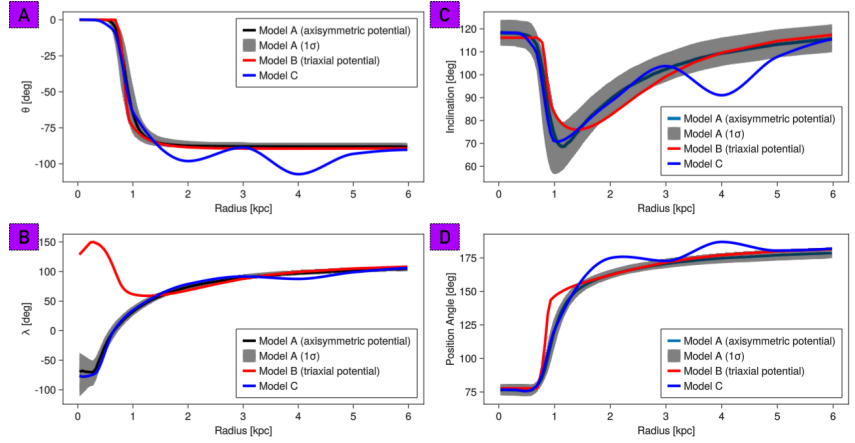
3.5.1 Parameters

In this section we report our results on fitting all data with our three model setups, **A**, **B** and **C**. The first two describe the time-dependent evolution of a set of tilted rings within a triaxial or axisymmetric bulge potential accordingly. Model C uses a generic interpolation scheme that is initiated from the results of A and B allowing more flexibility and possible deviations from these. The best set of parameters for each model have been estimated using the maximum a posteriori (MAP) of the inferred parameter distributions and presented in table 3.1.

Parameter	Model A	Model B	Model C
M_*	$1.7 \times 10^{11} M_\odot$	$1.6 \times 10^{11} M_\odot$	$2.1 \times 10^{11} M_\odot$
M_{vir}	$3.4 \times 10^{12} M_\odot$	$5.4 \times 10^{12} M_\odot$	$2.5 \times 10^{12} M_\odot$
r_a	2.26 kpc	2.7 kpc	2.1 kpc
r_b	2.26 kpc	2.26 kpc	-
r_c	2.54 kpc	2.4 kpc	-
θ_0	-87.8°	-89°	-
λ_0	112°	114°	-
α	60.6°	54.9°	-
c_{vir}	7.4	7.4	7.4
τ	120 Myrs	380 Myrs	-
i_{Bulge}	61.7°	63.8°	62°
PA_{Bulge}	257°	258°	257°

Table 3.1: Resulting parameters for the model A and B and C. M_* is the bulge stellar mass, r_a , r_b , r_c are the three axes scales and i_{Bulge} , PA_{Bulge} the orientation of the axis c relative to observer. M_{vir} is the virial mass and c_{vir} the concentration parameter for the dark matter. θ_0 and λ_0 are the starting values of the disk orientation. α is the dissipation settling angle and τ the time after the initial values.

Figure 3.17: Modeling results: main geometrical parameters as function of radius. The gray band represents the 1σ confidence level of the parameters posterior distribution regarding the axisymmetric model. **A:** azimuthal angle of the disk in the galaxy coordinates, **B:** line of nodes in the galaxy coordinates, **C:** Inclination, **D:** Position Angle.



Panels A and B of Figure 3.17 show the resulting geometry in the galactic plane, characterized by the angles $\theta(t, r)$ and $\lambda(t, r)$, as defined in the previous section. Panels C and D of the same figure display the inclination and position angle of the rings as observed in the plane of the sky.

Given the resulting 3D structure, we can observe the molecular gas from an alternative viewpoint (Figure 3.18), where we see a spiral-like structure as the gas moves towards the central disk. In Figure 3.20 we present the rotational velocity and its components. The best-fitting geometrical parameters reveal that the disk has settled into a stable configuration within the central 600 pc (the inner disk) after 100 – 400 Myrs from its initial configuration. Most of the emission observed in the inner disk is a result of the projection of multiple positions of the disk, with the primary contribution coming from the inner disk itself and a smaller contribution from the rapidly warping outer regions. This explains the observed velocity dispersion and the small asymmetry of the emission along the inner disk’s major axis. The orientation of the disk rapidly changes over the next ~ 1 kpc, with similar changes in the azimuthal angle reproduced by both the axisymmetric and the triaxial models due to the dominant diffusion term. However, the change in the longitude of the ascending node (λ) shows a different behavior in the two models, with the disk in the triaxial model shifting inward of 1.5 kpc to align

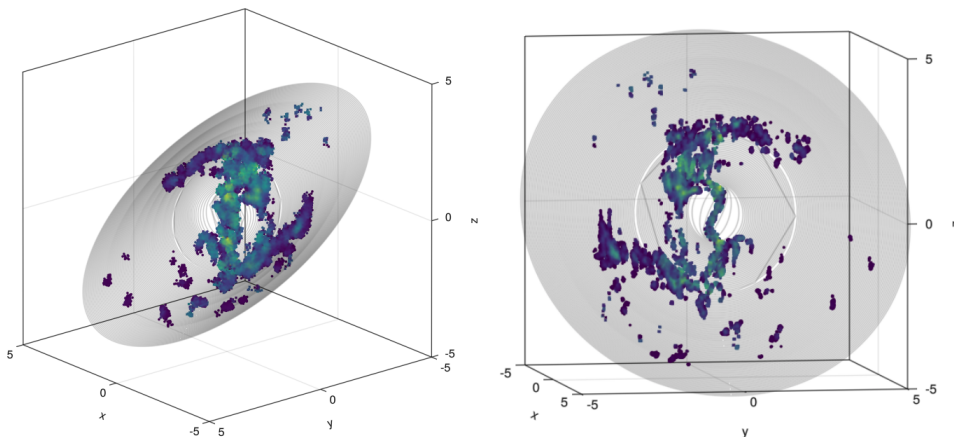


Figure 3.18: 3D distribution of the CO(2 – 1) and CO(3 – 2) cloudlets and tilted ring of the model A at two random observable orientations. X and Y axes represent the ra, dec sky coordinates and Z the line of sight. The color represents the integrated flux of each cloud. The units of the axes are in kpc.

with a secondary preferred axis. This results in slight differences in the observed inclination and position angle curves, which can be seen in the 3D data plane by projecting the results onto several positional velocity slits (as shown in Figure 3.19).

3.5.2 Residuals as non-rotating gas components

In all three models, exist molecular gas regions that cannot be fitted by circular orbits (deviating by a fiducial velocity of 50 km s^{-1} or more from each best-fitting model) and are thus considered kinematic outliers. Specifically, models A and B fit 80% of all molecular clouds, while model C fits 94% of them. The residuals correspond to clouds of interest for inflows/outflows, and they are clustered in the four areas (R1, R2, R3, R4) shown in Figure 3.19.

Two of these regions are located in the central disk region: a set of CO(3 – 2) clumps (referred to as **R1**) in the very center ($\leq 120 \text{ pc}$) and a CO(2 – 1) clump located at a projected distance of $R \approx 200 \text{ pc}$ in the NW (PA = -50° to -60°) referred to as **R2**. Both of these regions exhibit

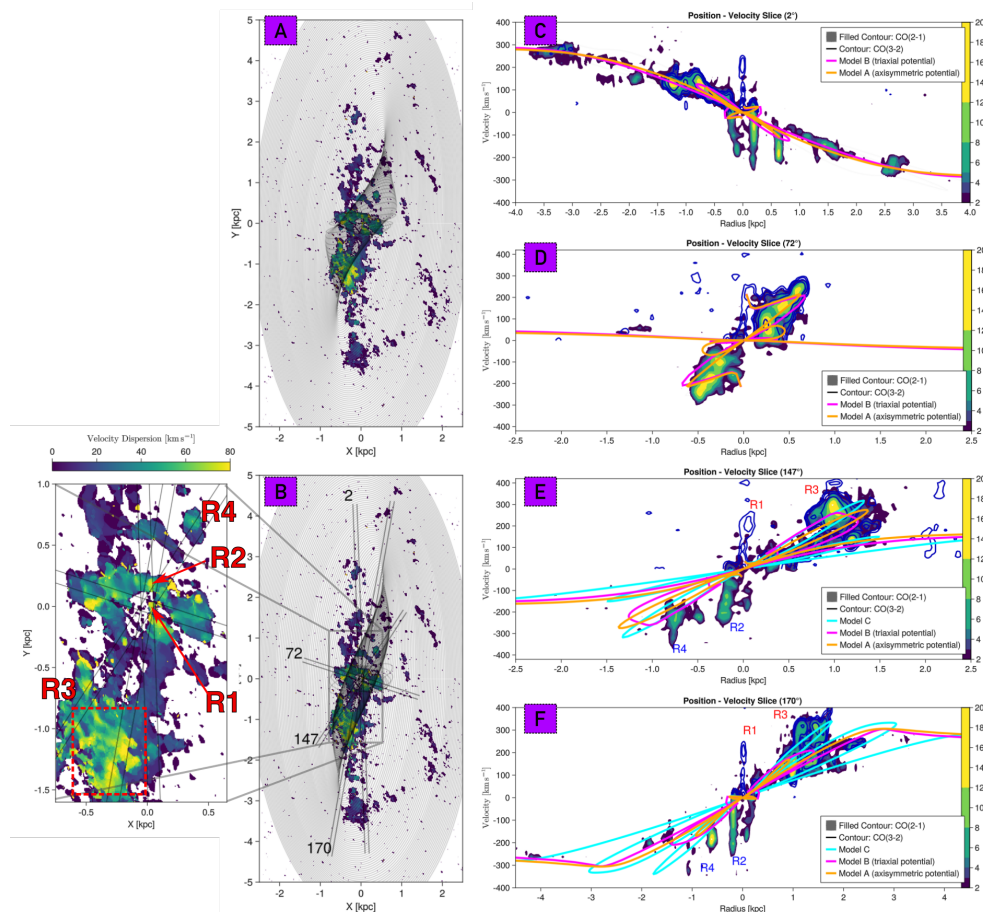


Figure 3.19: Position velocity slices of CO(2-1) and CO(3-2) emission cubes. Panels A and B: Sky projected tilted rings for the axisymmetric potential model (A) and triaxial potential model (B) embedded on top of the CO(2-1) dispersion map. Panels C and D: Slices at angles of 2° and 72° , covering most of the gas emission and the major axes of the inner disk, respectively. Superimposed on these slices are the velocity projections of models A and B. Model C is omitted to avoid clutter, as its projected velocities are similar to those of the other models. The colormap represents the signal-to-noise ratio. Panels E and F: Position velocity slices along the PA of 147° and 170° where we observe the maximum gas dispersion. Embedded in these slits are also the velocity projections of models A and B and C.

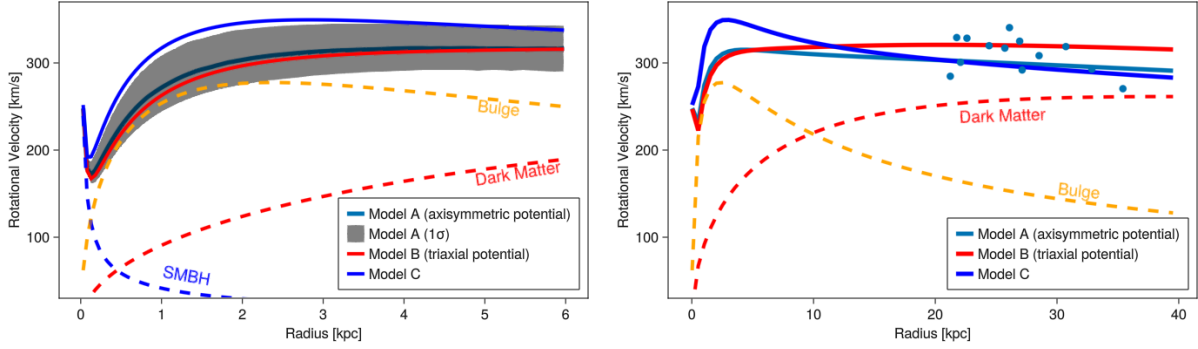


Figure 3.20: Rotational Velocity. The black line represents the best solution of the axisymmetric model, red the triaxial, and blue the generic interpolating model. The gray band represents the 1σ confidence level of the posterior distribution of the parameters with respect to the axisymmetric model.

deviations of more than 100 km s^{-1} from the circular velocity model (panel C in Figure 3.21).

Examining Model Sensitivity

To investigate the sensitivity of these results to our models we conducted a model-independent study assuming only circular motions and boundaries in the total rotation curve. The question we want to answer is if the regions R1 and R2 could be located in larger radii (i.e. in kpc scales), with different intrinsic kinematical and geometrical properties but are projected in the central region giving the observed deviations from the local disk emission.

We start with R2, the region that exhibits the highest deviation ($dV \sim -150 \text{ km s}^{-1}$), to investigate whether it could be located at kpc scales. Its maximum projected velocity can be estimated using the equation $V_{\text{los}} = V(r) \frac{\sin i \sin \delta\phi}{\sqrt{1 + \tan^2 i \cos^2 \delta\phi}}$, where $\delta\phi = \phi - \text{PA}$ is the angular distance between the position angle of the orbit and the position of the cloud, and $V(r)$ is the intrinsic rotational velocity. By combining this equation with $R(\phi)$, the sky-projected distance of the orbit with radius r , we can compute the maximum projected velocity as:

$$V_{\text{los}}^{\text{max}}(R; r, i) = V(r) \frac{R}{r} \cos i \sqrt{\tan^2 i - \left(\frac{r}{R}\right)^2 - 1} \quad (3.56)$$

For an intrinsic rotational velocity of 350 km s^{-1} at $r = 650 \text{ pc}$, the maximum projected velocity would be $\sim 100 \text{ km s}^{-1}$ (panel A in Figure 3.21). For larger distances, this value would decrease, indicating that there is no possible circular orbit projection that can explain the observed deviation. Therefore, R2 must be located in the inner disk. Furthermore, its projected velocity ($200 - 250 \text{ km s}^{-1}$) is close to the maximum value that the potential can support (and higher than our best-fitting value). This implies that R2 must be close to the position angle of a nearly edge-on orbit, which contradicts the evidence that the rest of the gas at similar radii is moving in the reverse direction and with a different orientation ($\text{PA} = 72^\circ$). Therefore, if R2 is not counter-rotating, it must be in an outflow (or an inflow).

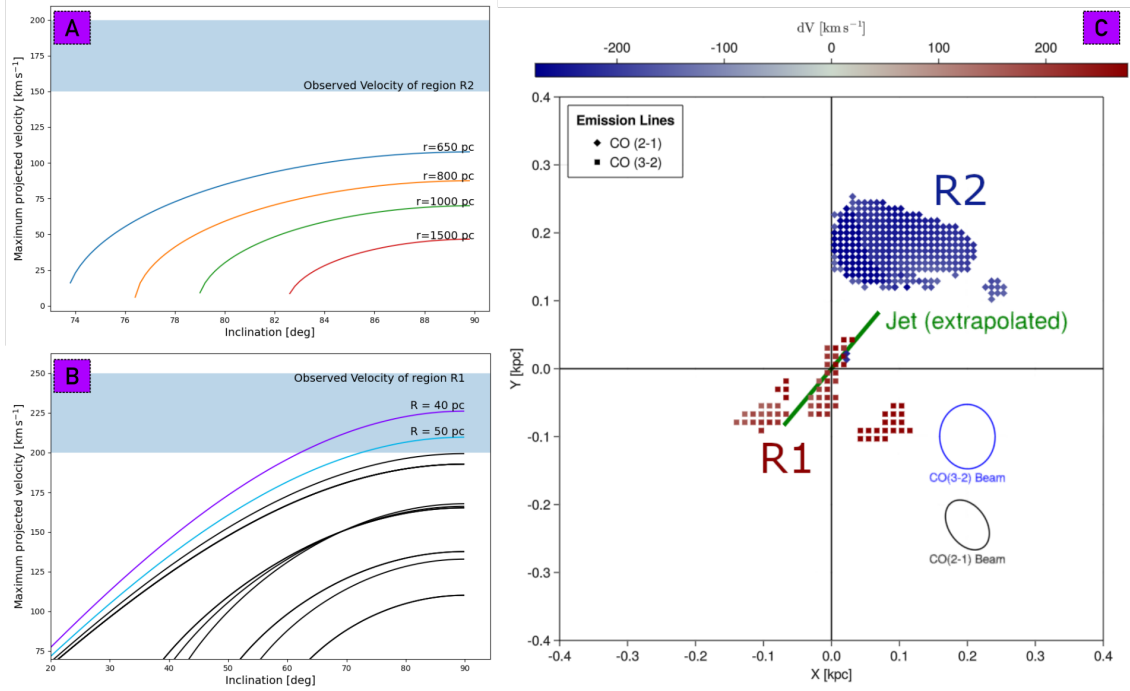


Figure 3.21: Residuals in the central disk region. **A:** Maximum projected velocity based of a clump located at a projected radius $R = 200$ pc for different possible orbit radii and inclinations. The blue band represents the observed projected velocity of the CO(2 – 1) emission lines. **B:** Maximum projected velocity based of a clump located in the central $R \approx 50$ pc for different possible orbit radii and inclinations. The blue band represents the observed projected velocity of the CO(3 – 2) emission lines. **C:** Emission line residuals ($\delta V > 100 \text{ km s}^{-1}$) in the central 500 pc disk area in the sky plane. Circles represent the CO(2 – 1) emission and rectangles CO(3 – 2). The green vector is the extrapolated direction of the jet.

Regarding the high-velocity structure R1, similar conclusions can be drawn. High distances are ruled out by Equation 3.56. On the contrary, very small distances (≤ 120 pc from the center) and beam smearing (with a CO(3 – 2) beam of 95 pc) can potentially raise doubts about its central location. If the gas were regularly rotating and the deviation were induced by a beam smearing effect, then its sky-projected distance from the center must be $R < 50$ pc (panel B of Figure 3.21). However, to its maximum extent, R1 reaches a distance of $R \approx 120$ pc from the center (panel C of Figure 3.21), greater than the major axis of the CO(3 – 2) beam (93 pc). Thus, we can safely conclude that R1 is also a non-rotating clump. In conclusion, the two central components R1 and R2 are unlikely to be attributed to a regularly rotating disk, but instead they are tracing outflowing (or inflowing) gas.

Non rotating components as outflows

Both components exhibit high velocity dispersion, implying that the gas is either in a highly turbulent dynamical state or experiences a large velocity gradient ($> 200 \text{ km s}^{-1}/100 \text{ pc}$) due to acceleration. Previous observations of NGC6328 also indicate the presence of both inflowing and outflowing gas, based on their relative velocity to the source. In front of the radio source, Maccagni et al. (2018) observed a CO(2-1) clump in absorption, redshifted at $\sim 340 \text{ km s}^{-1}$ and with a velocity dispersion of $\sim 60 \text{ km s}^{-1}$. Absorption features have also been detected in HI (Maccagni et al. 2014). One of them is broad, with a width of 65 km s^{-1} , and it is

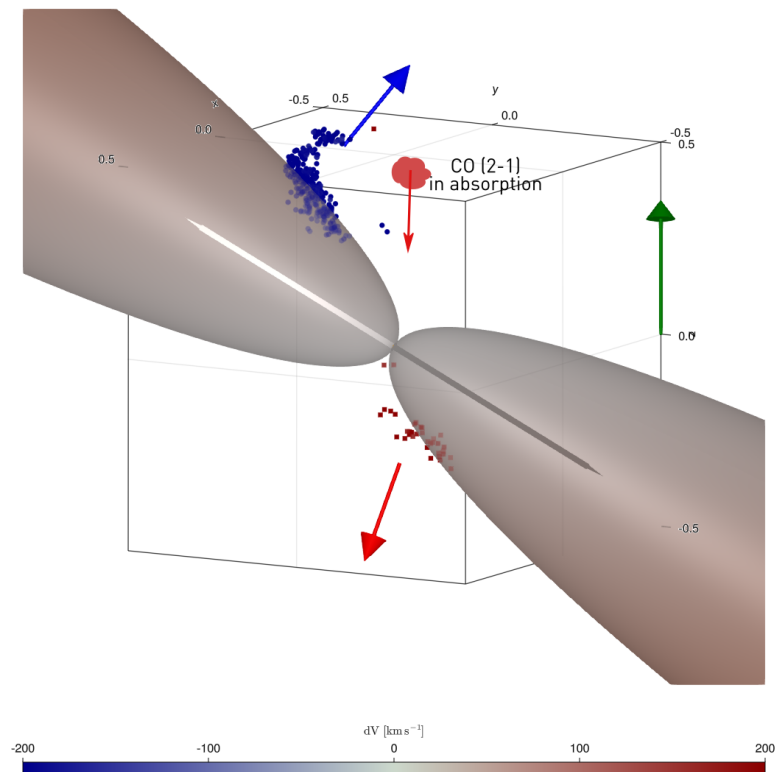


Figure 3.22: Emission line residuals ($dV > 100 \text{ km s}^{-1}$) in the central 500 pc disk from another perspective angle. Circles represent the CO(2-1) emission and rectangles CO(3-2). The conical shapes represent a hypothetical jet driven bubble responsible for the molecular gas outflow. The green vector shows the direction of the observer. Blue and red vectors show a possible direction of the observed outflows.

redshifted to a velocity of 26 km s^{-1} . The second one is narrower, with a width of 43 km s^{-1} , and it is blueshifted to a velocity of -74 km s^{-1} .

Based on the gas kinematic model and the observed dust extinction, we can deduce that the northern side of the inner disk corresponds to its near side (between the center of the galaxy and the observer). Hence, the blueshifted clump is outflowing from the disk. Similarly, the redshifted southern component R1, on the far side of the inner disk, is also outflowing. This scenario is depicted in Figure 3.22.

The outflow scenario is also supported by two other arguments. The first is the existence of a broad kinematic component at the same locations in the ionized gas emission, as seen in recent optical, X-shooter data. The

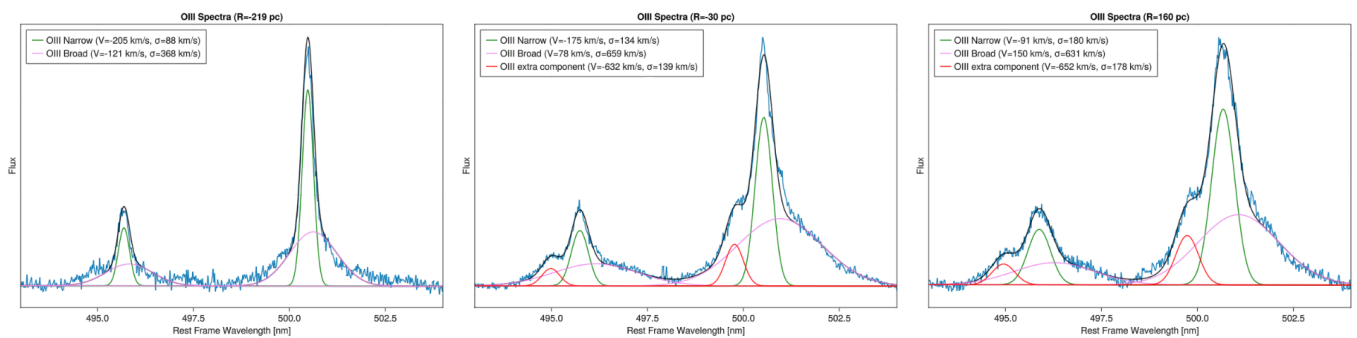


Figure 3.23: [OIII] spectrum centered in 3 different positions along a 240 pc-wide slit (PA 160°). From left to right, -220 pc , -30 pc and 160 pc from the nucleus. For every position, the signal (blue) is averaged over four pixels, corresponding to a physical width of 142 pc along the slit. In each spectrum, we have fitted one narrow and one broad component. At the -30 pc and 160 pc positions, an additional blueshifted ($\approx 600 \text{ km s}^{-1}$) component was required to obtain a good fit.

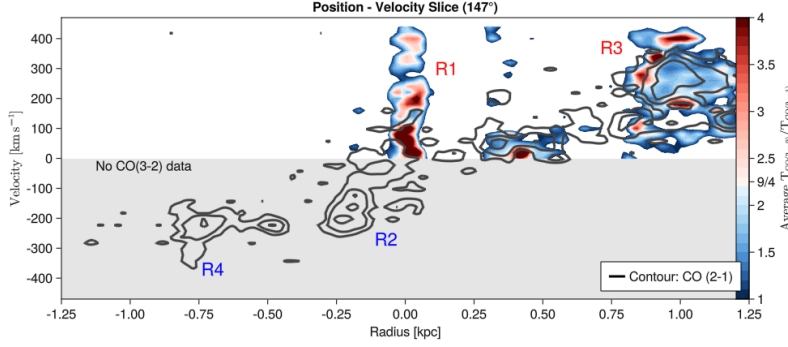


Figure 3.24: Position velocity slice along the PA of 147° . The values represent the average value of $T_{\text{CO}(2-1)}/T_{\text{CO}(3-2)}$ and the contours the CO(2 – 1) intensity.

spectra, extracted from a slit with $\text{PA}=160^\circ$, are shown in Figure 3.23. They illustrate the 5007 Angstrom [OIII] emission at three different positions along this slit: R2, located 219 pc North-East (NE) of the center, the central region at -30 pc, and the SW region at 160 pc. The spectra at each location are summed over four spectral pixels, and cover a width of >100 pc. For all regions, the gas exhibits similar narrow ($\sigma = 80 - 180 \text{ km s}^{-1}$) and broad ($\sigma = 460 - 660 \text{ km s}^{-1}$) emission line components, and in the last two regions, an extra blueshifted high velocity component is seen at $\approx 630 \text{ km s}^{-1}$. All these findings constitute direct evidence of the presence of strong winds in the inner disk of NGC6328.

The second argument favoring the existence of an outflow is the CO excitation. From the ratio of CO(3 – 2) and CO(2 – 1) cubes (both re-imaged to a common resolution), we estimated the excitation of the gas. The cube of the brightness temperature ratio $T_{\text{CO}(3-2)}/T_{\text{CO}(2-1)}$ significantly exceeds the value of an optically thick gas in local thermodynamic equilibrium (LTE):

$$\frac{T_{\text{CO}(3-2)}}{T_{\text{CO}(2-1)}} = \frac{I_{\text{CO}(3-2)}}{I_{\text{CO}(2-1)}} \left(\frac{v_{\text{CO}(2-1)}}{v_{\text{CO}(3-2)}} \right)^2 \stackrel{\text{LTE}}{=} \frac{9}{4} \quad (3.57)$$

We observe significantly higher brightness-temperature ratios in (and close to) R1, while the bulk of the regularly rotating molecular gas is sub-thermally excited (Figure 3.24). The high excitation ratio can be the result of extra density components, of evaporation of the outer cloud layers that makes them optically thin, or of the presence of extra excitation mechanisms (e.g., shocks, cosmic rays) in the outflow. Similar results have been obtained for molecular gas excitation in the nearby galaxies IC 5063 (Dasyra et al. 2016) and NGC3100 (Ruffa et al. 2022), and demonstrated to be induced by an interaction between the radio jets and the surrounding cold gas. These results also suggest that the high velocity clump in R1 corresponds to a co-spatial and also kinematically deviating warm H_2 component (Maccagni et al. 2016b).

Possibility for extended outflows

The other two locations of interest cover part of the high velocity dispersion regions at kpc distances, to the SW (R3) and NE (R4) of the center (as previously mentioned in Section 3.2.2). For these regions, the fraction of fitted clouds shows a significant discrepancy between models A, B (63% fitted) and model C (91% fitted) when introducing a $10^\circ - 20^\circ$ wobble

in the $\theta(r)$ curve (panel A of Figure 3.17). This wobble can be caused by more than one asymmetry of the total potential such as stronger bulge triaxiality, non-spherical dark-matter potential, a disk or a bar. Similar wobbles in the polar angle have been observed at 100 pc scales in M84 (Quillen and Bower 1999), where the authors also suggest the presence of torques caused by the AGN radiation pressure.

However, the lack of strong observable asymmetry signatures (e.g., bars) in optical or near-infrared images raises the possibility that R3 and R4 are also regions of non-circular motions, and - namely, outflows. The scenario of these extended outflows can be supported by the excitation (as seen in figure 3.24) where in R3 some CO-emitting clouds that are more excited than average are also identified. The ionized gas kinematics there does not show a broad emission component but velocities different from those of the disk.

Leaving the outflow scenario as an open option, we proceed to the identification of the driving mechanism of the certainly outflowing gas.

3.6 Relevant discussion

3.6.1 What drives the inner outflows

The energetic and momentum arguments are often used as indicators of the outflow driving mechanism. To estimate the mass outflow rate, kinetic power, and momentum, we considered the starting position, velocity, and geometry of the outflow. This is assumed to emanate from a central region and travel outward, so its geometry can be approximated by a cone or sphere. In this context, the term r_{out} refers to the distance the outflow has traveled from its origin, representing a measure of how far the material has been carried by the outflow. This simplifying assumption may not always hold, but is frequently made in the literature.

The outflow mass rate can then be described by the equation:

$$\dot{M}_{\text{out}} = C \frac{M_{\text{out}} V_{\text{out}}}{r_{\text{out}}} \quad (3.58)$$

where M_{out} and V_{out} represent the mass and velocity of the outflow, respectively, and C is a parameter that depends on the outflow history (Lutz et al. 2020). We use a value of $C = 1$, which assumes that the outflow we are observing now has started at a point in the past and has continued with a constant mass outflow rate until now. Another value used in the literature is $C = 3$, which takes into account that the outflowing gas has a constant average volume density in a cone or a sphere. For the outflow travel distance, we assumed an indicative value of $r_{\text{out}} \simeq 100$ pc, as this is a typical distance if the outflow has originated locally, from a nearby part of the disk (instead of the center of the galaxy). For the outflowing mass, we used a conversion factor of $a_{\text{CO}} = 0.8 M_{\odot} (\text{K kms}^{-1} \text{ pc}^2)^{-1}$. This value is lower than that typically adopted, as we made the assumption that both R1 and R2 have optically thin parts due to interaction with the AGN or jet (Cicone et al. 2014; Dasyra et al. 2016; Ruffa et al. 2022).

To calculate the outflow velocity, V_{out} , we used the velocity deviating from the best-fitting model. However, this value needs to be corrected for the outflow angle. We tried two different approaches in estimating V_{out} , first by using the estimation of $V_{\text{out}} = |\Delta v| + 0.12\sigma_V$ proposed by Lutz et al. 2020, where σ_V is the velocity dispersion of each cloudlet (emission line per pixel) in the outflow. Then, we used a projection angle based on a uniform distribution from -30 to 30° from the disk and adopted the mean value. This represents all the possible angles in a cone centered to the disk itself with a maximum opening towards the observer. Both methods provided similar results, which are presented in Table 3.2 and compared to molecular outflows detected in the literature in Figure 4.4. In case the outflow originated from the center of the galaxy and had a constant average volume density (i.e. $C = 3$), these results would only be a factor of two higher.

Region	Mass	\dot{M}_{out}	Kinetic Power	Momentum Rate
	$10^6 M_\odot$	$M_\odot \text{yr}^{-1}$	$10^{40} \text{erg s}^{-1}$	10^{33}dyn
R1	0.12	0.2	0.3	0.23
R2	1.9	2.9	2.4	2.8
Total	2.02	3.1	2.7	3

Table 3.2: Molecular Outflow Properties

We are able to estimate the likelihood of the observed outflow being driven by energy injection from local star formation (supernovae) or from the AGN. Based on the formula presented in Sullivan et al. 2006, the rate of Type Ia supernovae is given by $\Gamma = 5.3 \times 10^{-3} \frac{M}{10^{11} M_\odot} + 3.9 \times 10^{-4} \frac{\text{SFR}}{M_\odot \text{yr}^{-1}} \text{SN yr}^{-1}$. This leads to an estimated power output of:

$$\frac{\dot{E}_{\text{SN}}}{\text{ergs}^{-1}} = 1.68 \times 10^{41} \frac{M}{10^{11} M_\odot} + 1.24 \times 10^{40} \frac{\text{SFR}}{M_\odot \text{yr}^{-1}} \quad (3.59)$$

Our estimate of the total stellar mass within a radius of 200 pc, as derived from our modeling, is $10^9 M_\odot$ (or 0.6% of the total stellar mass). Using this value and assuming that the star formation rate (estimated to be $1 - 2 M_\odot \text{yr}^{-1}$, according to (Willett et al. 2010)) is proportional to the stellar mass distribution, we estimate the supernovae (SN) kinetic power to be $1.8 \times 10^{39} \text{erg s}^{-1}$. This is an order of magnitude below the lower limit of the outflow total kinetic power. This suggests that the power from supernovae alone is not the main driver of the outflow.

On the other hand, for the low-luminosity AGN ($L_{\text{AGN}}/c \approx 4.3 \times 10^{31} \text{dyn}$) the kinetic energy ratio of $\dot{E}_{\text{out}}/L_{\text{AGN}} \sim 0.02$ is consistent with a scenario of a wind driven by the AGN radiation pressure. However, the momentum rate ratio of $\dot{p}_{\text{out}}/L_{\text{AGN}}/c \sim 60$ is large even for an intermittent AGN episode scenario, as noted in Zubovas and Nardini 2020.

The power of the radio jet in NGC6328 has been estimated to be $2 \times 10^{42} \text{erg s}^{-1}$ through Spectral Energy Distribution (SED) fitting (Sobolewska et al. 2022). However, the use of the calorimetric scaling relation involving the $L_{1.4\text{GHz}}$ luminosity from Willott et al. 1999, Bîrzan et al. 2008 and Cavagnolo et al. 2010 yield a similar value of $2 - 3 \times 10^{43} \text{erg s}^{-1}$, which is an order of magnitude higher than the estimate obtained from SED fitting. According to Wójtowicz et al. 2020, the minimum jet power is estimated to be $2.7 \times 10^{42} \text{erg s}^{-1}$ under the assumption of energy equipartition between the magnetic field and radio-emitting electrons within the lobes.

Even with this minimum estimate, it is still clear that the jet has more than enough energy to drive the outflow and play a significant role in boosting or supporting the AGN's overall impact on its surroundings. Numerical hydrodynamic simulations by Mukherjee et al. 2016 have shown that low-powered jets can have a greater impact on the interstellar medium (ISM) due to their prolonged interaction and difficulty in escaping into intergalactic space.

3.6.2 Why we cannot see the jet?

The fact that the outflow observed in NGC6328 is further away from the nucleus than the currently detected radio emission is consistent with other sources where molecular winds trace previously undetected radio jets, as seen in cases such as NGC1377 (Aalto et al. 2016), 4C31.04 (Zovaro et al. 2019), ESO420-G13 (Fernández-Ontiveros et al. 2020) and HE 00401105 (Singha et al. 2023).

One potential explanation for the lack of radio emission in NGC6328 could be due to recurrent jet-launching powered by stochastic feeding which can vary on timescales from years to million years (Schawinski et al. 2015; Gilli et al. 2000). In this scenario, the energy from previous jets may have been deposited onto large bubbles of kpc scales a long time ago, leading to the cooling of cosmic rays in these bubbles and thus to the lack of detected radio emission. Similar evidences have been observed also in samples of molecular gas outflows in local galaxies (Fluetsch et al. 2019; Lutz et al. 2020)

Using our inferred properties we estimate that the outflow has originated $t_{\text{out}} = 200 - 700$ kyrs ago (depending on the possible values of r_{out}). The magnetic field at pc scales is estimated to be $B \approx 10^{-2}$ G (Tingay et al. 1997), and the synchrotron cooling time at 0.1 kpc scales is computed to be $t_{\text{cool,syn}} \approx 150$ kyrs. This cooling time could be significantly reduced if Inverse Compton (IC) cooling is taken into account or if the magnetic field during the previous cycle of the jet was significantly higher. By comparing these two timescales, it can be argued that a highly-magnetized relic of a turned-off jet can fade away within an AGN duty cycle due to synchrotron cooling, shock-induced cooling, and adiabatic losses. Such a jet would have been capable of providing mechanical and radiative feedback to the intergalactic medium up to kpc scales. In the case of a mass-loaded jet, where hadronic radiative processes are important (Reynoso et al. 2011; Rieger 2017), cavities will be observed in cold molecular gas due to photo-dissociation by X-ray and gamma-ray photon fields emanating from the jets (Maloney et al. 1996; Wolfire et al. 2022).

Another scenario that could explain the lack of radio emission in NGC6328 is the relativistic de-boosting. This occurs when the radio emission from the jet is directed away from the observer, reducing its apparent luminosity and making it more challenging to detect. To assess the impact of relativistic de-boosting, we used radio imaging and the velocity of the radio blobs, as determined through VLBI (estimated to $\beta_{\text{app}} = 0.13 \pm 0.06$ from (Angioni et al. 2019)), to calculate the jet/counter-jet flux density ratio, which we estimated to be $R = 1.4 \pm 0.1$ at 8.4 GHz. By solving the set of equations for the intrinsic β and jet inclination θ_{jet}

$$\beta_{\text{app}} = \frac{\beta \sin \theta}{1 - \beta \cos \theta} \quad R = \left(\frac{1 + \beta \cos \theta}{1 - \beta \cos \theta} \right)^{p-\alpha} \quad (3.60)$$

where $\alpha = -1.5$ is the spectral index and p is a parameter that takes the values 2 or 3 depending on whether R is calculated from an integrated flux across a continuous jet or a single component (Angioni et al. 2019). Assuming $p = 3$ for a single moving component that dominates the 8.4 GHz core radio flux we estimated $\beta = 0.14 \pm 0.05$ and $\theta_{\text{jet}} = 68^\circ \pm 17^\circ$. These results are robust to variations in the p parameter; using $p = 2$ yields similar values within the error margins, with θ having a central value of 62° . Based on these parameters, the Lorentz factor Γ is approximately 1.02, and the corresponding relativistic boost factor $\delta \sim 1.02$. Given the modest value of δ , it is unlikely that relativistic de-boosting is responsible for obscuring the jet from detection.

However, jet acceleration and collimation in AGN have been observed to occur over distances of $10^4 - 10^6 R_s$ (Blandford et al. 2019; Kovalev et al. 2020; Okino et al. 2022; Baczko et al. 2022; Roychowdhury et al. 2023) which corresponds to $0.3 - 40$ pc for a black hole with a mass of $4 \times 10^8 M_\odot$. This length scale is similar to the size of the radio structure (~ 2 pc) observed by VLBI in the present case. Assuming an inclination angle of $\approx 65^\circ$ suggests that under sufficient acceleration ($\Gamma > 5$ a typical value for relativistic jets) the jet could reach a de-boosting factor of $\delta^4 \gtrsim 0.01$, making it too faint to be detected by radio telescopes. Additionally, the decrease in magnetic field strength (roughly r^{-1} for a collimated jet; (Vlahakis and Königl 2004; Fendt 2006; Porth et al. 2011)) could further reduce the radio luminosity and explain the lack of radio flux beyond 100 kpc. At the same time, efficient inverse-Compton cooling due to an abundance of ambient photons could explain the extended X-ray (Beuchert et al. 2018) and gamma-ray (Migliori et al. 2016) components observed in the source spectrum, and explain the suppression of any extended radio emission by insufficient synchrotron cooling. The presence of a hidden, extended jet would offer greater kinetic power than the current estimations through SED fitting ($\approx 10^{43}$ erg s $^{-1}$), and could transfer energy over kpc scales, possibly contributing to the observed excited warm H $_2$ (Maccagni et al. 2016b) and extended soft X-ray component (Beuchert et al. 2018).

3.6.3 Comparison of the gas distribution with simulations and other observations

Our models indicate that the majority of the observed warped gas distribution in NGC6328 evolved from an initial uniform disk configuration over a timescale of $100 - 400$ Myrs (section 3.5.1), suggesting a merger episode. This behavior aligns with findings from van de Voort et al. (2015), who examined gas accretion processes in an early-type galaxy within the FIRE cosmic simulation (Hopkins et al. 2014). In their study, the authors focused on a merger event involving the (simulated) galaxy m13 and a gas-rich galaxy, monitoring the subsequent developments. The selected galaxy in their simulation shares similar characteristics with NGC6328 ($M_* \approx 10^{11} M_\odot$, $M_{\text{vir}} \approx 10^{13} M_\odot$). Following an initial

major merger event, the gas becomes misaligned with the bulge's stellar distribution, initiating a late accretion process. The torques exerted by the stellar component (whose distribution is slightly affected) and the internal torques from dissipative forces cause the gas to undergo differential warping and eventually settle into one of the most stable configurations, either co-rotating or counter-rotating with the stars, as it reduces its angular momentum.

Apart from simulated galaxies, this process has also been observed in real galaxies such as NGC5077 (Raimundo 2021) and NGC3100 (Ruffa et al. 2022; Maccagni et al. 2023), where misaligned cold gas feeds the SMBH and triggers similar outflows.

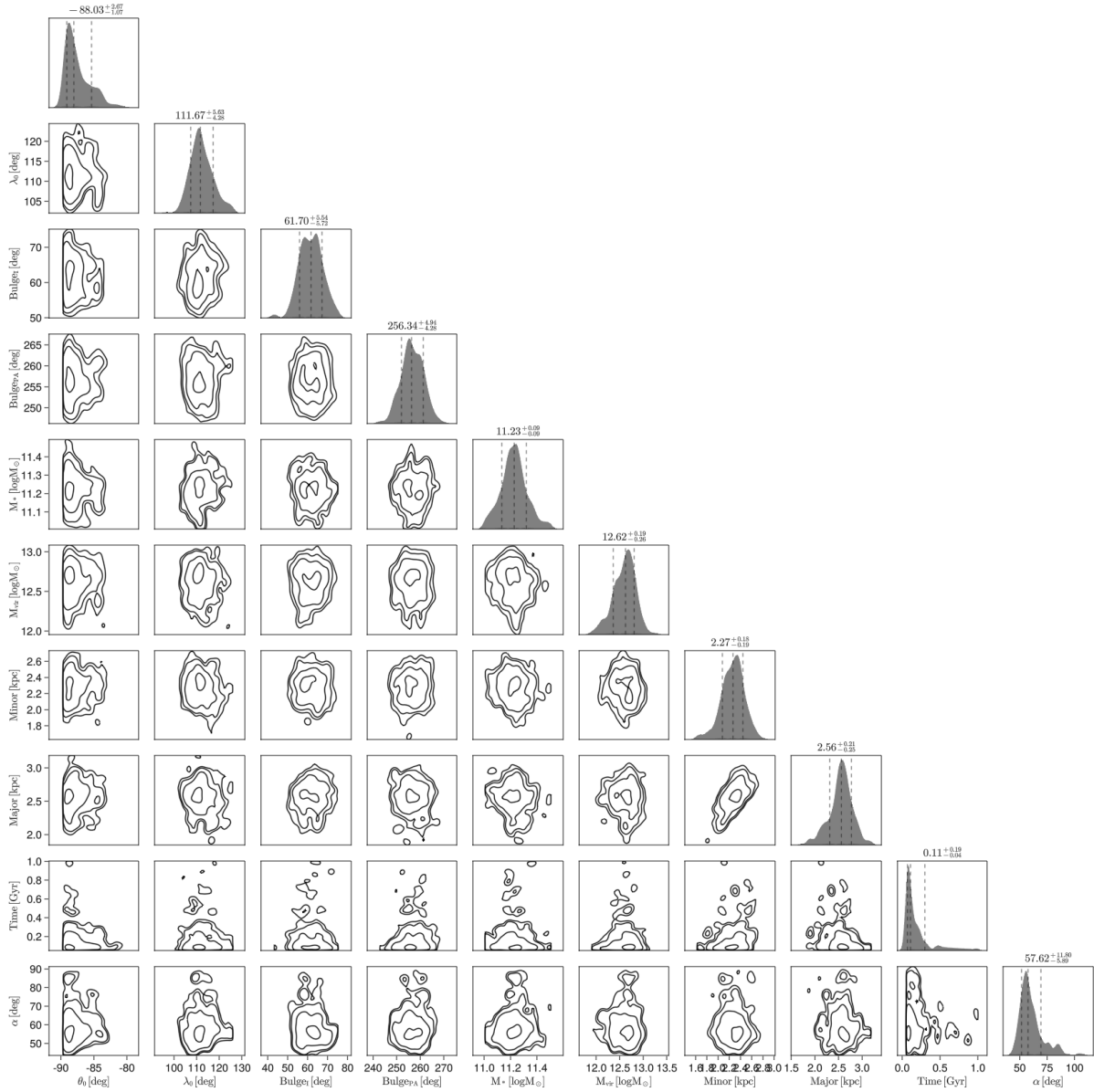


Figure 3.25: Corner plot of the parameters for the axisymmetric potential model.

Extended discussion: The jet-outflow connection in nearby galaxies with massive outflows of cold molecular gas

4

Note on Authorship: The majority of the work conducted in this chapter was conducted by Athanasia Gkogkou and the PI, Kaliopi Dasyra, and it was part of her master thesis. My contribution, along with the rest of our research team, was in data mining, qualification, and interpretation of the results. This work has been published in Papachristou et al. (2023)

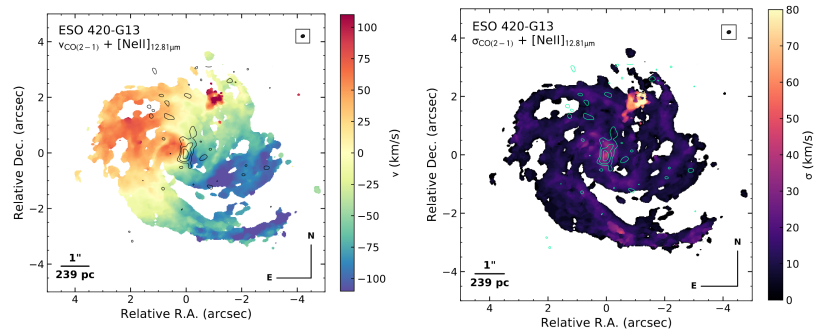
Motivated by the possibility of a jet-ISM interaction in NGC6328, we evaluated whether the role of jets as drivers of gas outflows could be underestimated in previous studies. In the literature, the main indication of a jet presence is the observed radio flux. However, not only jets can produce radio emission. Star formation in galaxies generates a spectrum of electromagnetic emissions, including radio. The crux of this radio emission lies in the activities of young stellar populations and their subsequent interactions with the ISM. During a starburst episode, a cascade of supernovae (SNR) is triggered. The remnants of these SNRs serve as potent accelerators for cosmic rays (CRs), hurling them at high velocities into the surrounding ISM. These high-speed CRs, composed of protons and electrons, interact with the ISM particles, generating γ -rays. However, a significant part of the story unfolds in the magnetic fields that pervading the galactic environment. The CR electrons gyrating in these magnetic fields emit synchrotron radiation that is predominantly detectable at radio frequencies. Thus the radio emission from star-forming galaxies (SFGs) will be correlated with far-infrared luminosity. This correlation has been confirmed with measurements at 1.4 GHz ($L_{1.4\text{GHz}}$ and far-infrared (FIR) (Helou et al. 1985; Kornecki et al. 2022). This implies a selection criterion that is encapsulated in the parameter q_{ir} (Ivison et al. 2010), defined as the logarithmic ratio of the observed far-infrared flux to the 1.4 GHz radio flux. q_{ir} falling below a critical value (indicating radio excess) has been interpreted as a criterion of radio loudness (Ivison et al. 2010). In a recent compilation of 45 local galaxies with massive molecular outflows, most galaxies were not associated with a radio jet based on this criterion, and consequently jets were considered a rare outflow-launching mechanism (Fluetsch et al. 2019).

However, the discovery of galaxies with jet-shaped outflows but without (strong) associated radio emission (Zovaro et al. 2019; Fernández-Ontiveros et al. 2020 and NGC6328 in this work) demonstrated that radio excess is an unsafe criterion. Outflows can be induced by low-power or faded away jets or the radio emission could be de-boosted due to jet geometry. We thus re-evaluated the jet-outflow connection in these sources primarily by spatial distribution criteria, and secondarily by energetic criteria.

To evaluate the fraction of galaxies that our results concern, we gathered literature-based evidence for links between jets and local galactic outflows. For this purpose, we used a recent compilation of local galaxies with molecular outflows (Fluetsch et al. 2019), which we expanded with four more galaxies with a molecular outflow detection (NGC6328, NGC1377, NGC3100 ESO420-613). Instead of the radio excess as a criterion for the examination of the jet-outflow connection, we used the following classification scheme for the AGN in the sample

- ▶ sources with a jet that accelerates molecular gas along its trajectory
- ▶ sources with a jet that accelerates atomic gas along its trajectory, which can then entrain molecular gas in a multi-phase wind model (Zubovas and King 2012)
- ▶ sources with a jet that could be related to the gas acceleration, as it spatially coincides or extends in a similar direction with the outflow.

Figure 4.1: ESO420-613 molecular gas velocity and velocity dispersion. The outflow is located in the north and west at 340 pc from the center. From Fernández-Ontiveros et al. 2020



The first group of sources comprises IC5063, M51 and NGC1068, NGC1377, ESO420-613 and NGC6328. In these galaxies, **the jet is associated with part of the molecular gas acceleration**, with accelerated blobs and outflow starting points associated with the jet path. IC5063, with at least 4 outflow starting points in addition to the nucleus, is the prototype of this category (Dasyra et al. 2015). In the Seyfert 2 galaxy M51, outflowing molecular blobs are detected near the radio jet outline and the gas excitation changes as a function of the distance from the jet (Querejeta et al. 2016; Matsushita et al. 2015). In NGC1068, molecular gas is being entrained in known regions of jet-cloud interaction along the spatially resolved radio jet. This jet-launched outflow adds to the mass of a wind launched by the AGN accretion disk (García-Burillo et al. 2019). The radio-quiet galaxy NGC1377 hosts a molecular outflow that is spatially-resolved and jet-shaped, with a width of only $\sim 5 - 20$ pc along a length of 150 pc. The outflow revealed the existence of a radio jet, which remained elusive in radio images (Aalto et al. 2020). In the Seyfert 2 galaxy ESO420-613, ALMA CO data of 30 pc resolution revealed the existence of a massive outflow far from the nucleus and along the minor axis with a jet-trailing shape: filamentary emission precedes bifurcated emission at a presumed jet-ISM impact point (Fernández-Ontiveros et al. 2020), as in IC5063. Weak radio emission encompasses the outflow location, but its intrinsic shape is unknown, as the resolution of the data is considerably lower than that of ALMA.

In the second group, **the jet is proven to accelerate atomic gas**, with wind starting points along its path. A molecular outflow also exists in these sources, but its connection with the jet remains to be proven. Still, in the current view of multiphase outflows, the passage of an ionized wind by molecular clouds initiates a molecular outflow as ram pressure and hydrodynamic instabilities peel off the outer cloud layers. Thus, any wind is likely to have both atomic and molecular content. A prototype for this category is Mrk1014, in which an ionized oxygen wind, seen in [OIII], exists at a radio hot spot ~ 3 kpc away from the nucleus (Fu and Stockton 2009). An OH outflow, unresolved on these scales, also exists in the nucleus (Veilleux et al. 2013). In 4c12.50, atomic hydrogen is seen in absorption in front of the radio-jet tip (Morganti et al. 2004).

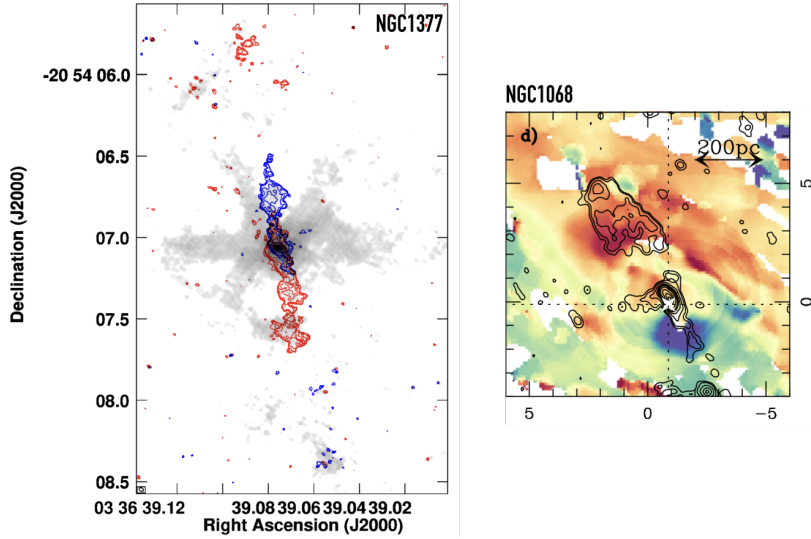


Figure 4.2: **Left:** Collimated molecular gas outflows (colored contours) in NGC1377 (Aalto et al. 2020). In grayscale the total CO(3-2) intensity. **Right:** Kinematic residuals in NGC1068 probing outflows. In black contours the radio emission tracing the jet. From García-Burillo et al. 2019.

A high-velocity nuclear CO outflow, again unresolved on the radio-jet scales, is also detected (Fotopoulou et al. 2019). In NGC1266, high-velocity $H\alpha$ is seen inside and near the spatially resolved jet, probed by its 1.4 and 5GHz emission (Davis et al. 2012). A nuclear molecular outflow, offset in positive and negative velocities along a similar orientation, was detected in CO Alatalo et al. 2011. In NGC5643, an ionized outflow delineates the jet axis (Cresci et al. 2015), while a potential CO detection (Alonso-Herrero et al. 2018) is here treated as an upper limit.

The third group comprises sources in which the **jet could be related to the outflow** because it spatially coincides or extends in the same direction with the outflow. In NGC613, which is a spiral galaxy with a resolved radio jet and nuclear outflow with an extremely high momentum rate ($\sim 400L_{AGN}/c$), an offset between blue-shifted and red-shifted CO emission is seen in the jet direction (Audibert et al. 2019). In the merging system NGC3256, the southern nucleus shows a disk plus a bipolar jet radio map; an outflow is located at both jet edges (Sakamoto et al. 2014). Other galaxies with molecular outflows in the direction of large- or small-scale jets comprise NGC1433 (Combes et al. 2013), NGC6764 (Leon et al. 2007), Circinus (Zschaechner et al. 2016; Harnett 1987), and Mrk273 (Cicone et al. 2014; González-Alfonso et al. 2017). In PKS1549-79, an [OIII] wind fills a trajectory gap between a massive nuclear CO outflow and the radio jet Oosterloo et al. 2019. In HE1353-1917, a spectacular [OIII] and $H\alpha$ wind, which leaves the galactic disk at the point of a jet-cloud interaction, could have a molecular counterpart, which we treat as an

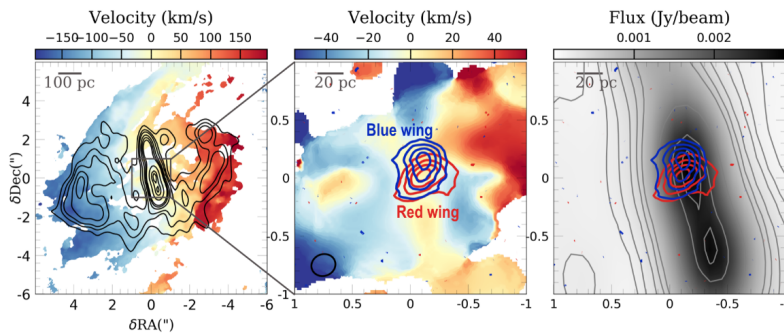


Figure 4.3: Molecular outflows (traced from CO(3-2)) (red and blue contours) in the center of NGC613. The black contours and grayscale image on the right panel represent the radio emission.

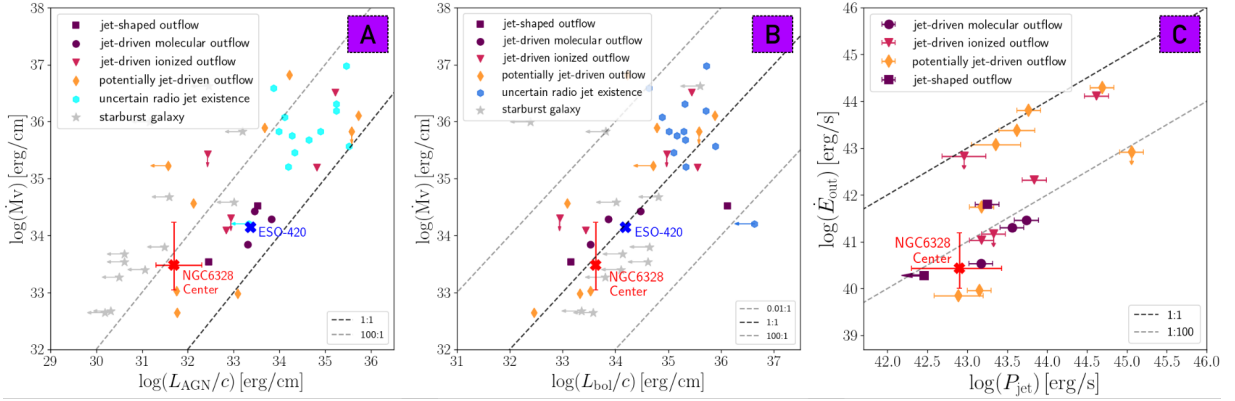


Figure 4.4: Wind vs. driving mechanism energetics for local galaxies with massive molecular wind detections. **A:** Wind momentum rate vs. radiation pressure of AGN photons. **B:** Wind kinetic luminosity vs. jet power. The dashed lines indicate different ratios of the plotted parameters. **C:** Outflow’s momentum rate relation with the total photon momentum output of the galaxy. The dashed lines denote the different values of the ratio of outflow’s momentum rate over bolometric luminosity. The arrows denote upper limit values.

upper limit (Husemann et al. 2019b). In 3C273 the [OIII] kinematics show counter-motions with respect to the disk along the jet trail; a molecular arc perpendicular to the jet trail is associated with the cocoon Husemann et al. 2019a. We again, treat it as an upper limit. Another source that can be included in this third group is NGC3100 (Ruffa et al. 2022), which is a lenticular galaxy with young, resolved radio jets (total linear extent ≈ 2 kpc). Here outflowing, optically-thin molecular gas with very high excitation temperatures (i.e. $T_{\text{ex}} \gg 50$ K) is detected around the jet path, indicating that an ongoing jet-cold gas coupling is altering the physics and kinematics of the involved gas fraction.

In Figure 4.4, we plot the outflow kinetic energy vs. the jet power, as well as the outflow kinetic luminosity vs. the AGN radiation pressure, color coding galaxies based on the classification scheme mentioned above. Outflow and galaxy properties are summarized in Table 4.1. Outflowing masses are consistently computed using an X_{CO} of $4 \times 10^{19} \text{ cm}^{-2} (\text{K km s}^{-1})^{-1}$ in all galaxies but IC5063. We find that, in nearly all low luminosity AGN, there is either a certain or a plausible link between the jet and the outflow. The only exception is NGC4418, for which the presence of a radio jet is unclear (but cannot be ruled out) based on its 5GHz clumpy and elongated morphology (Varenius et al. 2014). Even at high AGN luminosities, certain galaxies have unambiguously jet-driven outflows. In all AGNs (low and high luminosity), momentum boosting would have been required to explain the observed outflow if it had originated from the AGN radiation pressure alone (Cicone et al. 2014). The energy deposition by the jet softens or revokes the need for momentum boosting, which occurs during an adiabatic expansion of a radiatively-driven bubble of an AGN. It also reduces the need for alternative explanations to momentum boosting such as AGN variability. In the variability scenario, the ongoing outflows were driven by radiation during the earlier, more luminous phases of AGN activity (Zubovas and Nardini 2020). Instead, the jet could energetically fully sustain the outflows in these galaxies, as its power exceeds the outflow kinetic energy. To deduce the jet power, we used the observed 1.4 GHz flux of each galaxy as follows. The radio emission of the starburst (from its supernovae) was computed from its far-infrared dust emission (Ivison et al. 2010) and subtracted from the observed 1.4 GHz flux. The residual synchrotron

luminosity was converted into total jet power, i.e., combined mechanical power of the cavity dominated by hadrons and radiative power of the synchrotron dominated by leptons, following a widely used calibration (Birzan et al. 2008), which encapsulates that the jet power of the jet is typically dominated the cavity power (Cavagnolo et al. 2010).

We find that a plausible jet-outflow connection exists in about half of the examined AGN since the jet coincides or extends in the same direction of the outflow. This is true for almost all AGNs with low luminosity ($\lesssim 10^{11} L_{\odot}$). From an energetics viewpoint, the jet can sustain the outflow in nearly all spatially identified cases, as the jet power (with the cavity and synchrotron included) exceeds the outflow kinetic energy. Therefore, the impact of jets on the molecular ISM could concern a high fraction of local AGN with massive outflows.

Table 4.1: Outflow and AGN properties of galaxies with molecular outflows are from Allison et al. 2014, unless otherwise indicated. For 4C12.50, properties are presented for the nuclear outflow component, as the extended components add little to the energetics (Fotopoulou et al. 2019). Likewise, the infrared luminosity fraction of the southern nucleus comes from resolved star formation rates (Lira et al. 2002). The radio power P_{jet} (for the sources with a certain radio jet detection) is calculated as in Birzan et al. 2008 after the subtraction of the starburst contribution as indicated in the text. Alternative radio power (P_{jet}) computations are as follows: * 43.96 for the synchrotron radiation (Fotopoulou et al. 2019), ** 39.3 for the X-ray cavity (Urquhart et al. 2018). *** 43.86 averaged value Punsly and Kharb 2016. **** To find the 1.4GHz flux fraction assigned to the southern nucleus of this galaxy merger, we used the information from spatially-resolved 5 GHz data (Neff et al. 2003). ¹Condon et al. 1998. ²Allison et al. 2014. ³Fotopoulou et al. 2019. ⁴Baan and Klöckner 2006. ⁵Ryder et al. 1996. ⁶Dumas et al. 2011. ⁷Condon et al. 1996. ⁸Urrutia et al. 2009. ⁹Greene et al. 2012. ¹⁰Clemens et al. 2008. ¹¹Clemens et al. 2010. ¹²Audibert et al. 2019. ¹³Davies et al. 2017. ¹⁴Fernández-Ontiveros et al. 2020. ¹⁵Oosterloo et al. 2019. ¹⁶Drake et al. 2004. ¹⁷Husemann et al. 2019b. ¹⁸Shimizu et al. 2017. ¹⁹Marvil et al. 2015. ²⁰Ohyama et al. 2015. ²¹Sakamoto et al. 2014. ²²Ruffa et al. 2022. ²³Ruffa et al. 2019b. ²⁴Husemann et al. 2019a. ²⁵Lanz et al. 2016. ²⁶Gruppioni et al. 2016

Galaxy	z	V_{out} km s ⁻¹	\dot{M}_{out} M_{\odot} yr ⁻¹	$\log(L_{\text{AGN}})$ erg s ⁻¹	$F_{1.4\text{GHz}}$ Jy	$\log(P_{\text{jet}})$ erg s ⁻¹
NGC1377	0.00578	110	5	42.93	<0.0015 ¹	<42.46
NGC1068	0.00379	150	28	43.94	4.85 ²	43.56
4C12.50	0.1217	800 ³	652 ³	45.7	5.1 ⁴	44.62 [*]
NGC1433	0.0036	100	0.7	42.24	0.0034 ⁵	42.45
Mrk231	0.04217	700	350	45.72	0.31 ⁴	...
IC5063	0.011	300	10	44.3	1.87 ²	43.74
M51	0.002	100	11	43.79	1.4 ⁶	43.17 ^{**}
Mrk1014	0.16311	268	93	45.29	0.0225 ¹	43.84
NGC1266	0.00719	177	11	43.31	0.115 ⁴	43.18
NGC5643	0.003999	500	85	42.91	0.203 ⁷	42.96
IRASF08572+3915	0.04311	800	403	45.72	0.0049 ¹	...
IRASF10565+2448	0.189	450	100	44.81	0.0576 ¹	...
IRASF11119+3257	0.06438	1000	203	46.2	0.106 ⁸	43.77
IRASF23365+3604	0.02448	450	57	44.67	0.0287 ⁴	...
NGC6240	0.123	400	267	45.38	0.427 ²	...
SDSSJ1356+1026	0.04256	500	118	46	0.49 ⁹	...
IRAS05189-2524	0.007268	491	219	44.47	0.0291 ¹	...
NGC4418	0.06764	134	19	43.81	0.0414 ⁴	...
IRASF14378-3651	0.030761	425	180	45.12	0.0349 ¹	...
IRAS13120-5453	0.08257	549	1115	44.35	0.065 ²	...
IRASF14348-1447	0.04295	450	420	44.59	0.018 ¹⁰¹¹	...
NGC613	0.00495	300 ¹²	19 ¹²	42.6 ¹³	0.223 ²	43.18
ESO420-613	0.01205	379 ¹⁴	14 ¹⁴	44.0 ¹⁴	0.1 ¹⁴	43.25
PKS1549-79	0.15	600 ¹⁵	1733 ¹⁵	44.7 ²⁵	5.36 ¹⁶	44.69
3C273	0.15834	245 ²⁴	439 ²⁴	46.06 ²⁶	55 ¹	45.06 ^{***}
HE1353-1917	0.03502	145 ¹⁷	22 ¹⁷	43.42 ¹⁸	0.0128 ¹	
NGC6764	0.00807	170	1	42.23	0.113 ¹⁹	43.15
Circinus	0.0014	150	1	43.57	1.2 ²	42.89
Mrk273	0.03777	620	200	44.16	0.145 ¹	43.62
NGC3256S	0.00926	1400 ²¹	19 ²¹	42.04 ²⁰	0.0168 ^{****}	42.97
NGC3100	0.0088	200 ²²	0.12 ²²	42.78 ²²	0.5 ²³	43 ²²
NGC6328	0.014	150	3.1	42.11	0.32	42.35

5.1 Conclusions

In this thesis, we have explored the role of jets as feedback mechanisms through two approaches. The first approach involved associating jetted AGNs with their radio emission and constructing a catalog, named CO-ARC, that combines molecular gas observations with radio-emission data. Given the foundational role of molecular gas as a precursor to star formation, analyzing the molecular gas content of jetted AGNs in juxtaposition with main sequence galaxies and different AGN types has provided insightful results.

We found that in the local universe, the mass function for radio galaxies (RGs) is significantly lower—by 2-4 orders of magnitude—compared to main sequence galaxies and simulated star-forming or starburst AGNs, yet it matches the AGN-dominated simulations. The molecular gas content in RGs is less than in star-forming galaxies, with this gap decreasing from 1-2 orders of magnitude in the local universe to nearly no difference at $z \gtrsim 0.1$.

At higher redshifts ($1 < z < 2.5$), we observed that RGs, when detectable, possess significantly larger amounts of molecular gas, often exceeding what is expected for typical galaxy halos of that epoch. However, due to observational limitations and the nature of RGs' continuum spectrum, the count of RGs at these redshifts is lower, and so is the mass function of their gas compared to simulations. Despite these challenges, the corrected molecular gas content evolution at higher redshifts aligns with that observed in AGN1 and AGN2 in the local universe. This suggests a continuity in molecular gas content across different epochs, indicating a dynamic balance influenced by inflows, star formation, and radio-mode feedback.

These findings underscore the intricate relationship between jet activity and molecular gas content in AGNs across various redshifts. The establishment of the CO-ARC catalog serves as a pivotal foundation for further research, guiding future studies into the nuanced interplay of these cosmic phenomena.

The second approach transitioned our focus onto the specific case of NGC6328, a part of our sample that, due to intriguing findings, prompted a meta-analysis on the driving mechanisms of molecular outflows. Our detailed analysis of NGC6328's molecular disk unveiled several pivotal insights. Initially, we discerned that gas initiated from a merger could traverse to the AGN region in under 500 million years, which provides more insight on the feeding mechanisms of the AGN. In the case of NGC6328 the gas inflow is induced from the loss of angular momentum through a combination of torques from the stellar distribution and inner torques from dissipative forces.

Furthermore, we identified, at a minimum, two outflows with a combined mass outflow rate of $3.1 M_{\odot} \text{ yr}^{-1}$ which surpass the current star formation of the galaxy $1 - 2 M_{\odot} \text{ yr}^{-1}$, hinting to a plausibly impact on the star

formation future of the galaxy. These outflows are driven by the jet, despite the jet not being visibly extended to the outflow area. Together with recent similar findings on other sources this hints at a potential underestimation of jet extents and impacts. Consequently, motivated from these examples a meta-analysis on a molecular outflows survey was conducted, revealing a significant association between many of the outflows and the jet.

These results suggests that jet-induced outflows could be instrumental across varying scales of feedback—from the large-scale ‘maintenance mode’ where intergalactic gas is deterred from cooling and gravitating towards the galaxy, to more localized kpc scales within the galaxy.

5.2 Future Work: Exploring Warped Disks via Physics Informed Neural Networks

We have discussed the various challenges posed by gas accretion into the SMBH on the host galaxy. A critical question is, how does the gas reach the SMBH in the first place? To traverse from stable orbits at about 10 kpc down to a mere 10 pc, the gas needs to shed roughly 99.9% of its angular momentum. Although large-scale gravitational torques triggered by galaxy bars and interactions can propel gas towards central regions, their effect diminishes at sub-kpc scales. The dynamic journey of gas inflow, marked by spirals, rings, clumps, and nested structures, reveals a complex and discontinuous pathway, adding layers of complexity to the relationship between morphological features and AGN activity.

Our analysis of NGC6328 illuminated the pivotal role of the stellar bulge and viscous forces in determining gas distribution geometry, emphasizing the necessity for a thorough approach. While our insights are valuable, the intricacy of the gas inflow issue required making several assumptions to simplify the problem. Notable assumptions include neglecting radial velocities and simplifying the equations concerning viscous forces.

Drawing inspiration from the works of Papaloizou and Pringle (1983), Pringle (1992), Nixon and King (2016), and Martin et al. (2019), we incorporated both external torques from gravitational potential and internal torques from stress between neighboring rings into the equation of angular momentum evolution, as shown below:

$$\frac{\partial \mathbf{L}}{\partial t} = \frac{1}{r} \frac{\partial}{\partial r} \left\{ \frac{(\partial/\partial r) [v_1 \Sigma r^3 (-\Omega')]}{\Sigma (\partial/\partial r) (r^2 \Omega)} \mathbf{L} \right\} \quad (5.1)$$

$$+ \frac{1}{r} \frac{\partial}{\partial r} \left[\frac{1}{2} v_2 r |\mathbf{L}| \frac{\partial \mathbf{L}}{\partial r} \right] \quad (5.2)$$

$$+ \frac{1}{r} \frac{\partial}{\partial r} \left\{ \left[\frac{\frac{1}{2} v_2 r^3 \Omega |\partial \mathbf{L} / \partial r|^2}{(\partial/\partial r) (r^2 \Omega)} + v_1 \left(\frac{r \Omega'}{\Omega} \right) \right] \mathbf{L} \right\} \quad (5.3)$$

$$+ \mathbf{T}(t, r) \quad (5.4)$$

where $\mathbf{L} = \Sigma \Omega r^2 \hat{l}$ is the specific angular momentum, \hat{l} denotes the angular momentum orientation, and Σ represents the surface density.

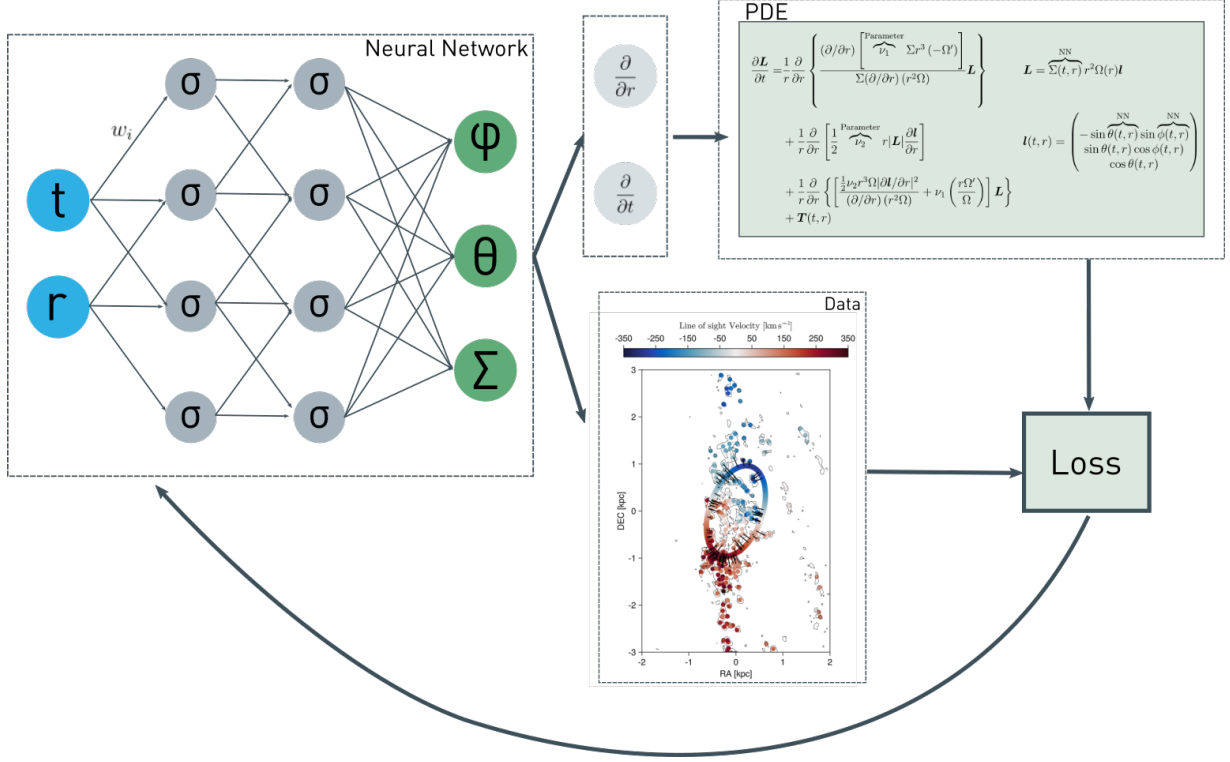


Figure 5.1: PINN sketch. At the left we have the representations of the functions as NN. We estimate the PDE loss by evaluating and summing the PDE value at a number of collocation points in the (t, r) space. At the same time we estimate the data loss using the NN functions. We minimize the loss by adjusting the NN weights w_i .

Tackling this set of Partial Differential Equations (PDE) alongside any data is a formidable task, further complicated by the unknown nature and non-parameterizable aspects of $\hat{l}(r, t)$ and $\Sigma(r, t)$. Even under a feasible constant initial condition for $\hat{l}(r, 0) = \hat{l}_0$, the same doesn't hold for $\Sigma(r, 0)$, especially in molecular gas disks where clumpiness is a strong feature. Even if we could numerically solve the equations, we would need several extra steps on comparing with the data (i.e. ALMA cube, or source detected clumps as we did in NGC6328) which makes the problem highly computationally demanding.

This led us to explore the potential and capabilities of Physics Informed Neural Networks (PINNs), which represent an innovative fusion of physics' fundamental principles and the advanced computational prowess of neural networks. At their essence, Neural Networks (NNs) function similarly to the human brain, with capabilities for pattern recognition, decision-making, and learning through experience. These networks are structured as layers of interconnected nodes, or "neurons," each capable of processing and transmitting information. In the context of PINNs, NNs stand out for their remarkable ability to act as universal approximators, meaning they can, with the right design and adequate data, approximate any continuous function to a high degree of accuracy. This unique attribute allows them to capture and model the complex, nonlinear dynamics found in a wide array of datasets, making them a powerful tool in various fields. In the context of our research, the integration of these neural network capabilities with physical laws offers a promising way for exploring complex physical phenomena.

In employing PINNs, we represent any unknown functional quantities

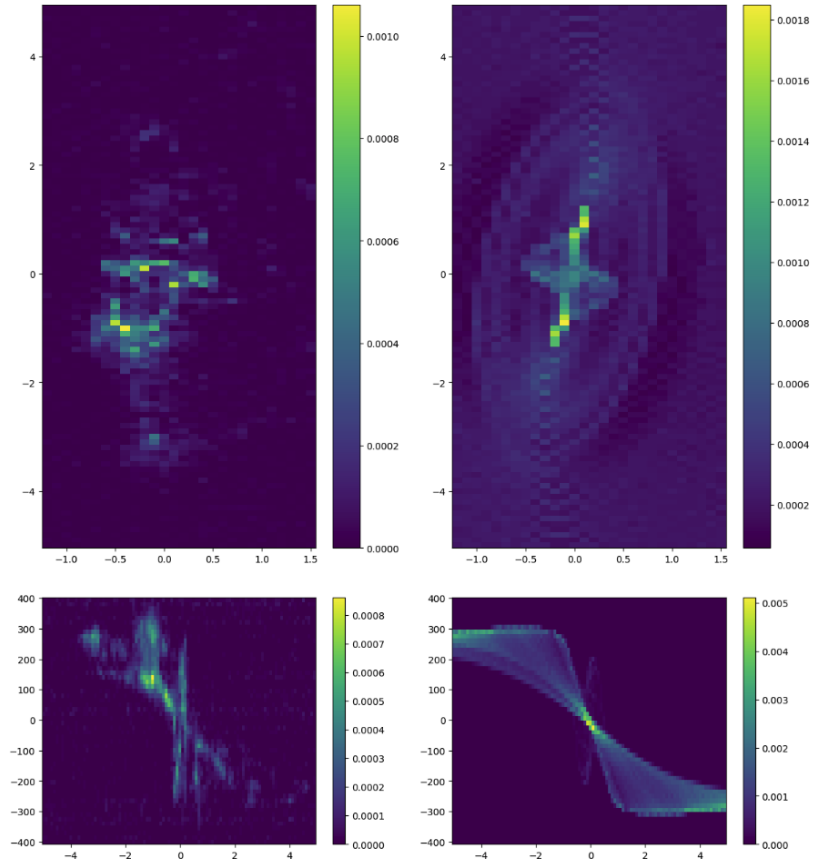


Figure 5.2: Draft results of the PINN disk fit. On the left is the NGC6328 data, integrated in space (top) and velocities (bottom). On the right the results of the NN representation of the disk.

using neural networks (NNs). In our problem such functional quantities are the surface density $\Sigma(t, r)$ and the two geometrical properties $\theta(t, r)$ and $\phi(t, r)$. Training a NN is process which uses a loss function which needs to be minimized by optimizing the NN parameters which are the weights of the inner nodes interconnections. In most applications the loss function incorporates the distance between observed data and the NN output, so the NN learns any hidden patterns of the data and can predict new values. An example could be the training of a time-series where we want to predict the future given some variables or features. In the case of PINNs however, we construct multiple loss functions. Apart from any loss function that compare the NN output with observed data we also incorporate and one or more physics loss function. This special function measure the distance between the NN functional quantities and some physical laws that we know the system must obey. One of the most revolutionary aspect of NN is their efficient differentiation capabilities. Using the partial derivatives of the functional quantities represents as NN we can construct complex system of partial equations as physics loss functions. So, in our problem set-up we can built the equations at play for $\theta(r, t; \mathbf{W}_\theta)$, $\phi(t, r; \mathbf{W}_\phi)$ and $\Sigma(r, t; \mathbf{W}_\Sigma)$ and their derivatives. Here we have created a NN representation of each quantity we want to estimate and their corresponding parameters \mathbf{W} .

Thus we define the physics loss functions as

$$\mathcal{F}(t, r; \mathbf{W}_\phi, \mathbf{W}_\theta, \mathbf{W}_\Sigma) = \frac{\partial L}{\partial t} - \frac{1}{r} \frac{\partial}{\partial r} \left\{ \frac{(\partial/\partial r) [v_1 \Sigma r^3 (-\Omega')]}{\Sigma (\partial/\partial r) (r^2 \Omega)} L \right\} \quad (5.5)$$

$$- \frac{1}{r} \frac{\partial}{\partial r} \left[\frac{1}{2} v_2 r |L| \frac{\partial L}{\partial r} \right] \quad (5.6)$$

$$- \frac{1}{r} \frac{\partial}{\partial r} \left\{ \left[\frac{\frac{1}{2} v_2 r^3 \Omega |\partial L / \partial r|^2}{(\partial/\partial r) (r^2 \Omega)} + v_1 \left(\frac{r \Omega'}{\Omega} \right) \right] L \right\} \quad (5.7)$$

$$- T(t, r) \quad (5.8)$$

where $L = L(t, r; \mathbf{W}_\phi, \mathbf{W}_\theta, \mathbf{W}_\Sigma)$ and $\Sigma = \Sigma(t, r; \mathbf{W}_\Sigma)$.

In optimizing the collocation points (t_c, r_c) within the (t, r) coordinates, our methodology allows for dynamic adjustment during the optimization process. This flexibility helps the neural network (NN) adapt to various time-space regions, ensuring that the learning is comprehensive without overfitting specific areas. The optimizer's role is to hone in on the weights $\mathbf{W}_\phi, \mathbf{W}_\theta, \mathbf{W}_\Sigma$ that yield the lowest loss function value. A minimal loss suggests that the NN, within its architectural constraints, has successfully approximated the real, yet unknown functions. It's crucial to incorporate additional loss functions that anchor the NN outputs to measured data or adhere to predetermined boundary conditions. This dual approach allows for simultaneous estimation of required quantities that are in harmony with observational data—an innovative leap facilitated by PINNs. Unlike traditional methods that rely on iterative simulations and data comparisons, this technique integrates convergence into the learning process itself.

This investigation remains ongoing and, while there are several complexities yet to be addressed, we have made substantive progress. Our preliminary results have shown consistency with empirical data, as demonstrated in figure 5.2. The application of Physics Informed Neural Networks (PINNs) in this context represents a significant step towards a more nuanced understanding of gas accretion dynamics. By integrating physical laws directly into the neural network architecture, we are developing a tool that adapts and learns from both the spatial and temporal aspects of the problem. As we continue to refine our model and address its current limitations, the goal is to reveal deeper insights into the mechanisms driving gas towards the SMBH, shedding light on the angular momentum conundrum. The path forward is clear: to iterate, improve, and validate our models against a growing body of observational data, thereby enhancing our understanding of these cosmic processes.

A

Appendix

A.1 Projection effects

A.1.1 Galaxy Frame

The angular velocity of circular orbit $\omega = v(R)/R$ inclined with galaxy equator is

$$\vec{\omega} = \omega \hat{n} = \begin{pmatrix} -\sin \theta \sin \lambda \\ \sin \theta \cos \lambda \\ \cos \theta \end{pmatrix} \quad (\text{A.1})$$

where θ is the polar angle and λ is a modified azimuthal angle termed as the Line of Nodes (LON) angle¹. The LON specifies the point where the ring intersects the x, y plane of the galaxy's coordinate system.

The transformation matrix between the $x_{\text{gal}}, y_{\text{gal}}, z_{\text{gal}}$, the Cartesian coordinates in the galaxy plane as

$$\begin{bmatrix} \hat{x} \\ \hat{y} \\ \hat{z} \end{bmatrix} = \begin{bmatrix} -\sin \theta \cos \lambda & -\cos \theta \sin \lambda & -\cos \lambda \\ \sin \theta \cos \lambda & \cos \theta \cos \lambda & -\sin \lambda \\ \cos \theta & -\sin \theta & 0 \end{bmatrix} \begin{bmatrix} \hat{\omega} \\ \hat{\theta} \\ \hat{\lambda} \end{bmatrix} \quad (\text{A.3})$$

and the reverse

$$\begin{bmatrix} \hat{\omega} \\ \hat{\theta} \\ \hat{\lambda} \end{bmatrix} = \begin{bmatrix} -\sin \theta \sin \lambda & \sin \theta \cos \lambda & \cos \theta \\ -\cos \theta \sin \lambda & \cos \theta \cos \lambda & -\sin \theta \\ \cos \lambda & -\sin \lambda & 0 \end{bmatrix} \begin{bmatrix} \hat{x} \\ \hat{y} \\ \hat{z} \end{bmatrix} \quad (\text{A.4})$$

If we define the points of an orbit with oriented at θ, λ with radius R as $\vec{r}_{\text{orbit}} = (x_{\text{orbit}}, y_{\text{orbit}}, z_{\text{orbit}})$ then the plane of the orbit is found by the equation $\vec{n}_{\text{orbit}} \cdot \vec{r}_{\text{orbit}} = 0$ or $z_{\text{orbit}} = \tan i (x_{\text{orbit}} \sin \lambda - y_{\text{orbit}} \cos \lambda)$. Parameterizing the position in the orbit with a angle $0 \leq \phi \leq 2\pi$ as $x_{\text{orbit}} = \omega \cos \phi$ and $y_{\text{orbit}} = \omega \sin \phi$ and using $x_{\text{orbit}}^2 + y_{\text{orbit}}^2 + z_{\text{orbit}}^2 = r^2$ we get the polar distance as

$$\omega_{\text{orbit}}(\phi; \theta, \lambda, r) = \frac{r}{\sqrt{1 + \tan^2 \theta \cos^2(\phi - \lambda)}} \quad (\text{A.5})$$

A.1.2 Sky Frame

Now we introduce a different set of angles in order to describe the orbit, inclination i and position angle PA which are selected in order to reproduce the astronomy definitions of inclination and position angle.

¹: λ is shifted by 90° relative to regular ϕ angle used in standard spherical coordinates

$$\vec{n} = \begin{pmatrix} \sin \theta \cos \phi \\ \sin \theta \sin \phi \\ \cos \theta \end{pmatrix} \quad (\text{A.2})$$

So, introducing $\phi = \lambda + \frac{\pi}{2}$ gives us the transformations $\cos \phi = -\sin \lambda$ and $\sin \phi = \cos \lambda$

Inclination is defined as the angle between Earth and the normal vector of the orbit and position angle as the angle measuring from the north where the LOS velocity is maximum (and positive, redshifted). As we did earlier we define the normal vector of the orbit in this frame of reference as

$$\vec{\omega}_{\text{sky}} = \omega \begin{pmatrix} \sin i \cos \text{PA} \\ \sin i \sin \text{PA} \\ \cos i \end{pmatrix} \quad (\text{A.6})$$

Using the same technique as in the galactic frame we can estimate the projection of the ring on the sky plane (RA,DEC) as the intersection of this plane with a sphere centered in the center of the galaxy at (0,0) on the sky plane and radius r . This gives as an ellipse equation of the form

$$R(\phi) = \frac{r}{\sqrt{1 + \tan^2 i \cos^2(\phi - \text{PA})}} \quad (\text{A.7})$$

with the projected los velocity to be $v_{\text{los}} = (\vec{\omega} \times \vec{r}) \cdot \hat{z}$ or

$$v_{\text{los}}(\phi) = \frac{v \sin(i) \sin(\phi - \text{PA})}{\sqrt{1 + \tan^2 i \cos^2(\phi - \text{PA})}} \quad (\text{A.8})$$

where ϕ the polar angle from the x axes (East) and v the intrinsic rotational velocity.

A.1.3 Connecting the two frames

Now we need to connect these two reference frames using a 3×3 rotation matrix \mathbf{R} . A rotation matrix can found using 3 successive planar rotations angles around x, y and z axes, the so called Euler angles. However, in this work we used a different approach. We first define a primal vector on the galactic frame of reference. We use for simplicity the z axis $\hat{N}_g = (0, 0, 1)^T$. Now we need to answer the question of how this vector is visible from the observer reference \hat{N}_s . As we defined the inclination and position angle angles we only need these two specific angles which we define as B_i and B_{PA} . So,

$$\hat{N}_s = \begin{pmatrix} \sin B_i \cos B_{\text{PA}} \\ \sin B_i \sin B_{\text{PA}} \\ \cos B_i \end{pmatrix} \quad (\text{A.9})$$

Now the rotation matrix is estimated using the Rodrigues rotation formula

$$\mathbf{R} = \mathbf{I} + \mathbf{U} + \frac{\mathbf{U} \cdot \mathbf{U}}{1 + \hat{N}_g \cdot \hat{N}_s}$$

where \mathbf{U} is the skew-symmetric cross-product matrix of $u = \hat{N}_g \times \hat{N}_s$,

$$\mathbf{U} = \begin{bmatrix} 0 & -u_3 & u_2 \\ u_3 & 0 & -u_1 \\ -u_2 & u_1 & 0 \end{bmatrix}$$

The reason of why this approach is much more useful than using 3 successive rotation angles is dictated from the definition of B_i and B_{PA} as they are describing the shape of the stellar bulge which can be estimated from photometry methods.

After we have calculated \mathbf{R} we can now estimate the orientation of a ring in the sky plane

$$\hat{n}_{\text{sky}} = \mathbf{R} \cdot \begin{pmatrix} -\sin \theta \sin \lambda \\ \sin \theta \cos \lambda \\ \cos \theta \end{pmatrix} \quad (\text{A.10})$$

so the angular velocity on the sky frame is $\vec{\omega}_{\text{sky}} = \omega \hat{n}_{\text{sky}}$ and the LOS projected velocity

$$v_{\text{los}} = (\vec{r} \times \vec{\omega}_{\text{sky}}) \cdot \hat{z} \quad (\text{A.11})$$

Finally, the position angle and inclination are calculated as

$$\text{PA} = \arctan\left(\frac{\hat{m}_y}{\hat{m}_x}\right) - \frac{\pi}{2} \quad (\text{A.12})$$

$$i = \pi - \arccos(\hat{n}_{\text{sky}} \cdot \hat{z}_{\text{sky}}) \quad (\text{A.13})$$

where $\hat{m} = \hat{n}_{\text{sky}} \times \hat{z}_{\text{sky}}$.

A.1.4 A note regarding similar work in the literature

In the literature, and especially in the codes which are used to infer the kinematical properties of galaxies, it is often used this expression for the LOS velocity

$$v_{\text{los}}(r, \theta) = v_t(r) \cos \theta \sin i + v_r(r) \sin \theta \sin i \quad (\text{A.14})$$

where the plane of the galaxy is (r, θ) , i is the disk inclination, V_t is the tangential (circular) velocity and V_r radial velocity. **Note the different symbols with our work.** This expression is useful in estimating the velocity field in the sky plane as using the transformations:

$$\cos \theta = \frac{-(x - x_0) \sin \phi + (y - y_0) \cos \phi}{R} \quad (\text{A.15})$$

$$\sin \theta = \frac{-(x - x_0) \cos \phi - (y - y_0) \sin \phi}{R \cos(i)} \quad (\text{A.16})$$

we get

$$v_{\text{los}}(x, y; R, \phi, i) = \frac{\sin i}{R} \left[v_t(R)(-x \sin \phi + y \cos \phi) + v_r(R)(-x \cos \phi - y \sin \phi) \right] \quad (\text{A.17})$$

where we have assumed $x_0 = y_0 = 0$ the center of the galaxy in the sky plane.

In this framework we can also add non-axisymmetric flows using an

approximate form

$$v_t(r, \theta) = \bar{v}_t(r) + \sum_{m=1}^{\infty} v_{m,t}(r) \cos [m\theta + \theta_{m,t}(r)] \quad (\text{A.18})$$

$$v_r(r, \theta) = \bar{v}_r(r) + \sum_{m=1}^{\infty} v_{m,r}(r) \cos [m\theta + \theta_{m,r}(r)] \quad (\text{A.19})$$

However, we have avoided using these tools for two reasons. First, as we mentioned also in the 3.3.1 this framework is mostly useful in disks which are generally flat, with small warps only on the outskirts. The second reason is mostly conceptual. In expressions like A.14 there is a mix between the galactic coordinates θ angle and the projected parameter i that confuses the reader, but also makes it harder to use again in a warped disk scenario.

Bibliography

Here are the references in citation order.

- Schwarzschild, Karl (1999). 'On the gravitational field of a sphere of incompressible fluid according to Einstein's theory'. In: *arXiv preprint physics/9912033* (cited on page 1).
- Kormendy, John and Luis C Ho (2013). 'Coevolution (or not) of supermassive black holes and host galaxies'. In: *Annual Review of Astronomy and Astrophysics* 51, pp. 511–653 (cited on page 1).
- Merritt, David (2003). 'Single and binary black holes and their influence on nuclear structure'. In: *arXiv preprint astro-ph/0301257* (cited on page 1).
- Wolfe, A. M. and G. R. Burbidge (Aug. 1970). 'Black Holes in Elliptical Galaxies'. In: 161, p. 419. doi: [10.1086/150549](https://doi.org/10.1086/150549) (cited on page 2).
- Ghez, Andrea M et al. (2008). 'Measuring distance and properties of the Milky Way's central supermassive black hole with stellar orbits'. In: *The Astrophysical Journal* 689.2, p. 1044 (cited on page 2).
- Genzel, Reinhard et al. (2010). 'The Galactic Center massive black hole and nuclear star cluster'. In: *Reviews of Modern Physics* 82.4, p. 3121 (cited on page 2).
- Penrose, Roger (1965). 'Gravitational collapse and space-time singularities'. In: *Physical Review Letters* 14.3, p. 57 (cited on page 2).
- Schmidt, Maarten (1963). '3 C 273: a star-like object with large red-shift'. In: *Nature* 197.4872, pp. 1040–1040 (cited on page 2).
- Uchiyama, Yasunobu et al. (2006). 'Shedding new light on the 3C 273 jet with the Spitzer Space Telescope'. In: *The Astrophysical Journal* 648.2, p. 910 (cited on page 2).
- Kerr, Roy P (1963). 'Gravitational field of a spinning mass as an example of algebraically special metrics'. In: *Physical review letters* 11.5, p. 237 (cited on page 3).
- Shapiro, Stuart L et al. (1983). 'The physics of compact objects'. In: *Wiley, New York* 19832, pp. 119–123 (cited on page 3).
- Marconi, Alessandro et al. (2004). 'Local supermassive black holes, relics of active galactic nuclei and the X-ray background'. In: *Monthly Notices of the Royal Astronomical Society* 351.1, pp. 169–185 (cited on page 3).
- Merloni, Andrea et al. (2004). 'Tracing the cosmological assembly of stars and supermassive black holes in galaxies'. In: *Monthly Notices of the Royal Astronomical Society* 354.3, pp. L37–L42 (cited on page 3).
- Abramowicz, M. A. et al. (Dec. 1980). 'Thick accretion disks with super-Eddington luminosities'. In: 242, pp. 772–788. doi: [10.1086/158512](https://doi.org/10.1086/158512) (cited on page 3).
- Hardcastle, Martin J et al. (2007). 'Hot and cold gas accretion and feedback in radio-loud active galaxies'. In: *Monthly Notices of the Royal Astronomical Society* 376.4, pp. 1849–1856 (cited on page 4).
- Best, PN and TM Heckman (2012). 'On the fundamental dichotomy in the local radio-AGN population: accretion, evolution and host galaxy properties'. In: *Monthly Notices of the Royal Astronomical Society* 421.2, pp. 1569–1582 (cited on page 4).
- Heckman, Timothy M. and Philip N. Best (Aug. 2014). 'The Coevolution of Galaxies and Supermassive Black Holes: Insights from Surveys of the Contemporary Universe'. In: *Annual Review of Astronomy & Astrophysics* 52, p. 589. doi: [10.1146/annurev-astro-081913-035722](https://doi.org/10.1146/annurev-astro-081913-035722) (cited on pages 4, 12).
- Hardcastle, M. J. (Apr. 2018). 'A simulation-based analytic model of radio galaxies'. In: 475.2, pp. 2768–2786. doi: [10.1093/mnras/stx3358](https://doi.org/10.1093/mnras/stx3358) (cited on page 4).
- Thorne, Jessica et al. (Mar. 2022). *AGN Unification Diagram*. Was originally created to be included in the introduction of Thorne J. E., et al., 2022, MNRAS, 509, 4940. doi: [10.5281/zenodo.6381013](https://doi.org/10.5281/zenodo.6381013). URL: <https://doi.org/10.5281/zenodo.6381013> (cited on page 4).
- Heckman, Timothy M. and Philip N. Best (Aug. 2014). 'The Coevolution of Galaxies and Supermassive Black Holes: Insights from Surveys of the Contemporary Universe'. In: 52, pp. 589–660. doi: [10.1146/annurev-astro-081913-035722](https://doi.org/10.1146/annurev-astro-081913-035722) (cited on page 5).
- Shakura, N. I. and R. A. Sunyaev (Jan. 1973). 'Black holes in binary systems. Observational appearance.' In: 24, pp. 337–355 (cited on page 5).

- Novikov, I. D. and K. S. Thorne (Jan. 1973). 'Astrophysics of black holes.' In: *Black Holes (Les Astres Occlus)*, pp. 343–450 (cited on page 5).
- Frank, Juhan et al. (2002). *Accretion Power in Astrophysics: Third Edition* (cited on page 5).
- Esin, Ann A. et al. (Nov. 1997). 'Advection-Dominated Accretion and the Spectral States of Black Hole X-Ray Binaries: Application to Nova Muscae 1991'. In: 489.2, pp. 865–889. doi: [10.1086/304829](https://doi.org/10.1086/304829) (cited on page 5).
- Esin, Ann A. et al. (Oct. 1998). 'Spectral Transitions in Cygnus X-1 and Other Black Hole X-Ray Binaries'. In: 505.2, pp. 854–868. doi: [10.1086/306186](https://doi.org/10.1086/306186) (cited on page 5).
- Narayan, Ramesh and Insu Yi (May 1995). 'Advection-dominated Accretion: Self-Similarity and Bipolar Outflows'. In: 444, p. 231. doi: [10.1086/175599](https://doi.org/10.1086/175599) (cited on page 5).
- Fender, R. P. et al. (Dec. 2004). 'Towards a unified model for black hole X-ray binary jets'. In: 355.4, pp. 1105–1118. doi: [10.1111/j.1365-2966.2004.08384.x](https://doi.org/10.1111/j.1365-2966.2004.08384.x) (cited on page 5).
- Done, Chris et al. (Dec. 2007). 'Modelling the behaviour of accretion flows in X-ray binaries. Everything you always wanted to know about accretion but were afraid to ask'. In: 15.1, pp. 1–66. doi: [10.1007/s00159-007-0006-1](https://doi.org/10.1007/s00159-007-0006-1) (cited on page 5).
- Ichimaru, S. (June 1977). 'Bimodal behavior of accretion disks: theory and application to Cygnus X-1 transitions.' In: 214, pp. 840–855. doi: [10.1086/155314](https://doi.org/10.1086/155314) (cited on page 5).
- Narayan, Ramesh and Insu Yi (June 1994). 'Advection-dominated Accretion: A Self-similar Solution'. In: 428, p. L13. doi: [10.1086/187381](https://doi.org/10.1086/187381) (cited on page 5).
- Abramowicz, Marek A. et al. (Jan. 1995). 'Thermal Equilibria of Accretion Disks'. In: 438, p. L37. doi: [10.1086/187709](https://doi.org/10.1086/187709) (cited on page 5).
- Tchekhovskoy, Alexander et al. (Nov. 2011). 'Efficient generation of jets from magnetically arrested accretion on a rapidly spinning black hole'. In: 418.1, pp. L79–L83. doi: [10.1111/j.1745-3933.2011.01147.x](https://doi.org/10.1111/j.1745-3933.2011.01147.x) (cited on pages 5, 6).
- Bisnovaty-Kogan, G. S. and A. A. Ruzmaikin (May 1974). 'The Accretion of Matter by a Collapsing Star in the Presence of a Magnetic Field'. In: 28.1, pp. 45–59. doi: [10.1007/BF00642237](https://doi.org/10.1007/BF00642237) (cited on page 5).
- Tchekhovskoy, Alexander et al. (July 2012). 'General Relativistic Modeling of Magnetized Jets from Accreting Black Holes'. In: *Journal of Physics Conference Series*. Vol. 372. Journal of Physics Conference Series, 012040, p. 012040. doi: [10.1088/1742-6596/372/1/012040](https://doi.org/10.1088/1742-6596/372/1/012040) (cited on page 5).
- McKinney, Jonathan C. et al. (July 2012). 'General relativistic magnetohydrodynamic simulations of magnetically choked accretion flows around black holes'. In: 423.4, pp. 3083–3117. doi: [10.1111/j.1365-2966.2012.21074.x](https://doi.org/10.1111/j.1365-2966.2012.21074.x) (cited on page 5).
- Blandford, R. D. and D. G. Payne (June 1982). 'Hydromagnetic flows from accretion disks and the production of radio jets.' In: 199, pp. 883–903. doi: [10.1093/mnras/199.4.883](https://doi.org/10.1093/mnras/199.4.883) (cited on page 6).
- Blandford, R. D. and R. L. Znajek (May 1977). 'Electromagnetic extraction of energy from Kerr black holes.' In: 179, pp. 433–456. doi: [10.1093/mnras/179.3.433](https://doi.org/10.1093/mnras/179.3.433) (cited on pages 6, 9).
- Zubovas, Kastytis and Andrew King (Feb. 2012). 'CLEARING OUT A GALAXY'. In: *ApJ* 745.2, p. L34. doi: [10.1088/2041-8205/745/2/L34](https://doi.org/10.1088/2041-8205/745/2/L34) (cited on pages 7, 82).
- Tchekhovskoy, Alexander et al. (Mar. 2010). 'Black Hole Spin and The Radio Loud/Quiet Dichotomy of Active Galactic Nuclei'. In: 711.1, pp. 50–63. doi: [10.1088/0004-637X/711/1/50](https://doi.org/10.1088/0004-637X/711/1/50) (cited on page 9).
- Mukherjee, Dipanjan et al. (Sept. 2016). 'Relativistic Jet Feedback in High-Redshift Galaxies - I. Dynamics'. In: *Monthly Notices of the Royal Astronomical Society* 461, pp. 967–983. doi: [10/f8489c](https://doi.org/10/f8489c) (cited on pages 10, 11, 76).
- Fabian, A. C. (Sept. 2012). 'Observational Evidence of AGN Feedback'. In: *Annu. Rev. Astron. Astrophys.* 50.1, pp. 455–489. doi: [10.1146/annurev-astro-081811-125521](https://doi.org/10.1146/annurev-astro-081811-125521) (cited on pages 10, 15).
- McNamara, B. R. and P. E. J. Nulsen (May 2012). 'Mechanical Feedback from Active Galactic Nuclei in Galaxies, Groups and Clusters'. In: *New Journal of Physics* 14, p. 055023. doi: [10/gm5rqk](https://doi.org/10/gm5rqk) (cited on page 10).
- Wagner, A. Y. and G. V. Bicknell (2011). 'Relativistic Jet Feedback in Evolving Galaxies'. In: *ApJ* 728.1, p. 29. doi: [10.1088/0004-637X/728/1/29](https://doi.org/10.1088/0004-637X/728/1/29) (cited on page 11).
- Wagner, A. Y. et al. (Oct. 2012). 'Driving Outflows with Relativistic Jets and the Dependence of Active Galactic Nucleus Feedback Efficiency on Interstellar Medium Inhomogeneity'. In: 757.2, 136, p. 136. doi: [10.1088/0004-637X/757/2/136](https://doi.org/10.1088/0004-637X/757/2/136) (cited on page 11).
- Mukherjee, Dipanjan et al. (May 2018). 'The Jet-ISM Interactions in IC 5063'. In: *Monthly Notices of the Royal Astronomical Society* 476.1, pp. 80–95. doi: [10/gdc6m8](https://doi.org/10/gdc6m8) (cited on pages 11, 17).

- Talbot, Rosie Y. et al. (Aug. 2022). 'Blandford-Znajek jets in galaxy formation simulations: exploring the diversity of outflows produced by spin-driven AGN jets in Seyfert galaxies'. In: 514.3, pp. 4535–4559. doi: [10.1093/mnras/stac1566](https://doi.org/10.1093/mnras/stac1566) (cited on page 11).
- Kroupa, Pavel (2001). 'On the variation of the initial mass function'. In: *Monthly Notices of the Royal Astronomical Society* 322.2, pp. 231–246 (cited on page 11).
- Woo, Jong-Hak et al. (July 2013). 'Do Quiescent and Active Galaxies Have Different $M_{BH}-\sigma_*$ Relations?' In: 772.1, 49, p. 49. doi: [10.1088/0004-637X/772/1/49](https://doi.org/10.1088/0004-637X/772/1/49) (cited on page 12).
- Madau, Piero and Mark Dickinson (Aug. 2014). 'Cosmic Star-Formation History'. In: *Annu. Rev. Astron. Astrophys.* 52.1, pp. 415–486. doi: [10.1146/annurev-astro-081811-125615](https://doi.org/10.1146/annurev-astro-081811-125615) (cited on page 14).
- Strateva, Iskra et al. (Oct. 2001). 'Color Separation of Galaxy Types in the Sloan Digital Sky Survey Imaging Data'. In: 122.4, pp. 1861–1874. doi: [10.1086/323301](https://doi.org/10.1086/323301) (cited on page 14).
- Baldry, Ivan K. et al. (Jan. 2004). 'Quantifying the Bimodal Color-Magnitude Distribution of Galaxies'. In: 600.2, pp. 681–694. doi: [10.1086/380092](https://doi.org/10.1086/380092) (cited on page 14).
- Toomre, Alar and Juri Toomre (Dec. 1972). 'Galactic Bridges and Tails'. In: 178, pp. 623–666. doi: [10.1086/151823](https://doi.org/10.1086/151823) (cited on page 14).
- Toomre, Alar (Jan. 1977). 'Mergers and Some Consequences'. In: *Evolution of Galaxies and Stellar Populations*. Ed. by Beatrice M. Tinsley and D. Campbell Larson Richard B. Gehret, p. 401 (cited on page 14).
- Schweizer, Francois et al. (Dec. 1990). 'Correlations between Line Strengths and Fine Structure in Elliptical Galaxies'. In: 364, p. L33. doi: [10.1086/185868](https://doi.org/10.1086/185868) (cited on page 14).
- Springel, Volker et al. (Aug. 2005). 'Modelling feedback from stars and black holes in galaxy mergers'. In: 361.3, pp. 776–794. doi: [10.1111/j.1365-2966.2005.09238.x](https://doi.org/10.1111/j.1365-2966.2005.09238.x) (cited on page 14).
- Schawinski, Kevin et al. (Dec. 2007). 'Observational evidence for AGN feedback in early-type galaxies'. In: 382.4, pp. 1415–1431. doi: [10.1111/j.1365-2966.2007.12487.x](https://doi.org/10.1111/j.1365-2966.2007.12487.x) (cited on page 14).
- Kauffmann, Guinevere et al. (Dec. 2003). 'The host galaxies of active galactic nuclei'. In: 346.4, pp. 1055–1077. doi: [10.1111/j.1365-2966.2003.07154.x](https://doi.org/10.1111/j.1365-2966.2003.07154.x) (cited on page 14).
- Tremonti, Christy A. et al. (July 2007). 'The Discovery of 1000 km s⁻¹ Outflows in Massive Poststarburst Galaxies at z=0.6'. In: 663.2, pp. L77–L80. doi: [10.1086/520083](https://doi.org/10.1086/520083) (cited on page 14).
- Dubois, Yohan et al. (Dec. 2016). 'The HORIZON-AGN simulation: morphological diversity of galaxies promoted by AGN feedback'. In: 463.4, pp. 3948–3964. doi: [10.1093/mnras/stw2265](https://doi.org/10.1093/mnras/stw2265) (cited on pages 14, 16).
- Sakelliou, I. et al. (Sept. 2002). 'High resolution soft X-ray spectroscopy of M 87 with the reflection grating spectrometers on XMM-Newton'. In: 391, pp. 903–909. doi: [10.1051/0004-6361:20020900](https://doi.org/10.1051/0004-6361:20020900) (cited on page 14).
- Peterson, J. R. et al. (June 2003). 'High-Resolution X-Ray Spectroscopic Constraints on Cooling-Flow Models for Clusters of Galaxies'. In: 590.1, pp. 207–224. doi: [10.1086/374830](https://doi.org/10.1086/374830) (cited on page 14).
- Benson, A. J. et al. (Dec. 2003). 'What Shapes the Luminosity Function of Galaxies?' In: 599.1, pp. 38–49. doi: [10.1086/379160](https://doi.org/10.1086/379160) (cited on page 14).
- Croton, Darren J. et al. (Jan. 2006). 'The many lives of active galactic nuclei: cooling flows, black holes and the luminosities and colours of galaxies'. In: 365.1, pp. 11–28. doi: [10.1111/j.1365-2966.2005.09675.x](https://doi.org/10.1111/j.1365-2966.2005.09675.x) (cited on page 14).
- Dubois, Y. et al. (Oct. 2014). 'Dancing in the dark: galactic properties trace spin swings along the cosmic web'. In: 444.2, pp. 1453–1468. doi: [10.1093/mnras/stu1227](https://doi.org/10.1093/mnras/stu1227) (cited on pages 15, 16).
- Kaviraj, S. et al. (June 2017). 'The Horizon-AGN simulation: evolution of galaxy properties over cosmic time'. In: 467.4, pp. 4739–4752. doi: [10.1093/mnras/stx126](https://doi.org/10.1093/mnras/stx126) (cited on page 15).
- Naab, Thorsten and Jeremiah P. Ostriker (Aug. 2017). 'Theoretical Challenges in Galaxy Formation'. In: 55.1, pp. 59–109. doi: [10.1146/annurev-astro-081913-040019](https://doi.org/10.1146/annurev-astro-081913-040019) (cited on page 15).
- González, Valentino et al. (July 2011). 'Evolution of Galaxy Stellar Mass Functions, Mass Densities, and Mass-to-light Ratios from z ~7 to z ~4'. In: 735.2, L34, p. L34. doi: [10.1088/2041-8205/735/2/L34](https://doi.org/10.1088/2041-8205/735/2/L34) (cited on page 15).
- Bielby, R. M. et al. (Aug. 2014). 'The WIRCam Deep Survey. II. Mass selected clustering'. In: 568, A24, A24. doi: [10.1051/0004-6361/201322814](https://doi.org/10.1051/0004-6361/201322814) (cited on page 15).
- Daddi, E. et al. (Mar. 2002). 'The K20 survey. II. The different spatial clustering of z ~1 old and dusty star-forming EROs'. In: 384, pp. L1–L5. doi: [10.1051/0004-6361:20020112](https://doi.org/10.1051/0004-6361:20020112) (cited on page 15).

- Bernardi, M. et al. (Nov. 2013). 'The massive end of the luminosity and stellar mass functions: dependence on the fit to the light profile'. In: 436.1, pp. 697–704. doi: [10.1093/mnras/stt1607](https://doi.org/10.1093/mnras/stt1607) (cited on page 15).
- Moustakas, John et al. (Apr. 2013). 'PRIMUS: Constraints on Star Formation Quenching and Galaxy Merging, and the Evolution of the Stellar Mass Function from $z = 0-1$ '. In: 767.1, 50, p. 50. doi: [10.1088/0004-637X/767/1/50](https://doi.org/10.1088/0004-637X/767/1/50) (cited on page 15).
- Tomczak, Adam R. et al. (Mar. 2014). 'Galaxy Stellar Mass Functions from ZFOURGE/CANDELS: An Excess of Low-mass Galaxies since $z = 2$ and the Rapid Buildup of Quiescent Galaxies'. In: 783.2, 85, p. 85. doi: [10.1088/0004-637X/783/2/85](https://doi.org/10.1088/0004-637X/783/2/85) (cited on page 15).
- Song, Mimi et al. (July 2016). 'The Evolution of the Galaxy Stellar Mass Function at $z = 4-8$: A Steepening Low-mass-end Slope with Increasing Redshift'. In: 825.1, 5, p. 5. doi: [10.3847/0004-637X/825/1/5](https://doi.org/10.3847/0004-637X/825/1/5) (cited on page 15).
- Davidzon, I. et al. (Sept. 2017). 'The COSMOS2015 galaxy stellar mass function . Thirteen billion years of stellar mass assembly in ten snapshots'. In: 605, A70, A70. doi: [10.1051/0004-6361/201730419](https://doi.org/10.1051/0004-6361/201730419) (cited on page 15).
- Beckmann, R. S. et al. (Nov. 2017). 'Cosmic Evolution of Stellar Quenching by AGN Feedback: Clues from the Horizon-AGN Simulation'. In: *Monthly Notices of the Royal Astronomical Society* 472.1, pp. 949–965. doi: [10.1093/mnras/stx1831](https://doi.org/10.1093/mnras/stx1831) (cited on page 15).
- Feruglio, C. et al. (Nov. 2015). 'The multi-phase winds of Markarian 231: from the hot, nuclear, ultra-fast wind to the galaxy-scale, molecular outflow'. In: 583, A99, A99. doi: [10.1051/0004-6361/201526020](https://doi.org/10.1051/0004-6361/201526020) (cited on page 15).
- Morganti, Raffaella et al. (Sept. 2016). 'Another piece of the puzzle: The fast H I outflow in Mrk 231'. In: 593, A30, A30. doi: [10.1051/0004-6361/201628978](https://doi.org/10.1051/0004-6361/201628978) (cited on page 15).
- King, Andrew (Oct. 2003). 'Black Holes, Galaxy Formation, and the $M_{BH}-\sigma$ Relation'. In: 596.1, pp. L27–L29. doi: [10.1086/379143](https://doi.org/10.1086/379143) (cited on page 17).
- Harrison, C. M. (July 2017). 'Impact of supermassive black hole growth on star formation'. In: *Nature Astronomy* 1, 0165, p. 0165. doi: [10.1038/s41550-017-0165](https://doi.org/10.1038/s41550-017-0165) (cited on page 17).
- Bieri, Rebekka et al. (Jan. 2017). 'Outflows driven by quasars in high-redshift galaxies with radiation hydrodynamics'. In: 464.2, pp. 1854–1873. doi: [10.1093/mnras/stw2380](https://doi.org/10.1093/mnras/stw2380) (cited on page 17).
- Dasyra, K. M. et al. (Nov. 2016). 'ALMA Reveals Optically Thin, Highly Excited CO Gas in the Jet-Driven Winds of the Galaxy IC 5063'. In: *Astronomy & Astrophysics* 595, p. L7. doi: [10.1051/0004-6361/201629689](https://doi.org/10.1051/0004-6361/201629689) (cited on pages 17, 73, 74).
- Tadhunter, C. et al. (July 2014). 'Jet acceleration of the fast molecular outflows in the Seyfert galaxy IC 5063'. In: 511.7510, pp. 440–443. doi: [10.1038/nature13520](https://doi.org/10.1038/nature13520) (cited on page 17).
- Morganti, Raffaella et al. (Aug. 2015). 'The fast molecular outflow in the Seyfert galaxy IC 5063 as seen by ALMA'. In: 580, A1, A1. doi: [10.1051/0004-6361/201525860](https://doi.org/10.1051/0004-6361/201525860) (cited on page 17).
- Oosterloo, Tom et al. (Dec. 2017). 'Properties of the Molecular Gas in the Fast Outflow in the Seyfert Galaxy IC 5063'. In: *Astronomy & Astrophysics* 608, A38. doi: [10.1051/0004-6361/201731781](https://doi.org/10.1051/0004-6361/201731781) (cited on page 17).
- McNamara, B. R. et al. (June 2009). 'An Energetic AGN Outburst Powered by a Rapidly Spinning Supermassive Black Hole or an Accreting Ultramassive Black Hole'. In: 698.1, pp. 594–605. doi: [10.1088/0004-637X/698/1/594](https://doi.org/10.1088/0004-637X/698/1/594) (cited on page 17).
- Fabian, A. C. (Sept. 2012). 'Observational Evidence of Active Galactic Nuclei Feedback'. In: 50, pp. 455–489. doi: [10.1146/annurev-astro-081811-125521](https://doi.org/10.1146/annurev-astro-081811-125521) (cited on page 17).
- McNamara, B. R. and P. E. J. Nulsen (May 2012). 'Mechanical feedback from active galactic nuclei in galaxies, groups and clusters'. In: *New Journal of Physics* 14.5, 055023, p. 055023. doi: [10.1088/1367-2630/14/5/055023](https://doi.org/10.1088/1367-2630/14/5/055023) (cited on page 17).
- Fotopoulou, C. M. et al. (Sept. 2019). 'Complex molecular gas kinematics in the inner 5 kpc of 4C12.50 as seen by ALMA'. In: 629, A30, A30. doi: [10.1051/0004-6361/201834416](https://doi.org/10.1051/0004-6361/201834416) (cited on pages 17, 35).
- Oosterloo, Tom et al. (Dec. 2019). 'ALMA observations of PKS 1549-79: a case of feeding and feedback in a young radio quasar'. In: 632, A66, A66. doi: [10.1051/0004-6361/201936248](https://doi.org/10.1051/0004-6361/201936248) (cited on page 17).
- Aalto, S. et al. (Aug. 2020). 'ALMA resolves the remarkable molecular jet and rotating wind in the extremely radio-quiet galaxy NGC 1377'. In: 640, A104, A104. doi: [10.1051/0004-6361/202038282](https://doi.org/10.1051/0004-6361/202038282) (cited on page 17).

- Fernández-Ontiveros, J. A. et al. (Jan. 2020). 'A CO molecular gas wind 340 pc away from the Seyfert 2 nucleus in ESO 420-G13 probes an elusive radio jet'. In: 633, A127, A127. doi: [10.1051/0004-6361/201936552](https://doi.org/10.1051/0004-6361/201936552) (cited on page 17).
- Combes, F. et al. (Oct. 2013). 'ALMA observations of feeding and feedback in nearby Seyfert galaxies: an AGN-driven outflow in NGC 1433'. In: 558, A124, A124. doi: [10.1051/0004-6361/201322288](https://doi.org/10.1051/0004-6361/201322288) (cited on page 17).
- García-Burillo, S. et al. (July 2014). 'Molecular line emission in NGC 1068 imaged with ALMA. I. An AGN-driven outflow in the dense molecular gas'. In: 567, A125, A125. doi: [10.1051/0004-6361/201423843](https://doi.org/10.1051/0004-6361/201423843) (cited on page 17).
- Audibert, A. et al. (Dec. 2019). 'ALMA captures feeding and feedback from the active galactic nucleus in NGC 613'. In: 632, A33, A33. doi: [10.1051/0004-6361/201935845](https://doi.org/10.1051/0004-6361/201935845) (cited on page 17).
- Ruffa, Ilaria et al. (Mar. 2022). 'The AGN fuelling/feedback cycle in nearby radio galaxies - IV. Molecular gas conditions and jet-ISM interaction in NGC 3100'. In: 510.3, pp. 4485–4503. doi: [10.1093/mnras/stab3541](https://doi.org/10.1093/mnras/stab3541) (cited on pages 17, 30).
- Fluetsch, A. et al. (Mar. 2019). 'Cold Molecular Outflows in the Local Universe and Their Feedback Effect on Galaxies'. In: *Monthly Notices of the Royal Astronomical Society* 483, pp. 4586–4614. doi: [10.1093/mnras/sty344910](https://doi.org/10.1093/mnras/sty344910). [arXiv.1805.05352](https://arxiv.org/abs/1805.05352) (cited on pages 18, 76, 81).
- Lutz, D. et al. (Jan. 2020). 'Molecular Outflows in Local Galaxies: Method Comparison and a Role of Intermittent AGN Driving'. In: *Astronomy & Astrophysics* 633, A134. doi: [10/gghjvmp](https://doi.org/10/gghjvmp) (cited on pages 18, 74–76).
- Weiß, A. et al. (July 2012). 'On the Variations of Fundamental Constants and Active Galactic Nucleus Feedback in the Quasi-stellar Object Host Galaxy RXJ0911.4+0551 at $z = 2.79$ '. In: 753.2, 102, p. 102. doi: [10.1088/0004-637X/753/2/102](https://doi.org/10.1088/0004-637X/753/2/102) (cited on page 18).
- Feruglio, C. et al. (Dec. 2017). 'On the discovery of fast molecular gas in the UFO/BAL quasar APM 08279+5255 at $z = 3.912$ '. In: 608, A30, A30. doi: [10.1051/0004-6361/201731387](https://doi.org/10.1051/0004-6361/201731387) (cited on page 18).
- Carniani, S. et al. (Sept. 2017). 'AGN feedback on molecular gas reservoirs in quasars at $z \approx 2.4$ '. In: 605, A105, A105. doi: [10.1051/0004-6361/201730672](https://doi.org/10.1051/0004-6361/201730672) (cited on page 18).
- Vayner, Andrey et al. (Dec. 2017). 'Galactic-scale Feedback Observed in the 3C 298 Quasar Host Galaxy'. In: 851.2, 126, p. 126. doi: [10.3847/1538-4357/aa9c42](https://doi.org/10.3847/1538-4357/aa9c42) (cited on page 18).
- Fan, Lulu et al. (Mar. 2018). 'ALMA Detections of CO Emission in the Most Luminous, Heavily Dust-obscured Quasars at $z > 3$ '. In: 856.1, L5, p. L5. doi: [10.3847/2041-8213/aab496](https://doi.org/10.3847/2041-8213/aab496) (cited on page 18).
- Brusa, M. et al. (Apr. 2018). 'Molecular outflow and feedback in the obscured quasar XID2028 revealed by ALMA'. In: 612, A29, A29. doi: [10.1051/0004-6361/201731641](https://doi.org/10.1051/0004-6361/201731641) (cited on page 18).
- Herrera-Camus, R. et al. (Jan. 2019). 'Molecular and Ionized Gas Phases of an AGN-driven Outflow in a Typical Massive Galaxy at $z \approx 2$ '. In: 871.1, 37, p. 37. doi: [10.3847/1538-4357/aaf6a7](https://doi.org/10.3847/1538-4357/aaf6a7) (cited on page 18).
- Bland-Hawthorn, Joss and Martin Cohen (Jan. 2003). 'The Large-Scale Bipolar Wind in the Galactic Center'. In: 582.1, pp. 246–256. doi: [10.1086/344573](https://doi.org/10.1086/344573) (cited on page 18).
- Sofue, Y. and T. Handa (Aug. 1984). 'A radio lobe over the galactic centre'. In: 310.5978, pp. 568–569. doi: [10.1038/310568a0](https://doi.org/10.1038/310568a0) (cited on page 18).
- Heywood, I. et al. (Sept. 2019). 'Inflation of 430-parsec bipolar radio bubbles in the Galactic Centre by an energetic event'. In: 573.7773, pp. 235–237. doi: [10.1038/s41586-019-1532-5](https://doi.org/10.1038/s41586-019-1532-5) (cited on page 18).
- Ponti, G. et al. (Mar. 2019). 'An X-ray chimney extending hundreds of parsecs above and below the Galactic Centre'. In: 567.7748, pp. 347–350. doi: [10.1038/s41586-019-1009-6](https://doi.org/10.1038/s41586-019-1009-6) (cited on page 18).
- Su, Meng et al. (Dec. 2010). 'Giant Gamma-ray Bubbles from Fermi-LAT: Active Galactic Nucleus Activity or Bipolar Galactic Wind?' In: 724.2, pp. 1044–1082. doi: [10.1088/0004-637X/724/2/1044](https://doi.org/10.1088/0004-637X/724/2/1044) (cited on page 18).
- Dobler, Gregory et al. (July 2010). 'The Fermi Haze: A Gamma-ray Counterpart to the Microwave Haze'. In: 717.2, pp. 825–842. doi: [10.1088/0004-637X/717/2/825](https://doi.org/10.1088/0004-637X/717/2/825) (cited on page 18).
- Planck Collaboration et al. (June 2013). 'Planck intermediate results. IX. Detection of the Galactic haze with Planck'. In: 554, A139, A139. doi: [10.1051/0004-6361/201220271](https://doi.org/10.1051/0004-6361/201220271) (cited on page 18).
- Ackermann, M. et al. (Sept. 2014). 'The Spectrum and Morphology of the Fermi Bubbles'. In: 793.1, 64, p. 64. doi: [10.1088/0004-637X/793/1/64](https://doi.org/10.1088/0004-637X/793/1/64) (cited on page 18).
- Zubovas, K. et al. (July 2011). 'The Milky Way's Fermi bubbles: echoes of the last quasar outburst?' In: 415.1, pp. L21–L25. doi: [10.1111/j.1745-3933.2011.01070.x](https://doi.org/10.1111/j.1745-3933.2011.01070.x) (cited on page 18).

- Guo, Fulai and William G. Mathews (Sept. 2012). 'The Fermi Bubbles. I. Possible Evidence for Recent AGN Jet Activity in the Galaxy'. In: 756.2, 181, p. 181. doi: [10.1088/0004-637X/756/2/181](https://doi.org/10.1088/0004-637X/756/2/181) (cited on page 18).
- Yang, H. Y. K. et al. (Dec. 2012). 'The Fermi Bubbles: Supersonic Active Galactic Nucleus Jets with Anisotropic Cosmic-Ray Diffusion'. In: 761.2, 185, p. 185. doi: [10.1088/0004-637X/761/2/185](https://doi.org/10.1088/0004-637X/761/2/185) (cited on page 18).
- Mou, Guobin et al. (Aug. 2014). 'Fermi Bubbles Inflated by Winds Launched from the Hot Accretion Flow in Sgr A*'. In: 790.2, 109, p. 109. doi: [10.1088/0004-637X/790/2/109](https://doi.org/10.1088/0004-637X/790/2/109) (cited on page 18).
- Ruszkowski, M. et al. (May 2014). 'Fermi bubble simulations: black hole feedback in the Milky Way'. In: *The Galactic Center: Feeding and Feedback in a Normal Galactic Nucleus*. Ed. by L. O. Sjouwerman et al. Vol. 303, pp. 390–394. doi: [10.1017/S1743921314000994](https://doi.org/10.1017/S1743921314000994) (cited on page 18).
- Miller, Matthew J. and Joel N. Bregman (Sept. 2016). 'The Interaction of the Fermi Bubbles with the Milky Way's Hot Gas Halo'. In: 829.1, 9, p. 9. doi: [10.3847/0004-637X/829/1/9](https://doi.org/10.3847/0004-637X/829/1/9) (cited on page 18).
- Bland-Hawthorn, Joss et al. (Nov. 2019). 'The Large-scale Ionization Cones in the Galaxy'. In: 886.1, 45, p. 45. doi: [10.3847/1538-4357/ab44c8](https://doi.org/10.3847/1538-4357/ab44c8) (cited on page 18).
- Ruffa, I. et al. (Jan. 2022). 'The AGN Fuelling/Feedback Cycle in Nearby Radio Galaxies – IV. Molecular Gas Conditions and Jet-ISM Interaction in NGC3100'. In: *Monthly Notices of the Royal Astronomical Society* 510.3, pp. 4485–4503. doi: [10/gn9vfg](https://doi.org/10/gn9vfg) (cited on pages 19, 73, 74, 78, 84, 86).
- Scoville, N. Z. et al. (Aug. 1997). 'CO J = 3–2 Emission in the Radio Galaxy 53W002 at $z = 2.394$ '. In: 485.1, pp. L21–L24. doi: [10.1086/310807](https://doi.org/10.1086/310807) (cited on page 19).
- Papadopoulos, Padelis P. et al. (Jan. 2000). 'CO (4–3) and Dust Emission in Two Powerful High-Z Radio Galaxies, and CO Lines at High Redshifts'. In: 528.2, pp. 626–636. doi: [10.1086/308215](https://doi.org/10.1086/308215) (cited on page 19).
- De Breuck, Carlos et al. (Sept. 2003). 'CO emission from $z > 3$ radio galaxies'. In: 47.4–5, pp. 285–289. doi: [10.1016/S1387-6473\(03\)00040-X](https://doi.org/10.1016/S1387-6473(03)00040-X) (cited on page 19).
- De Breuck, C. et al. (Jan. 2005). 'Detection of two massive CO systems in 4C 41.17 at $z = 3.8$ '. In: 430, pp. L1–L4. doi: [10.1051/0004-6361:200400115](https://doi.org/10.1051/0004-6361:200400115) (cited on page 19).
- Greve, T. R. et al. (May 2004). 'Detection of CO J = 1–0 in the $z = 3.79$ radio galaxy 4C 60.07'. In: 419, pp. 99–107. doi: [10.1051/0004-6361:20035788](https://doi.org/10.1051/0004-6361:20035788) (cited on page 19).
- Nesvadba, N. P. H. et al. (Nov. 2008). 'Evidence for powerful AGN winds at high redshift: dynamics of galactic outflows in radio galaxies during the "Quasar Era"'. In: 491, pp. 407–424. doi: [10.1051/0004-6361:200810346](https://doi.org/10.1051/0004-6361:200810346) (cited on page 19).
- Emonts, B. H. C. et al. (June 2011). 'Molecular CO(1–0) Gas in the $z \sim 2$ Radio Galaxy MRC 0152–209'. In: 734.1, L25, p. L25. doi: [10.1088/2041-8205/734/1/L25](https://doi.org/10.1088/2041-8205/734/1/L25) (cited on page 19).
- Emonts, B. H. C. et al. (Mar. 2014). 'CO(1–0) survey of high- z radio galaxies: alignment of molecular halo gas with distant radio sources'. In: 438.4, pp. 2898–2915. doi: [10.1093/mnras/stt2398](https://doi.org/10.1093/mnras/stt2398) (cited on pages 19, 35).
- Castignani, G. et al. (Mar. 2019). 'Molecular gas in radio galaxies in dense megaparsec-scale environments at $z = 0.4$ – 2.6 '. In: 623, A48, A48. doi: [10.1051/0004-6361/201834066](https://doi.org/10.1051/0004-6361/201834066) (cited on page 19).
- Audibert, A. et al. (Dec. 2022). 'CO in the ALMA Radio-source Catalogue (ARC): The molecular gas content of radio galaxies as a function of redshift'. In: 668, A67, A67. doi: [10.1051/0004-6361/202243666](https://doi.org/10.1051/0004-6361/202243666) (cited on pages 19, 30).
- Ginsburg, Adam et al. (Mar. 2019). 'astroquery: An Astronomical Web-querying Package in Python'. In: 157.3, 98, p. 98. doi: [10.3847/1538-3881/aafc33](https://doi.org/10.3847/1538-3881/aafc33) (cited on page 21).
- Bonzini, M. et al. (Dec. 2013). 'The sub-mJy radio sky in the Extended Chandra Deep Field-South: source population'. In: 436.4, pp. 3759–3771. doi: [10.1093/mnras/stt1879](https://doi.org/10.1093/mnras/stt1879) (cited on page 22).
- Kellermann, K. I. et al. (Oct. 1989). 'VLA Observations of Objects in the Palomar Bright Quasar Survey'. In: 98, p. 1195. doi: [10.1086/115207](https://doi.org/10.1086/115207) (cited on page 22).
- Lim, Jeremy et al. (Dec. 2000). 'Molecular Gas in the Powerful Radio Galaxies 3C 31 and 3C 264: Major or Minor Mergers?' In: 545.2, pp. L93–L97. doi: [10.1086/317885](https://doi.org/10.1086/317885) (cited on page 22).
- Evans, A. S. et al. (Aug. 2005). 'Molecular Gas and Nuclear Activity in Radio Galaxies Detected by IRAS'. In: 159.2, pp. 197–213. doi: [10.1086/431345](https://doi.org/10.1086/431345) (cited on pages 22, 35).
- Ocaña Flaquer, B. et al. (July 2010). 'TANGO I: Interstellar medium in nearby radio galaxies. Molecular gas'. In: 518, A9, A9. doi: [10.1051/0004-6361/200913392](https://doi.org/10.1051/0004-6361/200913392) (cited on pages 22, 35).
- Ruffa, Ilaria et al. (Nov. 2019a). 'The AGN fuelling/feedback cycle in nearby radio galaxies - II. Kinematics of the molecular gas'. In: 489.3, pp. 3739–3757. doi: [10.1093/mnras/stz2368](https://doi.org/10.1093/mnras/stz2368) (cited on pages 22, 35).

- Russell, H. R. et al. (Dec. 2019). 'Driving massive molecular gas flows in central cluster galaxies with AGN feedback'. In: 490.3, pp. 3025–3045. doi: [10.1093/mnras/stz2719](https://doi.org/10.1093/mnras/stz2719) (cited on page 22).
- Dabhade, P. et al. (Nov. 2020). 'Search and analysis of giant radio galaxies with associated nuclei (SAGAN). II. Molecular gas content of giant radio galaxies'. In: 643, A111, A111. doi: [10.1051/0004-6361/202038676](https://doi.org/10.1051/0004-6361/202038676) (cited on page 22).
- Hales, S. E. G. et al. (July 1993). 'The 6C survey of radio sources. VI. The continuous zone $30^\circ < \delta < 51^\circ$, $0^h < \alpha < 09^h 05^m$ and $22^h < \alpha < 24^h$ '. In: 263, pp. 25–30. doi: [10.1093/mnras/263.1.25](https://doi.org/10.1093/mnras/263.1.25) (cited on page 23).
- Condon, J. J. et al. (May 1998). 'The NRAO VLA Sky Survey'. In: 115.5, pp. 1693–1716. doi: [10.1086/300337](https://doi.org/10.1086/300337) (cited on pages 23, 32).
- Wright, A. and R. Otrupcek (Jan. 1990). 'Parkes Catalog, 1990, Australia telescope national facility.' In: *PKS Catalog (1990)*, p. 0 (cited on page 23).
- Griffith, Mark R. et al. (Jan. 1994). 'The Parkes-MIT-NRAO (PMN) Surveys. III. Source Catalog for the Tropical Survey ($-29^\circ < \delta < -9^\circ$ $-3\text{pt}.5$)'. In: 90, p. 179. doi: [10.1086/191863](https://doi.org/10.1086/191863) (cited on page 23).
- Bennett, C. L. et al. (May 1986). 'The MIT-Green Bank (MG) 5 GHz Survey'. In: 61, p. 1. doi: [10.1086/191108](https://doi.org/10.1086/191108) (cited on page 23).
- Murphy, Tara et al. (Mar. 2010). 'The Australia Telescope 20 GHz Survey: the source catalogue'. In: 402.4, pp. 2403–2423. doi: [10.1111/j.1365-2966.2009.15961.x](https://doi.org/10.1111/j.1365-2966.2009.15961.x) (cited on page 23).
- Best, Philip N et al. (2003). 'CENSORS: A Combined EIS–NVSS Survey Of Radio Sources—I. Sample definition, radio data and optical identifications'. In: *Monthly Notices of the Royal Astronomical Society* 346.2, pp. 627–683 (cited on page 24).
- Brookes, MH et al. (2008). 'A Combined EIS–NVSS Survey Of Radio Sources (CENSORS)—III. Spectroscopic observations'. In: *Monthly Notices of the Royal Astronomical Society* 385.3, pp. 1297–1326 (cited on page 24).
- Kimball, Amy E and Željko Ivezić (2008). 'A unified catalog of radio objects detected by NVSS, first, WENSS, GB6, and SDSS'. In: *The Astronomical Journal* 136.2, p. 684 (cited on page 24).
- Hewett, Paul C. and Vivienne Wild (Apr. 2010). 'Improved Redshifts for SDSS Quasar Spectra: Improved SDSS Redshifts'. In: *Monthly Notices of the Royal Astronomical Society*, no–no. doi: [10.1111/j.1365-2966.2010.16648.x](https://doi.org/10.1111/j.1365-2966.2010.16648.x) (cited on page 24).
- Kolmogorov, An (1933). 'Sulla determinazione empirica di una legge di distribuzione'. In: *Giorn Dell'inst Ital Degli Att* 4, pp. 89–91 (cited on page 24).
- Smirnov, Nikolai V (1939). 'On the estimation of the discrepancy between empirical curves of distribution for two independent samples'. In: *Bull. Math. Univ. Moscou* 2.2, pp. 3–14 (cited on page 24).
- Press, William H (2007). *Numerical recipes 3rd edition: The art of scientific computing*. Cambridge university press (cited on page 25).
- McMullin, J. P. et al. (Oct. 2007). 'CASA Architecture and Applications'. In: *Astronomical Data Analysis Software and Systems XVI*. Ed. by R. A. Shaw et al. Vol. 376. Astronomical Society of the Pacific Conference Series, p. 127 (cited on page 29).
- Ruffa, Ilaria et al. (Apr. 2019b). 'The AGN fuelling/feedback cycle in nearby radio galaxies I. ALMA observations and early results'. In: 484.3, pp. 4239–4259. doi: [10.1093/mnras/stz255](https://doi.org/10.1093/mnras/stz255) (cited on pages 30, 86).
- Tacconi, L. J. et al. (May 2013). 'Phibss: Molecular Gas Content and Scaling Relations in $z \sim 1-3$ Massive, Main-sequence Star-forming Galaxies'. In: 768, 74, p. 74. doi: [10.1088/0004-637X/768/1/74](https://doi.org/10.1088/0004-637X/768/1/74) (cited on page 30).
- Bolatto, A. D. et al. (Aug. 2013). 'The CO-to-H₂ Conversion Factor'. In: 51, pp. 207–268. doi: [10.1146/annurev-astro-082812-140944](https://doi.org/10.1146/annurev-astro-082812-140944) (cited on page 30).
- Popping, Gergö et al. (May 2015). 'Evolution of the atomic and molecular gas content of galaxies in dark matter haloes'. In: 449.1, pp. 477–493. doi: [10.1093/mnras/stv318](https://doi.org/10.1093/mnras/stv318) (cited on pages 31, 32).
- Schmidt, Maarten (Feb. 1968). 'Space Distribution and Luminosity Functions of Quasi-Stellar Radio Sources'. In: 151, p. 393. doi: [10.1086/149446](https://doi.org/10.1086/149446) (cited on page 30).
- Schechter, P. (Jan. 1976). 'An analytic expression for the luminosity function for galaxies.' In: 203, pp. 297–306. doi: [10.1086/154079](https://doi.org/10.1086/154079) (cited on page 31).
- Riechers, Dominik A. et al. (Feb. 2019). 'COLDz: Shape of the CO Luminosity Function at High Redshift and the Cold Gas History of the Universe'. In: 872.1, 7, p. 7. doi: [10.3847/1538-4357/aafc27](https://doi.org/10.3847/1538-4357/aafc27) (cited on page 31).

- Bisigello, L. et al. (July 2021). 'Simulating the infrared sky with a SPRITZ'. In: 651, A52, A52. doi: [10.1051/0004-6361/202039909](https://doi.org/10.1051/0004-6361/202039909) (cited on page 33).
- Saintonge, Amélie et al. (Dec. 2017). 'xCOLD GASS: The Complete IRAM 30 m Legacy Survey of Molecular Gas for Galaxy Evolution Studies'. In: 233.2, 22, p. 22. doi: [10.3847/1538-4365/aa97e0](https://doi.org/10.3847/1538-4365/aa97e0) (cited on page 31).
- Fletcher, Thomas J. et al. (Feb. 2021). 'The cosmic abundance of cold gas in the local Universe'. In: 501.1, pp. 411–418. doi: [10.1093/mnras/staa3025](https://doi.org/10.1093/mnras/staa3025) (cited on page 31).
- Keres, Dusan et al. (Jan. 2003). 'CO Luminosity Functions for Far-Infrared- and B-Band-selected Galaxies and the First Estimate for Ω_{HI+H_2} '. In: 582.2, pp. 659–667. doi: [10.1086/344820](https://doi.org/10.1086/344820) (cited on page 31).
- Vallini, L. et al. (Feb. 2016). 'CO luminosity function from Herschel-selected galaxies and the contribution of AGN'. In: 456.1, pp. L40–L44. doi: [10.1093/mnrasl/slv173](https://doi.org/10.1093/mnrasl/slv173) (cited on page 31).
- Decarli, Roberto et al. (Sept. 2019). 'The ALMA Spectroscopic Survey in the HUDF: CO Luminosity Functions and the Molecular Gas Content of Galaxies through Cosmic History'. In: 882.2, 138, p. 138. doi: [10.3847/1538-4357/ab30fe](https://doi.org/10.3847/1538-4357/ab30fe) (cited on page 31).
- Condon, J. J. et al. (Aug. 2002). 'Radio Sources and Star Formation in the Local Universe'. In: 124.2, pp. 675–689. doi: [10.1086/341650](https://doi.org/10.1086/341650) (cited on page 32).
- Prandoni, I. et al. (Nov. 2010). 'Molecular disks in radio galaxies. The pathway to ALMA'. In: 523, A38, A38. doi: [10.1051/0004-6361/201015456](https://doi.org/10.1051/0004-6361/201015456) (cited on page 35).
- Olivares, V. et al. (Nov. 2019). 'Ubiquitous cold and massive filaments in cool core clusters'. In: 631, A22, A22. doi: [10.1051/0004-6361/201935350](https://doi.org/10.1051/0004-6361/201935350) (cited on page 35).
- Leon, S. et al. (Jan. 2003). 'Molecular gas in nearby Early-Type Powerful Classical Radio Galaxies'. In: *Active Galactic Nuclei: From Central Engine to Host Galaxy*. Ed. by Suzy Collin et al. Vol. 290. Astronomical Society of the Pacific Conference Series, p. 525 (cited on page 35).
- Taniguchi, Yoshiaki et al. (July 1990). 'Circumnuclear Molecular Gas in Seyfert Galaxies'. In: 358, p. 132. doi: [10.1086/168967](https://doi.org/10.1086/168967) (cited on page 35).
- Saripalli, L. and K. H. Mack (Apr. 2007). 'A search for molecular gas in restarting radio galaxies'. In: 376.3, pp. 1385–1392. doi: [10.1111/j.1365-2966.2007.11544.x](https://doi.org/10.1111/j.1365-2966.2007.11544.x) (cited on page 35).
- Nesvadba, N. P. H. et al. (Oct. 2010). 'Energetics of the molecular gas in the H₂ luminous radio galaxy 3C 326: Evidence for negative AGN feedback'. In: 521, A65, A65. doi: [10.1051/0004-6361/200913333](https://doi.org/10.1051/0004-6361/200913333) (cited on page 35).
- Lo, K. Y. et al. (Jan. 1999). 'A survey of molecular gas content of galaxies at $0.08 < Z < 1.06$ '. In: 341, pp. 348–354 (cited on page 35).
- Evans, A. S. et al. (Feb. 1996). 'A Search for CO Emission in High-Redshift Powerful Radio Galaxies'. In: 457, p. 658. doi: [10.1086/176761](https://doi.org/10.1086/176761) (cited on page 35).
- Papachristou, Michalis et al. (Nov. 2021). 'CO kinematics unveil outflows plausibly driven by a young jet in the gigahertz peaked radio core of NGC 6328'. In: *Astronomische Nachrichten* 342.1160, pp. 1160–1165. doi: [10.1002/asna.20210063](https://doi.org/10.1002/asna.20210063) (cited on page 39).
- Papachristou, M. et al. (Nov. 2023). 'A plausible link between dynamically unsettled molecular gas and the radio jet in NGC 6328'. In: 679, A115, A115. doi: [10.1051/0004-6361/202346464](https://doi.org/10.1051/0004-6361/202346464) (cited on page 39).
- Maccagni, F. M. et al. (Nov. 2014). 'What Triggers a Radio AGN?. The Intriguing Case of PKS B1718-649'. In: *Astronomy & Astrophysics* 571, A67. doi: [10.1051/0004-6361/201424334](https://doi.org/10.1051/0004-6361/201424334) (cited on pages 39, 42–44, 67, 71).
- Maccagni, F. M. et al. (Apr. 2016b). 'The Warm Molecular Hydrogen of PKS B1718–649: Feeding a Newly Born Radio AGN'. In: *Astronomy & Astrophysics* 588, A46. doi: [10.1051/0004-6361/201528016](https://doi.org/10.1051/0004-6361/201528016) (cited on pages 39, 49, 67, 73, 77).
- Maccagni, F. M. et al. (June 2018). 'ALMA Observations of AGN Fuelling: The Case of PKS B1718-649'. In: *Astronomy & Astrophysics* 614, A42. doi: [10.1051/0004-6361/201732269](https://doi.org/10.1051/0004-6361/201732269) (cited on pages 39, 43, 71).
- Sérsic, J. L. (Feb. 1963). 'Influence of the atmospheric and instrumental dispersion on the brightness distribution in a galaxy'. In: *Boletín de la Asociación Argentina de Astronomía La Plata Argentina* 6, pp. 41–43 (cited on page 40).
- de Vaucouleurs, Gerard (Jan. 1948). 'Recherches sur les Nebuleuses Extragalactiques'. In: *Annales d'Astrophysique* 11, p. 247 (cited on page 40).
- Veron-Cetty, M.-P. et al. (May 1995). 'PKS B1718-649: A Gas Rich Radio Galaxy.' In: *Astronomy & Astrophysics* 297, p. L79 (cited on pages 40, 42, 67).

- Bicknell, Geoffrey V. et al. (Aug. 1997). 'Unification of the Radio and Optical Properties of Gigahertz Peak Spectrum and Compact Steep-Spectrum Radio Sources'. In: *The Astrophysical Journal* 485, pp. 112–124. doi: [10/dfqj3n](https://doi.org/10/dfqj3n) (cited on pages 40, 41).
- Angioni, R. et al. (July 2019). 'Gamma-Ray Emission in Radio Galaxies under the VLBI Scope – I. Parsec-scale Kinematics and High-Energy Properties of γ -Ray Detected TANAMI Radio Galaxies'. In: *Astronomy & Astrophysics* 627, A148. doi: [10/gg23d4](https://doi.org/10/gg23d4) (cited on pages 40, 42, 76, 77).
- Tingay, S. J. et al. (Jan. 2015). 'THE SPECTRAL VARIABILITY OF THE GHZ-PEAKED SPECTRUM RADIO SOURCE PKS 1718-649 AND A COMPARISON OF ABSORPTION MODELS'. In: *AJ* 149.2, p. 74. doi: [10.1088/0004-6256/149/2/74](https://doi.org/10.1088/0004-6256/149/2/74) (cited on pages 40, 41).
- Filippenko, A. V. (Feb. 1985). 'New Evidence for Photoionization as the Dominant Excitation Mechanism in Liners'. In: *The Astrophysical Journal* 289, pp. 475–489. doi: [10.1086/162909](https://doi.org/10.1086/162909) (cited on pages 40, 42).
- O'Dea, Christopher P. and D. J. Saikia (Dec. 2021). 'Compact Steep-Spectrum and Peaked-Spectrum Radio Sources'. In: *Astron Astrophys Rev* 29.1, p. 3. doi: [10/gkrch5](https://doi.org/10/gkrch5) (cited on pages 40, 41).
- Kellermann, K. I. and I. I. K. Pauliny-Toth (Feb. 1969). 'The Spectra of Opaque Radio Sources'. In: 155, p. L71. doi: [10.1086/180305](https://doi.org/10.1086/180305) (cited on page 41).
- Tingay, S. J. et al. (June 1997). 'The Nearest GHz Peaked-Spectrum Radio Galaxy, PKS 1718-649'. In: *The Astronomical Journal* 113, p. 2025. doi: [10.1086/118414](https://doi.org/10.1086/118414) (cited on pages 41, 42, 76).
- Bicknell, Geoffrey V. et al. (Apr. 2018). 'Relativistic Jet Feedback II: Relationship to Gigahertz Peak Spectrum and Compact Steep Spectrum Radio Galaxies'. In: *Monthly Notices of the Royal Astronomical Society* 475.3, pp. 3493–3501. doi: [10.1093/mnras/sty070](https://doi.org/10.1093/mnras/sty070) (cited on page 41).
- Tingay, S. J. and M. de Kool (2003). 'Radio Spectral Variability of the Nearby GPS Galaxy PKS 1718-649'. In: *Publ. & Astron. Soc. Aust* 20.1, pp. 140–143. doi: [10.1071/AS02045](https://doi.org/10.1071/AS02045) (cited on page 41).
- Beuchert, T. et al. (Apr. 2018). 'Extended X-ray Emission in PKS 1718-649'. In: *Astronomy & Astrophysics* 612, p. L4. doi: [10.1051/0004-6361/201833064](https://doi.org/10.1051/0004-6361/201833064) (cited on pages 42, 43, 77).
- Maccagni, F. M. et al. (Feb. 2016a). 'PKS B1718-649: An HI and H2 Perspective on the Birth of a Compact Radio Source'. In: *Astron. Nachr.* 337.1-2, pp. 154–158. doi: [10.1002/asna.201512285](https://doi.org/10.1002/asna.201512285) (cited on page 43).
- Siemiginowska, Aneta et al. (May 2016). 'X-Ray Properties of the Youngest Radio Sources and Their Environments'. In: *The Astrophysical Journal* 823, p. 57. doi: [10/gg496z](https://doi.org/10/gg496z) (cited on page 42).
- Migliori, G. et al. (Apr. 2016). 'FIRST DETECTION IN GAMMA-RAYS OF A YOUNG RADIO GALAXY: FERMI -LAT OBSERVATIONS OF THE COMPACT SYMMETRIC OBJECT PKS 1718-649'. In: *ApJ* 821.2, p. L31. doi: [10.3847/2041-8205/821/2/L31](https://doi.org/10.3847/2041-8205/821/2/L31) (cited on pages 42, 77).
- Keel, William C. and Rogier A. Windhorst (Dec. 1991). 'The Ultraviolet Spectra of Nearby Radio Galaxies'. In: *ApJ* 383, p. 135. doi: [10.1086/170770](https://doi.org/10.1086/170770) (cited on page 42).
- Willett, Kyle W. et al. (Apr. 2010). 'SPITZER MID-INFRARED SPECTROSCOPY OF COMPACT SYMMETRIC OBJECTS: WHAT POWERS RADIO-LOUD ACTIVE GALACTIC NUCLEI?' In: *ApJ* 713.2, pp. 1393–1412. doi: [10.1088/0004-637X/713/2/1393](https://doi.org/10.1088/0004-637X/713/2/1393) (cited on pages 42, 53, 75).
- McMullin, J P et al. (2007). 'CASA Architecture and Applications'. In: p. 4 (cited on page 44).
- Larson, R. B. (Mar. 1981). 'Turbulence and star formation in molecular clouds.' In: 194, pp. 809–826. doi: [10.1093/mnras/194.4.809](https://doi.org/10.1093/mnras/194.4.809) (cited on page 46).
- Stahler, Steven W and Francesco Palla (2008). *The formation of stars*. John Wiley & Sons (cited on page 47).
- Solomon, P.M. and P.A. Vanden Bout (Sept. 2005). 'Molecular Gas at High Redshift'. In: *Annual Review of Astronomy & Astrophysics* 43.1, pp. 677–725. doi: [10.1146/annurev.astro.43.051804.102221](https://doi.org/10.1146/annurev.astro.43.051804.102221) (cited on page 47).
- Solomon, P. M. et al. (Mar. 1997). 'The Molecular Interstellar Medium in Ultraluminous Infrared Galaxies'. In: 478.1, pp. 144–161. doi: [10.1086/303765](https://doi.org/10.1086/303765) (cited on page 47).
- Bolatto, Alberto D. et al. (Aug. 2013). 'The CO-to-H₂ Conversion Factor'. In: *Annu. Rev. Astron. Astrophys.* 51.1, pp. 207–268. doi: [10.1146/annurev-astro-082812-140944](https://doi.org/10.1146/annurev-astro-082812-140944) (cited on page 47).
- Spekkens, Kristine and J. A. Sellwood (July 2007). 'Modeling Noncircular Motions in Disk Galaxies: Application to NGC 2976'. In: 664.1, pp. 204–214. doi: [10.1086/518471](https://doi.org/10.1086/518471) (cited on page 51).
- Sellwood, J. A. and Ricardo Zánmar Sánchez (June 2010). 'Quantifying non-circular streaming motions in disc galaxies'. In: 404.4, pp. 1733–1744. doi: [10.1111/j.1365-2966.2010.16430.x](https://doi.org/10.1111/j.1365-2966.2010.16430.x) (cited on page 51).

- Sellwood, J. A. and Kristine Spekkens (Sept. 2015). ‘DiskFit: a code to fit simple non-axisymmetric galaxy models either to photometric images or to kinematic maps’. In: *arXiv e-prints*, arXiv:1509.07120, arXiv:1509.07120. doi: [10.48550/arXiv.1509.07120](https://doi.org/10.48550/arXiv.1509.07120) (cited on page 51).
- Teodoro, EM Di and Filippo Fraternali (2015). ‘3D BAROLO: a new 3D algorithm to derive rotation curves of galaxies’. In: *Monthly Notices of the Royal Astronomical Society* 451.3, pp. 3021–3033 (cited on page 52).
- Davis, Timothy A. et al. (June 2020). *KinMS: Three-dimensional kinematic modelling of arbitrary gas distributions*. Astrophysics Source Code Library, record ascl:2006.003 (cited on page 52).
- Bouché, N. et al. (Jan. 2015a). *GalPaK 3D: Galaxy parameters and kinematics extraction from 3D data*. Astrophysics Source Code Library, record ascl:1501.014 (cited on page 52).
- (Sept. 2015b). ‘GalPak^{3D}: A Bayesian Parametric Tool for Extracting Morphokinematics of Galaxies from 3D Data’. In: 150.3, 92, p. 92. doi: [10.1088/0004-6256/150/3/92](https://doi.org/10.1088/0004-6256/150/3/92) (cited on page 52).
- Józsa, G. I. G. et al. (June 2007). ‘Kinematic modelling of disk galaxies. I. A new method to fit tilted rings to data cubes’. In: 468.2, pp. 731–774. doi: [10.1051/0004-6361:20066164](https://doi.org/10.1051/0004-6361/20066164) (cited on page 52).
- Hernquist, Lars (June 1990). ‘An Analytical Model for Spherical Galaxies and Bulges’. In: *ApJ* 356, p. 359. doi: [10.1086/168845](https://doi.org/10.1086/168845) (cited on page 52).
- Navarro, Julio F. et al. (May 1996). ‘The Structure of Cold Dark Matter Halos’. In: *The Astrophysical Journal* 462, p. 563. doi: [10.1086/177173](https://doi.org/10.1086/177173) (cited on page 53).
- Bullock, J. S. et al. (Mar. 2001). ‘Profiles of Dark Haloes: Evolution, Scatter and Environment’. In: *Monthly Notices of the Royal Astronomical Society* 321.3, pp. 559–575. doi: [10.1046/j.1365-8711.2001.04068.x](https://doi.org/10.1046/j.1365-8711.2001.04068.x) (cited on page 53).
- Tohline, J. E. et al. (Jan. 1982). ‘Using Gaseous Disks to Probe the Geometric Structure of Elliptical Galaxies’. In: *ApJ* 252, p. 92. doi: [10/chmzh6](https://doi.org/10/chmzh6) (cited on pages 54, 56, 57).
- Lake, G. and C. Norman (July 1983). ‘Stellar and Gaseous Dynamics of Triaxial Galaxies’. In: *ApJ* 270, p. 51. doi: [10.1086/161097](https://doi.org/10.1086/161097) (cited on page 54).
- Steiman-Cameron, Thomas Y. and Richard H. Durisen (Feb. 1988). ‘Evolution of Inclined Galactic Gas Disks. I. A Cloud-Fluid Approach’. In: *The Astrophysical Journal* 325, p. 26. doi: [10.1086/165981](https://doi.org/10.1086/165981) (cited on pages 54, 55, 57).
- Sparke, Linda S. (Dec. 1996). ‘A Dynamical Model for the Twisted Gas Disk in Centaurus A’. In: *The Astrophysical Journal* 473, p. 810. doi: [10/b28xvh](https://doi.org/10/b28xvh) (cited on page 54).
- Davis, Timothy A. and Martin Bureau (Mar. 2016). ‘On the Depletion and Accretion Time-Scales of Cold Gas in Local Early-Type Galaxies’. In: *Monthly Notices of the Royal Astronomical Society* 457, pp. 272–280. doi: [10.1093/mnras/stv2998](https://doi.org/10.1093/mnras/stv2998) (cited on page 54).
- Chandrasekhar, Subrahmanyan (Jan. 1969). *Ellipsoidal Figures of Equilibrium* (cited on page 55).
- Binney, James and Scott Tremaine (2008). *Galactic Dynamics: Second Edition* (cited on page 55).
- Johnson, Steven G. (2013). *QuadGK.jl: Gauss–Kronrod integration in Julia*. <https://github.com/JuliaMath/QuadGK.jl> (cited on page 57).
- Bezanson, Jeff et al. (July 2015). ‘Julia: A Fresh Approach to Numerical Computing’. In: *arXiv:1411.1607 [cs]* (cited on page 57).
- Revels, J. et al. (2016). ‘Forward-Mode Automatic Differentiation in Julia’. In: *arXiv:1607.07892 [cs.MS]* (cited on page 57).
- Rackauckas, Christopher and Qing Nie (2017). ‘DifferentialEquations.jl – A Performant and Feature-Rich Ecosystem for Solving Differential Equations in Julia’. In: *The Journal of Open Research Software* 5.1. Exported from <https://app.dimensions.ai> on 2019/05/05. doi: [10.5334/jors.151](https://doi.org/10.5334/jors.151) (cited on page 57).
- Tsitouras, Ch (2011). ‘Runge–Kutta pairs of order 5 (4) satisfying only the first column simplifying assumption’. In: *Computers & Mathematics with Applications* 62.2, pp. 770–775 (cited on page 57).
- Rosenbrock, HH (1963). ‘Some general implicit processes for the numerical solution of differential equations’. In: *The Computer Journal* 5.4, pp. 329–330 (cited on page 57).
- Fritsch, Frederick N and Judy Butland (1984). ‘A method for constructing local monotone piecewise cubic interpolants’. In: *SIAM journal on scientific and statistical computing* 5.2, pp. 300–304 (cited on page 58).
- Goodman, Jonathan and Jonathan Weare (Jan. 2010). ‘Ensemble Samplers with Affine Invariance’. In: *Communications in Applied Mathematics and Computational Science* 5.1, pp. 65–80. doi: [10.2140/camcos.2010.5.65](https://doi.org/10.2140/camcos.2010.5.65) (cited on page 61).

- Foreman-Mackey, D. et al. (2013). 'emcee: The MCMC Hammer'. In: *PASP* 125, pp. 306–312. doi: [10.1086/670067](https://doi.org/10.1086/670067) (cited on page 61).
- Vesselinov, Velimir V. and Daniel O'Malley (2013). *AffineInvariantMCMC.jl*. <https://github.com/madsjulia/AffineInvariantMCMC.jl> (cited on page 61).
- Wolff, Schuyler G. et al. (Dec. 2017). 'Hubble Space Telescope Scattered-light Imaging and Modeling of the Edge-on Protoplanetary Disk ESO-H α 569'. In: *ApJ* 851.1, p. 56. doi: [10/gjr9k2](https://doi.org/10/gjr9k2). (Visited on 04/22/2021) (cited on page 63).
- Davis, Timothy A. et al. (July 2017). 'WISDOM Project – II. Molecular Gas Measurement of the Supermassive Black Hole Mass in NGC 4697'. In: *Monthly Notices of the Royal Astronomical Society* 468.4, pp. 4675–4690. doi: [10/gjrrwc2](https://doi.org/10/gjrrwc2). (Visited on 04/21/2021) (cited on page 63).
- Smith, Mark D. et al. (May 2019). 'WISDOM Project - IV. A Molecular Gas Dynamical Measurement of the Supermassive Black Hole Mass in NGC 524'. In: *Monthly Notices of the Royal Astronomical Society* 485, pp. 4359–4374. doi: [10/gn7ntc](https://doi.org/10/gn7ntc). (Visited on 01/21/2022) (cited on page 63).
- Wolff, S. et al. (Mar. 2021). 'The Anatomy of an Unusual Edge-on Protoplanetary Disk I. Dust Settling in a Cold Disk'. In: *arXiv:2103.02665 [astro-ph]*. (Visited on 04/21/2021) (cited on page 63).
- McDonald, B. et al. (2013). *astrodendro, Astronomical Dendrograms in Python*. <https://github.com/dendrograms/astrodendro> (cited on page 65).
- Quillen, A. C. and Gary A. Bower (Sept. 1999). 'M84: A Warp Caused by Jet-induced Pressure Gradients?' In: *ApJ* 522.2, pp. 718–726. doi: [10/cpqnj2](https://doi.org/10/cpqnj2) (cited on page 74).
- Cicone, CLAUDIA et al. (2014). 'Massive molecular outflows and evidence for AGN feedback from CO observations'. In: *Astronomy & Astrophysics* 562, A21 (cited on pages 74, 83, 84).
- Sullivan, M. et al. (Sept. 2006). 'Rates and Properties of Type Ia Supernovae as a Function of Mass and Star Formation in Their Host Galaxies'. In: *ApJ* 648.2, pp. 868–883. doi: [10/fchxw9](https://doi.org/10/fchxw9) (cited on page 75).
- Zubovas, Kastytis and Emanuele Nardini (Sept. 2020). 'Intermittent AGN Episodes Drive Outflows with a Large Spread of Observable Loading Factors'. In: *Monthly Notices of the Royal Astronomical Society* 498.3, pp. 3633–3647. doi: [10.1093/mnras/staa2652](https://doi.org/10.1093/mnras/staa2652) (cited on pages 75, 84).
- Sobolewska, Małgosia et al. (Dec. 2022). 'The Origin of High Energy Emission in the Young Radio Source PKS 1718-649'. In: *ApJ* 941.1, p. 52. doi: [10.3847/1538-4357/ac98ba](https://doi.org/10.3847/1538-4357/ac98ba) (cited on page 75).
- Willott, Chris J. et al. (Nov. 1999). 'The Emission Line - Radio Correlation for Radio Sources Using the 7C Redshift Survey'. In: *Monthly Notices of the Royal Astronomical Society* 309.4, pp. 1017–1033. doi: [10.1046/j.1365-8711.1999.02907.x](https://doi.org/10.1046/j.1365-8711.1999.02907.x) (cited on page 75).
- Birzan, L. et al. (Oct. 2008). 'Radiative Efficiency and Content of Extragalactic Radio Sources: Toward a Universal Scaling Relation between Jet Power and Radio Power'. In: *The Astrophysical Journal* 686, pp. 859–880. doi: [10.1086/59141610.48550/arXiv.0806.1929](https://doi.org/10.1086/59141610.48550/arXiv.0806.1929) (cited on pages 75, 85, 86).
- Cavagnolo, K. W. et al. (Sept. 2010). 'A Relationship Between AGN Jet Power and Radio Power'. In: 720.2, pp. 1066–1072. doi: [10.1088/0004-637X/720/2/1066](https://doi.org/10.1088/0004-637X/720/2/1066) (cited on pages 75, 85).
- Wójtowicz, A. et al. (Apr. 2020). 'On the Jet Production Efficiency in a Sample of the Youngest Radio Galaxies'. In: *ApJ* 892.2, p. 116. doi: [10/gg24jb](https://doi.org/10/gg24jb) (cited on page 75).
- Aalto, S. et al. (June 2016). 'A Precessing Molecular Jet Signaling an Obscured, Growing Supermassive Black Hole in NGC 1377?' In: *Astronomy & Astrophysics* 590, A73. doi: [10.1051/0004-6361/201527664](https://doi.org/10.1051/0004-6361/201527664) (cited on page 76).
- Zovaro, Henry R. M. et al. (Apr. 2019). 'Jets Blowing Bubbles in the Young Radio Galaxy 4C 31.04'. In: *Monthly Notices of the Royal Astronomical Society* 484.3, pp. 3393–3409. doi: [10.1093/mnras/stz233](https://doi.org/10.1093/mnras/stz233) (cited on pages 76, 81).
- Fernández-Ontiveros, JA et al. (2020). 'A CO molecular gas wind 340 pc away from the Seyfert 2 nucleus in ESO 420-G13 probes an elusive radio jet'. In: *Astronomy & Astrophysics* 633, A127 (cited on pages 76, 81, 82, 86).
- Singha, M. et al. (2023). *The Close AGN Reference Survey (CARS): An interplay between radio jets and AGN radiation in the radio-quiet AGN HE 0040-1105* (cited on page 76).
- Schawinski, Kevin et al. (Aug. 2015). 'Active galactic nuclei flicker: an observational estimate of the duration of black hole growth phases of $\sim 10^5$ yr'. In: 451.3, pp. 2517–2523. doi: [10.1093/mnras/stv1136](https://doi.org/10.1093/mnras/stv1136) (cited on page 76).

- Gilli, R. et al. (Mar. 2000). 'The variability of the Seyfert galaxy NGC 2992: the case for a revived AGN'. In: 355, pp. 485–498. doi: [10.48550/arXiv.astro-ph/0001107](https://doi.org/10.48550/arXiv.astro-ph/0001107) (cited on page 76).
- Reynoso, MM et al. (2011). 'A lepto-hadronic model for high-energy emission from FR I radiogalaxies'. In: *Astronomy & Astrophysics* 531, A30 (cited on page 76).
- Rieger, Frank M. (Jan. 2017). 'Gamma-Rays from Non-Blazar AGN'. In: 1792, p. 020008. doi: [10.1063/1.4968893](https://doi.org/10.1063/1.4968893) (cited on page 76).
- Maloney, Philip R. et al. (July 1996). 'X-Ray-irradiated Molecular Gas. I. Physical Processes and General Results'. In: *The Astrophysical Journal* 466, p. 561. doi: [10.1086/177532](https://doi.org/10.1086/177532) (cited on page 76).
- Wolfire, Mark G. et al. (Aug. 2022). 'Photodissociation and X-Ray-Dominated Regions'. In: *Annual Review of Astronomy & Astrophysics, Volume 60*, pp. 247-318 60, p. 247. doi: [10.1146/annurev-astro-052920-010254](https://doi.org/10.1146/annurev-astro-052920-010254) (cited on page 76).
- Blandford, Roger et al. (Aug. 2019). 'Relativistic Jets from Active Galactic Nuclei'. In: 57, pp. 467–509. doi: [10.1146/annurev-astro-081817-051948](https://doi.org/10.1146/annurev-astro-081817-051948) (cited on page 77).
- Kovalev, Y. Y. et al. (July 2020). 'A transition from parabolic to conical shape as a common effect in nearby AGN jets'. In: 495.4, pp. 3576–3591. doi: [10.1093/mnras/staa1121](https://doi.org/10.1093/mnras/staa1121) (cited on page 77).
- Okino, Hiroki et al. (Nov. 2022). 'Collimation of the Relativistic Jet in the Quasar 3C 273'. In: 940.1, 65, p. 65. doi: [10.3847/1538-4357/ac97e5](https://doi.org/10.3847/1538-4357/ac97e5) (cited on page 77).
- Baczko, A.-K. et al. (Feb. 2022). 'Ambilateral Collimation Study of the Twin-Jets in NGC1052'. In: *Astronomy & Astrophysics* 658, A119. doi: [10.1051/0004-6361/202141897](https://doi.org/10.1051/0004-6361/202141897) (cited on page 77).
- Roychowdhury, Agniva et al. (Aug. 2023). 'CAGNVAS II. Proper Motions in the sub-kiloparsec Jet of 3C 78: Novel Constraints on the Physical Nature of Relativistic Jets'. In: *arXiv e-prints*, arXiv:2308.00842, arXiv:2308.00842. doi: [10.48550/arXiv.2308.00842](https://doi.org/10.48550/arXiv.2308.00842) (cited on page 77).
- Vlahakis, Nektarios and Ariele Königl (Apr. 2004). 'Magnetic Driving of Relativistic Outflows in Active Galactic Nuclei. I. Interpretation of Parsec-Scale Accelerations'. In: *The Astrophysical Journal* 605, pp. 656–661. doi: [10.1086/382670](https://doi.org/10.1086/382670) (cited on page 77).
- Fendt, Christian (Nov. 2006). 'Collimation of Astrophysical Jets: The Role of the Accretion Disk Magnetic Field Distribution'. In: *The Astrophysical Journal* 651, pp. 272–287. doi: [10.1086/507976](https://doi.org/10.1086/507976) (cited on page 77).
- Porth, Oliver et al. (Aug. 2011). 'Synchrotron Radiation of Self-collimating Relativistic Magnetohydrodynamic Jets'. In: *The Astrophysical Journal* 737, p. 42. doi: [10.1088/0004-637X/737/1/42](https://doi.org/10.1088/0004-637X/737/1/42) (cited on page 77).
- van de Voort, Freeke et al. (Aug. 2015). 'The Creation and Persistence of a Misaligned Gas Disc in a Simulated Early-Type Galaxy'. In: *Monthly Notices of the Royal Astronomical Society* 451, pp. 3269–3277. doi: [10.1093/mnras/stv1217](https://doi.org/10.1093/mnras/stv1217) (cited on page 77).
- Hopkins, Philip F. et al. (Nov. 2014). 'Galaxies on FIRE (Feedback In Realistic Environments): stellar feedback explains cosmologically inefficient star formation'. In: 445.1, pp. 581–603. doi: [10.1093/mnras/stu1738](https://doi.org/10.1093/mnras/stu1738) (cited on page 77).
- Raimundo, Sandra I. (June 2021). 'External Gas Accretion Provides a Fresh Gas Supply to the Active S0 Galaxy NGC 5077'. In: *Astronomy & Astrophysics* 650, A34. doi: [10/gn8dcv](https://doi.org/10/gn8dcv) (cited on page 78).
- Maccagni, F. M. et al. (July 2023). 'The AGN fuelling/feedback cycle in nearby radio galaxies. V. The cold atomic gas of NGC 3100 and its group'. In: 675, A59, A59. doi: [10.1051/0004-6361/202346521](https://doi.org/10.1051/0004-6361/202346521) (cited on page 78).
- Helou, G. et al. (Nov. 1985). 'Thermal Infrared and Nonthermal Radio : Remarkable Correlation in Disks of Galaxies.' In: *The Astrophysical Journal* 298, pp. L7–L11. doi: [10.1086/184556](https://doi.org/10.1086/184556) (cited on page 81).
- Kornecki, P. et al. (Jan. 2022). 'Exploring the physics behind the non-thermal emission from star-forming galaxies detected in γ rays'. In: 657, A49, A49. doi: [10.1051/0004-6361/202141295](https://doi.org/10.1051/0004-6361/202141295) (cited on page 81).
- Ivison, RJ et al. (2010). 'The far-infrared/radio correlation as probed by Herschel'. In: *Astronomy & Astrophysics* 518, p. L31 (cited on pages 81, 84).
- Dasyra, K. M. et al. (Dec. 2015). 'A Radio Jet Drives a Molecular and Atomic Gas Outflow in Multiple Regions within One Square Kiloparsec of the Nucleus of the Nearby Galaxy IC5063'. In: *The Astrophysical Journal* 815, p. 34. doi: [10.1088/0004-637X/815/1/3410.48550/arXiv.1503.05484](https://doi.org/10.1088/0004-637X/815/1/3410.48550/arXiv.1503.05484) (cited on page 82).
- Querejeta, M et al. (2016). 'AGN feedback in the nucleus of M 51'. In: *Astronomy & Astrophysics* 593, A118 (cited on page 82).

- Matsushita, Satoki et al. (Jan. 2015). 'Resolving the Bright HCN(1-0) Emission toward the Seyfert 2 Nucleus of M51: Shock Enhancement by Radio Jets and Weak Masing by Infrared Pumping?' In: *The Astrophysical Journal* 799, p. 26. doi: [10.1088/0004-637X/799/1/2610.48550/arXiv.1410.7863](https://doi.org/10.1088/0004-637X/799/1/2610.48550/arXiv.1410.7863) (cited on page 82).
- García-Burillo, S et al. (2019). 'ALMA images the many faces of the NGC 1068 torus and its surroundings'. In: *Astronomy & Astrophysics* 632, A61 (cited on pages 82, 83).
- Aalto, S et al. (2020). 'ALMA resolves the remarkable molecular jet and rotating wind in the extremely radio-quiet galaxy NGC 1377'. In: *Astronomy & Astrophysics* 640, A104 (cited on pages 82, 83).
- Fu, Hai and Alan Stockton (Jan. 2009). 'Extended Emission-Line Regions: Remnants of Quasar Superwinds?' In: *The Astrophysical Journal* 690, pp. 953–973. doi: [10.1088/0004-637X/690/1/95310.48550/arXiv.0809.1117](https://doi.org/10.1088/0004-637X/690/1/95310.48550/arXiv.0809.1117) (cited on page 82).
- Veilleux, S. et al. (Oct. 2013). 'Fast Molecular Outflows in Luminous Galaxy Mergers: Evidence for Quasar Feedback from Herschel'. In: *The Astrophysical Journal* 776, p. 27. doi: [10.1088/0004-637X/776/1/2710.48550/arXiv.1308.3139](https://doi.org/10.1088/0004-637X/776/1/2710.48550/arXiv.1308.3139) (cited on page 82).
- Morganti, R. et al. (Sept. 2004). 'The Unfriendly ISM in the Radio Galaxy 4C 12.50 (PKS 1345+12)'. In: *Astronomy & Astrophysics*, v.424, p.119-124 (2004) 424, p. 119. doi: [10.1051/0004-6361:20041064](https://doi.org/10.1051/0004-6361:20041064) (cited on page 82).
- Fotopoulou, C. M. et al. (Sept. 2019). 'Complex Molecular Gas Kinematics in the Inner 5 Kpc of 4C12.50 as Seen by ALMA'. In: *Astronomy & Astrophysics* 629, A30. doi: [10/gjvwdh](https://doi.org/10/gjvwdh) (cited on pages 83, 86).
- Davis, Timothy A. et al. (Oct. 2012). 'Gemini GMOS and WHT SAURON Integral-Field Spectrograph Observations of the AGN-driven Outflow in NGC 1266'. In: *Monthly Notices of the Royal Astronomical Society* 426, pp. 1574–1590. doi: [10.1111/j.1365-2966.2012.21770.x10.48550/arXiv.1207.5799](https://doi.org/10.1111/j.1365-2966.2012.21770.x10.48550/arXiv.1207.5799) (cited on page 83).
- Alatalo, K. et al. (July 2011). 'Discovery of an Active Galactic Nucleus Driven Molecular Outflow in the Local Early-type Galaxy NGC 1266'. In: *The Astrophysical Journal* 735, p. 88. doi: [10.1088/0004-637X/735/2/8810.48550/arXiv.1104.2326](https://doi.org/10.1088/0004-637X/735/2/8810.48550/arXiv.1104.2326) (cited on page 83).
- Cresci, Giovanni et al. (2015). 'The MAGNUM survey: positive feedback in the nuclear region of NGC 5643 suggested by MUSE'. In: *Astronomy & Astrophysics* 582, A63 (cited on page 83).
- Alonso-Herrero, A. et al. (June 2018). 'Resolving the Nuclear Obscuring Disk in the Compton-thick Seyfert Galaxy NGC 5643 with ALMA'. In: *The Astrophysical Journal* 859, p. 144. doi: [10.3847/1538-4357/aabe3010.48550/arXiv.1804.04842](https://doi.org/10.3847/1538-4357/aabe3010.48550/arXiv.1804.04842) (cited on page 83).
- Audibert, A et al. (2019). 'ALMA captures feeding and feedback from the active galactic nucleus in NGC 613'. In: *Astronomy & Astrophysics* 632, A33 (cited on pages 83, 86).
- Sakamoto, Kazushi et al. (Dec. 2014). 'An Infrared-luminous Merger with Two Bipolar Molecular Outflows: ALMA and SMA Observations of NGC 3256'. In: *The Astrophysical Journal* 797, p. 90. doi: [10.1088/0004-637X/797/2/9010.48550/arXiv.1403.7117](https://doi.org/10.1088/0004-637X/797/2/9010.48550/arXiv.1403.7117) (cited on pages 83, 86).
- Combes, F et al. (2013). 'ALMA observations of feeding and feedback in nearby Seyfert galaxies: an AGN-driven outflow in NGC 1433'. In: *Astronomy & Astrophysics* 558, A124 (cited on page 83).
- Leon, S. et al. (Oct. 2007). 'Nuclear Starburst-Driven Evolution of the Central Region in NGC 6764'. In: *Astronomy & Astrophysics*, Volume 473, Issue 3, October III 2007, pp.747-759 473.3, p. 747. doi: [10.1051/0004-6361:20066075](https://doi.org/10.1051/0004-6361:20066075) (cited on page 83).
- Zschaechner, Laura K. et al. (Dec. 2016). 'The Molecular Wind in the Nearest Seyfert Galaxy Circinus Revealed by ALMA'. In: *The Astrophysical Journal* 832, p. 142. doi: [10.3847/0004-637X/832/2/14210.48550/arXiv.1609.06316](https://doi.org/10.3847/0004-637X/832/2/14210.48550/arXiv.1609.06316) (cited on page 83).
- Harnett, J. I. (Aug. 1987). 'Radio Continuum Observations of Nearby Galaxies.' In: *Monthly Notices of the Royal Astronomical Society* 227, pp. 887–908. doi: [10.1093/mnras/227.4.887](https://doi.org/10.1093/mnras/227.4.887) (cited on page 83).
- González-Alfonso, E. et al. (Feb. 2017). 'Molecular Outflows in Local ULIRGs: Energetics from Multitransition OH Analysis'. In: *The Astrophysical Journal* 836, p. 11. doi: [10.3847/1538-4357/836/1/1110.48550/arXiv.1612.08181](https://doi.org/10.3847/1538-4357/836/1/1110.48550/arXiv.1612.08181) (cited on page 83).
- Oosterloo, Tom et al. (2019). 'ALMA observations of PKS 1549–79: a case of feeding and feedback in a young radio quasar'. In: *Astronomy & Astrophysics* 632, A66 (cited on pages 83, 86).
- Husemann, Bernd et al. (July 2019b). 'Jet-Driven Galaxy-scale Gas Outflows in the Hyperluminous Quasar 3C 273'. In: *The Astrophysical Journal* 879, p. 75. doi: [10.3847/1538-4357/ab24bc10.48550/arXiv.1905.10387](https://doi.org/10.3847/1538-4357/ab24bc10.48550/arXiv.1905.10387) (cited on pages 84, 86).

- Husemann, B et al. (2019a). 'The Close AGN Reference Survey (CARS)-A massive multi-phase outflow impacting the edge-on galaxy HE 1353- 1917'. In: *Astronomy & Astrophysics* 627, A53 (cited on pages 84, 86).
- Varenius, Eskil et al. (2014). 'The radio core structure of the luminous infrared galaxy NGC 4418-A young clustered starburst revealed?' In: *Astronomy & Astrophysics* 566, A15 (cited on page 84).
- Allison, J. R. et al. (May 2014). 'A Search for H I Absorption in Nearby Radio Galaxies Using HIPASS'. In: *Monthly Notices of the Royal Astronomical Society* 440, pp. 696–718. doi: [10.1093/mnras/stu28910.48550/arXiv.1402.3530](https://doi.org/10.1093/mnras/stu28910.48550/arXiv.1402.3530) (cited on page 86).
- Lira, P. et al. (Feb. 2002). 'Chandra Observations of the Luminous Infrared Galaxy NGC 3256'. In: *Monthly Notices of the Royal Astronomical Society* 330, pp. 259–278. doi: [10.1046/j.1365-8711.2002.05014.x10.48550/arXiv.astro-ph/0109198](https://doi.org/10.1046/j.1365-8711.2002.05014.x10.48550/arXiv.astro-ph/0109198) (cited on page 86).
- Urquhart, R. et al. (Apr. 2018). 'Multiband Counterparts of Two Eclipsing Ultraluminous X-ray Sources in M 51'. In: *Monthly Notices of the Royal Astronomical Society* 475, pp. 3561–3576. doi: [10.1093/mnras/sty01410.48550/arXiv.1801.01889](https://doi.org/10.1093/mnras/sty01410.48550/arXiv.1801.01889) (cited on page 86).
- Punsly, Brian and Preeti Kharb (Dec. 2016). 'The Detection of Diffuse Extended Structure in 3C 273: Implications for Jet Power'. In: *The Astrophysical Journal* 833, p. 57. doi: [10.3847/1538-4357/833/1/5710.48550/arXiv.1610.00658](https://doi.org/10.3847/1538-4357/833/1/5710.48550/arXiv.1610.00658) (cited on page 86).
- Neff, S. G. et al. (Dec. 2003). 'Radio Emission Associated with Ultraluminous X-Ray Sources in the Galaxy Merger NGC 3256'. In: *The Astrophysical Journal* 599, pp. 1043–1048. doi: [10.1086/37959610.48550/arXiv.astro-ph/0310499](https://doi.org/10.1086/37959610.48550/arXiv.astro-ph/0310499) (cited on page 86).
- Condon, J. J. et al. (May 1998). 'The NRAO VLA Sky Survey'. In: *The Astronomical Journal* 115, pp. 1693–1716. doi: [10.1086/300337](https://doi.org/10.1086/300337) (cited on page 86).
- Baan, W. A. and H.-R. Klöckner (Apr. 2006). 'Radio Properties of FIR-megamaser Nuclei'. In: *Astronomy & Astrophysics, Volume 449, Issue 2, April II 2006, pp.559-568* 449.2, p. 559. doi: [10.1051/0004-6361:20042331](https://doi.org/10.1051/0004-6361:20042331) (cited on page 86).
- Ryder, Stuart D. et al. (Apr. 1996). 'Neutral Hydrogen in the Ringed Barred Galaxies NGC 1433 and NGC 6300'. In: *The Astrophysical Journal* 460, p. 665. doi: [10.1086/17700010.48550/arXiv.astro-ph/9512043](https://doi.org/10.1086/17700010.48550/arXiv.astro-ph/9512043) (cited on page 86).
- Dumas, G. et al. (Feb. 2011). 'The Local Radio-IR Relation in M51'. In: *The Astronomical Journal* 141, p. 41. doi: [10.1088/0004-6256/141/2/4110.48550/arXiv.1012.0212](https://doi.org/10.1088/0004-6256/141/2/4110.48550/arXiv.1012.0212) (cited on page 86).
- Condon, J. J. et al. (Mar. 1996). 'A 1.425 GHz Atlas of the IRAS Bright Galaxy Sample, Part II'. In: *The Astrophysical Journal Supplement Series* 103, pp. 81–108. doi: [10.1086/192270](https://doi.org/10.1086/192270) (cited on page 86).
- Urrutia, Tanya et al. (June 2009). 'The FIRST-2MASS Red Quasar Survey. II. An Anomalously High Fraction of LoBALs in Searches for Dust-Reddened Quasars'. In: *The Astrophysical Journal* 698, pp. 1095–1109. doi: [10.1088/0004-637X/698/2/109510.48550/arXiv.0808.3668](https://doi.org/10.1088/0004-637X/698/2/109510.48550/arXiv.0808.3668) (cited on page 86).
- Greene, Jenny E. et al. (Feb. 2012). 'A Spectacular Outflow in an Obscured Quasar'. In: *The Astrophysical Journal* 746, p. 86. doi: [10.1088/0004-637X/746/1/8610.48550/arXiv.1112.3358](https://doi.org/10.1088/0004-637X/746/1/8610.48550/arXiv.1112.3358) (cited on page 86).
- Clemens, M. S. et al. (Jan. 2008). 'Modeling the Spectral Energy Distribution of ULIRGs. I. The Radio Spectra'. In: *Astronomy & Astrophysics, Volume 477, Issue 1, January I 2008, pp.95-104* 477.1, p. 95. doi: [10.1051/0004-6361:20077224](https://doi.org/10.1051/0004-6361:20077224) (cited on page 86).
- Clemens, M. S. et al. (June 2010). 'Starburst Evolution: Free-Free Absorption in the Radio Spectra of Luminous IRAS Galaxies'. In: *Monthly Notices of the Royal Astronomical Society* 405, pp. 887–897. doi: [10.1111/j.1365-2966.2010.16534.x10.48550/arXiv.1002.3334](https://doi.org/10.1111/j.1365-2966.2010.16534.x10.48550/arXiv.1002.3334) (cited on page 86).
- Davies, Rebecca L. et al. (Oct. 2017). 'Dissecting Galaxies: Separating Star Formation, Shock Excitation and AGN Activity in the Central Region of NGC 613'. In: *Monthly Notices of the Royal Astronomical Society* 470, pp. 4974–4988. doi: [10.1093/mnras/stx155910.48550/arXiv.1707.03404](https://doi.org/10.1093/mnras/stx155910.48550/arXiv.1707.03404) (cited on page 86).
- Drake, Catherine L. et al. (Sept. 2004). 'Radio-Excess IRAS Galaxies. III. Radio Properties'. In: *The Astronomical Journal* 128, pp. 969–984. doi: [10.1086/423219](https://doi.org/10.1086/423219) (cited on page 86).
- Shimizu, T. Taro et al. (Apr. 2017). 'Herschel Far-Infrared Photometry of the Swift Burst Alert Telescope Active Galactic Nuclei Sample of the Local Universe - III. Global Star-Forming Properties and the Lack of a Connection to Nuclear Activity'. In: *Monthly Notices of the Royal Astronomical Society* 466, pp. 3161–3183. doi: [10.1093/mnras/stw326810.48550/arXiv.1612.03941](https://doi.org/10.1093/mnras/stw326810.48550/arXiv.1612.03941) (cited on page 86).
- Marvil, Joshua et al. (Jan. 2015). 'Integrated Radio Continuum Spectra of Galaxies'. In: *The Astronomical Journal* 149, p. 32. doi: [10.1088/0004-6256/149/1/3210.48550/arXiv.1408.6296](https://doi.org/10.1088/0004-6256/149/1/3210.48550/arXiv.1408.6296) (cited on page 86).

- Ohyama, Youichi et al. (June 2015). 'Infrared and X-Ray Evidence of an AGN in the NGC 3256 Southern Nucleus'. In: *The Astrophysical Journal* 805, p. 162. doi: [10.1088/0004-637X/805/2/16210.48550/arXiv.1503.08555](https://doi.org/10.1088/0004-637X/805/2/16210.48550/arXiv.1503.08555) (cited on page 86).
- Lanz, Lauranne et al. (July 2016). 'Star Formation Suppression Due to Jet Feedback in Radio Galaxies with Shocked Warm Molecular Gas'. In: *The Astrophysical Journal* 826, p. 29. doi: [10.3847/0004-637X/826/1/2910.48550/arXiv.1511.05968](https://doi.org/10.3847/0004-637X/826/1/2910.48550/arXiv.1511.05968) (cited on page 86).
- Gruppioni, C. et al. (June 2016). 'Tracing Black Hole Accretion with SED Decomposition and IR Lines: From Local Galaxies to the High-z Universe'. In: *Monthly Notices of the Royal Astronomical Society* 458, pp. 4297–4320. doi: [10.1093/mnras/stw57710.48550/arXiv.1603.02818](https://doi.org/10.1093/mnras/stw57710.48550/arXiv.1603.02818) (cited on page 86).
- Papaloizou, J. C. B. and J. E. Pringle (Apr. 1983). 'The Time-Dependence of Non-Planar Accretion Discs'. In: *Monthly Notices of the Royal Astronomical Society* 202.4, pp. 1181–1194. doi: [10.1093/mnras/202.4.1181](https://doi.org/10.1093/mnras/202.4.1181). (Visited on 04/29/2023) (cited on page 88).
- Pringle, J. E. (Oct. 1992). 'A Simple Approach to the Evolution of Twisted Accretion Discs'. In: *Monthly Notices of the Royal Astronomical Society* 258.4, pp. 811–818. doi: [10.1093/mnras/258.4.811](https://doi.org/10.1093/mnras/258.4.811). (Visited on 04/29/2023) (cited on page 88).
- Nixon, Chris and Andrew King (2016). 'Warp Propagation in Astrophysical Discs'. In: vol. 905, pp. 45–63. doi: [10.1007/978-3-319-19416-5_2](https://doi.org/10.1007/978-3-319-19416-5_2). (Visited on 04/29/2023) (cited on page 88).
- Martin, Rebecca G. et al. (Apr. 2019). 'Generalised Warped Disk Equations'. In: *ApJ* 875.1, p. 5. doi: [10.3847/1538-4357/ab0bb7](https://doi.org/10.3847/1538-4357/ab0bb7). (Visited on 04/29/2023) (cited on page 88).